The Seismic Imaging and Interpretation of Faults: A Case Study from the Snøhvit Field, Barents Sea

by

Jennifer Elizabeth Cunningham MSc

Thesis submitted in fulfilment of
the requirements for degree of
PHILOSOPHIAE DOCTOR
(PhD)

University
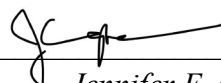of Stavanger

FACULTY OF SCIENCE AND TECHNOLOGY

DEPARTMENT OF ENERGY RESOURCES

2020

Preface

This thesis is submitted in fulfilment of the requirements for the degree of *Philosophiae Doctor* (PhD) at the university of Stavanger, Norway. This work was completed between March 2016 and October 2020 while I was enrolled in the PhD program in the Department of Energy Resources, Faculty of Science and Technology at UiS. This PhD was funded by the Research Council of Norway . My main supervisor is Professor Nestor Cardozo (UiS) and my co-supervisor is Dr Chris Townsend (Associate Professor at UiS). Dr Wiktor Weibull (UiS), Dr David Iacopini (formerly University of Aberdeen and currently University of Naples), Dr Richard Callow (Equinor) and Gard Ole Wærum (Equinor) were significant collaborators throughout this research. During my PhD I acted as a PhD Contact Person for PhD candidates in the Departments of Energy Resources and Energy and Petroleum Technology. This role included planning lunch seminars, department-wide sporting events, social events, conducting surveys to improve PhD studies, being the main communication hub for PhD candidates and being a friendly face for PhD candidates if they needed help or advice.

This thesis contains one published article and two manuscripts which were submitted for publication before the submission of this dissertation. Several aspects of the work have also been presented at industrial and academic conferences. The first part of this thesis introduces the general problems, motivation for the work, the data being used, methodology, results, discussion, conclusions and recommendations for future work. The second part is a compilation of the three papers which form the main body of the thesis. The appendices provide supplementary material.

Jennifer E. Cunningham
Stavanger, October 6th, 2020

Abstract

An accurate understanding of faults in the subsurface is critical to successful petroleum exploration and production. Faults define sediment distribution pathways during deposition, act as barriers or conduits to fluid flow, and can define or compromise hydrocarbon traps. Faults are commonly analysed in the petroleum industry using reflection seismic data, and more rarely core or borehole image data. Outcrop analogues are used to provide a more complete understanding of fault rock morphologies and properties. In seismic data however, faults are often imaged as discontinuities where geological horizons are vertically and horizontally displaced. Due to the limited resolution of seismic data (typically tens of metres) comparatively little can be concluded about fault morphology, internal structure or the detailed interaction of faults with seismic waves.

The first paper in this thesis focuses on bridging the knowledge gap in the seismic imaging of faults by analysing how the seismic processing methods of incidence angle stacking and azimuthal separation influence fault imaging. This first paper also studies the relationship between fault orientation and seismic acquisition direction, and the impact on the seismic imaging of faults in the subsurface. The paper also demonstrates that the internal complexity of faults can influence the dominant seismic frequencies observed in and adjacent to complex fault zones.

The second paper in this dissertation integrates established and newly developed analyses in fault interpretation and seismic imaging. Analyses of throw, dip distortion, seismic attributes, unsupervised fault facies and seismic amplitudes in seismic fault analysis were applied. These attributes were compared to establish the geological significance of the seismic signature in and around faults. The paper proposed a linkage between unsupervised seismic fault facies, throw and dip separation gradient which are inherently linked to the mechanical stratigraphy

which controls fault propagation and growth. Systematic variations in observed seismic amplitudes were found to be related to fault propagation folding and the formation of synclines and anticlines. The analyses applied in this paper can provide a more concrete methodology for analysing and understanding fault systems and when compared to conventional seismic interpretation methods, it can yield far more information on fault morphologies and interactions.

Faults in seismic data are commonly interpreted on a combination of reflection seismic data and attributes derived from the same reflection data. Fault sticks are typically interpreted on vertical sections through the data volumes and then these sticks are gridded into fault surfaces. This methodology has been in place for decades, but an investigation into the impact of fault and horizon interpretation methodologies on the geological accuracy of the resulting fault surfaces has not been published. The third paper in this dissertation tests five interpretation experiments with the aim of uncovering the impact of interpretation strategy on fault and horizon morphology, fault length, and vertical displacement. The most and least successful interpretation methods were further examined to demonstrate the impact of interpretation method on geological modelling workflows and the calculation of hydrocarbon volumes. This paper proves the importance of a denser fault interpretation methodology on the resulting structural analysis, geomodelling and the estimation of petroleum reserves. It also suggests a best practice on how to approach the interpretation and modelling workflow.

Having the best possible understanding of the imaging, seismic signature and interpretation of faults in seismic data is crucial for geoscientists working in hydrocarbon exploration and production. This thesis aims to strengthen the geoscientific understanding of faults and provides clear observations, conclusions and recommendations that can improve the use of existing seismic datasets and optimise the acquisition and processing of future seismic surveys.

Acknowledgements

List of Papers

Conference presentations and posters

Cunningham, Jennifer; Cardozo, Nestor; Weibull, Wiktor; Iacopini, David. (2019). How do seismic survey parameters and artefacts affect the imaging of normal faults? A case study from the Snøhvit Field, Barents Sea. Tectonic Studies Group AGM; 2019/14/01 – 2019/16/01. Oral Presentation.

Cunningham, Jennifer; Cardozo, Nestor; Townsend, Chris; Iacopini, David, Wærum, Gard Ole. (2018). Deformation, amplitude and unsupervised fault facies analysis of normal faults from the Snøhvit Field, Barents Sea. FORCE Challenges Related to Fault Modelling; 2018/20/06. Oral presentation.

Cunningham, Jennifer; Cardozo, Nestor; Iacopini, David, Townsend, Chris; Wærum, Gard Ole. (2018). Deformation analysis and unsupervised fault facies classification of normal faults from the Snøhvit Field, Barents Sea. EGU Annual General Meeting, Vienna; 2018/08/04 – 2018/13/04. Oral presentation EGU2018-14044.

Cunningham, Jennifer; Cardozo, Nestor; Townsend, Chris. (2017). A detailed analysis of fault morphology using seismic from the Snøhvit Field, Barents Sea. FORCE Fault Compartments Conference– 2017-24/05. Oral presentation.

Cunningham, Jennifer; Cardozo, Nestor; Townsend, Chris. (2016). An in-depth seismic analysis of fault architecture: A case study from the Askeladd Field area (SW Barents Sea). NGF Production Geoscience Conference, Geological Society of Norway 2016-01/11- 2016-02/11. Oral presentation.

Abbreviations

AVO- Amplitude versus Offset

DD- Dip distortion

CMY- Cyan, magenta, yellow (colour blend)

ECQ- Exponential constant Q

FD- Frequency decomposition

FE- Fault enhancement (attribute)

Fm – Formation

FW- Footwall

HW- Hanging wall

JL- Juxtaposed lithology

OBC- Ocean bottom cable

OBS- Ocean bottom seismic

P-wave- Primary wave

PS-wave- Converted wave

PSDM- Pre-stack depth migration

RMS- Root mean squared amplitude (attribute)

RGB- red, green blue (colour blend)

S-wave- Shear Wave

SOS- Structurally Oriented Semblance (attribute)

Table of Contents

1 Introduction

1.1 Faults

Understanding the location and geometry of faults in the subsurface is of vital importance to the petroleum industry due to the role of faults in either sealing or juxtaposing hydrocarbon bearing reservoirs. Understanding fault morphologies in the subsurface also allows us to fully understand structural histories and the systems forming around those structures. Faults can also control sediment distribution pathways during reservoir deposition and can act as key hydrocarbon trapping elements (e.g. Athmer *et al.* 2010; Athmer & Luthi 2011). The most common method of imaging faults in the subsurface on a large scale (km) is 2D, 3D or even 4D reflection seismic data. In seismic data faults are imaged as either discontinuities where reflectors are displaced (referred to in this dissertation as "discontinuity fault imaging"), or as a plane with its own seismic reflection (referred as "fault plane imaging"). Fault plane imaging is created by the acoustic impedance contrast between the deformed rock within the fault zone and the surrounding undeformed strata. Seismic data, although lacking in small scale detail (cm-m), provides a broad 3D understanding of fault geometry, and can be used to reconstruct fault displacement profiles, the history of fault interaction and linkage, and even fault facies distributions (if also incorporating nearby well data). In seismic data faults are usually interpreted in vertical sections as discontinuities in seismic reflectors where the fault planes are commonly interpreted as "sticks", which can be gridded into a 3D surface representation of the fault plane. In reality, faults are 3D rock bodies (rather than planar structures) with complex internal structures and properties. Fault zones are made up of a core where the majority of displacement accumulates, and this is surrounded by a zone of damaged rock. These faulted zones often contrast strongly with the surrounding unfaulted strata (Caine *et al.* 1996; Wibberley *et al.* 2008). There is large variation in fault rocks which can greatly influence fluid flow. Fault zone

lithologies and their petrophysical properties control the potential for fluid flow or sealing across a fault and are crucial for the analysis of fault bounded or modified hydrocarbon traps. Depending on the lithological composition of the hanging wall (HW) and footwall (FW) strata mm-cm scale deformation bands can form in damage zones which can greatly reduce the effective permeability and therefore influence the fluid flow across a fault (e.g. Aydin 1978, 1999; Antonellini & Aydin 1994; Fossen & Bale 2007; Rotevatn *et al.* 2007). However, in seismic data, most of the small scale (cm-m) detail is not imaged due to the seismic resolution of the data (e.g. Townsend *et al.* 1998; Dutzer *et al.* 2010; Long & Imber 2010). Figure 1 illustrates the detail of an outcropping fault from the Gulf of Corinth Greece which is compared to the simplicity of a fault in modern high quality-seismic data from the Snøhvit Field (Barents Sea, Norway). Based on knowledge of faults in outcrop, it is possible to speculate that the fault in the Snøhvit dataset is likely to be much larger in both length and depth and more internally complex than the example from the Gulf of Corinth but a simple discontinuity is the only aspect which is captured in the seismic data.
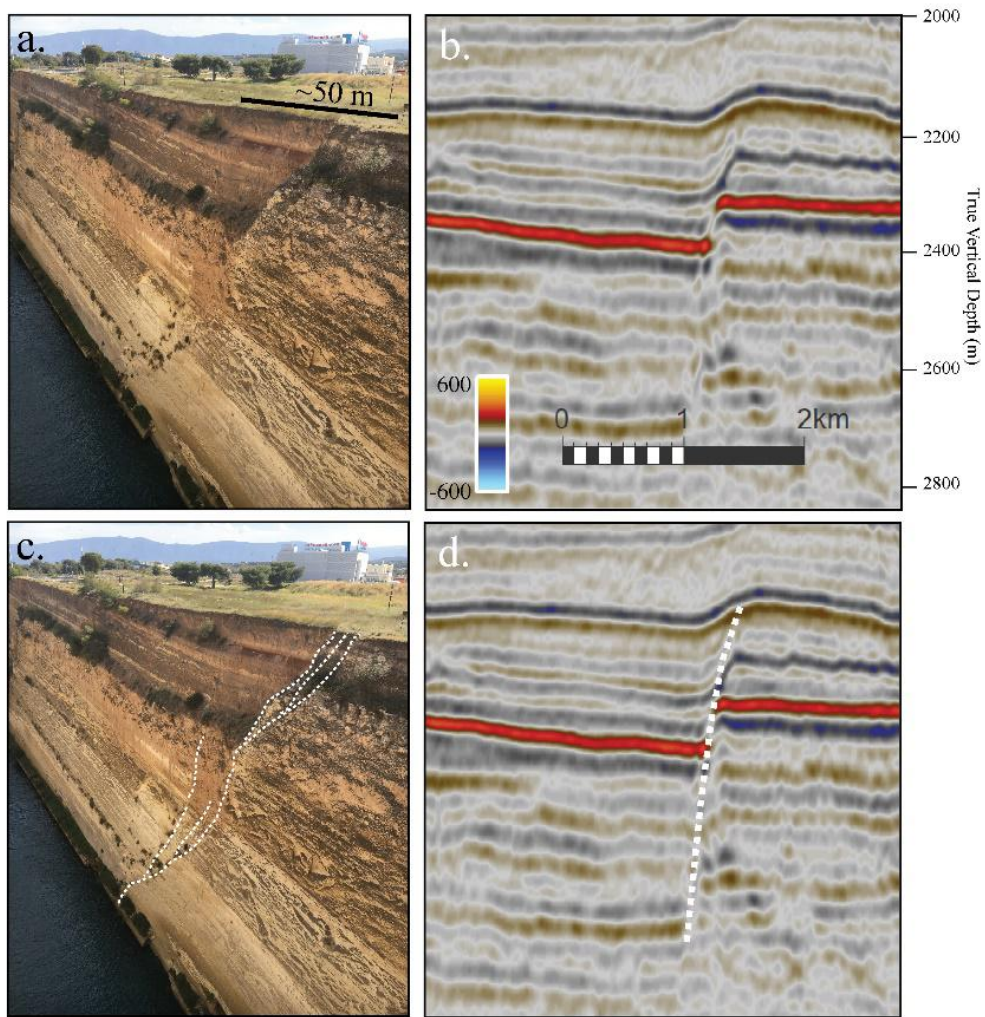
Figure 1: a. An image of a fault taken in the Corinth region of Greece (Photo from the personal collection of the author), b. an image of a normal fault in seismic data from the Snøhvit field, Barents Sea, Norway. The seismic is from IL 3443 of volume ST15M04 in the Snøhvit Field. c. and d. Images of a. and b. respectively with fault interpretations overlaid.

1.2 Fault elements, terminology and architecture

Faults have a substantial dictionary of terminology associated with describing their size, displacement and morphology (Peacock *et al.* 2000). As mentioned, in seismic data faults are commonly interpreted in vertical sections as 2D fault sticks which are then gridded into fault surfaces. This thesis only analyses normal faults in which the hanging wall is displaced downwards relative to the footwall. In an isolated normal fault, as seen in Figure 2, dip separation (displacement) is greatest at a fault centre and decreases gradually to zero at the fault tip line (e.g. Rippon 1985; Barnett *et al.* 1987; Walsh & Watterson 1987, 1990). In seismic data these patterns can be observed by projecting the displaced horizon FW and HW onto the fault plane diagram as the respective cutoff-lines (e.g. Gill 1935; Hills 1940; Nicol *et al.* 1995; Knipe 1997; Davatzes & Aydin 2005). The distance between the FW and HW cutoff-lines measured along the dip direction is the dip separation and is a function of fault displacement (e.g. Gill 1935; Hills 1940, Fig. 2; Muraoka & Kamata 1983). The vertical and horizontal components of the dip separation are the throw and heave respectively (e.g. Gill 1935; Hills 1940; Fig. 2, left inset). This relationship is also explained in the graphical inset of Fig. 2. Fault length and width are defined as the horizontal distances along the strike and dip direction between the points of zero displacement on the interpreted fault (tip line). Fault length and width are used to define the maximum extent of displacement due to faulting (Fig. 2).

Although isolated normal faults are the simplest to understand (Rippon 1985; Barnett *et al.* 1987; Walsh & Watterson 1987), faults occur more commonly as a part of an interlinked network of surfaces. They initiate as a series of small single faults which grow and propagate until the individual displacements of two or more growing faults begin to affect each other (Peacock & Sanderson 1991; Childs *et al.* 1995; Peacock *et al.* 2000, 2017; Peacock 2002). When several faults propagate, they can eventually grow to connect and to form a linked system (e.g. Pollard &

Aydin 1984; Walsh & Watterson 1991; Crider & Pollard 1998). Linkages are defined as "hard" where two faults intersect (to form a branch line) or "soft", when the interaction between the two faults is achieved by the ductile strain of a rock wall and without a visible intersection (Walsh & Watterson 1991). When two synthetic normal faults overstep one another in map view, they form ramps of strained rock between the overlapping fault segments. This structure is called a relay ramp (or simply, a relay) and is an example of a soft linkage (Chadwick 1986; Larsen 1988; Walsh & Watterson 1991; Peacock & Sanderson 1994).
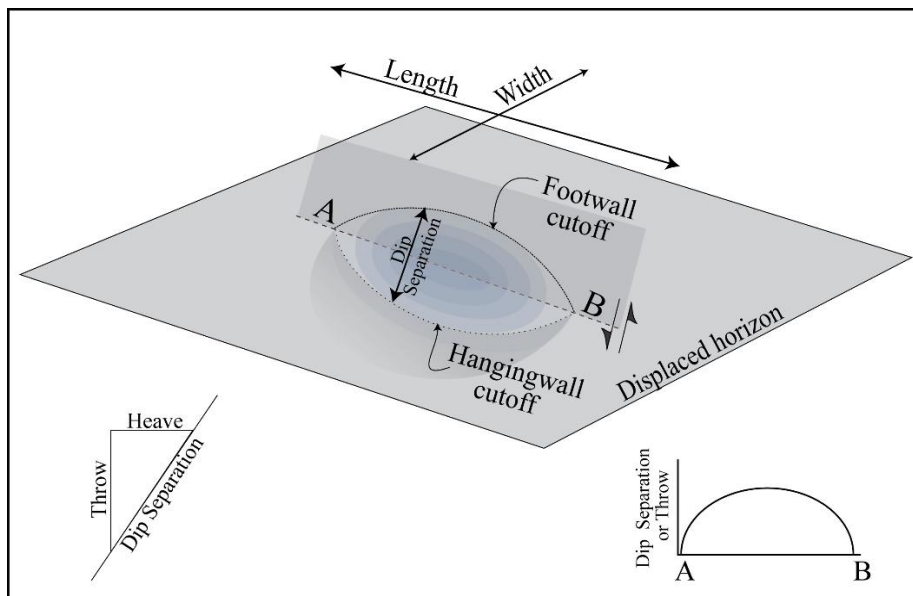
Figure 2: 3D diagram of a normal fault showing the field of displacement, hanging wall and footwall cutoff-lines, fault length and width, dip separation, throw and heave on a schematic of an isolated normal fault. The graphical inset represents throw or dip separation along the length of the fault plane. Concepts in this schematic are based on the findings of Gill (1935), Hills (1940), Rippon 1985; Watterson 1986; Barnett *et al.* 1987; Walsh & Watterson 1987, 1988, 1990.

1.3 State of the art fault analyses: Interpretation, seismic volume analysis and forward modelling

Structural analysis of faults in seismic data is a well-established method used by structural and petroleum geologists (e.g. Badley *et al.* 1990; Freeman *et al.* 1990; Townsend *et al.* 1998; Rotevatn *et al.* 2007; Yielding & Freeman 2016). Typical interpretation techniques involve interpreting fault sticks on vertical section, before gridding the sticks into 3D surfaces. Displacement can then be estimated by comparing horizon intersections with the faults. Badley et al. (1990) pioneered a systematic approach to the seismic interpretation of faults using fault displacement analysis and horizon correlations across multiple intersections. Freeman et al (1990) described the use of fault displacement in the quality control process of fault interpretation by analysing patterns in HW and FW cutoff-lines. Longitudinal (LS) and shear strain (SS), the along dip and along strike dip separation gradients, respectively, can be used to improve the quality control process of fault interpretation by assigning a geologically realistic upper and lower limit of strain in order to see inaccurate interpretations (Freeman *et al.* 2010). More recently issues regarding uncertainty and bias in seismic analysis have also been analysed and proved that fault interpretation is greatly impacted by interpretation biases (e.g. Bond 2015; Alcalde *et al.* 2017; Schaaf & Bond 2019). Long & Imber (2011, 2012) took fault interpretation to a new level with the introduction of seismic reflector dip sampling techniques to generate maps of fault related dip (dip distortion) in both a relay and multi fault array. Dutzer *et al.* (2010) used seismic attributes to study the architecture of faults and to analyse sealing potential.

A number of studies have attempted to further characterize faults in seismic data and to improve our understanding of the seismic imaging of faults (both through actual fault plane imaging and through the imaging of discontinuities in seismic reflectors). Townsend *et al.* (1998) was the

6

first study to offer a comprehensive look into faults using amplitude analysis in seismic data. Iacopini & Butler (2011) and Iacopini *et al.* (2012) combined semblance, tensor and instantaneous phase attributes, opacity filtering and frequency decomposition to characterize the deformation patterns in thrust faults in a deep marine environment. Iacopini *et al.* (2016) cross plotted these same attributes to investigate the seismic expression of fault damage. They also suggest the concept of seismic disturbance zones (SDZs) and proposed the idea of using unsupervised seismic fault facies to identify and characterize them.

A complementary method that can be applied to fault analysis in seismic is 2D and 3D seismic forward modelling (Carcione *et al.* 2002 and sources cited within). In real seismic data, the internal structure of faults, the rock properties and the way seismic waves interact with the fault zone are poorly constrained. The advantage of using seismic modelling is that most or all of the geological and acoustic properties of a geo-model are assumed and assigned, the reflection and refraction patterns of waves can often be determined, and the processing workflows can be optimized to match the objectives of the study. Synthetic modelling studies support a correlation between amplitude variation in faults and fault related deformation and have analysed the effects of scale, illumination direction and frequency on fault imaging and have been used in a study of fluid flow in a relay structure (Botter *et al.* 2014, 2016b, 2017a).

Purpose of the study:

The purpose of this work is to provide a better understanding of the seismic imaging, characterization of fault signal and interpretation of faults through the analysis of real seismic data from the Snøhvit Field, Barents Sea. This work complements and follows a study that was carried out at the University of Stavanger in the PhD Dissertation of Charlotte Botter (2016) which focused on forward seismic modelling. Following on from this, the current work aims to bridge the gap between the findings of forward modelled fault imaging and real data.

We will focus on aspects of seismic survey geometry, seismic data processing, the characterization of the seismic signal in and around faults, and the effect of interpretation methods on faults in seismic data in this thesis. The thesis is comprised of three papers:

Paper I: *Investigating the Seismic Imaging of Faults Using PS data from the Snøhvit Field, Barents Sea and Forward Seismic Modelling.*

Paper II: *Fault Deformation, Seismic Amplitude and Unsupervised Fault Facies Analysis: Snøhvit Field, Barents Sea.*

Paper III: *The Impact of Seismic Interpretation Methods on the Analysis of Faults: A Case Study from the Snøhvit Field, Barents Sea.*

1.4 An introduction to the methodology

A fault analysis workflow has been developed and applied to real data from the Snøhvit Field (Papers I-III) and 2D synthetic seismic data (Paper I only). The workflow was designed to improve our understanding of fault imaging in seismic from both an imaging and an interpretation perspective.

The workflow has been subdivided into processes that are seismic volume based and ones that are interpretation based (Fig. 3). Paper I is a seismic volume focused study that aims to understand the discontinuity fault imaging resulting from seismic processing methods such as incidence angle stacking and azimuthal separation. Paper I also investigates how the internal complexity of fault zones influence the observed frequencies in the fault zone and adjacent to the fault zone just outside of the intersection of the horizontal reflection with the fault zone. Paper II applies both seismic volume and interpretation-based analyses with the aim to further understand the seismic signal surrounding faults and to classify that signal using unsupervised seismic fault facies. Finally, Paper III concentrates on interpretation techniques and their implication on fault studies and geomodelling. Each aspect of the

8

workflow will be introduced in section 3 (Methodology), while more specific information and the parameters used are described in the papers pertaining to each stage of the workflow.

Fault analysis workflow	Paper 1	Paper 2	Paper 3
Seismic volume based analyses			
Data conditioning		✓	
Attribute study	✓	✓	
Fault facies classification		✓	
Amplitude study		✓	
AVO attribute stack analysis	✓		
Incidence angle/ azimuthal separation analysis	✓		
Frequency study	✓		
Interpretation based analyses			
Horizon and fault interpretation		✓	✓
Horizon/ structural map analysis		✓	✓
Fault morphology/ length/ interaction analysis		✓	✓
Throw analysis		✓	✓
Dip distortion analysis		✓	
Juxtaposed lithology analysis		✓	✓
Study of dip separation gradient			✓
Geological and petrophysical modelling		✓	✓
Calculation of petroleum reserves			✓

Figure 3: The fault analysis workflow. a. Seismic volume-based analyses. b. Interpretation based analyses. Each aspect of the workflow that is incorporated into each paper is defined in the three columns on the right (Papers 1-3).

1.5 Doctoral candidate contributions to the work

The writing of this thesis was completed by Jennifer Cunningham, the doctoral candidate. The three papers contained in this thesis were a combined effort with contributions from additional scientists. Here the authors contributions to each individual paper will be clarified.

Paper I: The analysis of the Snøhvit case study data using attributes and frequency decompositions was completed by the author. The forward seismic modelling was designed by Wiktor Weibull, the author, and Nestor Cardozo with the final forward modelling and processing being completed by Wiktor Weibull. The final comparison of the two data types and writing of the paper was completed by the candidate with advice and minor contributions from Nestor Cardozo, Wiktor Weibull and David Iacopini (co-authors in the paper).

Paper II: The complete fault analysis workflow was designed and implemented by the candidate with scientific contributions from Nestor Cardozo. Co-author Chris Townsend aided with structural modelling aspects. Gard Ole Wærum provided seismic processing and field specific assistance from within Equinor when needed. The final compilation of the paper was completed by the author with scientific and editorial contributions from all co-authors.

Paper III: The interpretation experiments and the fault analysis workflow were designed by the candidate with scientific contribution from Nestor Cardozo. The workflow was implemented by the candidate with some assistance from co-authors Chris Townsend and Richard Callow. Chris and the candidate collaborated on the design and application of the geomodelling. Richard aided in the execution, and upscaling of the petroleum reserve calculations and contributed on discussions related to the petroleum implications. The candidate drafted the manuscript and figures with scientific contributions and proofing from all co-authors.

2 The data

2.1 Snøhvit case study

2.1.1 The data

Two seismic data sets were used in the analysis of the Snøhvit Field. In Paper I, ocean bottom seismic (OBS) converted wave (PS) data volume ST15M01 was used to understand the effect of incidence angle stacking and azimuthal separation on the imaging of faults. A study on the effect of fault complexity on frequency was also carried out. The data were collected in 2013 by Magseis for Statoil AS (currently Equinor AS) and their partners in the Snøhvit Field. To acquire the data, cables were oriented E-W on the ocean floor in order to optimize the imaging below a shallow gas cloud in the field. Seismic acquisition vessels also travelled in an E-W-E trajectory. The data were collected in both PP and PS time and depth but in this study, only PS in time were used to avoid potential artefacts caused by stretching of amplitudes. During processing, the data were separated into E and W azimuth and near, mid, far, ultra-far partial incidence angle stack and full stack volumes.

In Papers II and III merged seismic volume ST15M04 of five 3D seismic streamer surveys was used. The data is a zero-phase, pre-stack depth migrated (PSDM) dataset that was available in partial and full angle stacks. For both Paper II and III it is assumed that the velocity model used in the PSDM was correct and that the vertical scale of the data is a true representation of depth. The ST15M04 near stack volume was the best option when imaging faults so this volume was used in the interpretation for these studies.

In both ST15M01 and ST15M04 a downwards increase in acoustic impedance is represented as a red peak while a downward decrease in

acoustic impedance is represented as a blue trough. The inline and crossline spacing in both datasets is 12.5 m.

2.1.2 Geological history of the Snøhvit Field and Hammerfest Basin

Snøhvit is a gas and condensate field in the Hammerfest Basin on the SW margin of the Barents Sea (Fig. 4a; Linjordet & Olsen 1992). The Hammerfest Basin is an ENE-WSW trending ellipsoidal shaped basin that is approximately 70 by 150 km in size (Fig. 4b). The basin is bound by the Loppa High to the north, Finnmark Platform to the southeast and Tromsø Basin to the west (Fig. 4a). Rifting in the basin began in the Late Carboniferous and continued through to the Early Permian causing the formation of the main basin bounding faults (Gudlaugsson *et al.* 1998). A second phase of rifting in the Early Jurassic reactivated basin bounding faults, formed an E-W trending fault system and created differential subsidence across the basin (Fig. 4b, Sund *et al.* 1984; Linjordet & Olsen 1992; Doré 1995; Ostanin *et al.* 2012). These E-W trending faults define the structural traps for gas and condensate (Sund *et al.* 1984) and are the focus of this thesis. Sediment accumulations are thicker in the W than in E due to differential subsidence across the Hammerfest Basin in the second phase of rifting (Linjordet & Olsen 1992). The system has three potential source rocks: Triassic Kobbe and Snadd fms, and the Jurassic Hekkingen Fm (Fig. 4c; Worsley *et al.* 1988; Linjordet & Olsen 1992; Ostanin *et al.* 2012). The reservoirs are the Jurassic Tubåen, Nordmela and Stø fms and the seals are the Jurassic Fuglen and Hekkingen fms.

2.2 Forward modelled 2D seismic data (Paper I)

2D seismic forward modelling can be used to systematically investigate the seismic imaging of faults. The acoustic properties and geometry of geological strata are defined in the forward modelling workflow, whereas these properties are less well constrained in real seismic data. In addition, seismic forward modelling makes it possible to accurately
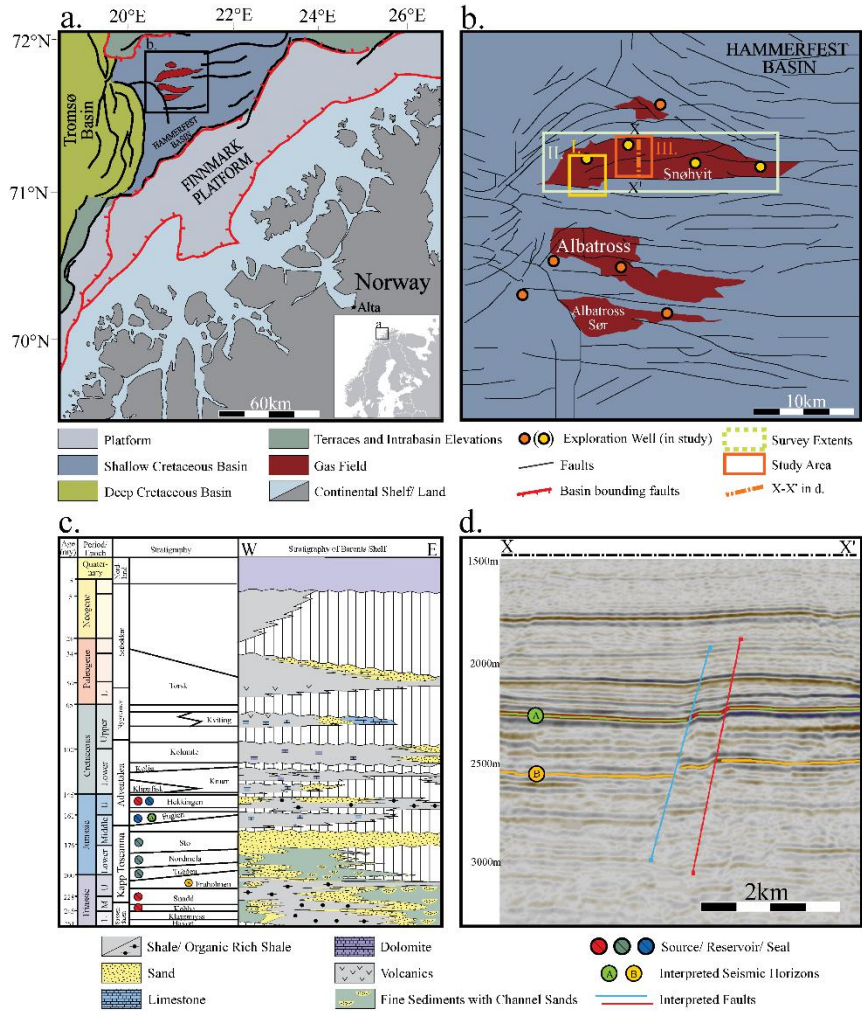
Figure 4: a. Geologically significant structures offshore northern Norway. The area in b is highlighted by a black box in the Hammerfest Basin (Map modified from NPD Factmaps). b. The main gas fields of the Hammerfest Basin, including the Snøhvit field in the north (Map modified from Ostanin et al. (2012). The areas of interest for papers I, II and III are labelled as yellow, white and orange boxes respectively. c. Lithostratigraphic column of the Barents shelf with labels of the main source, reservoir and seal of the Snøhvit field. Modified from Ostanin et al. (2012). d. N-S seismic section 3342 from volume ST15M04 (Paper II) exhibits an example of two important faults in the field as well as the Top Fuglen and Top Fruholmen surfaces (yellow and green coloured respectively).

trace the refraction patterns of waves interacting with geological boundaries (e.g. Carcione *et al.* 2002; Botter *et al.* 2014, 2016a, 2017a). In Paper I, two forward seismic modelled experiments are compared with real seismic data from the Snøhvit Field. Experiment 1 was designed to test the effect of incidence angle and azimuthal separation on discontinuity fault imaging. Experiment 2 tests the effect of fault zone complexity on the observed frequencies in and around faults (Fig. 5).

2.2.1 Experiment 1

In this experiment, the data acquisition and processing were designed to test how stacks of incidence angle and azimuthal separation influence the imaging of discontinuities created in horizons due to faulting where no fault plane reflection is captured (discontinuity fault imaging) and to understand how the data compares with the Snøhvit case study. To forward model seismic data, a finite-difference solution to the elastic wave equation was used to generate synthetic seismic data across a 14 km long, relatively simple elastic model (Virieux 1986). A single geological layer with a thickness of 300 m was placed at 2500 m depth and was displaced 150 m by a 55° westward dipping normal fault to mimic the observed faults in the Snøhvit Field (Figs 5a & 6). In the model the fault is a discontinuity rather than a fault body with distinct properties (Figs 5a & 6). Removing the actual fault body from modelling was a conscious decision since there is still a discontinuity which mimics a fault but is also more in line with what is observed in the Snøhvit data. A P-wave velocity model was generated using upscaled P-wave data from the nearby well, NO 7121/5-1 (Figs 4b and 6a, d), while an S-wave velocity model (Fig. 6b, e) was generated using half of the P-wave velocity. A model of background density was extracted from the P-wave data using Gardner's relation (Fig. 6c, f):

$$\rho = \alpha V_P^{\beta}$$
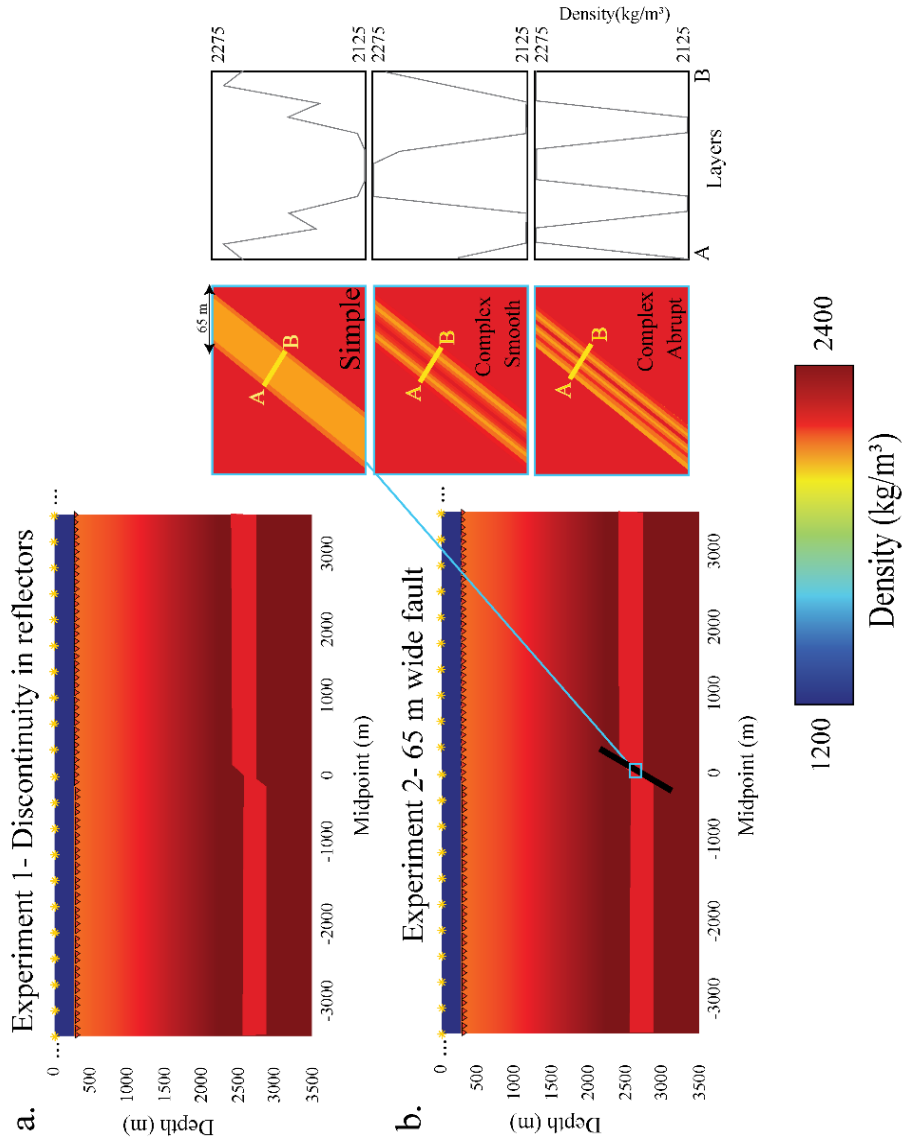
Figure 5: Geological models and fault velocity transitions for the synthetic seismic modelling experiments in Paper I. a. Experiment 1 and b. Experiment 2. For more information on the seismic acquisition process refer to Paper I.

15
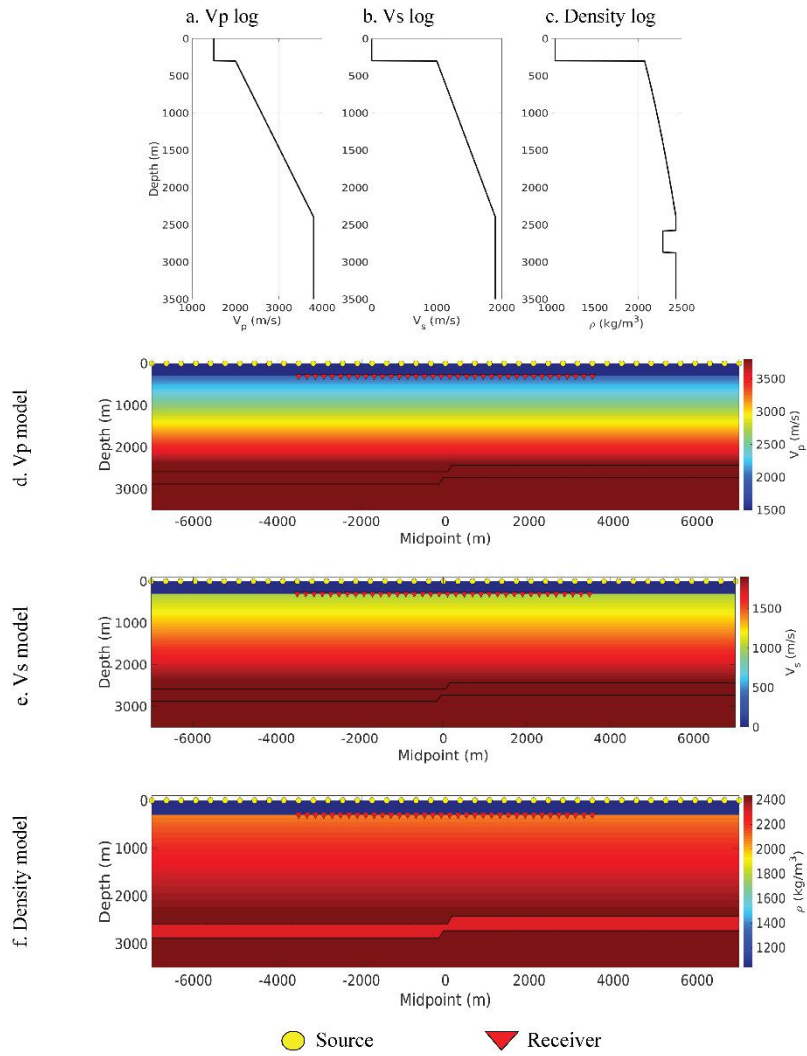
The data

Figure 6: The Vp (a), Vs (b) and density (c) data extracted from wellbore 7121/5-1 and the respective Vp (d), Vs (e) and density (f) models used in the seismic forward modelling.

The data

The displaced geological layer in the model was allocated a density contrast of -150 kg/m^3 with respect to the background density (Fig. 6c, f). To acquire the forward modelled data, 41 sources were placed at 0 m depth (on top of a water column) and positioned between +/- 7000 m midpoint distance in the models (350 m spacing between each making the model 14 km long). 1401 dual component receivers (x and z) were placed with a 5 m spacing on the seabed below a 300 m water column between +/-3500 m midpoint distance in the models (Fig. 5a, 6). In the processing of the data, the direct wave was muted, and the data separated into east (receivers to the right of the source) and west (receivers to the left of the source) azimuths. The data were also separated into partial incidence angle stacks (near, mid and far) and full stacks (azimuth and stacking to match the Snøhvit case study). Reverse time migration and a smoothed velocity model were used in the migration of the data (Hokstad *et al.* 1998; Weibull & Arntsen 2013). Data are also available as images highlighting individual source locations and videos which are found in the supplementary material of Paper I. More specific information on modelling methods can be found in Paper I (Section 3.2.1 and Supplementary Materials 1-3).

2.2.2 Experiment 2

This experiment was designed to investigate how changes in the layering of a fault zone can influence dominant frequencies of faults in seismic data (O'Doherty & Anstey 1971; Anstey & O'Doherty 2002; Weibull *et al.* 2019). In this experiment all aspects of the geological model mimicked experiment 1 (2.2.1 and Fig. 6) except that in this case a 65 m thick fault body was modelled in the data (Fig. 5b). Three seismic sections were acquired using three slightly different density transitions in the 65 m wide fault. The first fault is a simple homogenous fault zone model (Fig. 5b, top). The second and third faults were complex, heterogeneous fault zone models exhibiting smooth and abrupt velocity transitions respectively (Fig. 5b, middle and bottom). The source/

The data

receiver placement and the seismic processing were the same as for Experiment 1 but for simplicity the data were processed into full stack (not separated into azimuths or partial stacks as seen in Experiment 1). Frequencies were extracted from within the fault body, adjacent to the fault at the upper boundary and ~ 800 m from the fault at the upper boundary. The aim of these extractions was to understand how fault zone complexity influences both the frequencies from within a fault and in the horizontal reflector imaging nearest to the fault zone.

3 Fault analysis methodology

Aspects of the fault analysis workflow were incorporated into three studies to improve our understanding of:

a. The effect of incidence angle stacking and azimuthal separation on the imaging of discontinuity faults and the effect of fault zone complexity on frequencies in and adjacent to faults (Paper I).
b. The characterization of the seismic signal in and around faults through the classification of deformation, unsupervised seismic fault facies and seismic amplitudes surrounding and on fault planes (Paper II).
c. The effect and implication of five fault and horizon interpretation methods on fault studies, geological modelling and petroleum volume calculations (Paper III).

In Paper I only seismic volume-based approaches were implemented. Paper II applied a combination of both volume and interpretation-based methods, while Paper III was solely based on interpretation (Fig. 3). The methodology defined in this section is aimed to give a concise introduction to the stages of the fault analysis workflow, a brief description of their application and the reasoning for applying them. For a more detailed overview of how each process was applied and the parameters used please refer to the methods section of the respective paper listed in the fault analysis workflow (Fig. 3).

3.1 Seismic volume-based analyses

Seismic volume-based analyses are here defined as processes that are implemented on the seismic volume in its entirety in order to improve the imaging of faults planes and discontinuities in seismic reflectors or to understand the signal in and around faults in the data before seismic interpretation methods are applied. Analyses of the seismic volume were

incorporated into Papers I and II. Here the steps in the seismic volume analysis portion of the fault analysis workflow will be defined (Fig. 3a).

3.1.1 Data conditioning

Data conditioning was only incorporated in Paper II to increase the signal to noise ratio in areas that were affected by the presence of shallow gas in seismic volume ST15M04. The workflow was aimed at attenuating noise in the seismic volume while also normalizing amplitudes and was applied in two steps (Gilani & Gómez-Martínez 2013). In areas where the amplitudes were identified as low due to the presence of shallow gas, an aggressive noise cancellation and amplitude scaling were applied. In areas with good signal, a more passive noise attenuation with no amplitude scaling was applied. This data conditioning workflow was run in the software, Geoteric™. For more information on data conditioning see Paper II, Section 3.1 and/or Gilani and Gómez-Martínez (2013).

3.1.2 Attribute study

Fault enhancing attributes were applied on both ST15M01 and ST15M04 in Papers I and II to aid in the imaging of faults in the seismic data. The three most important fault enhancing attributes in this thesis were tensor, semblance and dip (see e.g. Botter *et al.* 2016b). Tensor is defined as a measurement of the local reflector orientation which is generated using a locally oriented symmetric tensor (Bakker 2002). Semblance (similar to coherency or variance) is defined as a measurement of reflector discontinuity and measures lateral changes to reflectors in the seismic volume (Marfurt *et al.* 1998). Dip is the measurement of the inclination of the seismic reflector with respect to the horizontal and is commonly applied to image stratigraphic or structural edges in the seismic volume (Barnes 2000; Marfurt 2006). These structure enhancing attributes were all generated in Geoteric™ using specific window sizes suitable for large faults. The envelope attribute (a measurement of amplitude strength; Bakker 2002) was applied in Paper I to analyse the changing amplitude

strength with increasing incidence angle. More specific information can be found for all attributes in Papers I and II.

Attributes were also combined to generate multi-attribute blends (e.g. Purves & Basford 2011; Iacopini *et al.* 2012; Botter *et al.* 2016a). The attributes were equally weighted in a single CMY combined volume and a single colour: cyan, magenta and yellow (CMY) were assigned to tensor, semblance and dip respectively. Anywhere where all colours in the blend overlap is defined as black in the colour bar and these areas were assumed to represent faults in their fullest extent relative to what is visible in each individual attribute. Since none of the seismic volumes used in this thesis imaged a fault plane the attributes measurement of the discontinuity fault imaging.

3.1.3 Fault facies classification

Unsupervised seismic fault facies were only classified in Paper II in order to further understand the seismic signal coming from faults. The term unsupervised means that they are not facies in the classical sense of being calibrated to rock types and lithological properties, but are based on a seismic signal classification (Iacopini *et al.* 2012). Fault facies were classified by applying a fault enhancement filter on a greyscale volume of the CMY colour blend volume (tensor, semblance and dip). Fault enhancement is a Gaussian filter that detects and enhances edges whilst also suppressing noise in the data volume (Chopra & Marfurt 2007). The highest values in the fault enhancement volume were subdivided by value into four unsupervised seismic fault facies representing specific seismic attribute responses. Fault facies were then analysed using opacity filtering (e.g. Iacopini & Butler 2011) and by cross-plotting the data according to attribute and fault facies. This was done in order to understand the relationship between the seismic signal and fault enhancement fault facies. For specific attribute parameters refer to Paper II.

3.1.4 Amplitude study

The seismic amplitudes surrounding faults were analysed in Paper II in order to determine if there is a relationship between fault related folding observed in the seismic reflectors near faults and the amplitude magnitude of these reflectors. To complete this analysis structural modelling was used to subdivide chosen areas into grid cells. An RMS amplitude volume of the seismic was calculated using predetermined window sizes to match the grid cell dimensions. The RMS values were re-sampled back into the grid cells of interest. These data could then be cross plotted by distance to fault and magnitude of RMS amplitude in order to determine if a relationship between folding and amplitude could be established. For more information on the parameters used in this aspect of the fault analysis workflow, please refer to Paper II.

3.1.5 AVO attribute stack analysis

The blending of parameters from near, mid and far offset volumes into a single colour blend is termed AVO colour blends (Gomez 2015). Each attribute blend combines three equally scaled attributes of the near (**r**ed), mid (**g**reen) and far (**b**lue) to create an **RGB** blend. In Paper I AVO attribute colour blends were made using the tensor attribute volumes of partially stacked and azimuthally separated data (Section 3.1.2) in order to understand how the imaging of faults differed with incidence angle and azimuth in the Snøhvit case study. The results are best viewed on a time slice and more information can be found in Paper I.

3.1.6 Incidence angle and azimuthal separation analysis

Incidence angle and azimuthal separation were aspects of processing that were applied to the Snøhvit case study in Paper I. The data were processed into east (E, only containing data from receivers located to the east of the source) and west (W, only containing data from receivers

located to the west of the source) azimuth volumes. The data were also separated into near, mid and far incidence angle stacks. To analyse the effect of both incidence angle and azimuthal separation on the imaging of faults seismic attributes were run on both the E and W partial and full stacks and then compared. The reason for conducting this analysis was to see if the faults were imaged differently in the E versus W azimuth partial stack data. The results of these comparisons were used to speculate what might be causing the imaging difference, with respect to survey geometry. The use of seismic attributes in the analysis of E and W azimuth partial stack data was performed on the case study data and the results were compared with the 2D forward modelled reflection seismic data. Since the forward modelled data was 2D, the attributes could not be run on them, but a comparison of image quality was still possible.

3.1.7 Frequency study

An analysis of seismic frequency was conducted on both the case study and forward modelled data in Paper I. The analysis was applied to investigate the frequency content of the backscattered signal from within and around fault planes. In the case study, frequency decomposition blends were generated by equally scaling low, medium and high frequencies in an RGB frequency focused colour blend. In the modelled seismic data, an experiment was designed specifically to understand frequency (Paper I, section 2.2.2). To analyse the frequency content of faults in the modelled data, amplitude spectra were extracted from the middle of the fault, adjacent to the fault and ~800m from the fault on its HW side. The results of both the case study and the modelled experiment were compared. The details of these analysis can be found in Paper I.

3.2 Interpretation based analyses

Interpretation based analyses in this thesis are defined as processes that are run on interpreted horizons and/or fault surfaces. Interpretation-based

analyses were incorporated into Papers II and III. Here each of the stages in the interpretation-based analysis portion of the fault analysis workflow will be defined (Fig. 3b) but for more detailed descriptions of the parameters used and the definition of processes refer to the paper in question.

3.2.1 Horizon and fault interpretation

Horizon and fault interpretations were conducted in Papers II and III. A combination of 3D auto tracking and manual inline and crossline interpretations were used for interpreting horizons in both papers, and faults were interpreted using a combination of vertical and horizontal fault stick interpretation on reflection seismic and attribute volumes (section 3.1.2). Paper III tests the impact of seismic interpretation on fault analysis and several experiments were designed using a combination of different methods. The methods used are specific to each paper and/or experiment and are described in the methods section of the paper in question. All interpretations were completed in the software Petrel™.

Once interpretations were completed, they were all gridded into horizon or fault surfaces using a combination of methods specific to each paper.

3.2.2 Horizon / structure map analysis

Horizon surfaces (also known as structure maps) were analysed in both Papers II and III to visualize and understand the interaction of faults and the reflector displacement caused by faults. The specific gridding parameters can be found in the methodology of the paper in question. The data were gridded and displayed in map view during the analysis of the structure using Petrel™.

3.2.3 Throw analysis

Fault throw profiles were generated on fault planes in Papers II and III to improve our understanding of intra-fault relationships and displacement relationships along fault planes. When constraining the fault cutoff-lines, user-defined trim and patch distances were used to smooth away interpretation errors proximal to the fault (e.g. Wilson *et al.* 2009, 2013; Elliott *et al.* 2012). The trim is defined as the distance within which data are removed from both sides of the fault plane. The patch is defined as the distance and volume adjacent to the omitted data, of high confidence interpretation. The horizon data within the patch is projected onto the fault plane as HW and FW cutoff-lines and is used in the calculation of throw (Wilson *et al.* 2009, 2013; Yielding & Freeman 2016). The patch and trim distances used in each study were specific to the paper in question and are therefore explained in more detail in the respective papers.

3.2.4 Dip distortion analysis

Dip distortion (Paper II) is a measurement of fault related deformation where horizons depart from their original, undeformed regional dip (Long & Imber 2010, 2012b). The main input to calculate dip distortion is the interpreted seismic horizons. The surfaces are sampled along transect lines that ordinarily are chosen perpendicular to the average trend of the faults in the chosen area at a user-defined spacing. Measurements are taken along the transects defining reflector dip distortion; the output of the process is a dip distortion map for the horizon in question. The purpose of running a dip distortion analysis is to investigate fault related deformation, fault interactions and fault extents (especially if dipping on the reflectors occurs where a fault is not clearly segmenting the horizon in question). The calculation of dip distortion is completed in the software T7™ (formerly Trap Tester™) and is explained in its entirety in Paper II. Figure 4c in Paper II gives a more schematic description of this process.

3.2.5 Juxtaposed lithology analysis

Juxtaposed lithology (Papers II and III) is a projection of the overlapping HW and FW lithologies onto a fault plane, also referred to as an Allan Diagram (Allan 1989; Knipe 1997). Juxtaposed lithology is calculated using horizons, faults and horizon-fault intersection lines (i.e. HW and FW cutoff-lines) and well data (tied to the seismic) from the study area in question. The well data (wireline logs, core photos, well reports etc.) are used to identify key lithological tops/bases which are projected across the study area and onto the fault planes using the same HW and FW cutoff-lines used in the throw analysis section (3.2.3). Juxtaposed lithology is used as one aspect of fault seal analyses, where if a lithology is juxtaposed against shale it is probable to seal that area across the fault, while if there is sand-sand contact it is more likely the fault separating these lithological units can act as a conduit to fluid flow (Allan 1989; Knipe 1992). There are other aspects of fault seal that can also be analysed (e.g. shale gouge ratios, clay smear potential), but they were outside of the scope of this research (e.g. Yielding *et al.* 1997; Fisher & Knipe 1998; Færseth, Roald 2006; Færseth *et al.* 2007; Bastesen & Braathen 2010).

3.2.6 Study of dip separation gradient

Dip separation gradient, longitudinal strain and shear strain are measurements that have been proven very useful in seismic interpretation analyses (Freeman *et al.* 2010). Dip separation gradient is calculated using HW and FW cutoff-lines (as used in juxtaposed lithology or throw calculations) and measures the gradient of total displacement across the interpreted fault surface in the dip direction. The results are projected onto fault planes where they can be analysed. The along strike gradient of dip separation is called shear strain (SS) while the along dip gradient determines the longitudinal strain (LS; Walsh & Watterson 1989; Freeman *et al.* 2010). As with dip separation, the results of LS and SS are projected directly onto the fault plane. LS and SS are

characterized by being within or beyond a geologically acceptable threshold and if interpretations are above threshold value, there needs to be either a structural reason for this or the interpretation requires further quality control (Freeman *et al.* 2010). These measurements were implemented in Paper III using the program T7™ and were completed with the aim of understanding the validity of the seismic interpretation across five experiments using different interpretation methods.

3.2.7 Geological and petrophysical modelling

Geological modelling is defined in this thesis as the representation of geology using computationally derived gridded 3D cellular models and was conducted in both Papers II and III. In Paper II, interpreted surfaces were gridded and converted to a geological model. Seismic amplitudes, unsupervised seismic fault facies (Section 3.1.3) and dip distortion (Section 3.2.4) data were sampled back into the grid cells of the model as a mode of comparison between the three measurements. The purpose was to establish a relationship between fault displacement, seismic imaging and fault related folding.

In Paper III geological modelling was conducted on the least and most dense seismic interpretation methods analysed in the paper to understand the effect of seismic interpretation on modelling results and the calculation of in-place petroleum volumes in the area of interest. Petrophysical modelling (populating grid cells with upscaled lithological and porosity information from wells) was only incorporated in Paper III. The generation of the geological models in both papers were similar, although the parameters used in each varied slightly. Both geological and petrophysical modelling were completed in Petrel™. For the specific methodology and parameters used in each, refer to the respective paper.

3.2.8 Calculation of hydrocarbon reserves

The calculation of petroleum reserves was implemented in Paper III with the aim of characterizing the effect of seismic interpretation method on the resulting petroleum reserve calculations. To calculate petroleum reserves, an oil water contact (OWC) was drawn through the study area and water and oil saturations were assigned to the study area according to reservoir versus non reservoir lithology characterizations. The calculation of gross rock volume, pore volume and in place hydrocarbon volumes (STOIIP) were run using Petrel™. The results were finally upscaled across the Snøhvit Field and converted into monetary equivalents as an example of the potential economic impact of interpretation methods.

4 Results and discussion

4.1 The effect of incidence angle on discontinuity fault imaging (Paper I)

The effect of changing incidence angle on discontinuity fault imaging was investigated using a case study from the Snøhvit Field and 2D forward modelled seismic data.

In the case study reflection data was analysed together with seismic attributes (tensor and envelope) that were generated from the azimuthally separated partial stack PS seismic volumes. These data were analysed and compared on inline cross-sections (vertical) and time slices (horizontal). The tensor attribute was expressed as high values at the fault discontinuity and was used as the main attribute for comparison of discontinuity fault imaging between the partial stack seismic volumes. In the Snøhvit case study, imaging of the fault improved with increasing incidence angle. An improvement in imaging quality is defined by higher values of the tensor attribute, and an increase in the imaged fault length and width. The envelope attribute also exhibited a systematic increase in reflector strength with increasing incidence angle across the entire study area.

As with the Snøhvit data the 2D seismic modelling experiment generated seismic images of faulted horizons at a range of incidence angles, which were separated into both W and E azimuths. In all cases fault discontinuity planes were imaged despite the lack of a fault zone with contrasting acoustic properties. With increasing incidence angle the fault discontinuity was imaged more strongly in the E data while imaging quality decreased with increasing incidence in the W data. The amplitudes associated with the horizontal reflections in the modelled data increased with an increasing incidence angle, while the reflectors simultaneously became less sharp and more diffuse. Although clear

Results and discussion

trends were apparent in this modelled data, it was difficult to replicate the observations that were made in the Snøhvit case study. The only comparison that can be drawn between the two datasets is the increasing reflector strength with incidence angle.

The improved discontinuity imaging with increasing incidence angle that was observed in the Snøhvit data is here proposed to be a function of amplitude variations with incidence angle (see e.g. Jabbari & Innanen 2015). The decrease in frequency with increase in incidence angle can be explained by frequency attenuation due to the larger propagation distances that are associated with larger incidence angles. Unfortunately, the seismic modelling was not able to fully explain the observations seen in the Snøhvit Field.

4.2 The effect of azimuthal separation on discontinuity fault imaging (Paper I)

In the Snøhvit data it was clear that discontinuity fault imaging was greatly impacted by survey orientation and more specifically, fault orientation relative to the survey. The northern fault, which was more oblique to the survey orientation was imaged very differently in the W and E datasets. In contrast, the southern fault which was parallel to the survey showed little difference between the W and E azimuth data. Generally, the W azimuth partials stacks were better at picking up the discontinuity fault image than their E counterparts for all incidence stacks.

The 2D modelled seismic experiment also exhibited clearer imaging of the W data than the E data which was consistent with the Snøhvit data. However, the modelled data exhibited subtle differences in the way faults were imaged. Since there was no fault zone added to the geological model for this experiment, there was (as expected) a lack of a fault plane reflection in all 2D seismic lines. The decision to leave the fault zone from the model was a conscious decision to ensure consistency with the

Results and discussion

Snøhvit data (where fault zones are likely present but were not imaged). Despite the lack of a fault zone, a discontinuity plane was imaged due to lateral changes in acoustic properties across the displaced surface of the upper and lower boundaries in the models. The reflections off the W dipping discontinuity fault plane were stronger in the W than the E data. This was further proven by ray tracing whereby the ray paths from source to receiver from a single shot point returned more signal in the W data than the E data. The W data received signal from a wider range of shot point distances and incidence angles off the fault discontinuity plane (Paper I section 5.3 / Fig. 12). At the terminations of the upper and lower geological boundaries with the discontinuity there was a clear strengthening in observed signal of these terminations with strengthening of the discontinuity fault plane reflection. However, there was no significant change in the character of the horizontal reflections between the azimuthally separated partial stacks.

In the Snøhvit case study changes to the quality of discontinuity fault imaging are generated by increases in the tensor (reflector orientation; Bakker 2002) signal with azimuth. In the modelled data the amplitude of the seismic signal at the horizon-fault plane termination also increases with azimuth and occurs with a strengthening in observed signal from the discontinuity fault plane. The increase in tensor attribute and the terminations in the modelled data was interpreted to be a function of the interplay between diffractions from the discontinuity plane (waves scattered from a single point when a seismic wave interacts with a discontinuity; e.g. Landa & Keymar 1998; Taner *et al.* 2006; Landa 2012; Fomel *et al.* 2018) and the reflection from the horizontal surface. In the Snøhvit data the contrasts between the fault plane imaging and the horizontal reflections are less clear, although it is expected that diffraction-reflection interaction is likely to play a role. Diffractions are likely contributing to the discontinuity fault imaging in the case study despite the lack of fault plane reflections due to the generation of wave

31

diffractions from the discontinuity/structural edges (e.g. Landa & Keymar 1998; Taner *et al.* 2006; Landa 2012; Fomel *et al.* 2018).

In the Snøhvit case study the discontinuity fault imaging of the northern fault appears to be far more influenced by azimuth than the southern fault. The northern fault is near-orthogonal to the E-W-E oriented seismic survey. Incoming P-waves interact with the HW side of the fault resulting in the reflection of both specular and diffracted waves. In the W data these signals are more likely to be returned to seismic receivers due to the location of the source and receivers relative to the fault. In the E data the returned waves are likely to miss the receivers. The importance of survey geometry can be clearly seen in the individual shot points for the seismic experiment, which are azimuthally separated (Paper II, supplementary material 2). The parallel nature of the southern Snøhvit fault means there is very little difference in the reflection of seismic waves with azimuth and is therefore further proof of the impact of survey orientation, fault orientation and the resulting quality of discontinuity imaging of faults.

4.3 The seismic frequency in faults (Paper I)

To analyse seismic frequency, RGB frequency decompositions of the Snøhvit PS data were analysed and compared to a 2D forward modelled seismic experiment. Faults, although interpreted as planes in seismic data are complex and highly deformed three-dimensional bodies of rock which can have very different acoustic properties to those in the neighbouring undeformed areas (Faulkner *et al.* 2010 and sources within). The dominant frequency in and surrounding faults were higher than those observed in the nearby unfaulted signal in the Snøhvit PS data. The increased frequency in and around faults was observed regardless of the incidence angle or azimuth being analysed.

Three 2D seismic models were designed to investigate how changes in lithology (and therefore acoustic properties) through a fault zone can

Results and discussion

influence the dominant frequencies in the data being acquired (O'Doherty & Anstey 1971; Anstey & O'Doherty 2002; Weibull *et al.* 2019). The three models included; one simple homogeneous fault, one multi-layer fault with smooth P-wave velocity transitions assigned between layers and one multi-layer model with abrupt changes to the assigned P-wave velocity. Amplitude spectra were extracted from three locations in each of the three models: one from within the fault, one adjacent to the fault at the intersection of the upper boundary of the model and one ~800m away from the fault on the HW side. The results proved that the complex models had higher dominant frequencies than the simple model and of the two, the model with the complex velocity transitions exhibited the highest overall dominant frequencies. The extracted spectra at the terminations of the horizontal boundaries with the fault followed the same trend and appeared to be greatly impacted by fault signal. The spectra extracted from an ~800 m distance from the fault were not impacted by fault zone imaging or complexity and did not vary in the three experiments.

The exact reason for the predominance of high frequencies in the more complex models and in the case study from the Snøhvit area are not fully understood, although some hypotheses are suggested here. O'Doherty & Anstey (1971) established a linkage between the abruptness of velocity transitions and the high proportion of high frequency which is also proven by well-established theories in signal processing. Iacopini et al. (2012) suggested the tuning thickness might also be responsible for the enhancement of higher frequencies in thinly layered geometries. It is expected that both aspects are influencing both the fault imaging in the Snøhvit data and the 2D seismic volume in some capacity. The areas near to faults where horizons terminate at the discontinuity also proved in both the case study and models to have higher frequency than the surrounding unfaulted areas. The fault in the modelled experiment is far more exaggerated when compared to the upper and lower boundaries than what we see in the Snøhvit data and because of this exaggeration it

is difficult to draw a direct relationship between the model and the Snøhvit case study. However, it is possible for us to conclude through seismic forward modelling that the frequencies generated by the complex geometries in faults also affect the terminations of horizontal reflections near faults and are almost certainly linked to higher frequencies observed in the Snøhvit case study in and surrounding faults.

4.4 Seismic amplitude versus distance to fault (Paper II)

The motivation behind this aspect of Paper II was to understand how seismic amplitudes along interpreted horizons change with distance to the fault and to determine if there is a connection between fault related folding and the observed seismic amplitude. Amplitudes were studied by creating a geological grid along interpreted seismic horizons and resampling the RMS amplitude back into the grid cells. The results could then be plotted as distance to fault versus RMS amplitude. The results of the study revealed that there is a clear change in amplitude as a fault is approached in all five interpreted horizons. When there was no clear displacement, but fault related folding was evident (Top Kolje, Intra Kolje, Top Knurr) the dimming or brightening in amplitudes can be correlated to anticlinal and synclinal deformation respectively. In all cases where displacement is clear (deepest two horizons: tops Fuglen and Fruholmen), there were changes (dimming or brightening) in amplitude when approaching the fault which could not be conclusively linked to the structure. However, a sudden drop in amplitude where the interpreted fault plane is located was evident on all displaced horizons. The horizons which have systematic amplitude anomalies are dominated by shales, while the displaced horizons are sandier. It was concluded that these changes could be contributing to the magnitude of fault related folding and therefore the observed amplitude. There were several possible explanations for these amplitude anomalies: geometrical focussing and defocusing caused by the structural curvature of the horizon in question,

changes in acoustic properties, and changes in geometry and illumination. For more details refer to Paper II.

4.5 Unsupervised fault facies, dip distortion and deformation (Paper II)

Unsupervised seismic fault facies were classified by applying a fault enhancement (FE) filter on a greyscale volume of the RGB colour blend of tensor, semblance and dip attributes and subdividing the highest values of FE into facies. The highest fault facies values occur at a fault's centre and the values decrease radially towards its extremities. This radial decrease in fault facies is observable on both inline and depth slices and appears to correlate with the fault displacement. There is an abundance of higher facies accumulations in areas of the seismic data which are associated with the highest throw (NE of the study area). It is likely that fault facies are defined by lateral variations in the seismic signal as detected by attributes and that the lateral variations in signal are a function of displacement.

Dip distortion (DD; maps derived from horizon interpretations representing regional dip variations, apparent dip) were calculated with the aim of further understanding deformation around faults. Generally, the analysis of DD showed that the faults with the largest throws exhibited the largest values of DD. This was also the case for the horizons that have undergone the most displacement (tops Fuglen and Fruholmen). When observing the dip distortion patterns, much like throw, the highest values of dip distortion occur at a faults centre and decreased towards the fault tiplines. Dip distortion is a calculation of apparent dip on the interpreted seismic grid and is therefore directly related to displacement and deformation that is caused by faults.

In order to compare the results of unsupervised seismic fault facies and DD, for each horizon the two were sampled into the grid cells a 3D grid. A 3D geocellular model was used to allow easy comparison of the

attributes with the distance away from a fault. The results of this comparison showed that when the horizon is undergoing visible displacement by faulting, the dip distortion values, and fault enhancement facies remain at their highest and occur in the data closest to the interpreted fault plane. When the horizon is not visibly displaced but appears to have undergone fault related folding there are no assigned fault facies (i.e. values were too low to be classified as facies in the FE filter). However, DD picks up the subtleties in folding by showing slightly elevated values of DD throughout these regions. These observations support a linkage between displacement, unsupervised seismic fault facies and the highest values of DD. Because DD picked up the subtleties of folding, some areas where faults were not interpreted in the seismic data appear folded, this makes DD a useful tool in identifying small displacement faults and understanding the details of the structural deformation.

4.6 The effect of seismic interpretation method on fault and horizon morphology (Paper III)

Five seismic interpretation experiments were conducted on the same study area using seismic data from the Snøhvit Field. The aim of these experiments was to understand the effect of interpretation method on a fault analysis workflow and to assess the optimum interpretation method for both faults and horizons. The area chosen for this study was a relay ramp structure because of the important role of relays play in distributary pathways for sediment transport in a basin, as fluid conduits/seals and in defining traps. In Experiments 4 and 5 (most detailed interpretations), the results in horizon and fault interpretations were geologically realistic due to the interpretation density of horizons and the fact that fault interpretations in these experiments were the most complete with respect to fault length and overlap in the interpreted relay structure. When the interpretation density was very low (Experiment 1), there were serious implications to the fault throw and length estimations and therefore

serious implications to all other aspects of the fault analysis stages that were applied in Paper III (i.e. juxtaposed lithology, geomodelling, and calculation of petroleum reserves). The implications of misinterpreting the relay structure are depicted in Figure 7. The effect of interpretation method on seismic modelling and petroleum volume calculations (Paper III)

The geological models that were generated from both the most and least dense seismic interpretation methods (Experiments 4 and 1 respectively) exhibited very different depictions of the relay's structural detail which has implications on how its development is perceived. In Experiment 1 the relay was underdeveloped compared to Experiment 4 which exhibits a more geologically realistic morphology. An inaccurate and incorrect understanding of relay geometry has several implications for reservoir development, structural trap definition, and fluid migration and fault sealing (Fig. 7). In the model for Experiment 1 there were also some issues with "facies bleed" across the fault bodies and unclear relay definition due to the minimalistic approach to interpretation density. Such anomalies would deem the model unacceptable. In contrast the faults in the geological model generated from Experiment 4 exhibited vertical lineaments which are an artefact of an overly dense interpretation. Hence when modelling it is here recommended (in the interest of smooth fault boundaries) to delete unnecessary fault sticks in the main core of the fault and to maintain hight density fault interpretation density towards the fault tips, where it is critical to contain the absolute end of the displacement being imaged.

Calculations of petroleum reserves using 3D geomodels based on the above results, show an under-estimation of STOIIP of 0.46% in Experiment 1 when compared to Experiment 4. This seemingly small difference in STOIIP value was upscaled to the approximate size and reservoir properties of the Snøhvit Field to consider the potential implications of improper interpretation method. Though the STOIIP difference between experiments 1 and 4 is small, the upscaling results in

Results and discussion

an under estimation of ~11.6 million barrels (or approximately ~370 million USD) when comparing the experiments. This ~370 million USD is entirely caused by inaccuracies in modelling due to the chosen interpretation technique and not by any change in the understanding of the subsurface, proving the importance of interpretation method.
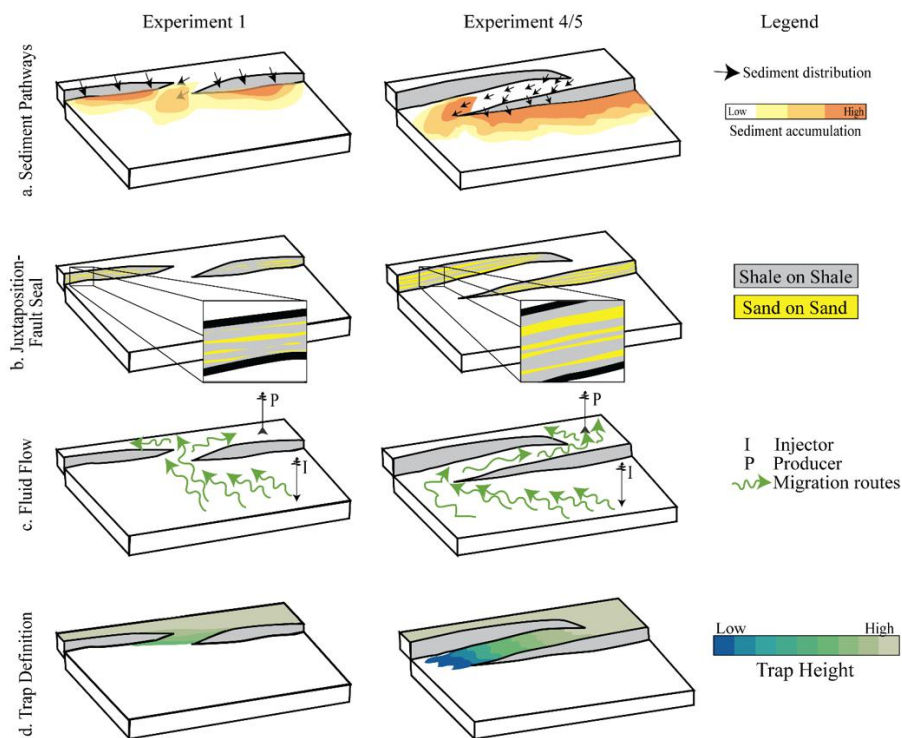
Figure 5: The implications of misinterpreting a relay structure with respect to a. sediment distribution pathways, b. juxtaposed lithology and fault seal, c. fluid flow and d. trap definition. Figures based on Peacock and Sanderson (1994), Knipe (1997), Rotevatn et al. (2007), Athmer et al. (2010), Athmer and Luthi (2011), Fachri et al. (2013) and Botter et al. (2017b).

5 Conclusions

This work provides an integrated analysis of faults in seismic data, focussing on three distinct aspects: the seismic imaging of faults (Paper I); characterizing seismic signal (Paper II); and seismic interpretation methods (Paper III). The main findings of each paper are summarized below.

Paper I:

- Incidence angle:
  - The quality of discontinuity fault imaging improved with increasing incidence angle. The seismic signal strengthened with increasing incidence angle across the study area. However, the forward modelling experiments did not show the same increases in amplitude with increasing incidence angle.
- Azimuthal separation:
  - In both the Snøhvit case study and forward modelled seismic the W azimuthally separated data (when the receivers are placed to the W of the source) exhibited the best discontinuity fault imaging. The improved fault imaging in the W azimuth data was linked to the strengthening of horizontal reflector terminations at the fault due to the interplay of diffractions from the fault with the horizontal reflections.
  - Azimuthal separation has great potential use in faulted areas. In order to use azimuthal separation effectively it is necessary to consider fault versus survey orientation due to the different returns of specular and diffracted energy in azimuthally filtered volumes.

Conclusions

- Frequency:
  - Complex fault layering can produce abrupt changes in acoustic properties within fault zones. Both real data and seismic forward models indicate that this layering is the most likely cause of the predominance of higher seismic frequencies in and near faults compared to areas unaffected by faulting.
  - Seismic forward modelling demonstrates that the highest frequencies within fault zones occur where the internal layering is most complex, and the fault layer transitions are most abrupt.
  - The high frequencies observed within fault zones were interpreted to result in increased frequency content adjacent to the faults which is observed in both the case study and the seismic forward modelled data.

Paper II:

- Unsupervised seismic fault facies, fault throw, and dip separation gradient were interpreted to be linked to fault deformation processes.
- The brightening and dimming of amplitudes adjacent to faults were caused either by geometrical focusing/defocussing, variations in acoustic properties caused by folding, or illumination direction (or some combination of the three).
- Dip distortion and fault throw were proven to be valuable tools to investigate the subtleties in fault related folding adjacent to fault planes. They provided a more detailed understanding of intra-fault relationships and fault morphology.

Conclusions

Paper III:

- The careful selection of seismic interpretation method is proven to be vital for the geologically improved interpretation in faulted systems as it greatly affected the perceived structural morphologies.
- Interpretation density has a significant impact on observed fault length, morphology and throw. This will have a significant impact on studies reliant on accurate interpretations (e.g. geomodelling, reservoir or fluid flow simulations).
- The choice of interpretation methodology is a balance between the time required to perform the interpretation versus the geological accuracy required from the resulting fault model. However, the least dense method of interpretation in this paper was deemed unacceptable.
- Geological modelling was severely impacted by use of inadequate interpretation density and this was shown to have a direct effect on the incorrect estimation of in-place hydrocarbon reserves.

6 Implications

The results of this work have direct implications for both geologists and geophysicists working with modern seismic data. In order to generate the most geologically realistic model of faults in an area it is important to understand:

- How to optimally design a survey in order to capture the most important reflections from the faults;
- How to process and filter data to build the most useful seismic volumes;
- How to select and combine the optimum seismic volumes for the area of interest;
- How to select the optimum seismic attributes that will capture the faults in the highest geophysical detail;
- How to best interpret the faults while maintaining a balance between the time required and the adequate level of geological detail.

The results of a detailed fault analysis have a wide range of implications for petroleum exploration and production including: reservoir, source rock and seal deposition; hydrocarbon or fluid migration; trap definition and breaching; fault seal analysis; geological modelling and volume calculation workflows. This thesis aims to bridge the knowledge gap between geologists and geophysicists by following the full path from seismic survey design and processing, to the results of geomodels. It is only by understanding the full range of geological and geophysical complexities associated with fault imaging that it will be possible to generate the most accurate and geologically realistic fault models from subsurface data. Detailed fault analyses of this kind will become ever more important in the coming years as companies use high resolution broadband and OBS seismic data to identify smaller and more subtle exploration targets and focus on maximising recovery from complex faulted and segmented fields.

7 Future work

This work provides an integrated analysis into the seismic imaging, characterization and interpretation of faults. The next logical step of this work will be to integrate fault rock lithology and the seismic signal of faults. Unfortunately, the ideal dataset for this work was not made available during this thesis. The perfect candidate for this type of analysis is the Wisting Field (Blocks 7324/7 & 8 Barents Sea; Stueland 2016). The exploration and development planning for the Wisting Field have been highly technical which makes it the ideal candidate for an academic analysis (Stueland 2016). The field is structurally segmented (Collanega *et al.* 2017), the reservoir is abnormally shallow (~250 m below the seabed) and so the seismic and fault imaging are of outstanding quality. Specialized high resolution 3D P-cable data was acquired in 2016 which has m-scale resolution of the reservoir and faults. The seismic data (TGS16004) has recently become available to those with access to the Diskos database which makes it readily available for academic use in Norway. Due to the segmentation of the field by faults, the exploration well 7324/7-3S was drilled (in PL537) across multiple fault zones to establish a better understanding of the oil-water contact and fault segmentation in the field. The combination of good well control and shallow focused seismic data makes this dataset the ideal candidate for further studies focusing on the effect of the internal fault structure on the seismic imaging of faults. This data allows for comparisons between lithology and seismic signal to be made. This suggestion would be the perfect continuation to the work contained in this PhD dissertation.

It may be possible to add more value to this fault study by acquiring shot gathers from the Snøhvit area, so it is possible to run a complete reprocessing. By doing so a forward modelled 3D seismic recreation of the Snøhvit could also be generated. These extensions to this work may provide more concrete geophysical conclusions related to fault imaging in seismic data.

Bibliography

Alcalde, J., Bond, C.E., Johnson, G., Ellis, J.F. & Butler, R.W.H. 2017. Impact of seismic image quality on fault interpretation uncertainty. GSA Today, 27, 4–10, https://doi.org/10.1130/GSATG282A.1.

Allan, U.S. 1989. Model for hydrocarbon migration and entrapment within faulted structures. American Association of Petroleum Geologists Bulletin, 73, 803–811, https://doi.org/10.1306/44b4a271-170a-11d7-8645000102c1865d.

Anstey, N.A. & O'Doherty, R.F. 2002. Cycles, layers, and reflections: Part 1. Leading Edge, 21, 44–51, https://doi.org/10.1190/1.1445847.

Antonellini, M. & Aydin, A. 1994. Effect of faulting on fluid flow in porous sandstones: petrophysical properties. American Association of Petroleum Geologists Bulletin, 78, 355–377, https://doi.org/10.1306/bdff90aa-1718-11d7-8645000102c1865d.

Athmer, W. & Luthi, S.M. 2011. The effect of relay ramps on sediment routes and deposition: A review. Sedimentary Geology, 242, 1–17, https://doi.org/10.1016/j.sedgeo.2011.10.002.

Athmer, W., Groenenberg, R.M., Luthi, S.M., Donselaar, M.E., Sokoutis, D. & Willingshofer, E. 2010. Relay ramps as pathways for turbidity currents: A study combining analogue sandbox experiments and numerical flow simulations. Sedimentology, 57, 806–823, https://doi.org/10.1111/j.1365-3091.2009.01120.x.

Aydin, A. 1978. Small faults formed as deformation bands in sandstone. Pure and Applied Geophysics PAGEOPH, 116, 913–930, https://doi.org/10.1007/BF00876546.

Aydin, A. 1999. Fractures, Faults and Hydrocarbon Migration and Flow.

Bibliography

Badley, M.E.E., Freeman, B., Roberts, A.M., Thatcher, J.S., Walsh, J.J., Watterson, J. & Yielding, G. 1990. Fault interpretation during seismic interpretation and reservoir evaluation. The Integration of Geology, Geophysics, Petrophysics and Petroleum Engineering in Reservoir Delineation, Description and Management, 224–241.

Bakker, P. 2002. Image Structure Analysis for Seismic Interpretation. Technische Universiteit Delft.

Barnes, A.E. 2000. Attributes for automating seismic facies analysis. In: SEG 70th Annual International Meeting. 553–556.

Barnett, J.A.M., Mortimer, J., Rippon, J.H., Walsh, J.J. & Watterson, J. 1987. Displacement geometry in the volume containing a single normal fault. AAPG Bulletin, 71, 925–937.

Bastesen, E. & Braathen, A. 2010. Extensional faults in fine grained carbonates - analysis of fault core lithology and thickness-displacement relationships. Journal of Structural Geology, 32, 1609–1628, https://doi.org/10.1016/j.jsg.2010.09.008.

Bond, C.E. 2015. Uncertainty in structural interpretation: Lessons to be learnt. Journal of Structural Geology, 74, 185–200, https://doi.org/10.1016/j.jsg.2015.03.003.

Botter, C. 2016. Seismic Imaging of Fault Zones: A Synthetic Workflow to Study the Impact of Faults on Seismic Images. University of Stavanger.

Botter, C., Cardozo, N., Hardy, S., Lecomte, I. & Escalona, A. 2014. From mechanical modeling to seismic imaging of faults: A synthetic workflow to study the impact of faults on seismic. Marine and Petroleum Geology, 57, 187–207, https://doi.org/10.1016/j.marpetgeo.2014.05.013.

Bibliography

Botter, C., Cardozo, N., Hardy, S., Lecomte, I., Paton, G. & Escalona, A. 2016a. Seismic characterisation of fault damage in 3D using mechanical and seismic modelling. Marine and Petroleum Geology, 77, 973–990, https://doi.org/10.1016/j.marpetgeo.2016.08.002.

Botter, C., Cardozo, N., Hardy, S., Lecomte, I., Paton, G. & Escalona, A. 2016b. Seismic characterization of fault damage in 3D using mechanical and seismic modelling. Marine and Petroleum Geology, 77, 973–990.

Botter, C., Cardozo, N., Qu, D., Tveranger, J. & Kolyukhin, D. 2017. Seismic characterization of fault facies models. Interpretation, 5, 1–18.

Caine, J.S., Evans, J.P. & Forster, C.B. 1996. Fault zone architecture and permeability structure. Geology, 24, 1025–1028.

Carcione, J.M., Herman, G.C. & ten Kroode, A.P.E. 2002. Seismic Modeling. Geophysics, 67, 1304–1325.

Chadwick, R.A. 1986. Extension tectonics in the Wessex Basin, southern England. Journal of the Geological Society, 143, 465–488, https://doi.org/10.1144/gsjgs.143.3.0465.

Childs, C., Watterson, J. & Walsh, J.J. 1995. Fault overlap zones within developing normal fault systems. Journal of the Geological Society, 152, 535–549.

Chopra, S. & Marfurt, K.J. 2007. Seismic Attributes for Prospect Identification and Reservoir Characterization. Tulsa, OK, United States of America, Society of Exploration Geophysicists and European Association of Geoscientists and Engineers.

Collanega, L., Massironi, M., Breda, A. & Kjølhamar, B.E. 2017. Onset of N-Atlantic rifting in the Hoop Fault Complex (SW Barents Sea): An orthorhombic dominated faulting? Tectonophysics, 706–207, 59–70, https://doi.org/10.1016/j.tecto.2017.04.003.

46

Bibliography

Crider, J.G. & Pollard, D.D. 1998. Fault linkage: Three-dimensional mechanical interaction between echelon normal faults. Journal of Geophysical Research, 103, 24373, https://doi.org/10.1029/98JB01353.

Davatzes, N.C. & Aydin, A. 2005. Distribution and nature of fault architecture in a layered sandstone and shale sequence: An example from the Moab fault, Utah. AAPG Memoir, 153–180, https://doi.org/10.1306/1033722m853134.

Doré, A.G. 1995. Barents Sea Geology, Petroleum Resources and Commercial Potential. Arctic, 48, 207–221.

Dutzer, J.-F., Basford, H. & Purves, S. 2010. Investigating fault-sealing potential through fault relative seismic volume analysis. Petroleum Geology Conference series, 7, 509–515.

Elliott, G.M., Wilson, P., Jackson, C.A.L., Gawthorpe, R.L., Michelsen, L. & Sharp, I.R. 2012. The linkage between fault throw and footwall scarp erosion patterns: An example from the Bremstein Fault Complex, offshore Mid-Norway. Basin Research, 24, 180–197.

Færseth, Roald, B. 2006. Shale smear along large faults: continuity of smear and the fault seal capacity. Journal of the Geological Society, 163, 741–751, https://doi.org/10.1144/0016-76492005-162.

Færseth, R.B., Johnsen, E. & Sperrevik, S. 2007. Methodology for risking fault seal capacity: Implications of fault zone architecture. AAPG Bulletin, 91, 1231–1246.

Fachri, M., Rotevatn, A. & Tveranger, J. 2013. Fluid flow in relay zones revisited: Towards an improved representation of small-scale structural heterogeneities in flow models. Marine and Petroleum Geology, 46, 144–164

Faulkner, D.R., Jackson, C.A.L., Lunn, R.J., Schlische, R.W., Shipton, Z.K., Wibberley, C.A.J. & Withjack, M.O. 2010. A review of recent

Bibliography

developments concerning the structure, mechanics and fluid flow properties of fault zones. Journal of Structural Geology, 32, 1557–1575.

Fisher, Q.J. & Knipe, R.J. 1998. Fault sealing processes in siliciclastic sediments. Geological Society Special Publication, 147, 117–134, https://doi.org/10.1144/GSL.SP.1998.147.01.08.

Fomel, S., Landa, E. & Turhan Taner, M. 2018. Post-stack velocity analysis by separation and imaging of seismic diffractions. Society of Exploration Geophysicists - SEG International Exposition and 76tth Annual Meeting 2006, SEG 2006, 2559–2563.

Fossen, H. & Bale, A. 2007. Deformation bands and their influence on fluid flow. American Association of Petroleum Geologists Bulletin, 91, 1685–1700, https://doi.org/10.1306/07300706146.

Freeman, B., Yielding, G. & Badley, M. 1990. Fault correlation during seismic interpretation. First Break, 8, 87–95, https://doi.org/10.3997/1365-2397.1990006.

Freeman, B., Boult, P.J., Yielding, G. & Menpes, S. 2010. Using empirical geological rules to reduce structural uncertainty in seismic interpretation of faults. Journal of Structural Geology, 32, 1668–1676, https://doi.org/10.1016/j.jsg.2009.11.001.

Gilani, S.F. & Gómez-Martínez, L. 2013. The application of data conditioning, frequency decomposition and DHI from RGB colour blending in the Gohta discovery (Barents Sea, Norway). First Break, 33, 39–45.

Gill, J.E. 1935. Normal and reverse faults. Journal of Geology, 43, 1071–1079.

Gomez, L. 2015. AVO Screening (Part 2): AVO colour blends. Geoteric™ Blog.

Bibliography

Gudlaugsson, S.T., Faleide, J.I., Johansen, S.E. & Breivik, A.J. 1998. Late Palaeozoic structural developments of the south-western Barents Sea. Marine and Petroleum Geology, 15, 73–102, https://doi.org/10.1016/S0264-8172(97)00048-2.

Hills, E.S. 1940. Outlines of Structural Geology. Methuen, London.

Hokstad, K., Mittet, R. & Landrø, M. 1998. Elastic reverse time migration of marine walkaway vertical seismic profiling data. Geophysics, 63, 1685–1695, https://doi.org/10.1190/1.1444464.

Iacopini, D. & Butler, R.W.H. 2011. Imaging deformation in submarine thrust belts using seismic attributes. Earth and Planetary Science Letters, 302, 414–422, https://doi.org/10.1016/j.epsl.2010.12.041.

Iacopini, D., Butler, R.W.H. & Purves, S. 2012. Seismic imaging of thrust faults and structural damage: A visualization workflow for deepwater thrust belts. First Break, 30, 77–84, https://doi.org/0.3997/1365-2397.30.5.58681.

Iacopini, D., Butler, R., Purves, S., McArdle, N. & De Freslon, N. 2016. Exploring the seismic expression of fault zones in 3D seismic volumes. Journal of Structural Geology, 89, 54–73.

Jabbari, S. & Innanen, K. 2015. PS and SP Converted Wave Reflection Coefficients and Their Application to Time-Lapse Difference AVO. Calgary, Canada.

Knipe, R.J.J. 1997. Juxtaposition and seal diagrams to help analyze fault seals in hydrocarbon reservoirs. AAPG Bulletin, 81, 187–195, https://doi.org/10.1306/522B42DF-1727-11D7-8645000102C1865D.

Landa, E. 2012. Seismic diffraction: where's the value? SEG Technical Program Expanded Abstracts, 1–4.

Bibliography

Landa, E. & Keymar, S. 1998. Seismic monitoring of diffraction images for detection of local heterogeneities. Geophysics, 63, 1093–1100.

Larsen, P.-H. 1988. Relay structures in a Lower Permian basement-involved extension system, East Greenland. Journal of Structural Geology, 10, 3–8, https://doi.org/10.1016/0191-8141(88)90122-8.

Linjordet, A. & Olsen, R.G. 1992. The Jurassic Snøhvit gas field, Hammerfest basin, offshore northern Norway. In: Giant Oil and Gas Fields of the Decade 1978-1988. American Association of Petroleum Geologists, 349–370.

Long, J.J. & Imber, J. 2010. Geometrically coherent continuous deformation in the volume surrounding a seismically imaged normal fault-array. Journal of Structural Geology, 32, 222–234, https://doi.org/https://doi.org/10.1016/j.jsg.2009.11.009.

Long, J.J. & Imber, J. 2011. Geological controls on fault relay zone scaling. Journal of Structural Geology, 33, 1790–1800.

Long, J.J. & Imber, J. 2012a. Strain compatibility and fault linkage in relay zones on normal faults. Journal of Sedimentary Petrology, 36, 16–26, https://doi.org/http://dx.doi.org/10.1016/j.jsg.2011.12.013.

Long, J.J. & Imber, J. 2012b. Strain compatibility and fault linkage in relay zones on normal faults. Journal of Sedimentary Petrology, 36, 16–26, https://doi.org/10.1016/j.jsg.2011.12.013.

Marfurt, K.J. 2006. Robust estimates of 3D reflector dip and azimuth. Geophysics, 71, 29–40.

Marfurt, K.J., Kirlin, R.L., Farmer, S.L. & Bahorich, M.S. 1998. 3-D seismic attributes using semblance-based coherency algorithm. Geophysics, 63, 1150–1165.

Bibliography

Muraoka, H. & Kamata, H. 1983. Displacement distribution along minor fault traces. Journal of Structural Geology, 5, 483–495.

Nicol, A., Walsh, J.J., Watterson, J. & Bretan, P.G. 1995. Three-dimensional geometry and growth of conjugate normal faults. Journal of Structural Geology, 17, https://doi.org/10.1016/0191-8141(94)00109-D.

O'Doherty, R.F. & Anstey, N.A. 1971. Reflections on Amplitudes. Geophysical Prospecting, 19, 430–458.

Ostanin, I., Anka, Z., di Primio, R. & Bernal, A. 2012. Identification of a large Upper Cretaceous polygonal fault network in the Hammerfest basin: Implications on the reactivation of regional faulting and gas leakage dynamics, SW Barents Sea. Marine Geology, 332–334, 109–125, https://doi.org/http://dx.doi.org/10.1016/j.margeo.2012.03.005.

Peacock, D.C.P. 2002. Propagation, interaction and linkage in normal fault systems. Earth-Science Reviews, 58.

Peacock, D.C.P. & Sanderson, D.J. 1991. Displacements, segment linkage and relay ramps in normal fault zones. Journal of Structural Geology, 13, 721–733, https://doi.org/10.1016/0191-8141(91)90033-F.

Peacock, D.C.P. & Sanderson, D.J. 1994. Geometry and development of relay ramps in normal fault systems. AAPG Bulletin, 78, 147–165, https://doi.org/10.1306/BDFF9046-1718-11D7-8645000102C1865D.

Peacock, D.C.P., Knipe, R.J.J. & Sanderson, D.J. 2000. Glossary of normal faults. Journal of Structural Geology, 22, 291–305, https://doi.org/10.1016/S0191-8141(00)80102-9.

Peacock, D.C.P., Nixon, C.W., Rotevatn, A., Sanderson, D.J. & Zuluaga, L.F. 2017. Interacting faults. Journal of Structural Geology, 97, 1–22, https://doi.org/10.1016/j.jsg.2017.02.008.

Bibliography

Pollard, D.D. & Aydin, A. 1984. Propagation and linkage of oceanic ridge segments. Journal of Geophysical Research, 89, 10017–10028.

Purves, S. & Basford, H. 2011. Visualizing geological structure with subtractive color blending. In: Marfurt, K. J., Gao, D., et al. (eds) Attributes: New Views on Seismic Imaging -- Their Use in Exploration and Production: 31st Annual. SEPM Society for Sedimentary Geology, 120–139.

Rippon, J.H. 1985. Contoured patterns of the throw and hade of normal faults in the Coal Measures (Westphalian) of north-east Derbyshire. Proceedings of the Yorkshire Geological Society, 45, 147–161, https://doi.org/https://doi.org/10.1144/pygs.45.3.147.

Rotevatn, A., Fossen, H., Hesthammer, J., Aas, T.E. & Howell, J.A. 2007. Are relay ramps conduits for fluid flow? Structural analysis of a relay ramp in Arches National Park, Utah. Geological Society, London, Special Publications, 270, 55–71, https://doi.org/10.1144/GSL.SP.2007.270.01.04.

Schaaf, A. & Bond, E.C. 2019. Quantification of uncertainty in 3-D seismic interpretation: Implications for deterministic and stochastic geomodeling and machine learning. Solid Earth, 10, 1049–1061, https://doi.org/10.5194/se-10-1049-2019.

Stueland, E. 2016. Wisting- Shallow Reservoir: Possibilities and Challenges. In: FORCE Underexplored Plays II. Stavanger, Norway.

Sund, T., Skarpnes, O., Nørgård Jensen, L. & Larsen, R.M. 1984. Tectonic development and hydrocarbon potential offshore Troms, Northern Norway. In: AAPG Special Publication Memoir: Future Petroleum Provinces of the World. 615–627.

Bibliography

Taner, M.T., Fomel, S. & Landa, E. 2006. Separation and imaging of seismic diffractions using plane-wave decomposition. 2401–2405, https://doi.org/10.1190/1.2370017.

Townsend, C., Firth, I.R., Westerman, R., Kirkevollen, L., Harde, M. & Andersen, T. 1998. Small seismic-scale fault identification and mapping. In: Faulting, Fault Sealing and Fluid Flow in Hydrocarbon Reservoirs, Special Publications 147. Geological Society of London, 1–25., https://doi.org/https://doi.org/10.1144/GSL.SP.1998.147.01.02.

Virieux, J. 1986. P-SV wave propagation in heterogeneous media. Geophysics, 51, 889–901, https://doi.org/10.1190/1.1442147.

Walsh, J.J. & Watterson, J. 1987. Distributions of cumulative displacement and seismic slip on a single normal fault surface. Journal of Structural Geology, 9, 1039–1046, https://doi.org/10.1016/0191-8141(87)90012-5.

Walsh, J.J. & Watterson, J. 1988. Analysis of the relationship between displacements and dimensions of faults. Journal of Structural Geology, 10, 239–247, https://doi.org/https://doi.org/10.1016/0191-8141(88)90057-0.

Walsh, J.J. & Watterson, J. 1989. Displacement gradients on fault surfaces. Journal of Structural Geology, 11, 307–316, https://doi.org/https://doi.org/10.1016/0191-8141(89)90070-9.

Walsh, J.J. & Watterson, J. 1990. New methods of fault projection for coalmine planning. Proceedings of the Yorkshire Geological Society, 42, 209–219, https://doi.org/10.1144/pygs.48.2.209.

Walsh, J.J. & Watterson, J. 1991. Geometric and kinematic coherence and scale effects in normal fault systems. The Geological Society of London, The Geomet, 193–203.

Bibliography

Watterson, J. 1986. Fault dimensions, displacements and growth. Pure and Applied Geophysics PAGEOPH, 124, 365–373, https://doi.org/10.1007/BF00875732.

Weibull, W.W. & Arntsen, B. 2013. Automatic migration velocity analysis using reverse-time migration. Geophysics, 55, 1070–1088.

Weibull, W.W., Ahmad, S.S., Brown, R.J., Rosland, B. & Nazi, H. 2019. A comparison of the effects of layering and attenuation on the seismic response of gas reservoirs. In: 81st EAGE Conference & Exhibition 2019. London, UK, EAGE.

Wibberley, C.A.J., Yielding, G., et al. 2008. Recent advances in the understanding of fault zone internal structure: a review. Geological Society, London, Special Publications, 299, 5–33, https://doi.org/10.1144/SP299.2.

Wilson, P., Hodgetts, D., Rarity, F., Gawthorpe, R.L. & Sharp, I.R. 2009. Structural geology and 4D evolution of a half-graben: New digital outcrop modelling techniques applied to the Nukhul half-graben, Suez rift, Egypt. Journal of Structural Geology, 31, 328–345.

Wilson, P., Elliott, G.M., Gawthorpe, R.L., Jackson, C. a. L., Michelsen, L. & Sharp, I.R. 2013. Geometry and segmentation of an evaporite-detached normal fault array: 3D seismic analysis of the southern Bremstein Fault Complex, offshore mid-Norway. Journal of Structural Geology, 51, 74–91, https://doi.org/10.1016/j.jsg.2013.03.005.

Worsley, D., Johansen, R., Kristensen, S.E. & 1988. The Mesozoic and Cenozoic succession of the Tromsoflaket. In: Dalland, A., Worsley, D., Ofstad, K. (Eds.), A.L.S. for the M. and C.S.O.M. 1988. The Mesozoic and Cenozoic succession of the Tromsoflaket. In: A Litho-Stratigraphic Scheme for the Mesozoic and Cenozoic Successions Offshore Mid- and Northern Norway: Norwegian Petroleum

Bibliography

Directorate (NPD), Bulletin No. 4. Northern Norway: Norwegian Petroleum Directorate (NPD), Bulletin No. 4. 42–87.

Yielding, G. & Freeman, B. 2016. 3-D Seismic-Structural Workflows – Examples Using the Hat Creek Fault System. In: Krantz, B., Ormand, C. & Freeman, B. (eds) M111: 3-D Structural Interpretation: Earth, Mind and Machine. 155–171.

Yielding, G., Freeman, B. & Needham, D.T. 1997. Quantitative fault seal prediction. AAPG Bulletin, 81, 897–917, https://doi.org/10.1306/522B498D-1727-11D7-8645000102C1865D.

Compilation of papers

PAPER I

INVESTIGATING THE SEISMIC IMAGING OF FAULTS USING PS DATA FROM THE SNØHVIT FIELD, BARENTS SEA AND FORWARD SEISMIC MODELLING

Cunningham, Jennifer; Weibull, Wiktor; Cardozo, Nestor;

Iacopini, David.

Investigating the Seismic Imaging of Faults Using PS Data from the Snøhvit Field, Barents Sea and Forward Seismic Modelling

Jennifer Cunningham*[1], Wiktor W. Weibull[1], Nestor Cardozo[1], David Iacopini[2]

[1]*Department of Energy Resources, University of Stavanger, 4036 Stavanger, Norway (+47 461 84 478*,*
[jennifer.e.cunningham@uis.no*](mailto:jennifer.e.cunningham@uis.no)*)*

[2] *DISTAR, Universita' degli Studi di Napoli Federico II*

Abstract

PS seismic data from the Snøhvit Field are compared with forward seismic modelling to understand the effect of azimuthal separation and incidence angle on the imaging of faults and associated horizon discontinuities. In addition, the frequency content of back scattered seismic waves from within and surrounding faults is analysed. Azimuthally separated W and E data demonstrate that fault imaging is more affected by azimuth when the faults are orthogonal to the survey orientation, and W data image the faults better. Partial stack data show that with increasing incidence angle there is a systematic improvement in the quality of fault imaging in both the E and W data. Low-medium frequencies are dominant within fault zones compared with higher frequencies in adjacent areas. Two synthetic experiments support these observations. The first experiment (planar fault) confirms a strengthening in the seismic signal from faults in the W data. This is due to the interaction of specular waves and diffractions which are more abundant in the W data. The second experiment (fault zone) proves that frequencies in the fault and adjacent areas increase with fault zone complexity. Integrating the observations from the Snøhvit Field with synthetic modelling provides a better understanding of the impact of survey geometry and processing workflows, the interaction of seismic waves with faults, and the frequency content in and around faults.

P1 1. Introduction

The analysis of faults in seismic data has been an important topic in the petroleum industry for decades due to the role of faults as critical elements in many oil and gas fields. Fault analysis in seismic data has evolved from simple interpretation on cross sections or time/depth slices, to detailed interpretation of faults using a range of structure-enhancing attributes (e.g. Iacopini & Butler 2011; Iacopini *et al.* 2012, 2016; Torabi *et al.* 2016). High resolution seismic imaging of faults in 3D is essential for the understanding of fault geometry, displacement profiles, fault juxtaposition and sealing, and fault formation through interaction and linkage (Dawers & Underhill 2000; Elliott *et al.* 2012; Long & Imber 2012b; Tvedt *et al.* 2013; Osagiede *et al.* 2014). Despite this, few studies focus specifically on understanding how faults are imaged with respect to both real and forward modelled data. Fault imaging is referred to in two different contexts in this study: fault plane imaging which is the imaging of the fault as a distinct reflector, and discontinuity imaging which is the identification of displaced seismic reflectors but without the imaging of the fault plane itself.

When P-waves (primary wave, compressional wave) penetrate the subsurface and reflect off a boundary, they can reflect as either a P-wave (PP reflection) or an S-wave (PS reflection). PP-wave reflection seismic data are by far the most common type of subsurface data used in fault interpretation, since they are the most common type of data collected by conventional towed-streamer marine seismic surveys. Improvements in seismic acquisition and processing technology have enhanced the imaging of faults on P-wave data alone. However, onshore surveys and offshore surveys using arrays of ocean-bottom nodes placed directly on the ocean floor can also record shear (S) waves. Since S-waves cannot travel through fluids the majority of studies that have focused on the application of ocean bottom seismic (OBS) data have applied these data to understand hydrocarbon fluid distributions, for example by comparing PP and PS surveys or Vp/Vs analysis (i.e. Ensley 1984; Granli *et al.* 1999; Rodriguez 2000; Stewart *et al.* 2003; Barkved *et al.* 2005; Xu & Tsvankin 2007; Farfour & Yoon 2016). Using PS data to analyse the specific seismic imaging of faults has so far been underexploited but is

demonstrated here to have great potential to improve the understanding of fault morphology and the way seismic waves interact with faults.

Seismic processing of PP or PS data from OBS surveys typically separate the signal by incidence/reflection angle in order to generate incidence angle/offset stacks (i.e. near, mid and far offsets). In addition to the use of angle stacks for AVO analysis (Ostrander 1984), the nearest stack is typically the most successful volume when imaging faults and structure in seismic data, while the far stack data have been applied to imaging of high angle faults (as proven by studies focusing on reflection coefficient versus incidence angle i.e. Shuey, 1985 and references therein). Processing workflows can also be applied to separate data from a chosen source-receiver azimuth using specialized cable nodes (e.g. Granli *et al.* 1999; Stewart *et al.* 2002, 2003; de Kok 2012). Directionally (azimuthally) separated seismic data have been used in both carbonate and clastic systems to determine fracture orientations by analysing differences between the AVO responses parallel and perpendicular to fluid-filled fracture networks (azimuthal AVO; e.g. Jenner 2002; Perez & Marfurt 2007; Xu & Tsvankin 2007; Gray 2008). The logical extension of this work is to apply similar techniques to the study of faults and fault networks, and to our knowledge, specific and systematic azimuthal data filtering has not yet been applied to detailed studies of fault imaging.

Forward seismic modelling reveals a direct correlation between seismic amplitude variations and the amount of fault related deformation (Botter *et al.* 2014, 2016a, 2017a, b). Furthermore, higher frequencies in the synthetic seismic source resulted in more detailed amplitude extractions from within the modelled fault zone (Botter *et al.* 2014). Despite these important observations, few studies have attempted to compare observations of faults in real seismic data with the results of forward seismic modelling. Such comparison is necessary in order to understand how seismic acquisition geometries influence the imaging of fault planes and displaced horizons, and how frequency changes within and near to fault zones. This study attempts to understand these aspects of fault imaging through comparison of a case study and forward seismic modelling.

Pre-stack depth-migrated PS data from the Snøhvit Field, Barents Sea are used to study the effects of azimuthal separation and incidence angle stacking on the imaging of faults in real seismic data, and to evaluate the seismic frequency contained in and around faults. Two simplified forward seismic modelling experiments were designed to better understand the fault imaging affects that are observed in the data.

P1 2. The Snøhvit Field: A Case Study

P1 2.1 Geological Setting

The Snøhvit gas and condensate field is in the centre of the Hammerfest Basin, southwest Barents Sea and consists of an up-thrown fault block bounded by E-W trending faults within the overall NE-SW trending faults that define the Hammerfest Basin (Fig. 1a, b). The Hammerfest Basin has dimensions of 150 x 70 km and is surrounded by the Loppa High, the Finnmark Platform and the Tromsø Basin to the north, east and west respectively (Fig. 1a, b; Sund *et al.* 1984; Doré 1995; Ostanin *et al.* 2012). Subsidence in the Hammerfest Basin was initiated by Late Carboniferous-Early Permian rifting, which generated the NE-SW trending basin-bounding faults (Gudlaugsson *et al.* 1998). A second rifting event following the same fault -trend occurred in the Late Jurassic- Early Cretaceous, during which the basin underwent the greatest subsidence on its northern and southern margins (Sund *et al.* 1984; Linjordet & Olsen 1992; Doré 1995; Ostanin *et al.* 2012). Due to differential subsidence through this period on the Barents Shelf, the Hammerfest Basin widens and deepens westward, resulting in thicker Triassic-Cretaceous sediments in the west where the study area in the Snøhvit Field is located (Linjordet & Olsen 1992). From the Early Jurassic-Early Cretaceous, a dome formed at the central axis of the basin which drove the formation of the E-W trending fault system that defines the structure of the Snøhvit Field (Sund *et al.* 1984; Linjordet & Olsen 1992). Key reservoir intervals in the Hammerfest Basin are Lower-Middle Jurassic sandstones of the Tubåen, Nordmela and Stø fms (Fig. 1e). Jurassic-Cretaceous marine shales (e.g. Fuglen, Hekkingen, Knurr and Kolje fms) are principal sealing intervals (Linjordet & Olsen 1992). The Triassic-Cretaceous units have undergone significant extensional faulting and are the focus of this study (Fig. 1e).
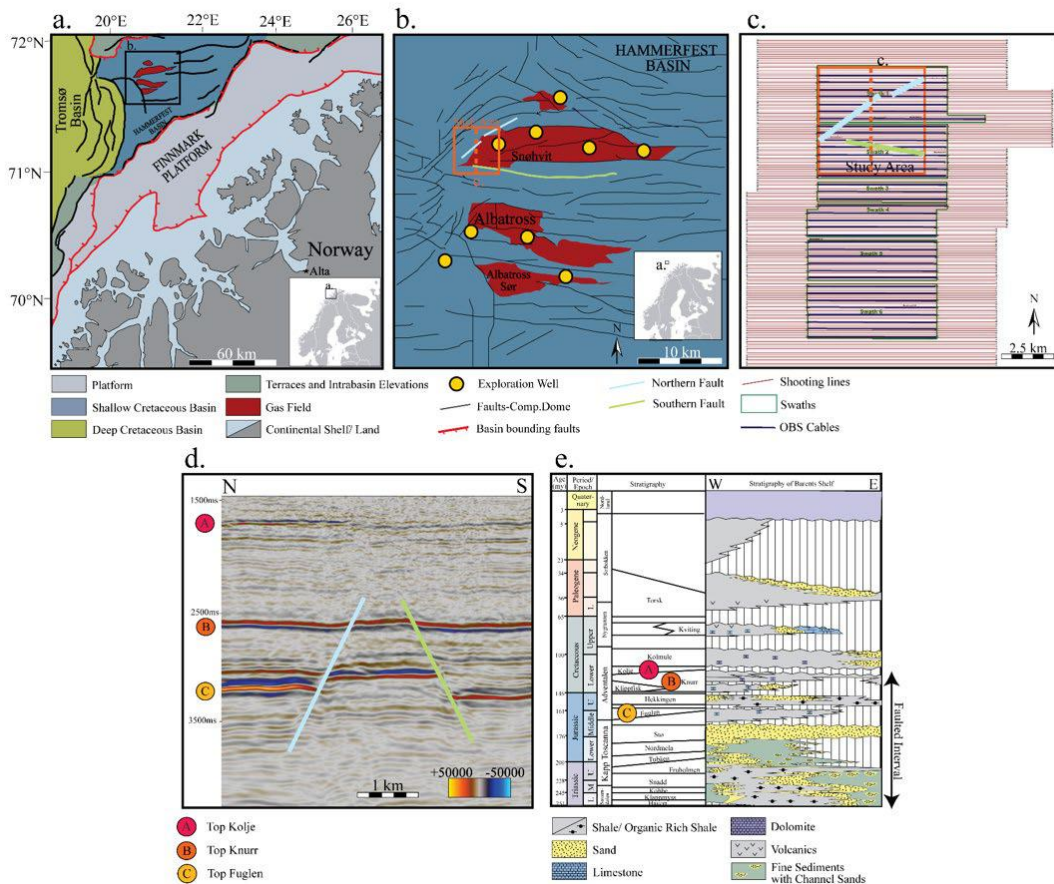
P1 Figure 1: (a) The Hammerfest Basin and its bounding areas. The area in b is marked by a black box. Modified from NPD Fact maps. (b) Hammerfest basin (blue background) and Lower-Middle Jurassic gas fields (red). The orange square is the study area at the western margin of the Snøhvit field. The orange dashed line is the inline pictured in (c). Map modified from Linjordet & Olsen (1992) and Ostanin et al. (2012). (c) The survey setup. The longer red lines represent the shooting lines, and the purple lines housed in green boundaries are the ocean bottom cables and swaths respectively. (d) Inline 4020 from the E full stack data volume with marker horizon placement for reference. (e) Generalized lithostratigraphic column of the Barents Sea with same marker horizon references as seen in (d). Modified from Ostanin et al. (2012). The northern (light blue) and southern (green) faults are overlaid for reference in b, c and d.

Shallow gas is common in the Barents Sea and causes dimming and reduction in quality in the seismic imaging of the reservoir intervals due to deterioration of the PP seismic signal (Ensley 1984; Sund *et al.* 1984; Linjordet & Olsen 1992; Ryseth *et al.* 2003; Ostanin *et al.* 2012; Mohammedyasin *et al.* 2016). Therefore, this study will focus on the PS data. A 5x5 km study area on the western margin of the Snøhvit Field was chosen for this investigation because of the presence of faults oriented both parallel to, and oblique to the shooting orientation of the seismic survey (Fig. 1a-c). The study area consists of an up-thrown fault block defined by a northern fault that trends NE-SW, dips ~54° NW and is oblique to the E-W survey orientation (Fig. 1b-d, blue fault) and a southern fault that trends WNW-ESE, dips 50° SSW and is largely parallel to the survey orientation (Fig. 1b-d, green fault).

P1 2.2 An introduction to OBS data, seismic acquisition and processing of the case study

Modern offshore seismic surveys begin by generating pressure waves (P-waves) using a man-made acoustic source (i.e. air-gun), the waves then reflect off of boundaries between layers with different acoustic impedance properties as P or converted S-waves (Fig. 2, e.g. Garotta & Granger 1988; Landrø & Amundsen 2010). P-waves can travel through both solids and liquids and can therefore be recorded both onshore and in conventional marine acquisition (acoustic source and streamer cables towed behind vessels in the water column). PP-surveys are the simplest, cheapest and therefore most readily used seismic surveys. S-waves cannot travel through fluids and therefore can only be collected by geophones on land or by receiver nodes on the ocean floor. Since S-waves cannot travel through fluid, converted wave data is sensitive only to changes in lithology and is not affected by pore fluids. Marine surveys that collect S-wave data may be referred to as ocean bottom seismic or ocean bottom cable/node surveys (OBS, OBC or OBN; Barr 1997). Multiple P- to S-wave conversions result in degradation of the seismic signal and the loss of high frequencies with depth (Stewart & Lawton 1996). Because converted-waves reflect asymmetrically about the normal to the reflector; depending on the strength of the observed
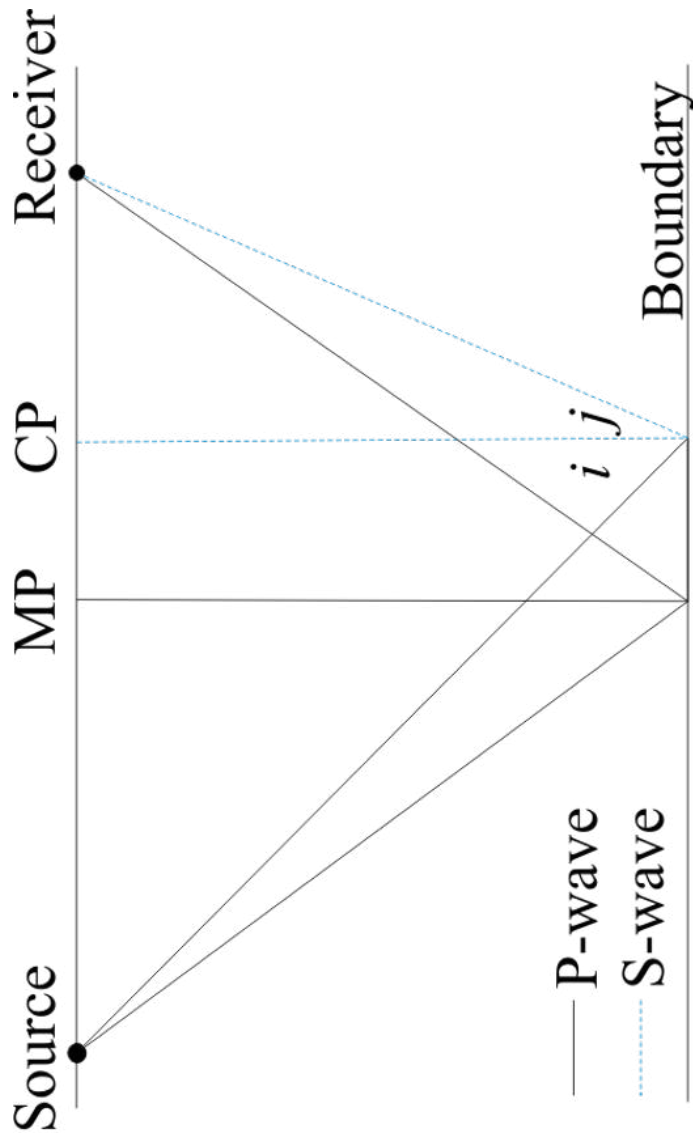
P1 Figure 2: A pure P-wave reflection compared with the reflection of a converted PS-wave. Notice the difference between the mid-point (MP) of the pure P-wave, and the conversion point (CP) of the converted-wave. The incidence angle *i* of the P-wave and the reflection angle *j* of the S-wave also differ. Modified from Stewart *et al.* (2002).

anisotropy, PS data can be more challenging to process than standard PP data (Fig. 2; Stewart *et al.* 2002).

Specialized 4-component (4C) node technology is used in modern surveys to collect P and S-wave data in the form of particle velocity in three Cartesian directions (X, Y, Z) and pressure (e.g. Granli *et al.* 1999; Stewart *et al.* 2002, 2003; de Kok 2012). These specialized nodes and swath acquisition design allow for the collection of high fold data and larger offset ranges than a standard streamer-towed marine survey (Landrø & Amundsen 2018). During processing, it is possible to filter the data by azimuth (i.e. the orientation of the receivers relative to the source; azimuthal separation) and by incidence angle (i.e. near, mid, far and full stacks).

This study uses the ST15M01 ocean-bottom seismic (OBS) survey that was collected by Magseis AS and processed by CGG on behalf of the Snøhvit license partners in 2013. The nodes and seismic vessel swaths were oriented E-W (90-270°) in order to optimize the imaging beneath a shallow gas cloud on the western flank of the Snøhvit Field (Fig. 1b, c). This analysis focuses only on the PS data (Fig. 1c) as these data are largely unaffected by the gas. In seismic pre-processing (Table 1), all unseparated data went through the same set of processes (Table 1, Steps 1-23) before they were separated into eastern (E, only containing data from receivers positioned to the east of the source) and western (W, only containing data from receivers positioned to the west of the source) azimuths. The azimuthally separated data were migrated using a Kirkoff pre-stack depth migration (PSDM) method. The process of separating data into E and W is referred to as 'azimuthal separation' and although this type of data separation is common in the petroleum industry, the effects of this processing step are largely unexplored in either qualitative or quantitative investigations of faulted reservoirs. Once separated and migrated, the azimuthal data were stretched to time and further converted into incidence angle where partial (near 10-25°, mid 20-45°, far 35-60°) and full stack volumes were defined (Table 1, post-migration processing). A post stack processing workflow was then applied (Table 1, post-stack processing). The converted wave data are presented in PS time to avoid the further unnecessary conversion back to depth. All depths are referred to in two-way travel time (TWT) in milliseconds. In

Processing Workflow ST15M01	
Stage	**Pre-processing**
1	Reformat from SEGY
2	Edits receivers
3	3 3C Reorientation
4	Anti alias filter, 94Hz 72dB/Oct
5	Resample from 2 to 4ms
6	Lowcut 3Hz 18dB/Oct
7	Impulsive noise attenuation
8	Tidal statics
9	Source depth statics
10	PZ sum cross-ghosting method with de-pegleg option
11	Vz noise attenuation
12	Zerophasing/Debubble/ refraction mute applied
13	2D shot interpolation 37.5 to 9.375m and 2D shotline interpolation from 25 to 12.5m
14	3D Tau-p mute and deconvolution
15	3D SRMM
16	Drop interpolated shotpoints
17	Diffracted multiple attenuation
18	Parabolic radon demultiple
19	Surface consistent amplitude corrections
20	TVF
21	Q-phase correction, where Q = 130, Freq. = 45Hz
22	5D regularization, offset/azimuth
23	3D Random noise attenuation
24	Separate azimuths 180-359 degrees (East) and azimuth 0-179 degrees (West)
25	PSDM Kirchhoff (using 1 iteration of TTI TOMOML velocity update)
Stage	**Post Migration Processing**
26	Stretch to time
27	Residual moveout corections
28	High resolution parabolic radon demultiple
29	3D Random noise attenuation
30	CDP trim statics
31	Angle mutes
Stage	**Post Stack Processing**
32	Full volume stack and angle stacks
33	Match ST9705Z14: Time shift =0.4msec Time variant amplitude scalars: 0.1 dB 0-900msec, 0.06dB 900-4800 msec
34	2D interpolation from 12.5x25 to 12.5x12.5 grid
35	Time variant gain, 3dB 0-3sec, 9dB at 4.8sec
36	Segy

P1 Table 1: The processing workflow applied to the Snøhvit case study data.

total, eight volumes (near, mid, far and full stack for both east and west azimuths) were incorporated into this study, and for each volume a downwards increase in acoustic impedance is represented as a red seismic peak and a decrease is represented by a blue trough.

P1 3. Methods

This study involves a comparison and analysis of faults using a case study (3.1) and forward seismic modelling (3.2).

P1 3.1 The seismic analysis of faults in the Snøhvit Field

P1 3.1.1 Fault imaging and incidence angle and azimuth

The aim of this part of the study was to compare the quality of fault discontinuity imaging in different incidence angle stacks and azimuthally separated seismic volumes (E versus W), for faults of different orientation (i.e. faults that are oblique to and parallel with the shooting direction). Two methods were applied in order to address this question. The first analysis examines reflection seismic and two volume attributes on the partial and full stack seismic data volumes of both azimuths.

Tensor was chosen because of its previous successful application to the analysis of faults in seismic data (i.e. Botter *et al.* 2016a; Iacopini *et al.* 2016; Cunningham *et al.* 2019) and because in this data it gives the clearest indication of fault imaging. Tensor is an attribute based on a local, structurally oriented symmetric tensor where the principle axes of the tensor define the weighted average orientation of the reflector (Bakker 2002). Tensor is sensitive to both seismic amplitude changes and reflector continuity and in the case of a fault displacing a surface will show higher values at the discontinuity than in unfaulted areas. The tensor attribute was optimized for large-scale faults, using a fault width and height of 7 and 21 voxels respectively (87.5 m and 84 ms). In this work a voxel in the x and y directions is proportional to the inline and crossline spacing of the data which in this case was 12.5 m (7 x 12.5 = 87.5 m), while in the z direction a voxel refers to the time sampling

interval which in this case was 4 ms (4 x 21= 84 ms). The envelope attribute was generated to visualize changes in amplitude with increasing incidence angle (Chopra & Marfurt 2007) across partial and full stack volumes. The original reflection data was also a part of the comparison and all data were displayed as a single inline slice (4000 inline) and a time slice (3128 ms) to capture how they image faults in a vertical and horizontal sense.

The second analysis blends the tensor responses of the near, mid and far angle stacks for both E and W azimuths. Colour blending makes it possible to compare the relative contribution of signal from each of the partial stacks. This type of blend is termed an AVO colour blend (Gomez 2015). The blend comprises three equally scaled tensor volumes representing the near (red), mid (green) and far (blue) data. When a single colour (red, green or blue) is visible in the colour blend, it means that a single volume has the highest relative response. If magenta, yellow or cyan are visible, it means that two volumes have a similar relative response. White is representative of a high response from all three volumes, while black represents very little or no response. Like the first attribute analysis, the results are displayed on a single time slice at 3128 ms (PS time) which is approximately located at the middle of the faulted stratigraphic interval (Fig. 1d).

P1 3.1.2 The seismic frequency of faults

Frequency decompositions (FD) of the E and W partial and full stack data were performed using the Exponential Constant Q method (ECQ) in Geoteric™. The frequency decompositions were generated by extracting a single power spectrum from the 3128 ms time slice of each of the seismic volumes. Using this power spectra as a guide, constant Q decomposition bands with low, medium and high central frequencies were chosen to fit within the extracted spectra (Jilinski & Wooltorton 2016). For the near, mid, far and full stack volumes of the E and W datasets, the same central frequencies of 8, 14 and 30 Hz were selected as they best fit the peaks in the frequency spectrum for each dataset and allowed for consistent comparison. Magnitude volumes were generated for each of the central frequencies. RGB colour blends were then generated by assigning red, green and blue to the equally scaled 8, 14 and 30 Hz magnitude volumes, respectively in order to give the best fault

imaging results. The reading of the colour in these blends is described in section 3.1.1. The frequency decomposition blends were displayed as a single inline, crossline and time slice to show a good representation of the frequency distributions in the study area and were analysed to ensure consistent results across the faulted interval.

More detailed information on this method can be found in both Jilinski & Wooltorton (2016) and Han (2017). This frequency decomposition method was chosen as it is the method that best honours the bandwidth of the seismic data at a user-defined time interval (3128 ms, PS time). Choosing a method that could be optimized for a single time slice was critical for our analysis of the centre of the faults in the Snøhvit data.

### P1 3.2 Forward seismic modelling

Two synthetic 2D seismic models were designed to improve our understanding on the effect of azimuthal separation, incidence angle stacking (experiment 1) and frequency content (experiment 2) on the imaging of faults. The seismic models are seismic representations of a simplified geological model with the aim to highlight potential causes for imaging anomalies in the case study from the Snøhvit Field. The models are not intended to be a fully accurate duplication or recreation of the Snøhvit data and are only to be used a proof of concept and a means of explanation for the observations made in the real seismic data.

P1 3.2.1 Experiment 1

The first synthetic experiment is designed to model the effects of azimuthal separation and incidence angle stacking on the seismic imaging of faults. The synthetic elastic data in 2D were generated using a finite-difference solution to the elastic wave equation (Virieux 1986) and a 14 km long relatively simple isotropic elastic model (Figs 3, 4a). A single geological layer with a uniform thickness of 300 m was placed at approximately 2500 m depth and was displaced 150 m vertically by a discontinuity dipping 55° to the west (left of the image). No fault body/plane was defined in the model in order to create the illusion of perfect dislocation or zero thickness. However, a deformation volume is normally formed during faulting. This method was chosen because no fault planes have been directly imaged in the Snøhvit data. The lack of a

69
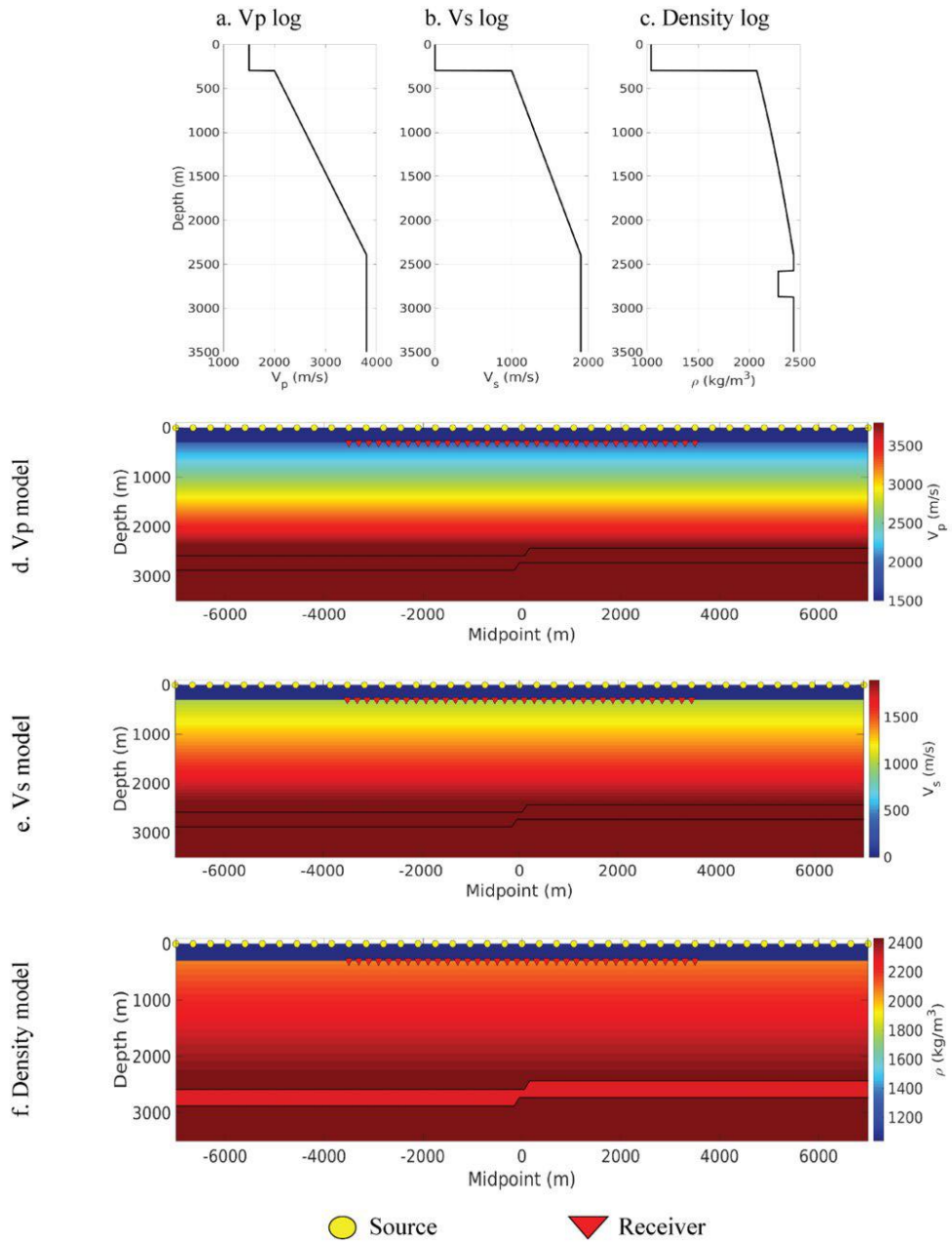
P1 Figure 3: P-wave velocity (a) S-wave velocity (b) and density curves extracted from well 7121/5-1 and the respective models (d-f).
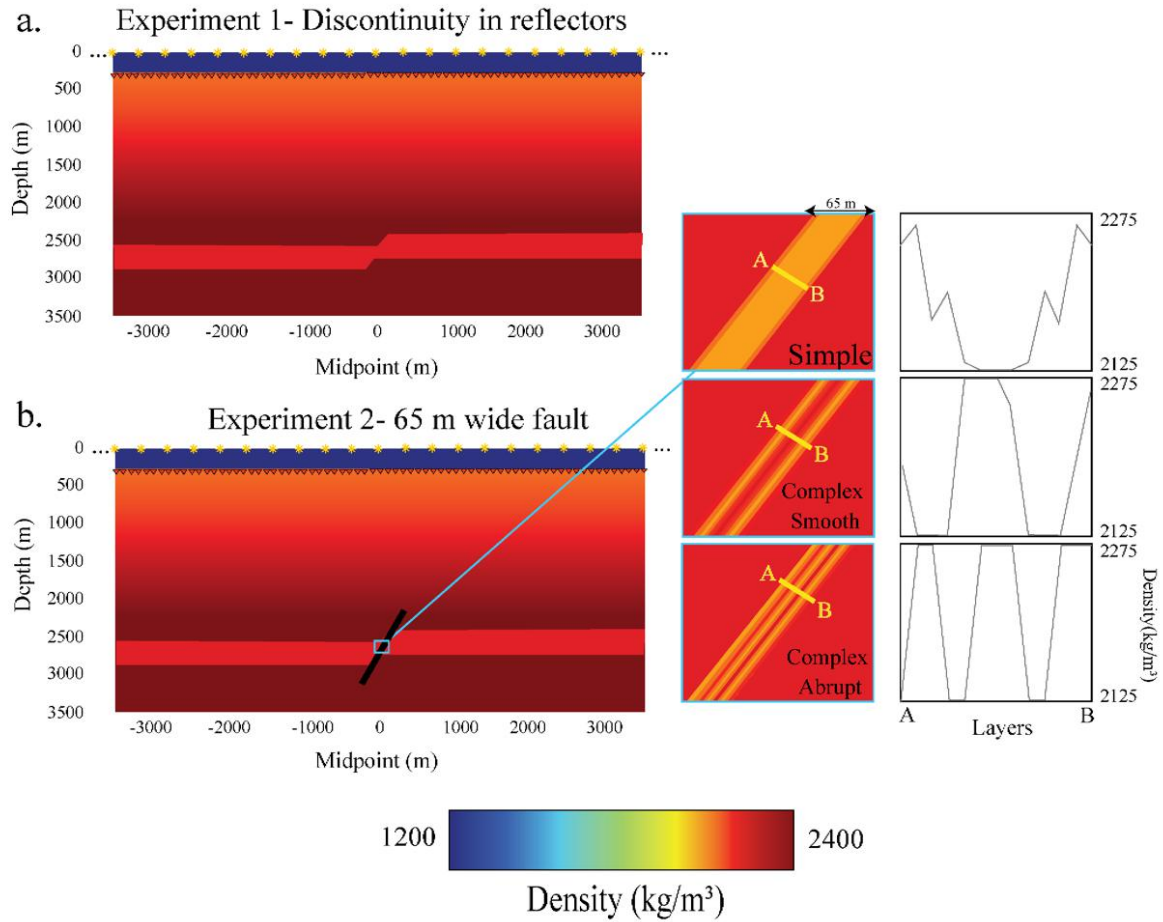
P1 Figure 4: Geological models for the synthetic seismic experiments. (a) Experiment 1 tests the effects of source location relative to the fault and azimuthal separation. This model shows a discontinuity in the displaced horizon that resembles a fault, but the fault body is not modelled. (b) Experiment 2 tests the seismic frequency contained in a simple, homogeneous fault (top inset) and two more complex heterogeneous faults (middle and bottom insets). The fault zone is 65m wide and exhibits a multi-layer morphology in the two heterogeneous fault zones. Graphs of the velocity transitions across the fault zones are also included.

fault plane allowed us to focus on how horizontal reflections can be influenced by the presence of a horizon dislocation (although it is likely that the Snøhvit faults are complex fault bodies which were not imaged). Although in the models the discontinuity appears as a straight line, it was created with a staircase geometry due to the gridded nature of the geological model. The P-wave velocity versus depth distribution used in the modelling was generated using upscaled P-wave data from nearby well NO 7121/5-1 (Fig. 3a). The S-wave velocity was extracted from the same well as half of the P-wave velocity, and the background density was extracted from the P-wave data using Gardner's relation (Fig. 3b, c). The displaced layer in the model was assigned a density contrast of -150 kg/m^3 compared to the background density (Figs 3f, 4a). The distribution of P- and S-wave velocities across the model were also included in Figure 3d and 3e for reference. Since the imaging of the fault discontinuity is the aim of this experiment, these density contrasts were chosen to represent lithologies with contrasting elastic properties. 41 sources were spaced 350 m apart and positioned at 0 m depth (i.e. sea surface). The survey geometry is a 2D geometry chosen to mimic the inline geometry of the real Snøhvit OBC survey (Fig 1c). The sources were placed at +/- 7000 m horizontally across the model (Fig. 3). 1401 dual component receivers (x and z) were placed at 300 m depth (seabed) with a 5 m spacing between midpoint positions +/-3500 m (Figs 3a, 4a). The source used to generate the seismic data was an isotropic pressure source with a zero-phase Tukey window wavelet consisting of a flat band between 4 and 40 Hz and half cosine ramp in the ranges 0-4 and 40-70 Hz. Dual component receivers were used because the analysis was only for P-S data in 2D. Free surface related multiples were suppressed using absorbing boundary conditions at all sides of the modelling domain. Interbed multiples are, however, still present in the data. During the data processing, the direct wave was muted, and the data were separated into incident angle stacks and by azimuth into east (receivers to the right of the source) and west (receivers to the left of the source) azimuths. The data in both x and z components were depth migrated using elastic reverse-time migration (Hokstad *et al.* 1998; Weibull & Arntsen 2013) with a smooth version of the true velocity model from the well. The results were available in the form of PS images of the partial angle stacks for both the E and W azimuths (as in the Snøhvit Field case study). A full incidence angle stack for the E and W azimuth (sum of all 41 sources

and all incidence angles) was also generated. For an in-depth explanation of the parameters used in the modelling and processing of this experiment as well as a complete set of individual shot point PS images please refer to the supplementary material.

This model is not intended to replicate the Snøhvit data and several simplifications have been made in order to understand the potential impact of a fault on horizon discontinuities created by faulting. The geological model has been simplified in order to understand the impact of two geological boundaries on discontinuity imaging. However, the geology in the Snøhvit data is more complex with many reflectors and lithologies that are displaced by faulting (Fig. 1d). The model does not incorporate a fault body which, although not imaged, almost certainly exists in the Snøhvit Field. The Snøhvit data are a 3D OBS survey, while the model is 2D. Despite these limitations, the purpose of the model as illustration of the concepts being studied justifies its use.

P1 3.2.2 Experiment 2

This experiment investigates how changes in lithology within a fault zone can influence and shift the dominant frequencies in seismic reflections compared to the adjacent unfaulted areas (O'Doherty & Anstey 1971; Anstey & O'Doherty 2002; Weibull *et al.* 2019). It also addresses how the observed seismic frequencies of displaced reflectors may vary near to and away from a fault. As was the case for experiment 1, P-wave velocities were extracted from log data of the NO 7121/5-1 well, and S-wave velocity and density were generated using a P-wave extraction (Fig. 3a-c). Also similar to experiment 1, a 300 m thick layer was vertically offset 150 m by a fault dipping 55º to the W (left of the model), and a density contrast of -150 kg/m^3 relative to the background elastic model was assigned to the displaced layer (Fig. 3f).

In this experiment however, a 65 m thick fault zone was added using a 5 x 5 cell staircase geometry (Fig. 4b). Such a thick fault body was chosen in order to exaggerate how variations in the geology/acoustic properties within the fault affect the seismic frequency content of the backscattered signal from the fault, and allows us to analyse how the presence of a layered fault zone might influence the frequency content of the displaced reflector near the fault zone. Seismic data were acquired using three

distinct layered fault geometries: a simple homogenous fault zone (Fig. 4b, top inset), and two more complex heterogeneous fault zone models (Fig. 4b, middle and bottom insets). Both heterogeneous fault zone models contain 13 fault-parallel layers with different acoustic properties: the first model exhibits smooth velocity transitions while the second model exhibits abrupt velocity transitions (Fig. 4b, middle and bottom insets). As in experiment 1, the model contained 1401 receivers which were placed below a 300m thick water column (Figs 3d-f, 4). The source-time function used in this experiment was a Tukey window wavelet with a flat spectrum between 4 and 40 Hz and half cosine ramps in the ranges of 0-4 and 40-70 Hz. The processing of this second experiment was the same as that in the first experiment. For simplicity the frequency content of the full stack data were analysed. Amplitude spectra were extracted from three locations for each of the models: the centre of the fault, at the upper horizontal reflection adjacent to the intersection of the horizon with the fault, and 800 m from the fault on the HW side. The S-transform of the trace was extracted from depth-to PS time converted data (Stockwell *et al.* 1996). No analysis window was used to extract these spectra. The time-frequency transformed data was then depth-converted and the amplitude spectra were displayed for the chosen depth point in each model. For an in-depth explanation of the parameters used in this experiment please refer to the supplementary material.

The second model also has some simplifications compared with the geology in the Snøhvit Field. Although fault planes have not been imaged directly in the Snøhvit data, fault bodies are expected to be present and these will impact nearby displaced reflectors. The modelled fault zones are thicker and simpler (layer cake) than the fault zones that can be expected in the Snøhvit Field, which are likely thinner than 65m and are likely to contain significant internal lateral and vertical heterogeneity (Cunningham *et al.* 2019). Despite these simplifications, the modelling experiment can be used as a proof of concept for the impact of layered fault zones on frequency content in and around faulted horizons, although drawing direct quantitative conclusions is not possible.

P1 4 Results

P1 4.1 Results from the Snøhvit Case Study

When analysing the Snøhvit data, fault imaging is discussed with respect to discontinuity fault imaging because there was no evidence of a seismic signal registered on the fault plane itself (Figs 1d, 5).

#### P1 4.1.1 *Faults and partial (incidence angle) stacks*

In the case study from the Snøhvit Field area, the northern (NE-SW trending) fault dips ~54° to the NW, and the southern (WNW-ESE trending) fault dips ~50° to the SSW. In the reflection data these faults are clearly visible on the inline (N-S orientation) analysis (Fig. 5a). The inlines all show a discontinuity where a fault has displaced horizontal reflections but in no partial or full stack image is the fault plane able to create a reflection. Tensor is the optimal attribute to image the lateral and vertical extent of the fault (Figs 5b, 6b). Both the inline (4000) and time slice (3128 ms) from the near, mid and far angle stacks of the E and W datasets show high tensor values (e.g. fault lateral extent, fault width and image detail). Imaging quality improves with increasing incidence angle stack (Figs 5b and 6b). This improvement in imaging quality is visible on the inline section (Fig. 5b) but is most clear on the time slice (Fig. 6b) which shows an increase in brightness, length and width of the faults with increasing offset (this occurs regardless of azimuthal separation). The envelope attribute (Figs 5c, 6c) exhibits an increase in magnitude and therefore reflector strength with increasing incidence angle stack (Figs 5 and 6c). This observation suggests that amplitudes across the entire study area are increasing with incidence angle stacks. The full stack data for both the E and W datasets are most comparable to the mid-stack data but, as expected, the full stack data contain a higher signal-noise ratio across all the studied attributes (Figs 5, 6: Full).

P1 4.1.2 *Fault imaging versus azimuthal direction*

The orientation of the northern (NE-SW trending) and southern (WNW-ESE trending) faults in the Snøhvit case make it possible to examine the effects of the E and W azimuth data on the imaging quality of these faults
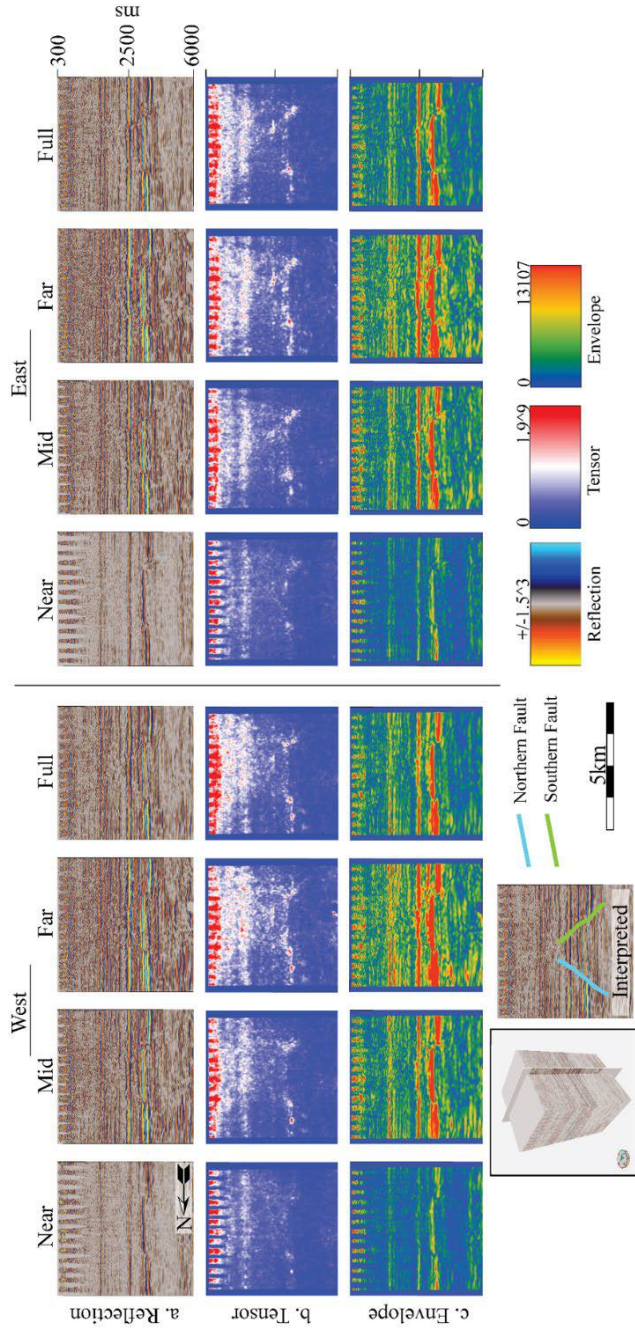
P1 Figure 5: Partial (near, mid, far) and full stacks of the W and E (a) reflection data, (b) tensor and (c) envelope attributes displayed on an inline (4000) through the centre of the study area.
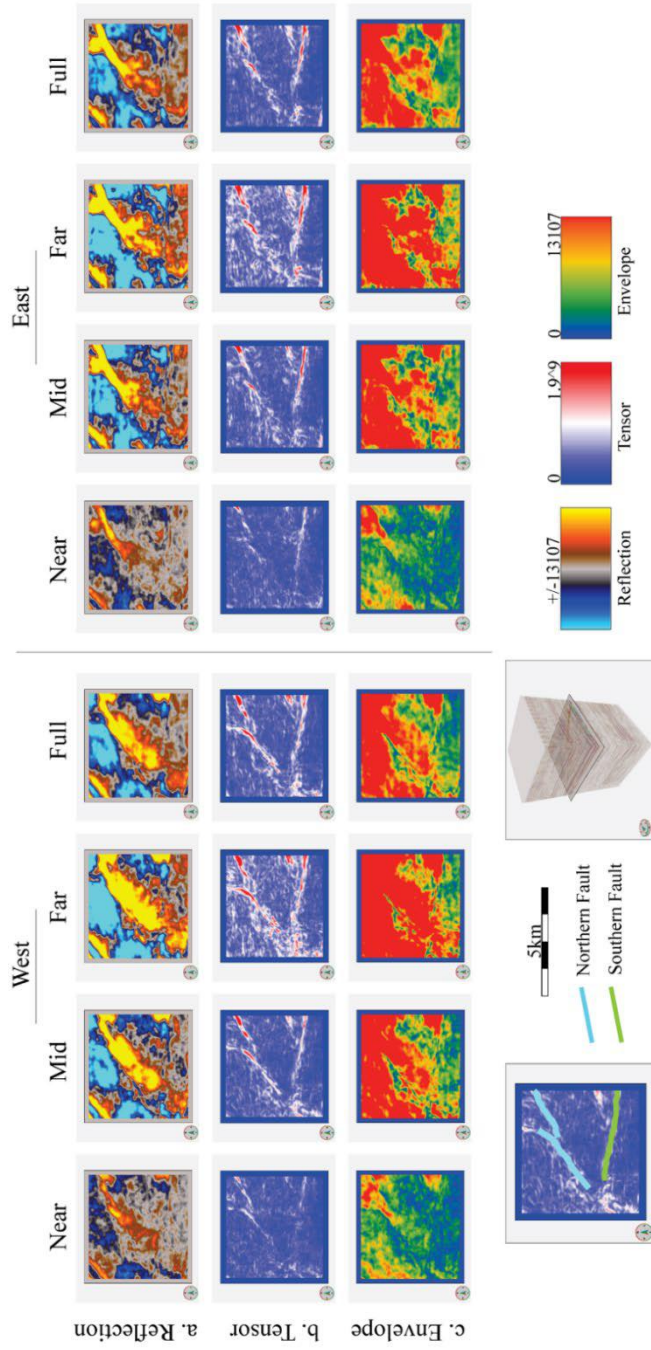
P1 Figure 6: Partial (near, mid, far) and full stacks of the W and E (a) reflection data, (b) tensor and (c) envelope attributes displayed on time slice 3128 ms (PS time). This slice is approximately at the middle of the main faulted interval.

(Fig. 1c). In general, the W data exhibit longer, slightly wider and more sharply defined tensor signals from the faults than the E data (Figs 5b and 6b). The improved imaging on the W data is much more significant for the NE-SW trending northern fault than for the southern WNW-ESE trending fault, and this is consistent across all azimuth volumes.

As tensor provides the clearest visualization of the discontinuity fault imaging, a comparison figure was made to only include partial stack time slices of the tensor attribute (Fig. 7a-c). An AVO colour blend of the tensor attribute was also generated to understand the azimuthal contribution each of the partial stack signal in more detail (Fig. 7d). The tensor data from the W-Near to the E-Near reveal that the E data show slightly higher amplitude, increased sharpness and greater lateral extent of the southern (WNW-ESE trending) fault, compared to the W data (Fig. 7a). The northern (SW-NE trending) fault is poorly imaged in near datasets but is slightly better resolved in the W data (Fig. 7a). In contrast, the northern fault is imaged very differently on the mid and far offset volumes as it is significantly higher amplitude and exhibits a longer and wider fault zone in the W data compared to the E data (Fig. 7b, c). The imaging quality also improves with increasing angle stack (Fig. 7b, c). The southern fault shows a slight increase in magnitude of the tensor attribute signal in the mid and far offset data from the E volume. The southern fault is therefore imaged with slightly higher amplitude in the E data, although the morphology and lateral extent of this fault is the same in both E and W datasets (Fig. 7b, c).

In the AVO tensor blend, faults are visualized as largely white bodies surrounded by a slight teal halo (Fig. 7d). The white colour indicates that the fault is imaged by all three partial stacks in equal amounts, whereas the teal colour suggests a widening of the fault with increasing incidence angle in the mid and far data. This observation is in-line with the observations of individual stacks (Fig. 7 a-c).

P1 4.1.3 Discontinuity imaging and seismic frequency

Frequency decomposition (FD) RGB colour blends were generated to explore the frequency content of the backscattered signal from the
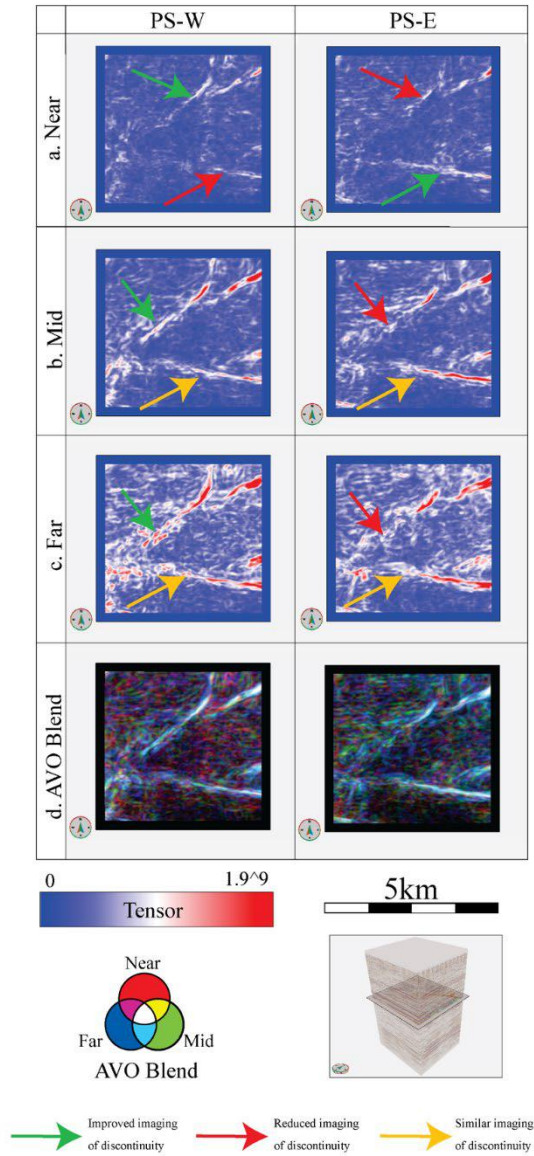
P1 Figure 7: Comparison of time slices of the W (left) and E (right) tensor attribute for the (a) near, (b) mid, and (c) far offsets and an RGB AVO colour blend (d) of the near (Red), mid (Green) and far (Blue) tensor attributes. These are all displayed on a time slice at 3128 ms (PS time), which is approximately at the middle of the main faulted interval.

79

northern and southern faults. These decompositions were optimized for the frequency content contained in a chosen time slice at 3128 ms (PStime) in the E and W data. At this slice, the frequency power spectrum (Fig. 8c, d) ranges between 3-35 Hz assuming a -20 dB cut-off criteria. Once optimized, the result of the FD are three magnitude volumes of a user-defined low, medium and high central frequencies (8, 14 and 30 Hz in this case study). Graphs displaying the power spectra and central frequencies for each of these magnitude volumes were used as a point of reference (Fig. 8c, d). Although the power of each stack increases with incidence angle in the E and W spectra, the overall trends of all spectra are similar (Fig 8c, d). Magnitude volumes were then blended into eight RGB FD colour blends, one for each of the E and W partial and full stack volumes (Fig. 8a, b).

On time slices of the frequency decomposition volumes, faults appear to have significantly lower frequency content relative to the surrounding data. The faults appear as darker, almost black lineaments on each FD. Analysis of these darker bodies reveals subtle and intermittent shadows of red-green in the dark bodies suggesting the presence of low-medium frequency (8-14 Hz) across the entire faulted interval (despite only being displayed in a single slice: Fig 8a, b). The areas surrounding the black fault lineaments are dominated by greenish and occasionally teal-blue haloes which coincide with slightly higher frequency content (14-30 Hz; Fig. 8a, b). The presence of dark fault lineaments with low-medium frequency shadows as well as the presence of medium to high haloes surrounding the faults are observed on all FDs and has no relationship to azimuth or incidence angle.

In the unfaulted background of the FDs there is a dominance of reddish hues with increasing incidence angle stack across the time slice (Fig. 8a, b, columns 1 to 3). Like the envelope attribute, power spectra from the FD exhibit the highest amplitude content in the far stack data suggesting an overall strengthening in the observed amplitudes with increasing incidence angle (Fig. 8c, d). In addition, the highest frequencies are most apparent in the shallowest sections of the FD volumes for all stacks, and frequencies decrease with depth, i.e. blue colours in shallow sections and more red in deep sections (Fig. 8a, b, inlines and crosslines). The FD results from the full stack volumes contain the average frequency range

80
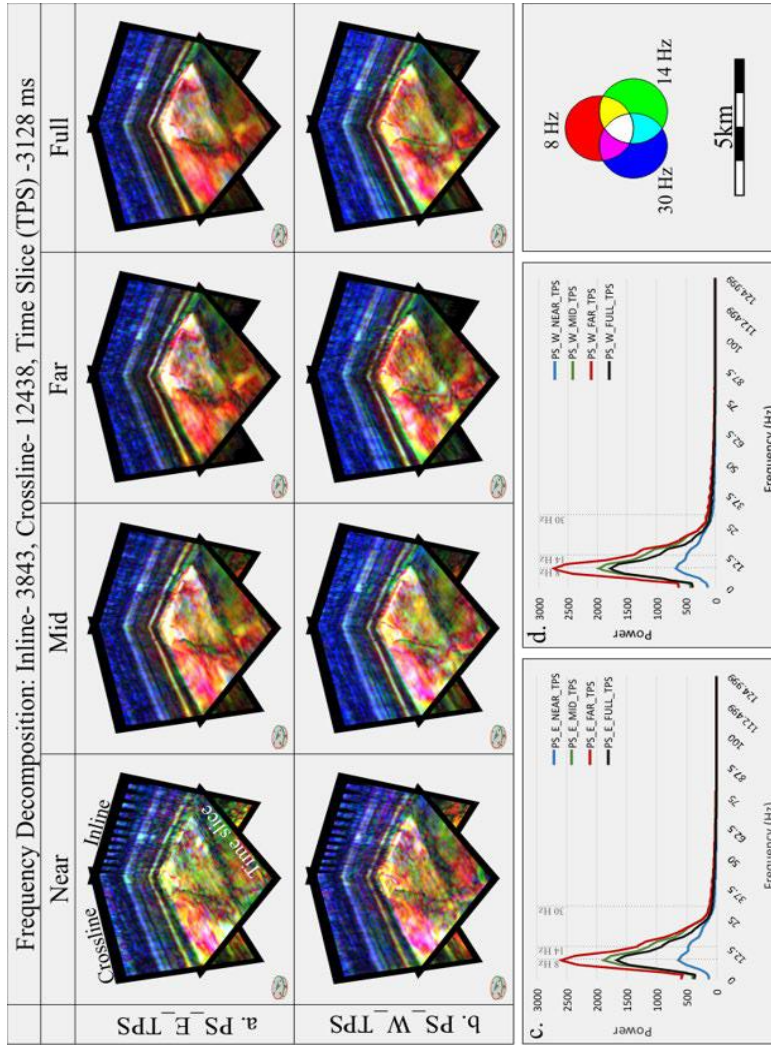
P1 Figure 8: Frequency decomposition of the E (a) and W (b) data for the near (column 1), mid (column 2), far (column 3) and full stacks (column 4). Power spectra of the E (c) and W (d) near (blue line), mid (green), far (red) and full (black) 3128 ms time slices. The frequency decompositions were generated using central frequency magnitude volumes of 8, 14 and 30 Hz (c, d; grey dashed lines). The frequency data are displayed in PS time on an inline (3843), crossline (12438) and time slice (3128 ms).

of the near, mid and far stacks (Fig. 8c, d, black lines).Despite the changes in frequency being relatively unaffected by azimuth, the lateral extent of the northern fault is more clearly imaged by the W data than the E data (see Fig. 8 and section 4.1.2). Conversely, the southern, WNW-ESE trending fault is imaged similarly in both E and W datasets and in all the partial stacks (see Fig. 7 and section 4.1.2).

In summary, faults in all FDs appear as black lineaments with very subtle red-green shadows running through them. The faults in all FDs are also surrounded with green-teal-blue haloes which indicate higher dominant frequencies relative to the surrounding unfaulted signal (red-yellow hues). These observations occur regardless of the azimuth or partial stack being analysed.

P1 4.2 Forward Seismic Modelling

Two 2D forward seismic models were designed as a proof of concept to understand the fault imaging observations of the Snøhvit case study with respect to azimuthal separation, incidence angle and frequency. The models should be used as a generalization to understand trends in fault imaging and how seismic waves, seismic processing and frequency may vary in the forward modelled data. The aim of these models is to provide some plausible explanations for the results in the case study (section 4.1). For the Snøhvit case study only fault imaging as discontinuities were observed. However, the models capture both horizon discontinuity imaging and fault plane imaging, and both are discussed.

P1 4.2.1 Experiment 1

The first experiment was designed to test the effect of azimuthal separation and incidence angle on the seismic imaging of a discontinuity created by a zero thickness fault that offsets a layer of contrasting acoustic properties (Fig. 9). The data are separated by azimuth and processed into near, mid, far and full stacks similarly to the Snøhvit data. In all stack images, the top of the displaced layer is represented by a white peak at the centre surrounded by two pairs of side lobes (black, white, black, white) and is representative of a downward increase in acoustic impedance, while the base of the layer has the opposite character.
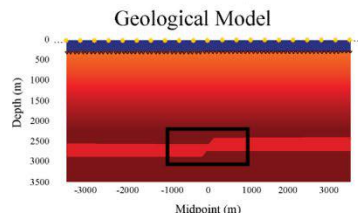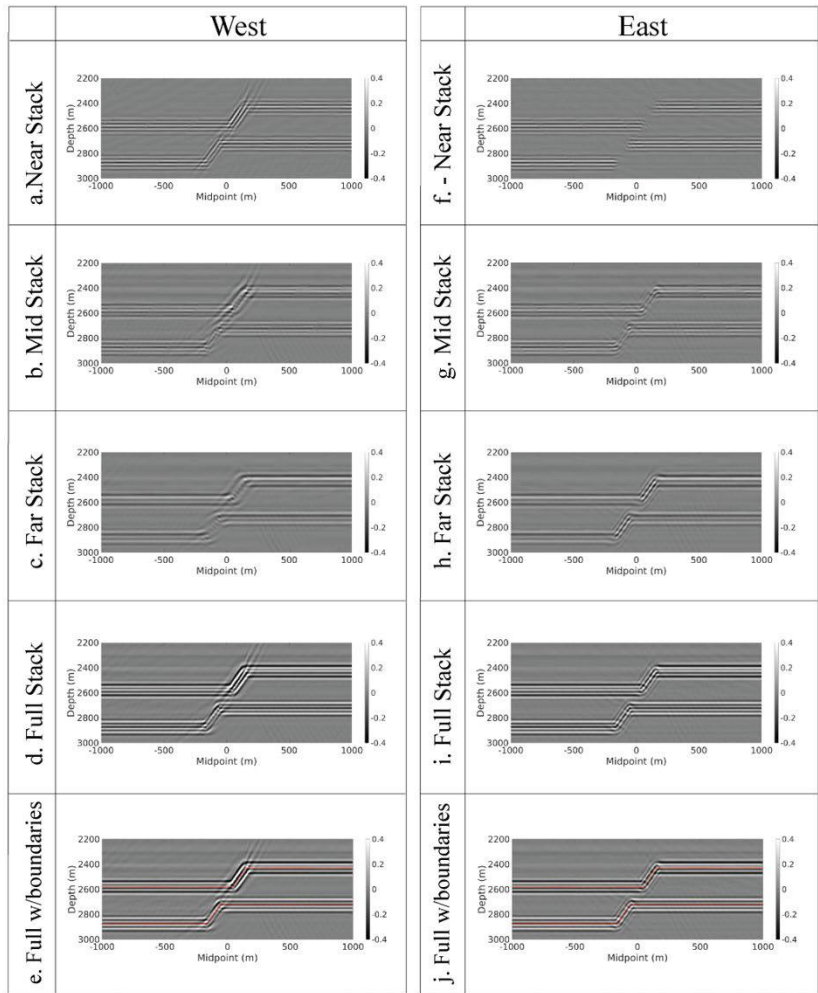
P1 Figure 9: Synthetic seismic experiment 1. The models are separated into W/E azimuth (left/ right columns) and incidence angle stacks: near (a/f), mid (b/g), far (c/g), full (d/i), and full with geological boundaries overlaid (e/j). The figures focus on the fault area indicated by the black rectangle on the geological model.

In the W data the horizontal reflectors have a slightly brighter amplitude but also become less sharply imaged with increasing incidence angle stack, making it slightly more difficult to distinguish the main peak and side lobes of the horizontal reflector with increasing incidence angle(Fig. 9a-c). As there is no fault plane in the model for this experiment there is no single reflection running along the length of the discontinuity. However, in areas where a lateral change in density occurs (due to the fault displacement) a planar reflector is imaged. This planar reflector resembles a fault plane even though the model lacks a distinct fault zone.

In the W data the planar reflector is imaged as a white peak with a pair of black-white sidelobes for the upper boundary (Fig. 9a-c). The lower boundary of this planar reflector has the opposite character. With increasing incidence angle stack, the imaging of the discontinuities appears to have a lower frequency (blurred) but are clearly visible in all partial and full stacks.

In the E data, the brightness of the horizontal reflectors increases similarly and becomes less sharply resolved with increasing incidence angle stack (Fig. 9f-h). In the E data the imaging of the fault discontinuity as a plane is slightly different. In the near data (Fig. 9f), only a discontinuity is imaged and no plane is visible while the mid and far stacks (Fig. 9 g, h respectively) exhibit a clear refection from the discontinuity where brightness and reflector sharpness (i.e. a more visible main peak/trough and side lobes) increase with incidence angle.

There is almost no difference in the imaging of the horizontal reflections between the W and E data. In contrast the discontinuity is more clearly imaged by the W near, mid and far stack (Fig. 9a-c in comparison to 9f-h), as demonstrated by the greater reflector strength in the W data. In all W stacks there is also a slight increase of amplitude of the horizontal plane at the intersection point between the horizontal reflector and the discontinuity/fault. In the E data these terminations are only clear when a fault plane is visible (cf. Fig. 9f) and show an increase in amplitude that correlates with the increasing amplitude of the fault plane with incidence angle stack (Fig. 9g, h).

Horizon imaging is extremely similar in the full stack data from the W and E azimuths. However, the fault discontinuity and the terminations of

the horizon at the discontinuity show some differences between the W and E full stacks (Fig. 9 d, e, i, j). As described for the partial stack data, lateral changes to density due to the presence of the discontinuity are imaged as distinct planes. In the W data (Fig. 9 d, e) these reflections from the discontinuity are stronger, and the character of each reflector is more easily distinguished than in the E data (Fig. 9 i, j). In the W data the terminations of the horizontal reflections with the discontinuity/ fault appear to a higher amplitude than in the E data. In the W data the discontinuity observed at the upper boundary is higher amplitude and more sharply defined than the lower boundary, while in the E data the amplitude of the upper and lower boundaries are comparable.

P1 4.2.2 Experiment 2

The second experiment was designed to investigate the impact of layered fault bodies on the seismic frequencies observed in and surrounding faults in three models: a simple homogenous fault, a more complex smooth, and abrupt heterogeneously layered fault (Fig. 4b, top, middle, and bottom insets and graphs respectively). Amplitude spectra (Fig. 10 columns 2-4) were analysed at the centre of the fault and two spectra were extracted from the upper horizontal boundary (adjacent to the fault and one ~800 away on the HW side of the fault). The location corresponding to the sampled spectra is marked with a coloured x in all models (Fig. 10, left column). The spectra were extracted from the same location in each model at a single point, without the use of a sampling window (supplementary material).

Full stack 2D seismic lines were generated for each of the three models. The 2D seismic for the simple-homogenous fault (Fig. 4b, top inset) shows no correlation between reflector strength in the fault plane with increasing depth (Fig. 10a column 1). However, the amplitude of the fault reflection changes consistently with depth between the upper and lower boundaries. The brightest amplitudes occur towards the top of the fault plane image at the intersection of the plane with the FW side of the displaced layer. The lowest amplitude imaging of the fault occurs at the middle sections on the fault between the upper and lower geological boundaries of the layer on both the HW and FW sides of the fault. The deepest section of the fault (below the displaced layer on the HW) is
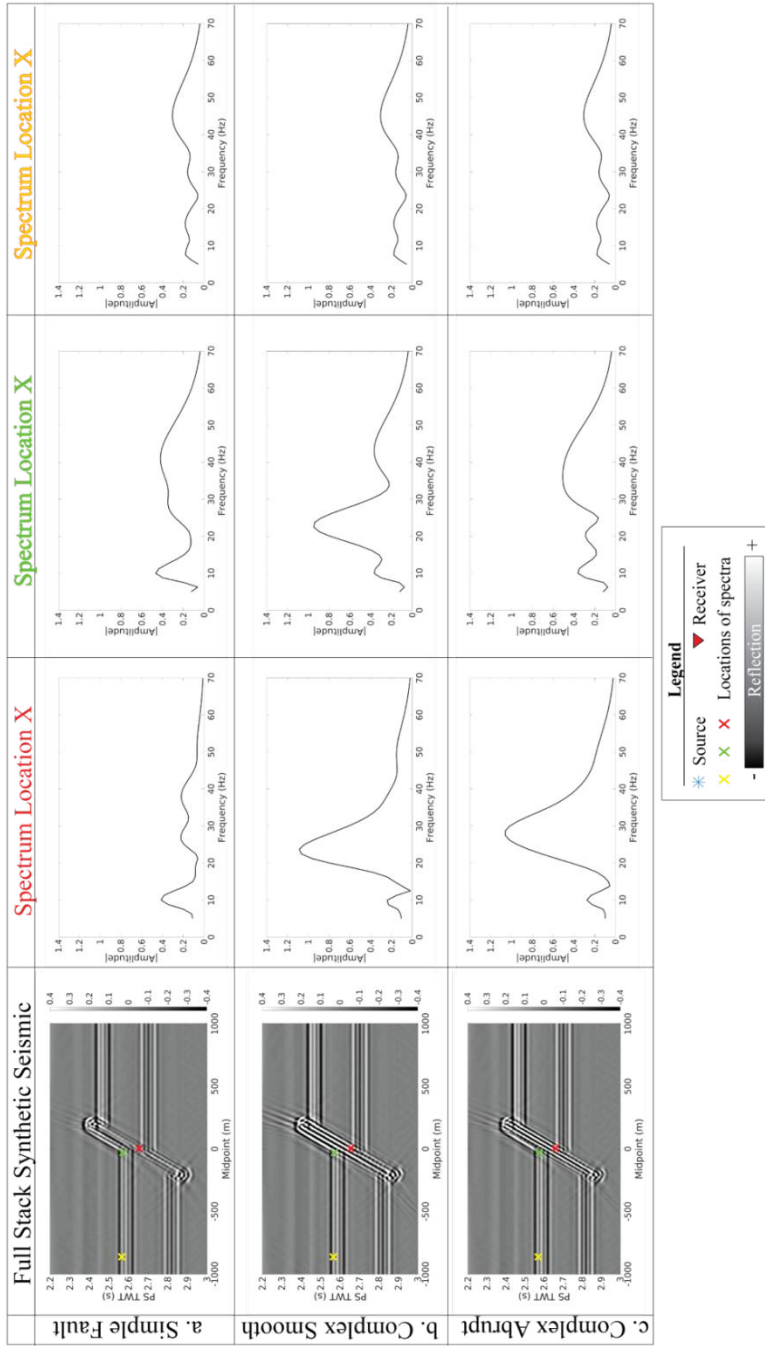
P1 Figure 10: Synthetic seismic experiment 2. A simple (homogeneous) and two more complex (heterogeneous) fault zone models (Fig. 4b) were used to generate three different full stack/azimuth seismic volumes and frequency extractions. The resulting full stack/azimuth seismic and amplitude spectra for the simple (a), the heterogeneous-smooth (b) and heterogeneous-abrupt fault models (c). The locations where the amplitude spectra were extracted are marked with a green, red and yellow X. These extraction points refer to the middle of the fault zone (red), the termination of the reflector with the fault zone (green), and unfaulted horizontal reflection (yellow).

slightly higher amplitude than the middle section of the fault but lower amplitude than the upper section of the fault. The 2D seismic for the smooth and abrupt heterogeneous faults (Fig. 10 b and c column 1 respectively) appear very similar in fault thickness, length and reflector strength but the abrupt model has more clearly imaged the internal geometry (as is expected since the model had more contrast in acoustic properties).

The extracted spectra from within the fault plane (Fig. 10a-c column 1 and 2, red X) generally show an increase in dominant frequency with increasing fault complexity. The amplitude spectrum for the homogeneous fault zone shows a peak in the low frequency signal (5-15 Hz, 0.2-0.4 magnitude) and a decrease towards the medium-high frequencies (15-70 Hz, 0-0.2 magnitude; Fig. 10a, column 2). The power spectrum of the heterogeneous smooth fault zone has a peak of medium frequency content (peak at ~23 Hz, decreasing towards 70Hz) and relatively little low frequency content (Fig. 10b, column 2). Finally, the power spectrum for the heterogeneous abrupt fault zone has a peak of higher frequency content (peak at 30 Hz, decreasing towards 70 Hz) and little low frequency content (4-20 Hz, Fig. 10c, right).

The observed frequencies within the displaced horizontal reflectors adjacent to and further away from the fault plane in the model were compared in order to understand the impact of a layered fault body on the seismic frequencies of horizontal reflectors. Generally, the spectra located on the displaced horizon immediately adjacent to its HW intersection with the fault plane (Fig. 10, green x and column 3) exhibit higher frequencies than those observed away from the fault (Fig. 10, yellow x and column 4) and the dominant frequency increases with increasing fault complexity. For example, with the homogeneous fault (Fig. 10a, columns 3 and 4) a peak of low frequency followed by a plateau of medium-high frequencies occur near to the fault (10 and 25-50 Hz respectively, 0.4 magnitude) while away from the fault, the reflector exhibits relatively consistent contributions from all frequencies at a magnitude of 0.2. The results of the heterogeneous smooth and complex abrupt cases show more significant differences with a higher abundance of medium (~15-25 Hz) and high (~30-50) frequency adjacent to the fault compared to the spectra sampled away from the

fault. The spectra extracted far from the fault are consistent for the three models and are unaffected by fault complexity (Fig. 10a-c column 4). The variations in seismic frequencies near the fault plane tend to increase with the increasing internal complexity of the fault, suggesting there is a linkage between the horizon imaging adjacent to the fault and the internal morphology of the fault body.

Since the model lacks realistic acoustic properties for the fault and boundaries it is best not to compare the modelling results directly with the Snøhvit data. Despite this it is significant that there is a consistent increase in frequency near the fault relative to away from it, indicating that the presence of a layered fault body affects the frequency content of horizons near the fault and that increasing fault complexity and layering results in an increase in overall frequency content.

P1 5 Discussion

P1 5.1 The imaging of faults in the Snøhvit data

The modelling experiments clearly demonstrate that fault plane reflections should be visible in the Snøhvit OBS data (Fig. 9). However, the analysis of the PS data in the Snøhvit case study (Fig. 5a) showed no evidence of fault plane imaging as a distinct reflection. Faults in this dataset are imaged only as discontinuities (where no actual fault plane is imaged). There are several possible explanations for why a fault plane might not be imaged, and these are discussed below.

The first possible reason is the survey geometry. If the incidence angles are collected in a narrow range and/or the survey is not large enough it is possible that waves reflecting off the fault would not be returned to receivers. This effect is evident in our E near modelled data and some individual shot points capture fault discontinuity imaging but no fault plane (Fig. 9f and supplementary material). However, the large size of the seismic survey for the Snøhvit data and the wide range of incidence angles acquired (0-65º) mean that it should be possible to image the fault planes despite the observed steep dips of the faults. It can be concluded from our modelling that survey geometry can play a role in fault plane imaging but is not likely to have prevented the imaging of fault planes in the Snøhvit data.

The next possible explanation for the lack of imaged fault planes involves the processing workflow applied to the Snøhvit data. It is possible to remove any signal in a seismic processing workflow through migration and signal filtering and dipping events are no exception to that (i.e. radon transform). In the workflow that was provided on seismic processing (Table 1) it is possible that the Radon demultiple stages (Table 1, steps 18 and 28) removed the reflections from the dipping fault plane (e.g. Yilmaz 2001).

Another reason that might have caused the lack of a seismically imaged fault plane is the geology itself. Although the faults are steep (>50°), the survey geometry should still allow for the fault planes to be imaged. In the forward models the only way to avoid imaging the dipping planes from the final seismic was by applying a smooth elastic properties transition across the dipping boundary. It is possible that the faults in the subsurface have smooth elastic property transitions which allows for a lack of a strong, sharp fault plane reflection but the size and variations in lithology across the Snøhvit faults (as observed by previous works) make this very unlikely (Cunningham et al. 2019). Unfortunately, without a wellbore or core transecting the fault zone it is impossible to conclude on the reason for the missing planes and the remainder of the discussion will focus more on the imaging of faults as discontinuities.

P1 5.2 Incidence angles

In the Snøhvit data the discontinuity fault imaging improved in the northern fault with increasing incidence angle in both the E and W azimuths (Fig. 7) whereas imaging quality was relatively unchanged for the southern fault. The discontinuity appeared to widen and lengthen with an increase in incidence angle as was depicted in the AVO colour blend of tensor as a teal halo (Fig. 7d). With an increase in incidence angle the Snøhvit case study exhibits a systematic increase in the strength and a decrease in frequency of reflections across the study area (Figs. 5c, 6c, envelope attribute and Fig. 8). The increase in strength can be explained as a function of amplitude variations with angle (Jabbari & Innanen 2015). While the decrease in dominant frequency with increase in incidence angle can be explained by a combination of higher intrinsic

attenuation due to the larger propagation distances, and migration stretch associated with steeper travel-time curves at wider angles.

The amplitudes of the upper and lower boundaries in the seismic modelling experiment increased with increasing incidence angle but also appear to be less sharply resolved. Discontinuities in the modelled data were imaged as planes without any observed systematic changes which could be linked to increasing incidence angle. To establish a better understanding of the discontinuity plane imaging, the envelope of the lateral gradient was computed on the modelled partial and full stack data (Fig. 11). This measurement resulted in a strengthening of the signal from the discontinuity plane with increasing incidence angle for the E data, and a decrease with incidence angle for the W data (Fig. 11).

The modelling does not provide an unequivocal explanation for the changes in amplitude and imaging quality with increasing incidence angle. The envelope attribute in the case study (Fig. 5c, 6c) demonstrates that reflector strength increases with increasing incidence angle across the entire study area. It is proposed that this change in reflector strength may be in part responsible for the improved imaging of the discontinuity which was observed in the tensor attribute for the Snøhvit data.

P1 5.3 Azimuthal separation

The Snøhvit data prove a clear linkage between the orientation of the seismic survey (E-W-E), the orientation of the faults in the survey and the resulting discontinuity imaging of the fault (Fig. 7). The northern fault is oriented orthogonally to the seismic acquisition direction and is more clearly imaged in the W data than in the E data. The southern fault (oriented approximately parallel to the survey) shows very little difference between the E and W azimuths.

The forward seismic modelling experiment (1) demonstrates that the W azimuth data was generally better at imaging the discontinuity fault planes than the E data (Fig. 9). Despite the absence of a distinct fault zone in our model, planes were imaged due to discontinuities in the model along the displaced plane of the upper and lower geological boundaries. In addition, the quality of discontinuity plane imaging appears to be linked to the increase in amplitude where the reflector
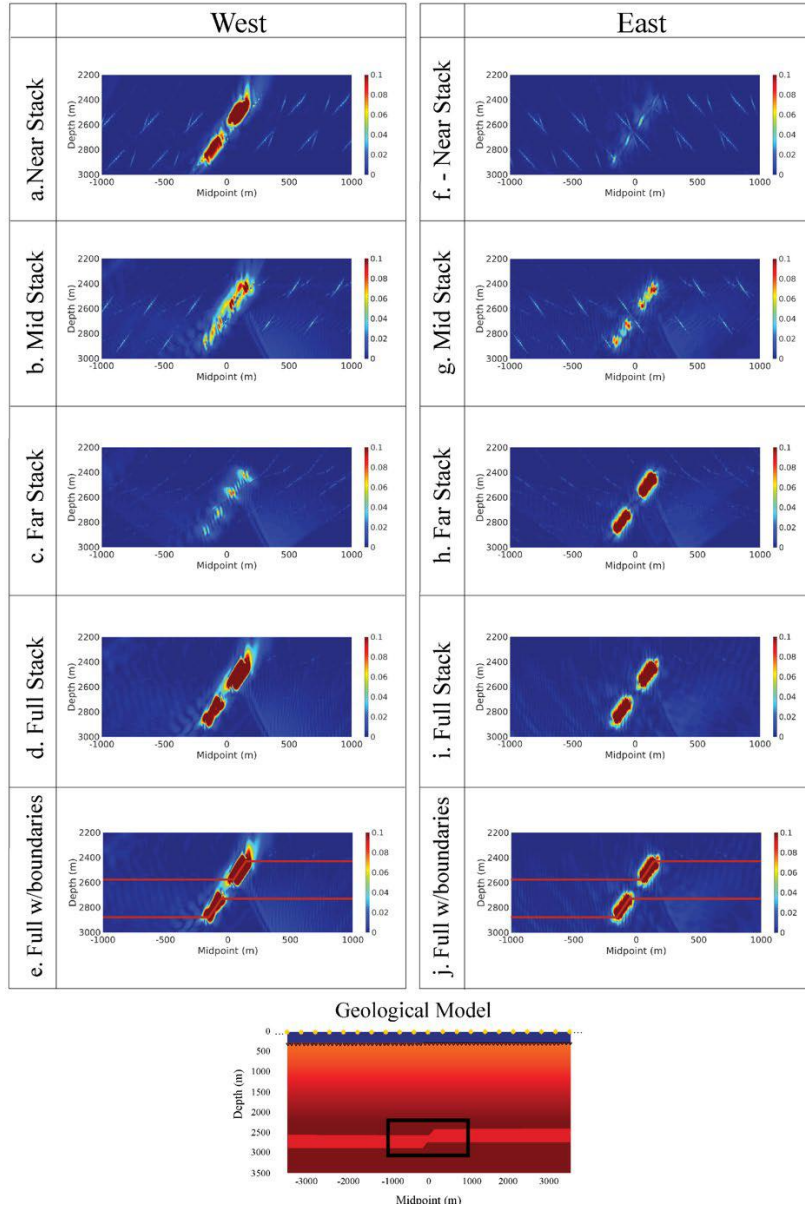
P1 Figure 11: Envelope of the lateral gradient attribute of experiment 1. The attributes are separated into W/E azimuth (left/right column) and by incidence angle stacks: near (a/f), mid (b/g), far (c/h), full (d/i), and full with geological boundaries overlaid (e/j). The data are also separated into W (left column) and E (right column) azimuths. The figures focus on the fault area indicated by the black rectangle on the geological model.

91

terminates at the plane. A ray tracing study was conducted on the model to understand the contribution of seismic signal coming from a single point on the upper discontinuity plane and to see how that signal point is imaged in individual shot points (Fig. 12). By counting the azimuthally separated ray paths in the raytracing diagram, the W azimuth has far more single shots returning signal to the receivers than the E azimuth (Fig. 12a). Raytracing was used to extract shot point position and incidence angle versus the reflection coefficient of the data (Fig. 12b, c). In the W data a reflection was returned from shot points ranging between -600 and -2050 m for a single point on the discontinuity plane, while the E data covers only shot points between -2050 to -2600 m (Fig 12b). In reflection coefficient versus incidence angle, the W data was able to return a reflection for incidence angles 20-55º while the E data was only imaged in the furthest incidence angles 55-65º (Fig. 12c). It is important to note that this incidence angle refers to the angle at which the wave reflects off the single point on the discontinuity plane and is not the same as the processed incidence angles used in partial stacking, which are based on the vertical variations of the P- and S-wave velocities and therefore assume incidence angles with respect to the normal of a horizontal reflector. Despite this difference in angles, the main thing to note is the data coverage in all aspects of the ray tracing study are clearly dominated by W azimuth reflections. This confirms the impact of seismic survey geometry relative to structure and azimuthally separating data on the imaging of faults or dipping surfaces.

The discontinuity planes also impact the imaging of reflector terminations in the model and like the Snøhvit data, the effects are more obvious in the W data. The model showed little difference in the imaging of the upper and lower boundaries while the terminations of these reflections with the discontinuity tended to strengthen and even change orientation slightly from horizonal. The signal of these terminations appeared strongest when the seismic imaging of the fault discontinuity plane was strongest in the W data (Fig. 9). Similarly, the E-near data shows no image of a discontinuity plane and there is no change in amplitude where the discontinuity intersects the horizon (Fig. 9f). When a seismic wave (P or S) reflects off a structural edge such as a fault, both specular and diffracted waves are generated (Landa & Keymar 1998; Khaidukov *et al.* 2004; Landa 2012; Fomel *et al.* 2018). Specular waves

92
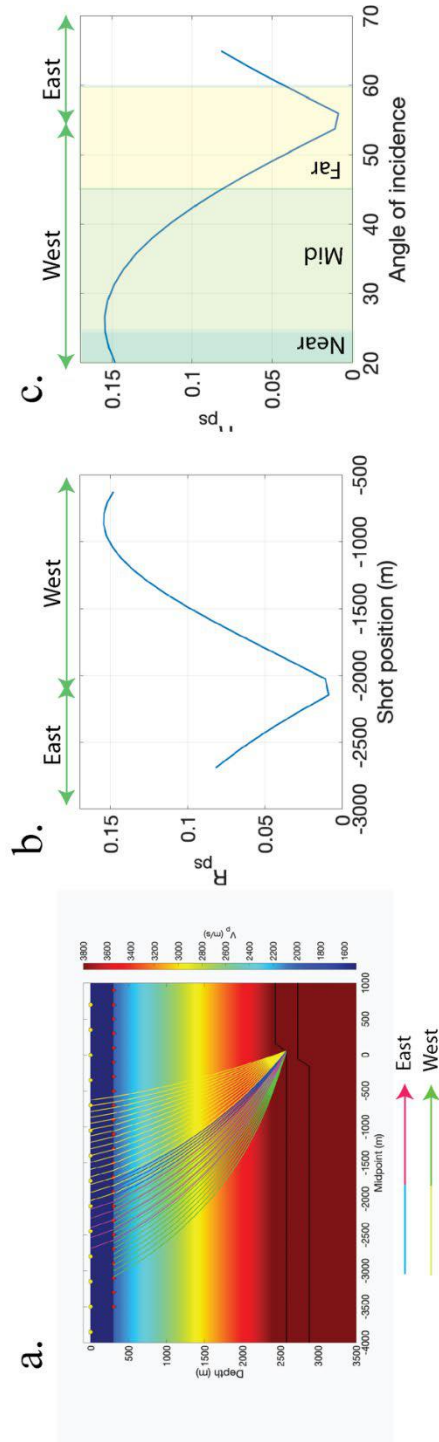
P1 Figure 12: Ray tracing study: (a) ray tracing of a single point on the upper boundary of the discontinuity plane the rays are coloured by azimuth. (b) Shot point versus PS reflection coefficient and (c) incidence angle versus reflection coefficient.

are conventionally used to image and interpret structural or stratigraphic features in seismic data and are generated by acoustic impedance contrasts in the subsurface (e.g. Taner *et al.* 2006). However, no evidence of specular waves is seen in the Snøhvit data. Diffractions, a common aspect of fault imaging in reflection seismology, are scattered from a single point when a seismic wave interacts with a discontinuity (e.g. a fault) or other heterogeneity (Landa & Keymar 1998; Taner *et al.* 2006; Landa 2012; Fomel *et al.* 2018). The increase in amplitude and slight signal variation at the reflector cutoff is interpreted to be a consequence of the interplay between diffractions from the fault plane and the reflection of the horizontal surface (see supplementary material videos).

Complex fault zones are likely present in the subsurface in the Snøhvit Field and are expected to influence the adjacent horizontal reflections. In the Snøhvit data the northern fault is approximately orthogonal to the survey and, compared to the southern fault, it is expected that more seismic waves will meet the hanging wall side of the northern fault than the southern. The more incoming P-waves that interact with the hanging wall, the more specular P- / S- waves and diffractions reflect and scatter off the fault. If these diffractions subtly modify/increase the amplitude and possibly alter the boundary reflections adjacent to the fault, the tensor (and all other fault/structural edge/ discontinuity enhancing attributes) signal will change. This subtle difference in the lateral contrast of the signal created by diffractions could be responsible for the differences in tensor attribute that are seen in the Snøhvit data where the imaging of the W data is clearly stronger than the E data. This phenomenon happens less in the E modelled data since more of the specular and diffracted energy either never encounters the fault or is lost due to the placement of the source and receivers relative to the fault. In the Snøhvit data this phenomenon can also explain why the southern (survey parallel) fault is almost identical in the E and W datasets. This shows the importance of seismic survey geometry, processing and wave interaction with respect to fault/discontinuity imaging.

P1 5.4 The frequency content of faults

Frequency decompositions in the Snøhvit data show faults as black lineaments with a lower overall frequency content than the surrounding

unfaulted data. Within the lineaments there were subtle shadows of low-medium frequency (8-12 Hz) content in all partial and azimuthally separated datasets (Fig. 8). Haloes of high frequency (14-30Hz) were observed around the faults which correlate with the termination of the discontinuity with the imaged horizons. In the surrounding areas that appear undisturbed by faulting, the frequency content is classified as low (< 8 Hz) throughout the study area and the proportion of low frequencies increases with increasing incidence angle stack (Fig. 8). Seismic waves decrease in average frequency content with increasing penetration depth so for the interval being investigated in the frequency decompositions (3128 ms, PS time) the abundance of low frequency data is expected (Stewart & Lawton 1996).

To further test the concept of seismic frequency in fault zones, a synthetic converted-wave seismic experiment was designed to compare a simple homogenous and two heterogeneously (smooth and abrupt velocity transitions) layered faults (Figs 10 and 4b). Three frequency extractions were taken from each of the seismic sections: one in the fault zone, one in the hanging wall termination of the fault with the upper geological boundary and one ~800 m away from the fault on the hanging wall side (Fig. 10). In the fault zone, frequencies increased with fault zone complexity suggesting a linkage between the geological complexity of the fault zone and the resulting increase in the dominant frequency (Fig. 10, red X). At the termination of the fault zone with the upper boundary of the model an increase in frequency with fault complexity was also observed (Fig. 10, green X). 800 m away from the fault there was no observed change in the frequency extraction with fault complexity (Fig. 10, yellow X). In the Snøhvit data the observed frequencies from within the fault zone are less obvious than in the model, since faults and boundaries in the model are largely exaggerated. We did observe slightly higher frequencies in the fault zone relative to the unfaulted signal in the Snøhvit data, but this relationship is not as obvious as in the models since the layering and complexity in the Snøhvit data is sub-seismic imaging resolution. The abundance of higher frequencies adjacent to faults is consistent in both the models and the case study. From the observations in the Snøhvit data and the supporting seismic modelling it is concluded that fault zones and the frequencies

attained in their imaging can influence the frequency content of adjacent seismic reflectors.

The reasons for the relative increase in high frequency content in and surrounding fault zones (as observed in the models) are not fully understood, although some hypotheses are presented here. Fault zones are often complex, heterogeneous rock bodies (i.e. Chester & Logan 1986; Caine *et al.* 1996; Davatzes & Aydin 2005; Bastesen & Braathen 2010; Faulkner *et al.* 2010) that have undergone large strain which can affect the mechanical and acoustic properties of the fault rock. O'Doherty & Anstey (1971) found that rapid and cyclical changes in lithology were linked to the attenuation of low frequencies in the backscattered data while gradual changes in lithology (e.g. due to changes in sedimentation) resulted in the higher frequencies being attenuated in the backscattered data. The observed increasing shift in dominant frequency in and around the faults is interpreted to be related to abrupt variations in elastic properties within the fault zone, which could be due to lithological variation. Smooth lithological changes result in lower dominant frequencies than abrupt transitions (Fig. 10; O'Doherty & Anstey, 1971). The seismic response of a subsurface model is approximately obtained by a convolutional process where the source wavelet is filtered by the impulse response of the subsurface model. It is therefore possible to design the subsurface model such that it behaves much like a bandpass filter. This work demonstrates that low frequency scattered signals can be obtained from a homogeneous fault zone (Fig. 10b), while scattered high frequencies are obtained using fault zone models with more abrupt and cyclical changes in elastic properties. These findings are consistent with the findings of O'Doherty & Anstey (1971) and well-known theories in signal processing/filtering.

Fault zone frequencies can have a great effect on the termination of horizontal reflections with the fault plane. This is observed in both the Snøhvit data and the modelled data as high frequency haloes and spectral extractions respectively. Despite the simplicity of the model, it is possible to suggest that regardless of the morphology of faults it is likely the signal created by a fault zone affects the imaging of horizon terminations as they approach the fault plane. Both O'Doherty & Anstey (1971) and Iacopini *et al.* (2012) supported the concept that lithological

changes within a fault generate amplitudes from thin beds which are tuned at specific frequencies (Widess 1973; Partyka *et al.* 1999). These fault zone frequencies were inversely proportional to the thickness of the structure imaged and therefore it is possible to use the frequency distribution through RGB blending to map variations in tuning thickness (McArdle & Ackers 2012). Higher frequencies were observed around the faults in the Snøhvit case study (Fig. 8) and in the two complex fault seismic experiments (Fig. 10b, c). Although it is much more difficult to test on real seismic data, it is likely that both tuning thickness and changes in mechanical properties played a role in generating higher frequencies around the studied faults (O'Doherty & Anstey 1971; Weibull *et al.* 2019). It is also possible, as observed in our models, that the seismic signal obtained from complex fault morphologies interferes with the signal adjacent to faults. Alaei & Torabi (2017) used frequency decompositions to generate a high frequency magnitude volume from seismic which was used as the most successful parameter in the imaging of faults. Their findings support the observations from the Snøhvit data where the faults are more clearly imaged on higher frequency data, and exhibit slightly higher frequency content than the surrounding unfaulted data. It is possible that more detailed seismic modelling could improve our understanding of these frequency anomalies, although given the limited resolution of seismic data and a clear understanding of fault zone morphology in the case study, it may be challenging to reach a firm explanation for these observations.

P1 6 Conclusions & Implications

This paper systematically explores the effects azimuthal separation, incidence angle and frequency have on the imaging of faults. In this study, PS data from the Snøhvit Field were used as they are much less affected by the presence of shallow gas in the overburden when compared to their PP counterparts. PS data are invaluable in cases where gas or other fluids in the overburden have deleterious effects on image quality and especially when faults play a critical role in the definition of a field or prospect. Both the case study and modelling showed that fault discontinuity image quality (brightness, length and width) varies systematically with azimuth. In general, faults were imaged more clearly in the W azimuth data than they were in the E data, especially in the

northern fault, which is oblique to the survey orientation. Azimuthal separation is shown to be a valuable method to study faults that are oriented oblique or orthogonal to the survey acquisition direction. When faults are parallel to the acquisition direction, there are little differences between the data collected from two diametrically opposed azimuths. Azimuthal separation is a useful tool in fault analysis and should be used to improve our understanding of wave propagation and the interaction of waves with specifically oriented structural (and possibly even stratigraphic) elements.

The Snøhvit case study resulted in improved imaging of faults as discontinuities with increasing incidence angle. With increasing incidence angle the observed increase in reflector strength may be responsible for the improvements to fault imaging in the tensor attribute with incidence angle, the same conclusion was not apparent in the results of modelled data.

Finally, a study on frequency showed faults in the Snøhvit Field to be dominated by low-medium frequency shadows in the fault zones, with haloes of medium-high frequencies surrounding the fault lineaments. The modelled seismic data confirms that complex fault morphologies resulted in higher frequency content in the fault zone than their less complex counterparts. This relative increase in dominant frequency is here proposed to reflect the variations in acoustic properties (in this case lithology), the heterogeneity of fault zones and tuning thickness. The modelled data also showed that regardless of fault complexity, the frequencies observed near to faults are also influenced by the fault generated frequencies.

Several recommendations are made based on the results of this study that can be applied to processing and interpretation workflows.

Processing: Azimuthal separation has great potential to be applied to fault characterization and structural analysis. If a survey is approximately perpendicular to the fault trend, it is highly advantageous to separate the diametrically opposed azimuths along the survey. Azimuthally separated data reveal significantly more contrast in fault imaging and enhance the effects of specular versus diffracted wave imaging. Standard generation of incidence angle stack data is also critical in areas where detailed fault

interpretation is necessary, as seen in the overall increase in fault image quality with increasing incidence angle (Snøhvit case study).

Interpretation: An understanding of the survey design is critical when interpreting faults in OBS seismic data. Interpretation on azimuthally separated volumes and incidence angle cubes results in improved understanding of faults in the subsurface, compared to interpretation on a full stack, full-azimuth seismic volume. Furthermore, the careful application of various kinds of seismic attributes and frequency decomposition methods can greatly increase the subsurface understanding of faults in standard seismic reflection data.

These results add considerable understanding to how faults are imaged and how survey geometry, processing techniques and frequency can influence fault imaging in PS data. This work may also improve the quality and accuracy of fault interpretation in OBS data. Since OBS surveys are becoming more often in both exploration and production (e.g. Clair, Ekofisk, Grane, Gullfacks, Johan Sverdrup, Oseberg and Vallhall fields; Barkved *et al.* 2005; Haugvaldstad *et al.* 2011; Bertrand *et al.* 2014; Eriksrud 2014; TGS, Axxis Geo Solutions in North Sea OBN seismic pact 2018; Eriksen 2018), it is vital that geoscientists understand how PP and PS data are acquired, processed and how seismic waves might interact with structure to extract the greatest amount of information from the subsurface.

P1 Acknowledgements

P1 References

Alaei, B. & Torabi, A. 2017. Seismic imaging of fault damaged zone and its scaling relation with displacement. Interpretation, 5, https://doi.org/10.1190/int-2016-0230.1.

Anstey, N.A. & O'Doherty, R.F. 2002. Cycles, layers, and reflections: Part 1. Leading Edge, 21, 44–51, https://doi.org/10.1190/1.1445847.

Bakker, P. 2002. Image Structure Analysis for Seismic Interpretation. Technische Universiteit Delft.

Barkved, O.I., Buer, K., Kristiansen, T.G., Kjelstadli, R.M. & Kommedal, J.H. 2005. Permanent seismic monitoring of the Valhall field, Norway. 2005 International Petroleum Technology Conference Proceedings, 1523–1527.

Barr, F.J. 1997. Dual-sensor OBC technology. The Leading Edge, 16, 45–52, https://doi.org/https://doi.org/10.1190/1.1437427.

Bastesen, E. & Braathen, A. 2010. Extensional faults in fine grained carbonates - analysis of fault core lithology and thickness-displacement relationships. Journal of Structural Geology, 32, 1609–1628, https://doi.org/10.1016/j.jsg.2010.09.008.

Bertrand, A., Folstad, P.G., et al. 2014. Ekofisk life-of-field seismic: Operations and 4D processing. The Leading Edge, 33, 142–148.

Botter, C., Cardozo, N., Hardy, S., Lecomte, I. & Escalona, A. 2014. From mechanical modeling to seismic imaging of faults: A synthetic workflow to study the impact of faults on seismic. Marine and Petroleum Geology, 57, 187–207, https://doi.org/10.1016/j.marpetgeo.2014.05.013.

Botter, C., Cardozo, N., Hardy, S., Lecomte, I., Paton, G. & Escalona, A. 2016. Seismic characterisation of fault damage in 3D using

mechanical and seismic modelling. Marine and Petroleum Geology, 77, 973–990, https://doi.org/10.1016/j.marpetgeo.2016.08.002.

Botter, C., Cardozo, N., Qu, D., Tveranger, J. & Kolyukhin, D. 2017a. Seismic characterization of fault facies models. Interpretation, 5, 1–18.

Botter, C., Cardozo, N., Lecomte, I., Rotevatn, A. & Paton, G. 2017b. The impact of faults and fluid flow on seismic images of a relay ramp over production time. Petroleum Geoscience, 23, 17–28.

Caine, J.S., Evans, J.P. & Forster, C.B. 1996. Fault zone architecture and permeability structure. Geology, 24, 1025–1028.

Chester, F.M.M. & Logan, J.M.M. 1986. Implications for mechanical properties of brittle faults from observations of the Punchbowl Fault Zone, California. PAGEOPH, 124, 79–106, https://doi.org/10.1007/BF00875720.

Chopra, S. & Marfurt, K.J. 2007. Seismic Attributes for Prospect Identification and Reservoir Characterization. Tulsa, OK, United States of America, Society of Exploration Geophysicists and European Association of Geoscientists and Engineers.

Cunningham, J., Cardozo, N., Townsend, C., Iacopini, D. & Wærum, G.O. 2019. Fault deformation, seismic amplitude and unsupervised fault facies analysis: Snøhvit Field, Barents Sea. Journal of Structural Geology, 118, 165–180, https://doi.org/10.1016/j.jsg.2018.10.010.

Davatzes, N.C. & Aydin, A. 2005. Distribution and nature of fault architecture in a layered sandstone and shale sequence: An example from the Moab fault, Utah. AAPG Memoir, 153–180, https://doi.org/10.1306/1033722m853134.

Dawers, N.H. & Underhill, J.R. 2000. The role of fault interaction and linkage in controlling synrift stratigraphic sequences: Late Jurassic, Statfjord East area, northern North Sea. AAPG Bulletin, 84, 45–64.

de Kok, R. 2012. Directions in ocean-bottom surveying. The Leading Edge, 31, 415–428, https://doi.org/10.1190/tle31040415.1.

Doré, A.G. 1995. Barents Sea Geology, Petroleum Resources and Commercial Potential. Arctic, 48, 207–221.

Elliott, G.M., Wilson, P., Jackson, C.A.L., Gawthorpe, R.L., Michelsen, L. & Sharp, I.R. 2012. The linkage between fault throw and footwall scarp erosion patterns: An example from the Bremstein Fault Complex, offshore Mid-Norway. Basin Research, 24, 180–197.

Ensley, R.A. 1984. Comparison of P- and S-wave seismic data - A new method for detecting gas reservoirs. Geophysics, 49, 1420–1431, https://doi.org/10.1190/1.1441771.

Eriksen, E. 2018. Contract for improved recovery on Johan Sverdrup. Equinor ASA Websitehttps://www.equinor.com/en/news/17jan2018-johan-sverdrup.html.

Eriksrud, M. 2014. Seabed permanent reservoir monitoring (PRM) - A valid 4D seismic technology for fields in the North Sea. First Break, 32, 67–73.

Farfour, M. & Yoon, W.J. 2016. A review on multicomponent seismology: A potential seismic application for reservoir characterization. Journal of Advanced Research, 7, 515–524, https://doi.org/10.1016/j.jare.2015.11.004.

Faulkner, D.R., Jackson, C.A.L., Lunn, R.J., Schlische, R.W., Shipton, Z.K., Wibberley, C.A.J. & Withjack, M.O. 2010. A review of recent developments concerning the structure, mechanics and fluid flow properties of fault zones. Journal of Structural Geology, 32, 1557–1575.

Fomel, S., Landa, E. & Turhan Taner, M. 2018. Post-stack velocity analysis by separation and imaging of seismic diffractions. Society of Exploration Geophysicists - SEG International Exposition and 76tth Annual Meeting 2006, SEG 2006, 2559–2563.

Garotta, R. & Granger, P.Y. 1988. Acquisition and processing of 3C × 3-D data using converted waves. In: SEG Technical Program Expanded Abstracts. 995–997., https://doi.org/10.1190/1.1892469.

Gomez, L. 2015. AVO Screening (Part 2): AVO colour blends. Geoteric Blog.

Granli, J.R., Arntsen, B., Sollid, A. & Hilde, E. 1999. Imaging through gas-filled sediments using marine shear-wave data. Geophysics, 64, 668–677, https://doi.org/10.1190/1.1444576.

Gray, D. 2008. Fracture detection using 3D seismic azimuthal AVO. CSEG Recorder, 40–49.

Gudlaugsson, S.T., Faleide, J.I., Johansen, S.E. & Breivik, A.J. 1998. Late Palaeozoic structural developments of the south-western Barents Sea. Marine and Petroleum Geology, 15, 73–102, https://doi.org/10.1016/S0264-8172(97)00048-2.

Han, C. 2017. Frequency Decomposition Part 2- Constant Q. Geoteric Bloghttps://blog.geoteric.com/frequency-decomposition-part-2-constant-q.

Haugvaldstad, H.H., Lyngnes, B., Smith, P. & Thompson, A. 2011. Ekofisk time-lapse seismic- a continuous process of improvement. First Break, 29, 113–120.

Hokstad, K., Mittet, R. & Landrø, M. 1998. Elastic reverse time migration of marine walkaway vertical seismic profiling data. Geophysics, 63, 1685–1695, https://doi.org/10.1190/1.1444464.

Iacopini, D. & Butler, R.W.H. 2011. Imaging deformation in submarine thrust belts using seismic attributes. Earth and Planetary Science Letters, 302, 414–422, https://doi.org/10.1016/j.epsl.2010.12.041.

Iacopini, D., Butler, R.W.H. & Purves, S. 2012. Seismic imaging of thrust faults and structural damage: A visualization workflow for

deepwater thrust belts. First Break, 30, 77–84, https://doi.org/0.3997/1365-2397.30.5.58681.

Iacopini, D., Butler, R., Purves, S., McArdle, N. & De Freslon, N. 2016. Exploring the seismic expression of fault zones in 3D seismic volumes. Journal of Structural Geology, 89, 54–73.

Jabbari, S. & Innanen, K. 2015. PS and SP Converted Wave Reflection Coefficients and Their Application to Time-Lapse Difference AVO. Calgary, Canada.

Jenner, E. 2002. Azimuthal AVO: Methodology and data examples. The Leading Edge, 21, 782–786, https://doi.org/10.1190/1.1503184.

Jilinski, P. & Wooltorton, T. 2016. Comparison of spectral enhancement techniques and application to improved well-to-seismic ties. In: GeoConvention 2016. Calgary, Canada, 1–4.

Khaidukov, V., Landa, E. & Moser, T.J. 2004. Diffraction imaging by focusing-defocusing: An outlook on seismic superresolution. Geophysics, 69, 1478–1490, https://doi.org/10.1190/1.1836821.

Landa, E. 2012. Seismic diffraction: where's the value? SEG Technical Program Expanded Abstracts, 1–4.

Landa, E. & Keymar, S. 1998. Seismic monitoring of diffraction images for detection of local heterogeneities. Geophysics, 63, 1093–1100.

Landrø, M. & Amundsen, L. 2010. Marine Seismic Sources Part 1. GEOExPro, 7.

Landrø, M. & Amundsen, L. 2018. Introduction to Exploration Geophysics and Recent Advances, 1st ed. Whaley, J. (ed.). Bivrost.

Linjordet, A. & Olsen, R.G. 1992. The Jurassic Snøhvit gas field, Hammerfest basin, offshore northern Norway. In: Giant Oil and Gas Fields of the Decade 1978-1988. American Association of Petroleum Geologists, 349–370.

Long, J.J. & Imber, J. 2012. Strain compatibility and fault linkage in relay zones on normal faults. Journal of Sedimentary Petrology, 36, 16–26, https://doi.org/10.1016/j.jsg.2011.12.013.

McArdle, N.J. & Ackers, M.A. 2012. Understanding seismic thin-bed responses using frequency decomposition and RGB blending. First Break, 30, 57–65.

Mohammedyasin, S.M., Lippard, S.J., Omosanya, K.O., Johansen, S.E. & Harishidayat, D. 2016. Deep-seated faults and hydrocarbon leakage in the Snøhvit Gas Field, Hammerfest Basin, Southwestern Barents Sea. Marine and Petroleum Geology, 77, 160–178, https://doi.org/10.1016/j.marpetgeo.2016.06.011.

O'Doherty, R.F. & Anstey, N.A. 1971. Reflections on Amplitudes. Geophysical Prospecting, 19, 430–458.

Osagiede, E.E., Duffy, O.B., Jackson, C.A.L. & Wrona, T. 2014. Quantifying the growth history of seismically imaged normal faults. Journal of Structural Geology, 66, 382–399, https://doi.org/10.1016/j.jsg.2014.05.021.

Ostanin, I., Anka, Z., di Primio, R. & Bernal, A. 2012. Identification of a large Upper Cretaceous polygonal fault network in the Hammerfest basin: Implications on the reactivation of regional faulting and gas leakage dynamics, SW Barents Sea. Marine Geology, 332–334, 109–125, https://doi.org/http://dx.doi.org/10.1016/j.margeo.2012.03.005.

Ostrander, W.J. 1984. Plane-wave reflection coefficients for gas sands at nonnormal angles of incidence. Geophysics, 49, 1637–1648, https://doi.org/10.1190/1.1441571.

Partyka, G., Gridley, J. & Lopez, J. 1999. Interpretational applications of spectral decomposition in reservoir characterization. The Leading Edge, 18, 353–360, https://doi.org/10.1190/1.1438295.

Perez, G. & Marfurt, K.J. 2007. New azimuthal binning for improved delineation of faults and fractures. Geophysics, 73, S7, https://doi.org/10.1190/1.2813136.

Rodriguez, C.S. 2000. Advanced Marine Seismic Methods: Ocean Bottom and Vertical Cable Analysis. University of Calgary.

Ryseth, A., Augustson, J.H., et al. 2003. Cenozoic stratigraphy and evolution of the Sørvestsnaget Basin, southwestern Barents Sea. Norwegian Journal of Geology, 83, 107–130.

Shuey, R.T. 1985. A simplification of the Zoeppritz equations. Geophysics, 50, 609–614, https://doi.org/https://doi.org/10.1190/1.1441936.

Stewart, R.R. & Lawton, D.C. 1996. P-S Seismic Exploration : A Mid-Term Overview. Calgary, Canada.

Stewart, R.R., Gaiser, J.E., Brown, R.J. & Lawton, D.C. 2002. Tutorial Converted-wave seismic exploration : Methods. Geophysics, 67, 1348–1363, https://doi.org/10.1190/1.1512781.

Stewart, R.R., Gaiser, J.E., Brown, R.J. & Lawton, D.C. 2003. Tutorial Converted-wave seismic exploration : Applications. Geophysics, 68, 40–57, https://doi.org/10.1190/1.1512781.

Stockwell, R.G., Mansinha, L. & Lowe, R.P. 1996. Localization of the Complex Spectrum: The S-Transform. IEEE Transactions on Signal Processing, 44, 998–1001, https://doi.org/10.1109/78.492555.

Sund, T., Skarpnes, O., Nørgård Jensen, L. & Larsen, R.M. 1984. Tectonic development and hydrocarbon potential offshore Troms, Northern Norway. In: AAPG Special Publication Memoir: Future Petroleum Provinces of the World. 615–627.

Taner, M.T., Fomel, S. & Landa, E. 2006. Separation and imaging of seismic diffractions using plane-wave decomposition. 2401–2405, https://doi.org/10.1190/1.2370017.

TGS, Axxis Geo Solutions in North Sea OBN seismic pact. 2018. Offshore Energy Today, 1.

Torabi, A., Alaei, B. & Kolyukhin, D. 2016. Analysis of fault scaling relations using fault seismic attributes. Geophysical Prospecting, 1–15, https://doi.org/10.1111/1365-2478.12440.

Tvedt, A.B.M., Rotevatn, A., Jackson, C.A.L., Fossen, H. & Gawthorpe, R.L. 2013. Growth of normal faults in multilayer sequences: A 3D seismic case study from the Egersund Basin, Norwegian North Sea. Journal of Structural Geology, 55, 1–20, https://doi.org/10.1016/j.jsg.2013.08.002.

Virieux, J. 1986. P-SV wave propagation in heterogeneous media. Geophysics, 51, 889–901, https://doi.org/10.1190/1.1442147.

Weibull, W.W. & Arntsen, B. 2013. Automatic migration velocity analysis using reverse-time migration. Geophysics, 55, 1070–1088.

Weibull, W.W., Ahmad, S.S., Brown, R.J., Rosland, B. & Nazi, H. 2019. A comparison of the effects of layering and attenuation on the seismic response of gas reservoirs. In: 81st EAGE Conference & Exhibition 2019. London, UK, EAGE.

Widess, M.B. 1973. How thin is a thin bed? Geophysics, 38, 1176–1180.

Xu, X. & Tsvankin, I. 2007. A case study of azimuthal AVO analysis with anisotropic spreading correction. The Leading Edge, 26, 1552–1561, https://doi.org/10.1190/1.2821942.

Yilmaz, O. 2001. Seismic Data Analysis: Processing, Inversion, and Interpretation of Seismic Data, 2nd ed. Tulsa, OK, United States of America, Society of Exploration Geophysicists.

PAPER II

FAULT DEFORMATION, SEISMIC AMPLITUDE AND UNSUPERVISED FAULT FACIES ANALYSIS: SNØHVIT FIELD, BARENTS SEA

Cunningham, Jennifer; Cardozo, Nestor; Townsend, Chris; Iacopini, David; Wærum, Gard Ole

Paper II

Fault deformation, seismic amplitude and unsupervised fault facies analysis: Snøhvit Field, Barents Sea

Jennifer Cunningham[a,*], Nestor Cardozo[a], Christopher Townsend[a], David Iacopini[b], Gard Ole Wærum[c]

[a] Department of Energy Resources, University of Stavanger, 4036, Stavanger, Norway
[b] Geology and Petroleum Geology, School of Geosciences, University of Aberdeen, Meston Building, AB24 FX, UK
[c] Equinor ASA, Margrete Jørgensens Veg 4, 9406, Harstad, Norway

ABSTRACT

We present an integrated seismic imaging and fault interpretation workflow to characterize the seismic expression in and around an E-W trending central fault system imaged in near-angle stack seismic data of the Snøhvit Field, Barents Sea. Three E-W normal fault systems offset five Triassic-Lower Cretaceous seismic horizons across the field. Fault throw is largest at depth and decreases with shallowing. Dip distortion (DD) decreases in magnitude and extent with shallowing. Fault enhancement (FE), a filter used to detect edges, was applied on a blend of tensor, semblance and dip attributes, and allowed us to classify fault zones into four unsupervised seismic fault facies (mid-high FE). High FE facies occur at the center of the fault zones and are abundant in the highest thrown eastern part of the field. The FE facies decrease radially outwards field wide. Facies correlate with throw and dip separation gradient, which are in turn related to mechanical stratigraphy controlling fault propagation. We observe systematic seismic amplitude variations: a major amplitude drop on the fault plane, and a brightening and dimming linked to fault-related synclines and anticlines, respectively. Our workflow establishes a methodology for fault interpretation, linking fault throw, DD, seismic attributes and fault facies classification.

1. Introduction

Outcrop studies provide a large amount of information pertaining to fault displacement, structure, and the chemical and physical processes involved in the formation and growth of faults on both large and small scales (e.g. Barnett et al., 1987; Childs et al., 1995, 2009; Eichhubl et al., 2005). However, in a subsurface environment, seismic and well data don't always give the necessary information about faults, and outcrop data are far more difficult to extrapolate to the subsurface (i.e. Townsend et al., 1998; Aarland and Skjerven, 1998; Færseth et al., 2007; Dutzer et al., 2010; Iacopini et al., 2016). In the rare chance that a well intersects a fault and core is collected from the well, vast amounts of geological and petrophysical information are collected from a small rock volume contained in the fault (Aarland and Skjerven, 1998; Færseth et al., 2007). These core data then need extrapolation across the field using seismic data. Since a well crosscutting a fault is a rarity, seismic data remain the most used method of investigation of faults in the subsurface (e.g. Townsend et al., 1998; Dutzer et al., 2010; Iacopini

et al., 2016). In comparison to well data, seismic data provide a broader 3D understanding of faults, their displacement, linkages, and facies changes both vertically and laterally. Seismic resolution, however, often presents a problem when interpreting subsurface faults (Gauthier and Lake, 1993; Townsend et al., 1998; Dutzer et al., 2010; Long and Imber, 2011). For typical exploration conditions (wavelet frequency = 30 Hz, velocity = 3000 m/s), the vertical resolution is about 25 m (¼ of the wavelength or tuning thickness), and the lateral resolution after data migration is about 50 m (½ of the wavelength or effective Fresnel zone diameter; Ashcroft, 2011). However, in the vertical a bed will still be detectable well below tuning thickness (Widess, 1973).

Another common issue in reflection seismology when imaging faults is diffraction, which occurs when a seismic wave interacts with a discontinuity (fault) or lateral heterogeneity, generating a radially scattered diffracted wave (Landa and Keymar, 1998; Townsend et al., 1998). Seismic data, however, are standardly processed for reflections (lithological boundaries) rather than diffractions (faults), which are

* Corresponding author.
E-mail addresses: jennifer.e.cunningham@uis.no (J. Cunningham), nestor.cardozo@uis.no (N. Cardozo), chris.townsend@uis.no (C. Townsend), d.iacopini@abdn.ac.uk (D. Iacopini), gawa@equinor.com (G.O. Wærum).

Paper II

J. Cunningham et al.

removed during data migration (Landa, 2007, 2012).

A number of studies have aimed to characterize in detail faults in seismic data. Townsend et al. (1998) was the first comprehensive analysis of small-scale faults using amplitude anomalies in seismic reflection data. Dutzer et al. (2010) used seismic attribute analysis to study fault architecture and sealing potential. Long and Imber (2010, 2012) introduced new techniques in seismic reflector dip sampling to generate maps of fault related deformation (dip distortion) in a normal fault array and a relay zone. These methods focused more on extracting deformation patterns from the interpreted data, rather than attributes applied specifically to the seismic data. Iacopini and Butler (2011) and Iacopini et al. (2012) designed a visualization workflow combining seismic attributes, opacity filtering and spectral decomposition to characterize deformation surrounding thrusts in deep marine settings. Iacopini et al. (2016) used crossplots of tensor, semblance and instantaneous phase attributes to resolve the seismic expression of normal fault damage. They also introduced the term seismic disturbance zones (complex volumes of disrupted seismic signal around faults; SDZ) and proposed methods to map unsupervised seismic fault facies within these zones (Iacopini et al., 2016). These facies are reconstructed through simple statistical cross plotting approaches but are not directly linked to actual geological data, such as log data or core samples (Dumay and Fournier, 1988; Posamentier and Kolla, 2003; Iacopini et al., 2016).

An alternative approach to investigate and understand the significance of seismic geobodies is through the use of forward seismic modelling (Carcione et al., 2002 and sources therein). Synthetic seismic modelling has been applied to simulate the seismic expression of faults and has uncovered a wealth of knowledge with respect to the seismic imaging of fault zones (e.g. Botter et al., 2014, 2016; 2017a,b). These studies concluded that there is a direct correlation between amplitude changes across the fault and fault-related deformation, thus confirming the plausibility of exploring fault zones through the use of seismic attributes (e.g. Botter et al., 2014, 2016).

The purpose of this work is to explore existing and new techniques in fault analysis to investigate the geological significance of seismic geobodies enveloping faults. We also test on real seismic data some of the findings from seismic modelling by Botter et al. (2014, 2016, 2017a,b). To accomplish these objectives, we use pre-stack depth migrated, near-angle stack and depth converted 3D seismic data from the Snøhvit Field, southwest Barents Sea, Norway. Our study focuses on fault-related deformation of the Upper Triassic-Lower Cretaceous interval (1.5–3 km depth) using a methodology that includes data conditioning, structure maps, fault throw, dip distortion, seismic attributes, seismic fault facies, and seismic amplitudes. The seismically interpreted fault structure lacks well control, but it correlates with structural parameters such as fault juxtaposition and dip separation gradient (strain). Thus, the proposed methodology has the potential for realistic unsupervised characterization of faults in the subsurface.

2. Geological setting

The Snøhvit Field is located in the Norwegian southwest Barents Sea in the center of the Hammerfest Basin (Fig. 1 a, b; Linjordet and Olsen, 1992). The Hammerfest Basin is a downthrown ENE-WSW rift basin, which began to develop during the Late Jurassic- Early Cretaceous (Fig. 1a; Sund et al., 1984; Berglund et al., 1986; Linjordet and Olsen, 1992; Ostanin et al., 2012). The basin is 150 km long by 70 km wide and is bound to the north by the Loppa High, along the southeast margin by the Finnmark Platform and to the west by the Tromsø Basin (Sund et al., 1984; Doré, 1995; Ostanin et al., 2012). The main subsidence of the Hammerfest Basin was controlled by NE-SW basin bounding faults in the Early Cretaceous (Fig. 1 a; Sund et al., 1984; Linjordet and Olsen, 1992). These faults are responsible for the preservation of Triassic and Jurassic sediments, and the subsequent deposition of the Cretaceous and Tertiary sediments (Berglund et al., 1986). The basin deepens and widens westward and therefore the

Triassic-Cretaceous succession is thicker in the west than in the east (Linjordet and Olsen, 1992). Upper Triassic-Lower Cretaceous pre- and syn-rift strata are the focus of this paper. An E-W trending central fault system that lies between the main basin bounding faults was formed during basin extension due to the presence of a dome parallel to the Hammerfest Basin axis (Sund et al., 1984). Some of these faults are the focus of this study (Fig. 1 a, b; Linjordet and Olsen, 1992).

The Snøhvit gas field was discovered in 1984 and at the time it was the largest gas find in the Barents Sea (Linjordet and Olsen, 1992). The generation, migration and distribution of hydrocarbons in the Snøhvit Field is controlled by the E-W trending fault system which segments the hydrocarbon plays into northern and southern provinces (Sund et al., 1984). The organic rich shales of the Triassic Kobbe and Snadd Fms and the Jurassic Hekkingen Fm are the main source rocks in the area (Linjordet and Olsen, 1992). The reservoir intervals are the Lower-Middle Jurassic sandstones of the Tubåen, Nordmela and Stø Fms (Linjordet and Olsen, 1992). The Jurassic Fuglen and Hekkingen Fms are the main sealing intervals (Linjordet and Olsen, 1992).

Five Upper Triassic-Early Cretaceous seismic horizons were chosen for interpretation as they give the most representative assessment of faulting throughout the studied interval (Fig. 1c and d; interpreted horizons E to A). The deepest Upper Triassic - Lower Jurassic Fruholmen Fm consists of open marine shales interbedded with fluvio-deltaic sandstones and coals (Dalland et al., 1988). The Middle-Upper Jurassic Fuglen Fm is present across the entire basin and consists of mudstones interbedded with limestones, which were deposited during a sea-level highstand in a fully marine environment (Dalland et al., 1988; Linjordet and Olsen, 1992). The Lower Cretaceous Knurr Fm (deposited in an open, distal marine environment) is a claystone containing interbeds of thin limestones and dolomites, as well as sandy intervals towards the base (Dalland et al., 1988). The Lower Cretaceous Kolje Fm (deposited in an open, distal marine environment) is a shale and claystone unit containing some minor interbeds of limestone, dolomite, siltstone and sandstone towards the top (Dalland et al., 1988).

3. Methodology

We integrate seismic interpretation, image processing and fault analysis methods into a single workflow (Fig. 2) that is designed to uncover information about the 3D geometry and internal structure of faults. The workflow integrates new and existent methods (Fig. 2). The newly introduced method is the analysis of seismic amplitude versus distance to fault. The data conditioning, seismic interpretation, fault throw analysis, dip distortion, and the use of seismic attributes are previously used methods that are combined in this study (Rippon, 1985; Long and Imber, 2010, 2012; Iacopini et al., 2012, 2016; Gilani and Gómez-Martínez, 2013; Wilson et al., 2013; Botter et al., 2017a). The computer programs Geoteric, OpendTect, Petrel and TrapTester (T7) were used to execute the workflow. 3D Seismic survey ST15M04, a merge of five 3D seismic surveys (produced by Equinor ASA and their partners) is the main dataset of the study. The area of interest, chosen directly above the Snøhvit Field, from within the ST15M04 vol, covers ~25 km in the E-W direction and ~5 km in the N-S direction, and has inline and crossline spacing of 12.5 m (orange rectangle, Fig. 1b). The data have been pre-stack depth migrated (Kirchhoff), zero phased, stacks were generated (full and partial), and finally the data were converted to the depth domain where it is assumed the velocity model is correct and the vertical scale of the data is depth. In this dataset an increase of impedance is represented by a red peak (blue-red-blue). All steps in the workflow were conducted on the near-angle (5–20°) stack since this volume maintains the most consistent reflector continuity and the best structural detail, as proved by studies of reflection coefficient versus incident angle (Shuey, 1985 and references therein). It is not possible to ascertain the shooting direction of this volume because, as mentioned, the data used are a merge of multiple datasets and vintages.
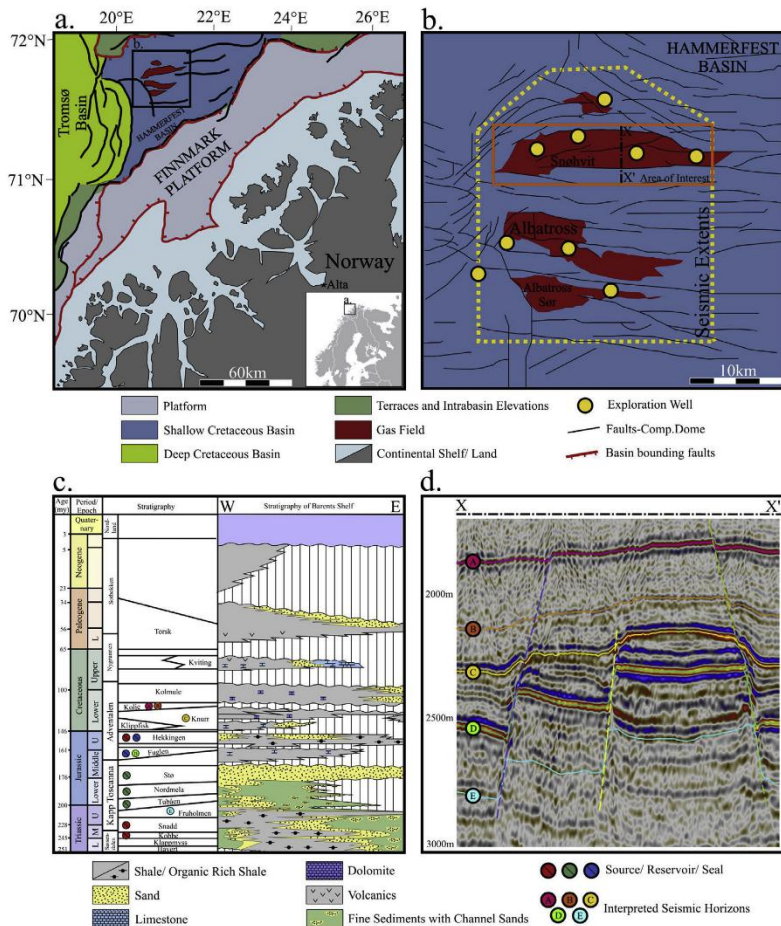
Fig. 1. a. Geologic setting of the Hammerfest Basin. The area in b is marked by a black box. Modified from NPD Factmaps. b. Snøhvit Field area. The dashed yellow line shows the extent of seismic data and the orange rectangle is the study area. Map modified from Linjordet and Olsen (1992) and Ostanin et al. (2012). The blue background of the map refers to the Jurassic Hammerfest Basin while the red shapes on the map identify the areal extents of lower-middle Jurassic gas fields. c. Generalized lithostratigraphic column of the Barents Sea highlighting the horizons of interest. Modified from Ostanin et al. (2012). d. North-south seismic line through the middle of the study area (X-X′ in b) with interpreted horizons and faults. Interpreted horizons are: A: top Kolje, B: intra-Kolje, C: top Knurr, D: top Fuglen, and E: top Fruholmen. (For interpretation of the references to color in this figure legend, the reader is referred to the Web version of this article.)

3.1. Data conditioning

In the area of interest, seismic data quality is generally excellent. However, shallow gas in the west and north, and a thick dolomite unit in the east significantly decreases the signal-noise ratio at the depth range of interpretation (1.5–3 km). To counter this problem, a noise attenuation and amplitude normalization workflow was applied (Fig. 3). There are two types of noise. First, an aggressive type of noise caused by gas and dolomites, and second, a minor coherent and random noise. To target these noise variations, two field-wide seismic volumes were generated using passive and aggressive noise attenuation (Fig. 3), following a procedure that involved two steps of noise cancelation, and filters described in detail by Gilani and Gómez-Martínez (2013). The

resultant volumes were merged using a chaos attribute mask volume (masked values: 6270–17000) that applies aggressive noise cancelation to areas with low signal-noise ratio and passive noise attenuation everywhere else (Fig. 3; Gilani and Gómez-Martínez, 2013). In areas of low amplitude (identified by the chaos mask volume), a scaling factor (1.75) was applied to normalize the seismic signal (Fig. 3; Gilani and Gómez-Martínez, 2013). During the application of data conditioning, it was important not only to remove noise, but also to maintain the signal that was already present in the data. The noise removed was monitored in each stage of the workflow to ensure only random noise was removed, and the signal associated with seismic reflectors and faults were unaltered.
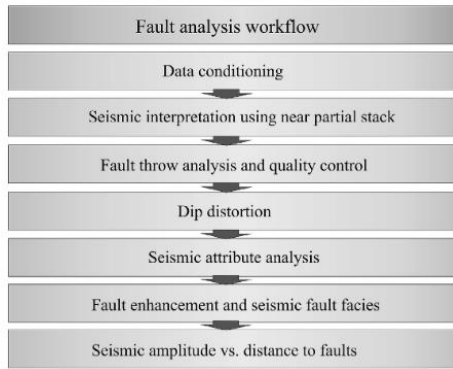
Fig. 2. Workflow used in this study.

3.2. Seismic interpretation using near-angle stack

The interpretations were completed on the near-angle stack (5–20°) volume that was created after data conditioning. The selected horizon tops are bright, laterally extensive reflectors, which can be interpreted across the entire field and main faulted interval. The horizon tops are picked on mostly peaks (top Fruholmen, top Fuglen, top Knurr and top Kolje) and a single trough (intra-Kolje). Faults were interpreted using a dense interpretation grid of 16 inlines, while horizons were auto-tracked between faults (Yielding and Freeman, 2016). The interpretations were quality controlled by studying the intersections between horizons and faults (fault cutoffs) and throw distribution on faults (next section).

3.3. Fault throw analysis

Fault throw is the vertical component of the dip separation, which is the vector connecting the hanging wall and footwall cutoffs along the fault dip direction (Fig. 4a). When constraining the fault cutoffs, user-defined trim and patch distances were used to account for interpretation errors near the fault (Fig. 4; Wilson et al., 2009, 2013; Elliott et al., 2012). 'Trim' is a distance applied to both sides of the interpreted fault plane that is designed to omit data too near the fault plane that may skew the overall throw results (Fig. 4b; Wilson et al., 2009). The 'patch'

is the distance immediately beyond the trim, which defines a volume of high horizon interpretation confidence that can be projected onto the interpreted fault plane to create the cutoffs (Fig. 4b; Wilson et al., 2009, 2013; Yielding and Freeman, 2016). Trim and patch distances of 50 and 75 m respectively were chosen after thorough testing, in order to produce the cutoffs that deliver the most representative displacement patterns for each horizon of interest. Anomalies in the throw distributions were used as a quality control process to identify inconsistencies in interpretation. These anomalies were fixed by editing fault and horizon interpretations where necessary.

3.4. Dip distortion

The term dip distortion (or apparent dip, DD) is used to describe the volume of deformation surrounding the faults, from which horizons depart from their regional dip (Long and Imber, 2010, 2012). The main input for calculating DD are the interpreted horizons, which were used to generate high-resolution triangulated surfaces (trimeshes). These trimeshes were sampled along N-S transect lines which are oriented approximately perpendicular to the E-W trending faults with the largest throw. Along each transect, there are points which coincide to corner points on the trimesh horizon (Fig. 4c, points A, B). Between each of these points a measurement of the distance (x) and the differential depth (z) between the points is taken. From these two values, θ or apparent dip (DD) is computed (Fig. 4c). The computed DD values are then reimported as point sets and used as the main input to create maps (Fig. 4c). These DD maps show the apparent dip projected onto a horizontal plane at the average horizon depth.

3.5. Seismic attribute analysis

Seismic attribute analysis was conducted to improve the imaging of faults and isolate seismic fault signatures. The near-angle stack, data conditioned seismic volume was used as the input for generating tensor, semblance, dip and envelope attribute volumes. These attributes were chosen as they were the three most successful attributes in fault detection for this study. The tensor attribute is based on a structurally-oriented symmetric tensor whose principal axes define the local reflector orientation (Bakker, 2002). This attribute is sensitive to changes in amplitude and reflector continuity and is suited to imaging large scale faults where seismic expression may differ laterally (Bakker, 2002). The semblance attribute identifies reflector discontinuity and distortions within the data volume (Marfurt et al., 1998). The dip attribute is defined as a measure of reflector inclination with respect to the horizontal (Barnes, 2000; Marfurt, 2006). The dip attribute can be used to calculate the orientation and magnitude of structural and/or
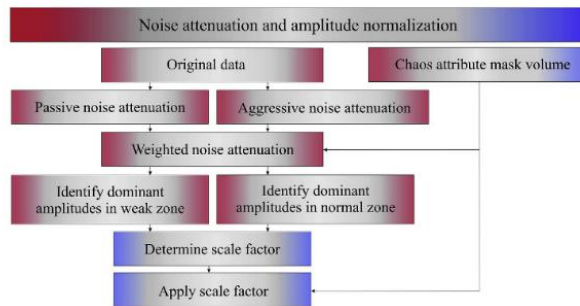

Fig. 3. Data conditioning (noise attenuation and amplitude normalization) workflow used to remove the noise associated with gas clouds and the northeast dolomite unit.
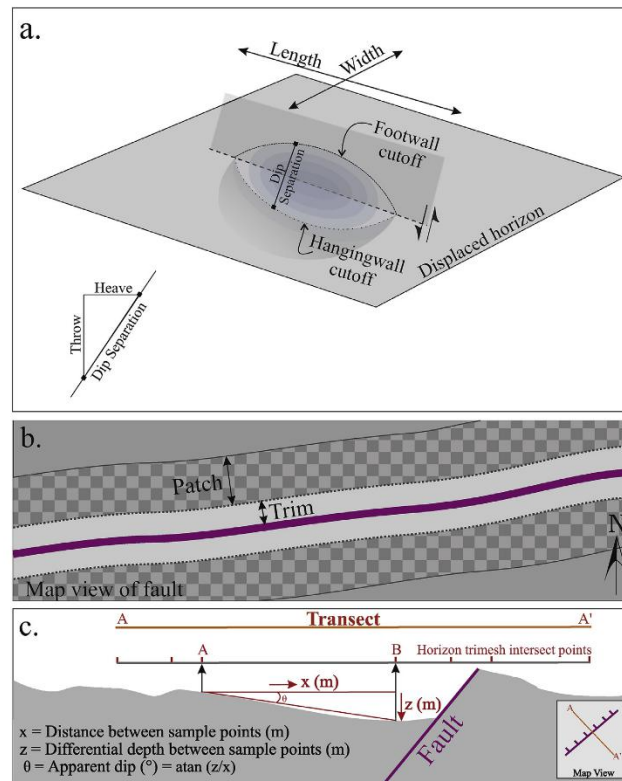
Fig. 4. Fault throw and dip distortion (DD). a. 3D image of a normal fault showing displacement field and hanging wall and footwall cutoffs, fault length and width, dip separation, throw and heave. b. Map view of a fault with trim and patch distances used in the cutoffs determination. c. Cross section explaining the calculation of DD.

stratigraphic edges within a seismic volume, for example faults or lateral lithological changes (Purves and Basford, 2011; Alaei, 2016). It is important to note that the dip attribute is a measurement of changes to the seismic reflector while the DD in section 3.4 is a measure of the apparent dip of the interpreted seismic horizons. Envelope is also known as instantaneous amplitude and is a measure of reflection strength (Taner et al., 1979). The tensor and semblance attributes were run using a fault width of 7 and a height of 21 voxels while the dip had a fault width of 5 and a height of 21 voxels (these settings were optimized for faults > 60 m long). An equally weighted CMY (Cyan, Magenta and Yellow) color blend of two coherence attributes (tensor and semblance) and a dip attribute provided a more complete understanding of the fault bodies. When high values of tensor, semblance and dip occur simultaneously, the color displayed is black. Since the blended attributes in this case are structure or edge enhancing, the dark colors in the CMY volume are associated to faults.

3.6. Fault enhancement and seismic fault facies

The fault enhancement (FE) filter is a Gaussian filter that is applied to enhance the edges in a seismic volume while also suppressing noise (Chopra and Marfurt, 2007). In this case the FE filter is applied to a greyscale conversion of the tensor, semblance and dip CMY color blend,

where the highest color saturations in the color blend are represented as the darkest greys in the greyscale volume. The application of the FE filter is defined using a three-dimensional matrix of sigma values corresponding to the standard deviation of the Gaussian filter. In this study, a matrix of weight factors of 3 (x direction), 3 (y direction) and 6 (z direction) were assigned to generate the FE volume. These factors represent the contribution of a voxel at a given location to the FE attribute in the center of the filter, where a factor of 3 or 6 means that 68% of the energy of the filter is localized within ± 3 or 6 voxels around the central voxel, respectively. After applying the FE filter, noise contained in the color blend volume of attributes is attenuated and dispersed across many voxels while the intensity of the discontinuity remains (Chopra and Marfurt, 2007). The greyscale volume was limited in depth to 2110–2750 m (to only include the top Fuglen and top Knurr) where the imaging of faults is the clearest and the least amount of noise is present. The dynamic range of the FE filter in a 16-bit seismic volume lays between 0 and 32767. High FE values were isolated using opacity filtering to remove all data that were outside the fault geobodies (in our case FE < 16000). These high values were subdivided approximately equally as follows: blue (16000–20200), green (20200–24400), yellow (24400–28600) and red (28600–32767). This grouping of FE ranges allowed us to define objects with specific seismic attribute response or seismic fault facies (Iacopini et al., 2012). Tensor, semblance, dip and

FE were crossplotted to explore the correlation between these attributes and obtain seismic fault facies. In the study area, as the wells do not directly transect the fault geobodies the seismic fault facies obtained are called "unsupervised" since they contain little to no direct linkage to geological information (Fournier and Derain, 1995). In an attempt to unravel the geological significance of these facies, we compared them to structural properties such as fault throw, dip separation gradient, and juxtaposed lithology (section 4).

3.7. Seismic amplitude versus distance to faults

An analysis of seismic amplitude versus distance to faults was conducted across two regions (~1 × 2 km) within the study area. These regions are not below the gas cloud and were chosen to strictly highlight the area near the end of one fault to the north (area 1), and near the center of the largest fault in the field (area 2). Structural modelling involved populating each of the areas with grid cells (12.5 m, i and j-direction) matching the approximate bin spacing of the seismic data. This cell size was chosen to maintain as much detail in each model as possible. In the depth (k) direction, the cells were also defined to be approximately 12.5 m, where the grid follows the general shape of the interpreted horizons. The volume data of interest was then re-sampled into the grid cells.

The workflow for the amplitude analysis included the following steps: First, we calculated the RMS volume out of the original (non-data conditioned) seismic amplitude data because we were interested in the magnitude of the amplitude rather than its polarity. In order to fit the predefined grid a window size of six traces was chosen to calculate the RMS. Next, the RMS amplitude volume was resampled into the grid. In the resampling, each cell's RMS amplitude value is representative of a weighted interpolation of the amplitudes of the four nearest cells. The grid cells were also populated with distance (m) to fault measurements. Finally, the cells were colored to distinguish three regions on the hanging wall and footwall, which are nearest, central and furthest from the interpreted fault plane.

For each of the five horizons (top Fruholmen to top Kolje), the grid cells were plotted with distance to fault (x-axis) versus normalized RMS amplitude (y-axis). For comparison, the RMS amplitude values for each horizon were then normalized. The points on the crossplots were then colored by the three user defined regions of the hanging wall and footwall. This methodology was also used to analyze how various parameters (e.g. DD and FE) differ with proximity to the fault plane on both the hanging wall and footwall.

4. Results

4.1. Data conditioning

Data conditioning (Fig. 3) resulted in a signal improvement and noise attenuation in specific areas of the seismic volume affected by shallow gas clouds and dolomite (Fig. 5). Fig. 5a shows an inline before (left) and after (right) the application of data conditioning. In the original image, the amplitude quality below the gas cloud is low and there is a muffling effect on the signal which is produced by noise. On the data conditioned image, the signal is stronger (normalized) and the noise dimming effect has decreased, especially below the shallow gas cloud. In all other areas (except below the gas cloud), there is a general decrease in noise, which overall improved data signal quality. At the depth range of interpretation (1.5–3 km), data conditioning increased the overall reflector continuity.

Fig. 5b shows a depth slice of the data cube (top) and dip, semblance, tensor and envelope attributes both imaged before (left) and after (right) the data conditioning. In the original amplitude data (Fig. 5b, left), the seismic shows clear amplitude dimming associated with the dolomite and the gas clouds. Both dip and semblance attributes show the effects of the gas clouds (west and north) and the dolomite

(northeast, Fig. 5b, left). Tensor and envelope attributes do not show major signs of the gas clouds or dolomite imaging. In the data conditioned seismic (Fig. 5b, right), the amplitude data show greatly improved seismic signal in areas affected by gas clouds and mildly improved imaging in dolomite areas. The dip and semblance depth slices illustrate well the noise reduction below the gas clouds. The noise associated with the gas cloud in the west has almost disappeared, and in the northern gas cloud, the noise has been strongly attenuated but not completely eliminated. There are improvements across the noisy dolomite unit, but they are marginal. Finally, the tensor attribute shows no changes with respect to the gas clouds and dolomite noise, but it shows an overall improvement in the imaging of faults. Since the amplitude is only scaled in areas where gas clouds influence the seismic signal, the envelope attribute is only slightly influenced by the application of data conditioning in these areas.

4.2. Seismic interpretation

Overall, the structure maps indicate the largest fault displacement at the top Fruholmen (oldest) and top Fuglen horizon levels, which is followed by an upwards decrease in displacement from the top Knurr to the top Kolje (youngest, Fig. 6a–e). Three main E-W trending normal fault systems offset the oldest top Fruholmen (Fig. 6e). The northern and central fault systems dip north, while the southern fault system dips south. The northern fault system is segmented into two faults (U and V), with fault U having a smaller NE-SW fault (U′) intersecting at the midway point. Fault U intersects constructively fault V in the east. Faults U and V have maximum vertical separation (VS_{max}) of ~180 m and ~290 m respectively. The central fault system is made of three faults, W, X and Y, with VS_{max} of ~100, 150 and 100 m respectively. Faults W and X form a relay. X intersects with Y, and V intersects with Y to form Y′ in the east. The southern fault system Z is a laterally extensive system that exhibits a VS_{max} of ~260 m, and complex linkage to the east. Here, fault Z in the south is joined by a smaller south dipping normal fault Z′ on its footwall. When referring to the thickness map of the Fruholmen Fm (Fig. 6j), it is clear that this unit is thicker in the west (~290 m) than in the east (~200 m) and sediment thickness is not controlled by faulting (pre-rift sequence).

The top Fuglen structure map (Fig. 6d) shows the same three main fault systems with the same orientations and linkages. The degree of fault displacement is comparable to the top Fruholmen with the exception of fault U′, which is much less prominent. Faults U and V have VS_{max} of ~180 m and 260 m which are respectively the same and less to the same faults for the top Fruholmen. Faults Y′ and Z have VS_{max} of 340 and 210 m respectively, these values are smaller to the observed values of the top Fruholmen. The lengths of all faults in the study area do not change drastically in comparison to the top Fruholmen. The complex linkages in the central (W/X relay) and southern (Z-Z′) fault systems are clearly visible. The thickness map of the Fuglen Fm (Fig. 6i) also suggests larger sediment accumulation in the west and pre-rift sedimentation.

The shallowest three horizons show significantly less fault displacement, segmentation and linkage. The top Knurr (Fig. 6c) is also displaced by the three main fault systems. However, the degree of fault displacement in this horizon is less than in the top Fuglen. The complexities in fault linkage are therefore less visible. Faults U and V (VS_{max} ~90 and 150 m) are still segmented, but they are shorter in length with respect to the deeper horizons. Faults W, X and Y/Y′ still exhibit segmentation, but the relay and fault linkages are less pronounced. Fault Z appears as a single fault extending across the map. VS_{max} of faults Y′ and Z are 140 and 120 m respectively, much smaller than the values observed in the deeper horizons. The intra-Kolje (Fig. 6b) shows the same main faults but with much less displacement than in the top Knurr. Fault segmentation is more difficult to establish on the intra-Kolje where $VS_{max} < 50$ m is observed on the northern and southern fault system; the central fault system exhibits slight folding. The top
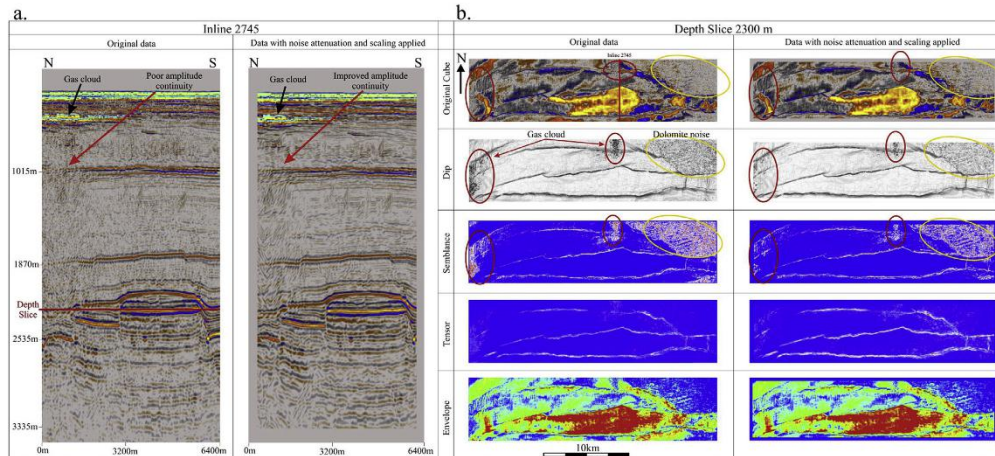
Fig. 5. Results of data conditioning. a. Inline 2745 before (left) and after (right) data conditioning. The gas cloud (~500 m) imaged on the inline causes poor amplitude distribution in deeper reflectors. This is improved by data conditioning. b. Seismic amplitude, dip, semblance, tensor and envelope attribute slices at 2300 m depth, before (left) and after (right) data conditioning. Improved noise attenuation associated with the gas clouds (red circles) and a thick dolomite unit (yellow circle) is clear in the dip and semblance attributes. (For interpretation of the references to color in this figure legend, the reader is referred to the Web version of this article.)

Kolje (Fig. 6a) is the least affected by faulting. Fault segmentation is no longer evident for the northern (U, V) and southern faults (Z, Z′) and VS_{max} is < 50 m. The central faults (W, X, Y) do not offset this horizon. The thickness maps of the Knurr and Kolje Fms suggest syn-rift sedimentation (Fig. 6f–h).

4.3. Fault throw analysis and quality control

Fault throw was computed using fault cutoffs from the five interpreted horizons (Fig. 7). Fault throw was used to quality control the interpretation. In areas of anomalous throw, changes were made to either horizon or fault interpretations to correct inconsistencies. All major throw anomalies were corrected but small (< 20 m) inconsistencies were ignored as they do not affect the overall fault throw distribution. An example of a minor throw anomaly can be seen in the middle of fault U at the top Knurr level, where the cutoffs and the throw undulate (Fig. 7).

The top Fruholmen and top Fuglen have the largest fault throws across the area (> 300 m in Y′ and > 290 m on fault V; Fig. 7). The top Fruholmen cutoffs exhibit the largest throw values on all faults except fault U, which has its largest throw at the top Fuglen level (~220 m). The largest fault throw maxima in the data volume is observed on fault Y′ (> 300 m, top Fruholmen). Fault throw follows an elliptical pattern on isolated single faults (W and X relay), and more complex patterns where fault linkages are present (U/V, V/Y, Y/X; Fig. 7). Faults W and X don't vary in throw near their relay (i.e. no suggestion of linkage). At fault intersections, faults transfer displacement: i) fault U transfers displacement to fault V, ii) fault V to fault Y to make the larger displacement fault Y′, and iii) fault Y to fault X. For example, at the intersection of U and V, the throws of fault U (~150 m) and fault V (~100 m) are transferred to the southern portion of fault V (~250 m). The same pattern is observed when fault V (~250 m throw) and Y (~50 m throw) intersect and their throws are transferred to Y′ (~300 m) east of the intersection.

The top Knurr cutoffs exhibit minimal (50 m or less) throw on faults V and Y and there is no discernible throw on all other faults, so the cutoffs appear to overlap. Fault W does not contain cutoffs for the intra-

Kolje and the top Kolje respectively because it doesn't propagate through these shallower units. The top Knurr, intra-Kolje, and top Kolje show < 50 m throw on most faults, such that there is a high fault throw gradient (100–200 m) between top Fuglen and top Knurr. This high fault throw gradient results in folding of the three uppermost horizons. We interpret these folds as fault-propagation folds (Withjack et al., 1990; Schlische, 1995; Corfield and Sharp, 2000; Rahman, 2012; Lewis et al., 2015; Paul and Mitra, 2015).

4.4. Dip distortion (DD)

The DD analysis measures fault-related deformation of horizons compared to their regional dip. DD and lateral fault continuity decrease up-section from the top Fruholmen to the top Kolje (Fig. 8). High DD values (> 10°, green to red) are associated with faults, while lower values (< 10°, blue to green) are linked to more gentle folds. Values below 3° (Fig. 8, dark blue) are considered insignificant.

The top Fruholmen DD map (Fig. 8e) shows all the main faults and some smaller faults observed in the structure map (Fig. 6e). DD is large (20–30°) and localized along the main faults (U, V, X, Y, Y′, Z). Along some of these faults, DD decreases towards the fault tips (U, V, X, Y). For example, fault U has DD values up to 30° in the center of the fault and 10–15° towards the tipline. Fault zone width indicated by high DD is ~500 m (fault Y′), 300 m (faults V and Z), and 100–200 m (faults U, W, X and Y). The faults with the highest throw (V, Y′, Z) are also the faults with the largest DD values (> 20°), and the widest distortion zones (> 300 m). DD also shows that some faults are more laterally extensive than in the structure map. Fault U extends further west and clearly links with the smaller fault U′ in the center. Faults W and X are more laterally extensive and enhance hard-linkage at the relay structure (Fig. 8e). The area to the east of fault Z exhibits more complexity than originally interpreted (Fig. 8e, question mark). Here there is likely a small relay structure. With the exception of the hanging wall of fault Z, there is not much folding around the faults. Top Fuglen shows similar DD patterns to the top Fruholmen (Fig. 8d). The main difference in these two maps is that fault X on top Fuglen extends so far northeast that it appears to intersect fault V at a bend. The area to the east of fault
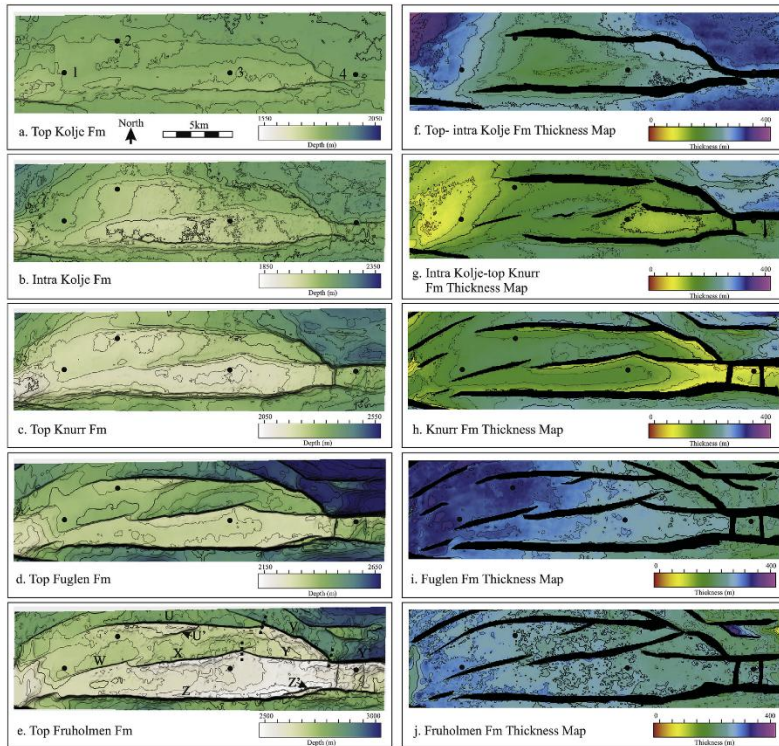
Fig. 6. Structure maps of the five interpreted horizons and vertical thickness maps calculated using distance between tops. a. Top Kolje (youngest). b. Intra-Kolje, c. Top Knurr, d. Top Fuglen, and e. Top Fruholmen (oldest). U-Z′ are faults. Dotted lines in e are the branch lines for the fault intersections UV, VY and YX. For comparison, a 500 m elevation range color bar is adjusted to a medial depth for each horizon. Vertical thickness maps of f. Top-intra Kolje, g. Intra-Kolje-top Knurr, h. Knurr Fm, i. Fuglen Fm, and j. Fruholmen Fm. All thickness maps are displayed on a color bar of 0–400 m. Wells 1–4 are included for reference on all structure and thickness maps. The contour interval for all maps is 25 m. (For interpretation of the references to color in this figure legend, the reader is referred to the Web version of this article.)

Z shows even more complexity at this level, suggesting a fractured relay ramp (Peacock and Sanderson, 1994).

The top Knurr DD map displays an entirely different pattern with respect to the two horizons below (Fig. 8c). DD highlights the three main fault systems, but DD is lower and more dispersed. Overall, faults are more segmented, and fault intersections (e.g. U-V and X-Y) and relays (e.g. W-X) are less apparent. On the hanging wall of the most displaced faults V, Y′ and Z, there are wide (~1 km), mid (5–15°) DD
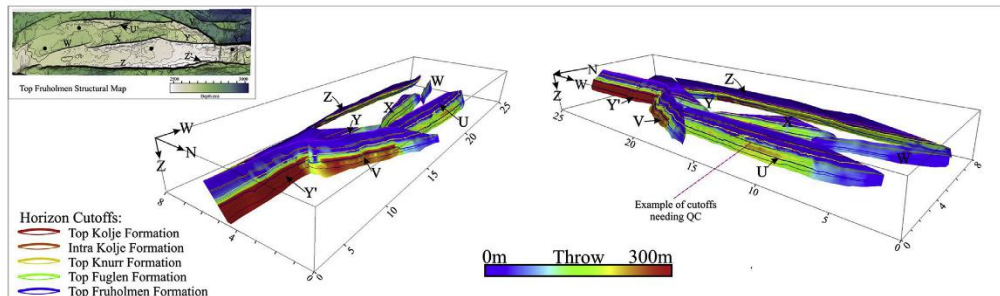

Fig. 7. Fault throw distribution on main fault planes. This was used to understand fault linkage and to quality control interpretations. Inset shows the faults on the top Fruholmen structure map.
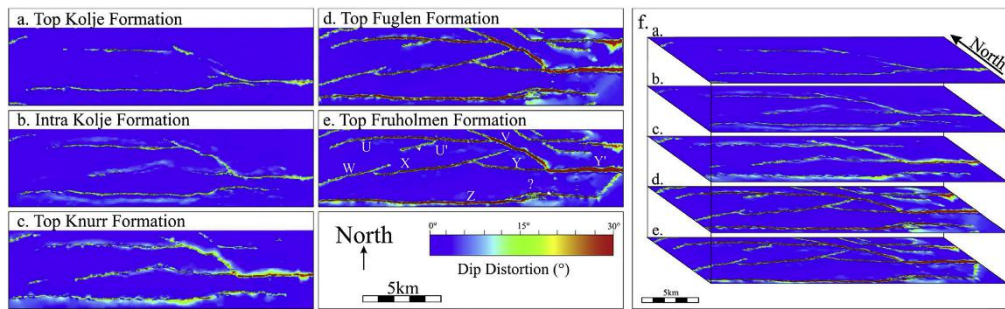
Fig. 8. Dip distortion (DD) of the a. Top Kolje, b. Intra-Kolje, c. Top Knurr, d. Top Fuglen, and e. Top Fruholmen. f. 3D view of DD. On each horizon, DD is calculated along N-S transects spaced every 100 m and is projected to the average horizon elevation.

areas indicating fault-related folding. Similar, although lower and narrower DD areas are present on the hanging walls of faults U, X and Y.

The central fault system (W-X-Y) is almost imperceptible at the intra-Kolje level (Fig. 8b). Along faults X and Y, there is gentle folding rather than faulting, mostly in the proto-hanging wall areas. In the northern (U-V-Y') and southern (Z) fault systems there is also gentle folding in the hanging wall areas. In the top Kolje DD map (Fig. 8a), only the northern and southern fault systems are visible, and the larger throw faults (Z and Y') are the only ones showing continuity along strike. There is also less folding at this uppermost level than at the intra-Kolje. In general, a comparison of DD values of the top and intra-Kolje to the top Knurr, shows that the faults appear much shorter with shallowing; for example, fault U is > 10 km long and ~1 km wide at the top Knurr level, while it is ~8 km long and < 500 m wide at the top Kolje. The higher DD values (> 30°) are evident for the top Knurr, while lower values (< 10°) are more dominant for the intra- and top Kolje. Also, it is more difficult to differentiate individual fault segments in the top and intra-Kolje (e.g. V-Y' or segments along Z).

In summary, top Fruholmen and top Fuglen are mostly offset by the faults, with large and localized DD, while top Knurr has lower, less localized DD and a high component of fault-related folding in the hanging walls. Faulting and folding decrease upwards to the intra-Kolje, in this horizon gentle folds are visible on the hanging walls of the main faults. The top Kolje is only slightly offset or folded (Fig. 8f).

4.5. Seismic attribute analysis

Fig. 9 shows the dip, tensor, semblance and envelope attributes, as well as a CMY color blend from the tensor, semblance and dip attributes on the five interpreted horizons. In general, the image quality of the original seismic and therefore the seismic attributes of the lowermost top Fruholmen are the worst. The top Fuglen and top Knurr show the best results with respect to seismic attributes as these display the clearest seismic signal. The contrast in the seismic attributes of the intra-Kolje and top Kolje is the least, as these are less faulted than deeper horizons.

Within the various selected attributes, the dip volume is the most successful single attribute for imaging faults in our dataset (Fig. 9a). Upthrown and downthrown fault blocks are visible as dark and light areas, respectively. These coincide with positive and negative dip values. Faults in the top Fruholmen are not well imaged by the dip attribute, while faults in the shallower four horizons are better imaged. The dip response in these horizons weakens upwards from top Fuglen to top Kolje. There is some noise in the three shallowest horizons, which was not removed by data conditioning. This coincides with shallow gas in the north and dolomite in the northeast.

The tensor attribute was the second most successful attribute in imaging faults while keeping noise to a minimum. It provides a high-quality image of faults in the top Fuglen and top Knurr (Fig. 9b). The other three horizons exhibit a weak tensor signal around faults. Unlike the dip cube, the tensor attribute has very little or no noise at all five

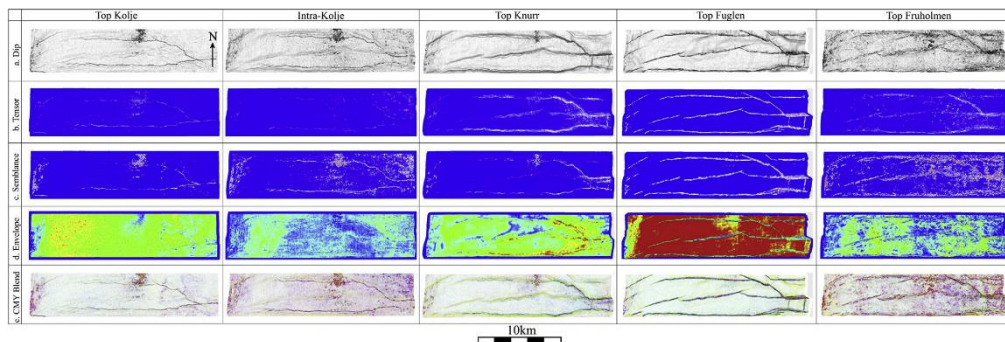**Fig. 9.** a. Dip, b. Tensor, c. Semblance, d. Envelope, and e. Cyan-magenta-yellow (CMY) color blend combining tensor (C), semblance (M) and dip (Y) attributes on the top Kolje (first column), intra-Kolje (second column), top Knurr (third column), top Fuglen (fourth column), and top Fruholmen (fifth column). (For interpretation of the references to color in this figure legend, the reader is referred to the Web version of this article.)

horizons.

The semblance volume also images the faults relatively well on each horizon (Fig. 9c). Noise caused by shallow gas in the north and dolomite in the northeast is visible at the top Knurr, intra- and top Kolje, and data quality is poor due to random noise at the top Fruholmen. Semblance is the third most successful attribute for imaging faults.

The envelope attribute images the amplitude strength contained in the volume (Taner et al., 1979). The strongest envelope values are present in the top Fuglen and top Knurr depth intervals (Fig. 9d). Fault definition in the tensor, semblance and dip attributes were also strongest at these horizon levels. Therefore, the envelope volume suggests a linkage between the strongest amplitudes and the best fault imaging. Envelope also images gas cloud noise as lower amplitude strengths at the top Fuglen and top Kolje levels.

The CMY color blend of the best three attributes, tensor (Cyan), semblance (Magenta) and dip (Yellow) clearly images faults. When the high values of these attributes overlap (black) the imaged fault displays visible facies (Fig. 9e). The best images are visible on the top Fuglen and top Knurr. There is also some noise in the CMY volume but overall this cube shows the best signal to noise ratio compared to the single attributes.

4.6. Fault enhancement and seismic fault facies

Fig. 10 shows the result of the FE analysis in 3D perspective (Fig. 10a), inlines (Fig. 10b–d), and depth slices at the average depth of the interpreted horizons (Fig. 10e–i). In both the inlines and depth slices, the FE maps and the data conditioned seismic are shown.

Inlines show that the highest FE facies (red) are present at the center of each fault and gradually transition outwards to lower FE facies (yellow to blue). This FE pattern was observed regardless of fault location (Fig. 10a–d). When comparing FE from the western and central parts (Fig. 10b and c) to the eastern part (Fig. 10d), there is an increase in the high FE facies (yellow to red) from west to east. This correlates with higher fault throw and vertical separations to the east (Figs. 6–9). The red to blue seismic fault facies pattern from the center to the edges of the fault zone is also evident in the depth slices (Fig. 10e–i). Similar to the CMY blend (Fig. 9e), there are seismic quality issues at the average top Fruholmen depth (Fig. 10i), and a decrease of seismic fault facies from top Fuglen to top Kolje (Fig. 10e–h). Faults at the top

Fruholmen average depth are poorly imaged, although faults V and Y' (Fig. 6) are relatively well imaged and display high FE facies (yellow to red) at their centers (Fig. 10i). The top Fuglen and top Knurr average depth slices have the highest concentration of seismic fault facies (Fig. 10g and h) with the same RYGB outward seismic facies pattern. Also, high FE facies (yellow and red) are more dominant in the east of the field (faults V, Y/Y' and Z; Figs. 6 and 10g-h). Along the faults, seismic fault facies are discontinuous. The intra-Kolje and top Kolje average depth slices exhibit low FE facies (green and blue), where green is at the fault center and blue is at the fault edges.

As some noise remained in the data conditioned seismic volume and is visible in the CMY color blend, it affects the FE maps. This noise, which is related to the gas cloud, is visible on the top Fruholmen, top Knurr, intra-Kolje and top Kolje average depth slices as a cloud of high FE values in the central northern part (Fig. 10e–g, i), although it is not conspicuous in the inlines (Fig. 10b–d). Some minor noise associated with the dolomite appears as a fine spotted/mottled texture in the northeast corner of the top Knurr and intra-Kolje (Fig. 10f and g).

Crossplots of attribute data further illustrate the significance of seismic fault facies in terms of the input attributes. In this analysis, we only use data within depths 2110–2750 m, encompassing the top Fuglen and top Knurr, as they offer the best fault images and least noise. Fig. 11 a-c shows crossplots of dip-semblance, dip-tensor and tensor-semblance, with the data points colored by the FE facies cutoffs. Semblance is proportional to dip, and FE increases with semblance and dip from the lowest (blue) to the highest (red) facies (Fig. 11a). Tensor is less proportional to dip and there is low correlation between seismic fault facies and tensor (Fig. 11b). Semblance and tensor correlate (as expected in Chopra and Marfurt, 2005), and seismic fault facies correlate with increasing semblance and to a less degree with increasing tensor.

The four seismic fault facies are filtered and individually imaged in Fig. 11d–g. The highest FE facies (red) is present across the entire area towards the center of the faults but is focused mostly in the east (Fig. 11d). The yellow facies follows a similar pattern but is farther away from the fault centers (Fig. 11e). The green facies is more widespread across the field area and delimits a wider faulted region than the yellow facies (Fig. 11f). The blue facies is the most laterally and across-fault extensive and is dominant across the entire study area (Fig. 11g).
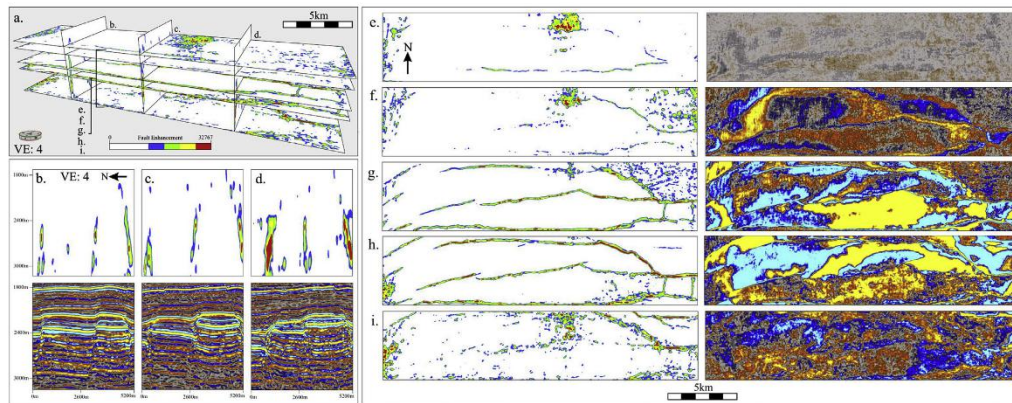
Fig. 10. Fault enhancement (FE) and comparison to seismic cube. a. Selected inlines and depth slices colored by five FE ranges: white is no fault, and blue to red are four unsupervised seismic facies within the fault zones. b, c and d are inline slices (3502, 2982 and 2473 respectively) of FE (top) and the data conditioned amplitude (bottom). e-i are depth slices of FE (left) and the data conditioned amplitude (right) at the average depth of the top Kolje (1800 m), intra-Kolje (2100 m), top Knurr (2300 m), top Fuglen (2400 m) and top Fruholmen (2750 m). (For interpretation of the references to color in this figure legend, the reader is referred to the Web version of this article.)

Fig. 11. a. Dip versus semblance, b. Dip versus tensor, and c. Tensor versus semblance of fault zone areas (FE > 16,000) in the interval 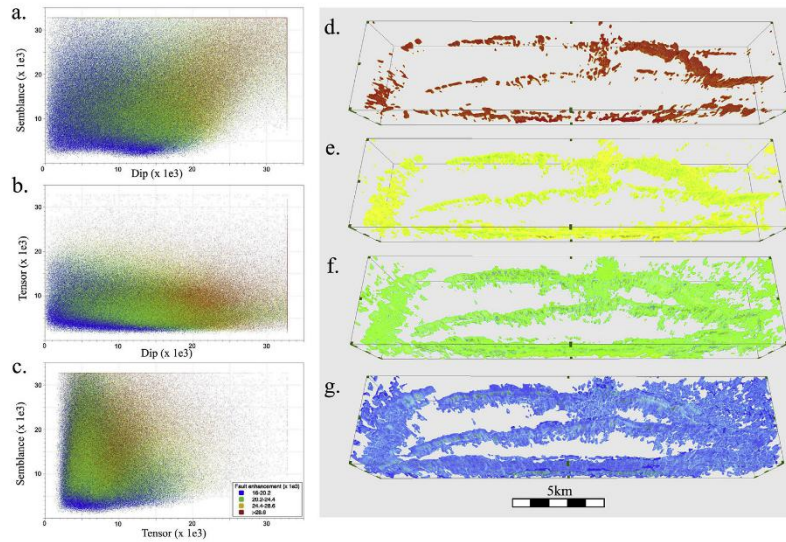between top Knurr and top Fuglen. In a-c, points are color coded by the four FE facies in Fig. 10 d-g. The four seismic fault facies displayed as geobodies on the selected depth interval. (For interpretation of the references to color in this figure legend, the reader is referred to the Web version of this article.)

4.7. Seismic amplitude versus distance to faults

The amplitude versus distance to fault analysis focuses on two smaller areas that have contrasting characteristics with respect to fault throw and related folding. Area 1 is across the northern fault U near its western tipline, while area 2 crosses the center of the largest throw fault Y' (red and yellow rectangles in Fig. 12a, respectively). These areas were investigated by generating horizon-based grids with a series of hanging wall and footwall regions associated with the distance from the interpreted fault plane (Fig. 12b and c). Fig. 12d-m shows crossplots of distance to fault versus normalized RMS amplitude for both areas. Each area is separated into hanging wall (left column, red-yellow-blue regions) and footwall (right column, teal-purple-green regions). In the top Fruholmen, top Fuglen and top Knurr, an additional (orange) region indicates cells associated with the fault plane. This region is displayed in the hanging wall crossplots. Best-fit lines for the hanging wall and footwall data illustrate the average trend of amplitudes change approaching the faults. On the right side of Fig. 12 (n, o) there are representative seismic inlines which are overlaid with lithology data from the wells (left), or the interpreted fault plane and nearest to furthest regions from it (right).

In area 1, the top Fruholmen shows a slight decrease in RMS amplitude towards the fault, both from the footwall and hanging wall (Fig. 12h). The intra-fault region (orange) exhibits an increase of amplitude compared to the outermost red region in the hanging wall. The top Fuglen (Fig. 12g) exhibits a slight decrease of amplitude towards the fault from the footwall, and a slight increase of amplitude towards the fault from the hanging wall. The intra-fault region (orange) shows a marked decrease in amplitude. The top Knurr (Fig. 12f) shows a decrease in amplitude towards the fault from the footwall, specifically in the green region near the fault, and an increase of amplitude towards the fault from the hanging wall, especially in the yellow and blue regions closer to the fault. The intra-Kolje (Fig. 12e) exhibits a decrease in amplitude towards the fault from the footwall, a slight increase of amplitude towards the fault in the outermost red and yellow regions of

the hanging wall, but a marked decrease in amplitude in the blue region closer to the fault. The top Kolje (Fig. 12d) shows a gradual increase in amplitude towards the fault from the footwall and hanging wall.

Area 2 shows different results. The top Fruholmen (Fig. 12m) shows an increase of amplitude from the footwall, particularly in the green region closest to the fault, a decrease of amplitude from the hanging wall in the red, yellow and blue regions, but a marked increase of amplitude in the intra-fault region (orange). The Top Fuglen (Fig. 12l) has relatively constant amplitude from the footwall, with a slight decrease of amplitude in the green region. From the hanging wall, the amplitude decreases towards the fault, with a sharp decrease in the intra-fault (orange) region. The top Knurr (Fig. 12k) holds the most varied data, the footwall drops in amplitude in the region furthest from the fault (teal) and is constant in amplitude in the next two regions (purple and green). In the hanging wall, the red region shows relative consistency, and then there is a large spike in amplitudes through the yellow and blue regions, followed by a sharp drop in the intra-fault (orange) region. The intra-Kolje (Fig. 12j) shows a gradual increase in amplitude towards the fault from the footwall, and in the hanging wall a slight increase in amplitude through the red region, followed by decreasing amplitude in the yellow and blue regions. The top Kolje (Fig. 12i) exhibits a gradual increase in amplitude towards the fault from the footwall, and in the hanging wall a decrease in amplitude through the red region, followed by an increase in amplitude in the yellow and blue regions. When comparing the two areas, the tops Fruholmen, Fuglen and Knurr show the most severe changes in amplitude, and area 2 shows more extreme amplitude variations.

The N-S seismic inlines for each of the areas (Fig. 12n and o) display folds next to the faults U and Y'. These folds run parallel to the faults and consist of hanging wall synclines and footwall anticlines (with the exception of top Fruholmen, top Fuglen and top Kolje in area 2, which exhibit a hanging wall anticline). These longitudinal folds show reoccurring patterns in the amplitude data. In the hanging wall syncline there is brightening or increase in amplitude towards the fault, while in the footwall anticline there is dimming or decrease in amplitude
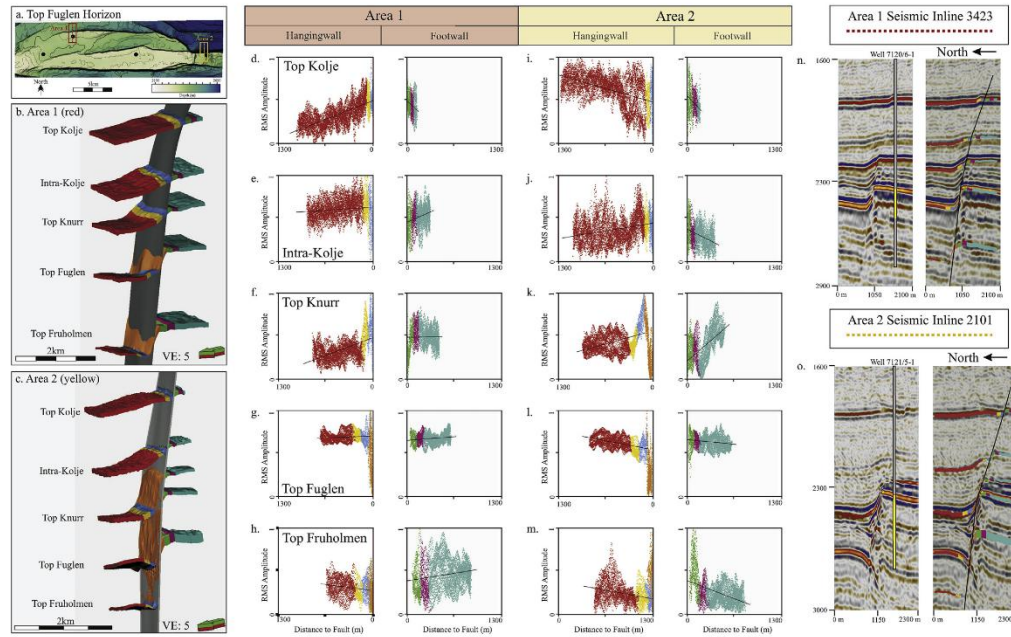
Fig. 12. Seismic amplitude versus distance to faults. a. Top Fuglen map showing areas 1 and 2 (red and yellow rectangles respectively). Area 1 is 2300 m long, 900 m wide and ranges from 1700 to 2800 m depth. Area 2 is 2300 m long, 900 m wide and ranges from 1900 to 2800 m depth. b. Structural model of area 1. c. Structural model of area 2. Both models are viewed from the northwest and their cells are colored as hanging wall (red to orange) and footwall (teal to green) regions. d-h. Area 1 hanging wall (left) and footwall (right) crossplots of distance to fault versus RMS amplitude (window size = 6) for the top Kolje, intra-Kolje, top Knurr, top Fuglen and top Fruholmen, respectively. i-m. Similar crossplots for area 2. (For interpretation of the references to color in this figure legend, the reader is referred to the Web version of this article.)

approaching the fault. In area 1, the shallowest four horizons show synclines in the hanging wall with brightening amplitudes towards the fault, and anticlines in the footwall, which with the exception of top Kolje exhibit dimming amplitudes approaching the fault (Fig. 12d–g). In area 2, despite the presence of hanging wall anticlines, the same pattern is also observed where anticlines correlate with dimming and synclines with brightening amplitudes towards the fault (Fig. 12i–m). These amplitude effects can be traced along strike.

5. Discussion

5.1. Improved seismic imaging and interpretation of faults

The data conditioning workflow (Gilani and Gómez-Martínez, 2013) contributed to a decrease in random and coherent noise as well as increased lateral continuity of reflectors below the shallow gas (Fig. 5). As the workflow is designed to remove the noise caused by shallow gas, it is reasonable that the noise associated with dolomite in the northwest of the study area wasn't completely removed. The application of the workflow in seismically explored areas containing shallow gas (e.g. the southwest Barents Sea) is an excellent way to improve seismic reflector continuity, and therefore fault imaging.

The structure maps (Fig. 6a–e) exhibit a concise summary of interpreted horizons and faults. Since the maps are based on what the geoscientist interprets, they are not always completely representative of all the faults but are a powerful starting point in understanding stratigraphic and structural relationships. In the Snøhvit area, the structure maps show a decrease in fault displacement and lateral extent, as well

as less fault connectivity and linkages with shallowing. From the top Knurr and upwards there is decreasing disruption of horizon continuity due to the tipping out of the main faults (Fig. 6a–e). Thickness maps of the five main intervals of interest suggest that the Fruholmen and Fuglen Fms are pre-rift, while the Knurr and Kolje Fms are syn-rift (Fig. 6f–j).

The fault throw analysis (Fig. 7) is also based on the interpretation of faults and horizons surfaces and their intersections (cutoffs). On isolated faults, an elliptical displacement pattern with highest displacement at the center was observed (W, X; Fig. 7). At fault intersections (U/V, V/Y, Y/X; Fig. 7), fault splays transfer displacement to the master faults (U to V, V to Y, and Y to X). Fault intersections or branch lines are generally aligned parallel to the extension direction (Yielding, 2016). In the three fault intersections above, branch lines trend between 014 and 023 (dotted lines, Fig. 6e), which is consistent with N-S extension.

DD (Fig. 8) shows departure of the interpreted horizons from regional dip and is linked to fault related deformation. The highest DD values are present in the deepest top Fruholmen and top Fuglen and decrease upwards. This pattern also applies to the width of the fault zones, which narrow with decreasing depth, to be replaced in the top Knurr and intra-Kolje levels by folding mostly in the hanging walls. These observations are consistent with fault-propagation folding (Withjack et al., 1990; Long and Imber, 2010). The central fault system (W, X, Y) exhibits only slight folding in the intra-Kolje and tips out completely in the top Kolje. This proves that the northern and southern fault systems are larger (and perhaps older) than the central system. DD is also useful for studying the lateral extent of faults. Fault X almost

J. Cunningham et al.

meets fault V in the top Fruholmen and intersects with fault V in the Fuglen DD maps, therefore extending 1.5 km further to the northeast than in the structure maps. Fault interaction at relays is enhanced: for example in the relay between faults X and W, and the complex fractured relay in the eastern portion of fault Z (Fig. 8d and e). DD, however, is limited by the sampling direction. Since the selected transects are N-S, faults with this strike are not imaged in the maps. This is not a major problem in the area where most faults strike E-W.

Seismic attributes also show decreasing faulting, narrowing fault zones, and less prominent fault segments with shallowing (Fig. 9). Dip, tensor and semblance are the most successful attributes in the imaging of faults in this study (Dutzer et al., 2010; Iacopini et al., 2012, 2016). The dip attribute does the best job overall in highlighting the faults. Tensor is successful on the top Fuglen and top Knurr, which have the best reflector image quality, but only manages a subtle image in the less displaced top and intra-Kolje. Semblance clearly images faults on all horizons but is the attribute most susceptible to gas cloud noise. By combining these three attributes into a color blend, it is possible to isolate fault bodies using: reflector orientation (tensor), discontinuity (semblance) and dip. Although seismic attributes do not give the information contained in the structure maps, fault throw and DD analysis, they are an excellent step to apply to a seismic volume before fault interpretation. The creation and usage of a color blend of structure enhancing attributes is a quick and easy way to get started on the interpretation of faults and their relationships on a preliminary basis. Seismic attributes provide the user with images of faults beyond the constraints of human interpretation and are therefore excellent to understand the details contained in the seismic signal surrounding faults.

5.2. The classification of unsupervised seismic fault facies

Unsupervised seismic fault facies were constructed by dividing the high FE values in four classes of increasing value (Fig. 10). The highest FE facies (red) are in the center of faults in the inline and depth slices, and they are more abundant to the northeast of the study area where the faults have the highest throw. Crossplots of seismic attribute data show that with increasing values of semblance, dip and to a minor degree tensor, FE increases (Fig. 11). FE is a relatively simple attribute to highlight faults and their damage zones. However, in order to understand the relationship between the unsupervised seismic fault facies and geological parameters such as fault throw or DD, some more comparisons and further analysis must be incorporated into the study.

FE is a filter that enhances the edges contained in a seismic volume; the magnitude of this measurement is linked to structural deformation. DD is a measurement of apparent dip on interpreted horizons. A comparison of these two measurements may explain the significance of the seismic fault facies with respect to horizon interpretations. This was done for the largest thrown fault (area 2, Fig. 12), where DD and FE data were resampled into the cells of the structural model (Fig. 13b and c). The data are displayed on distance to fault (x-axis) versus normalized RMS amplitude (y-axis) crossplots, but the data points are colored by DD (Fig. 13d–h) and FE (Fig. 13i–m). Due to the nature of the upscaling process of the DD trimeshes into the structural model, it was not possible to populate every cell with DD data. To ensure consistency between the two datasets, the missing points from the DD data clouds were also removed from the FE. In the structural models, it is evident that the highest values of DD and FE are in the three deepest, most offset horizons (Fig. 13b and c). With the exception of top Fruholmen in the footwall (Fig. 13m), high DD values (> 12°) in the top Fruholmen, top Fuglen and top Knurr correlate with the blue to red seismic fault facies, and hanging wall and footwall areas away from the fault show low DD (1–10°) and FE (< 16,000) values (Fig. 13f–h and k-m). In the uppermost intra- and top Kolje horizons, there is clear variation in DD (1–10°) mostly in the hanging wall, while the FE is overall low (< 16,000; Fig. 13d–e and i-j). Exceptions are the intra-Kolje in the hanging wall where there are blue and green fault facies at ~800 m

from the fault, which are related to a small-scale fault, and in the footwall close to the fault where high DD values (> 12°) correlate with the blue and green fault facies (Fig. 13j). High DD values in the footwall of top Kolje don't correlate with the seismic fault facies, suggesting that these values are rather spurious. The four seismic fault facies are thus related to high DD (> 12°), while low DD (1–10°) picks up the subtleties of fault related folding.

Long and Imber (2010, 2012) were the original proponent of DD mapping, where the relationship between fault displacement, its gradient and DD was established. We take their comparisons a step further by integrating fault throw, DD, and seismic fault facies. DD and FE classify fault deformation but only DD captures the subtleties associated with fault related folding. Iacopini et al. (2016) used seismic attribute correlation to identify unsupervised seismic fault facies. Botter et al. (2016, 2017b) used the FE filter to establish fault facies on synthetic seismic data where a correlation between fault deformation, seismic attribute response, and unsupervised seismic fault facies was established. Our workflow applies these same findings to real seismic data and establishes a methodology for fault interpretation, linking fault throw, DD, seismic attributes and fault facies classification.

To further explore the geological significance of the seismic fault facies, they are compared with fault throw, dip separation gradient and juxtaposed lithology by projecting these attributes onto the fault planes (Fig. 14). The results show a correlation between throw, dip separation gradient and the seismic fault facies (Fig. 14a, b, d). The highest FE facies correlate with the fault areas exhibiting the highest throw, and the highest dip separation gradient (a measure of strain; Fig. 14a, b, d). This result together with the correlation of the seismic fault facies with high DD (Fig. 13), demonstrates a clear link between the seismic fault facies and fault deformation. This is consistent with the findings of Botter et al. (2016, 2017b) in synthetic models.

As the seismic fault facies are unsupervised, in an attempt to understand their lithological significance, we compared them with the juxtaposed lithology on the faults (Fig. 14c). In the case of a sand dominated lithology, the faults propagated further and offset the sedimentary layers, with the resultant presence of high FE facies (green to red). In the uppermost shale dominated lithologies, the faults tip out, resulting in folding and low FE facies (blue to green). Thus, mechanical stratigraphy controls the distribution of the seismic fault facies in the field.

5.3. Understanding amplitude variations across fault zones

Seismic amplitude versus distance to fault (Fig. 12) proves that a brightening in amplitude occurs when approaching the fault through a syncline, and amplitude dims when approaching the fault through an anticline. This is clearly observed in the less faulted top Knurr, intra and top Kolje (Fig. 12d–f and i-k). In the deeper, more faulted horizons, there can be either dimming or brightening in amplitude towards the fault, although across a narrower distance. In area 1 the Fuglen and area 2 the Fruholmen and Fuglen fms are dominated by sandstones, which may be contributing to the nature of deformation evident in these sections and therefore the amplitude distributions (lithology data in wells; Fig. 12n and o). The top Knurr, intra and top Kolje are all associated with shales, which may play a key role in the formation of anticlines and synclines in these units (Fig. 12n and o). In the top Fuglen (area 1, 2) and the top Knurr (area 2), the results are conclusive with a major decrease in amplitude on the fault (Fig. 12 k, g, l, orange regions). The deepest horizon (top Fruholmen) is inconsistent with observed systematic amplitude patterns in both areas. In area 1, there is an increase in amplitude associated with the fault plane (Fig. 12h, orange region) but on further inspection it is clear that this is due to a second poorly-imaged subsidiary fault, slightly south of the main interpreted fault (Fig. 12, n). In area 2, the top Fruholmen also exhibits increasing amplitudes associated with the fault plane (Fig. 12m, orange region). Here, there may be another subsidiary fault influencing
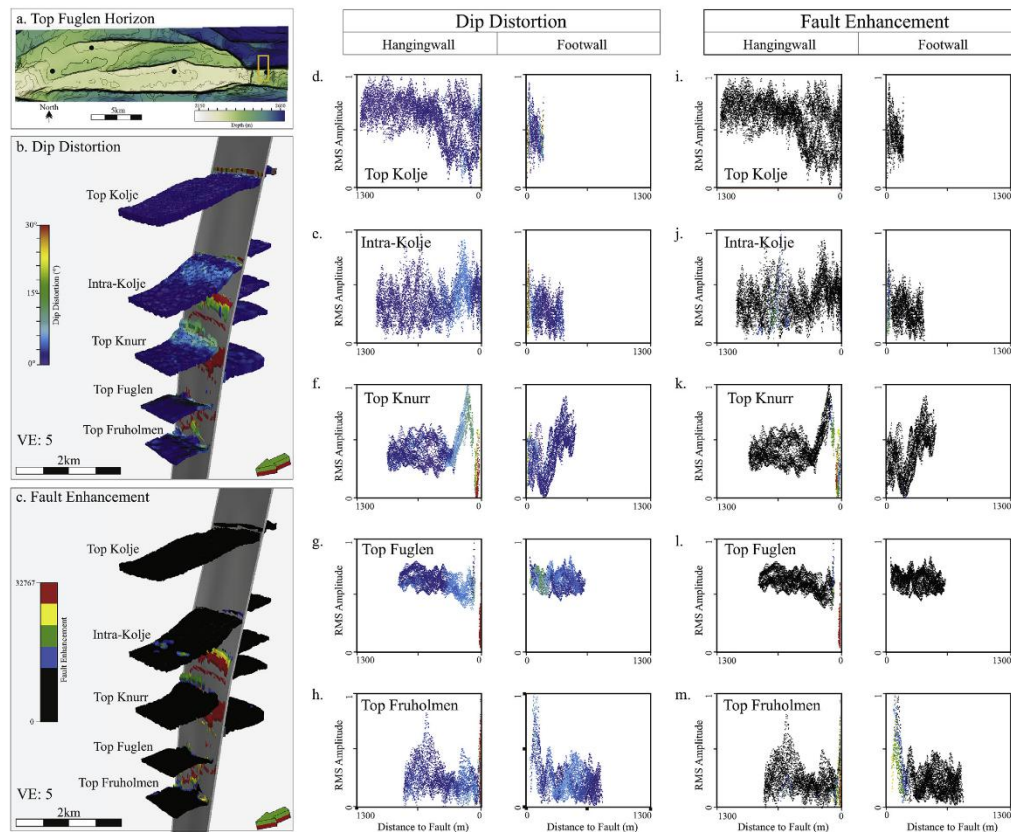
Fig. 13. a. Top Fuglen map showing area 2 (yellow rectangle). b. Structural model of area 2 with dip distortion (DD) resampled into the grid cells. c. Structural model of area 2 with FE resampled into the grid cells. Both models are viewed from the northwest. d-h. Hanging wall (left) and footwall (right) crossplots of distance to fault versus RMS amplitude (window size = 6) with data points colored by DD for the top Kolje, intra-Kolje, top Knurr, top Fuglen and top Fruholmen, respectively. i-m. Same crossplots but with data points colored by FE. (For interpretation of the references to color in this figure legend, the reader is referred to the Web version of this article.)

reflector continuity, although with the low signal/noise ratio of the data at this depth (Fig. 12o) this is difficult to define. There are several explanations for the observed changes in amplitude across faults:

a   *Geometrical focusing and defocusing of the seismic signal caused by reflector curvature*- Relative to a flat plane, the reflected seismic energy is spread over a larger surface when the reflection occurs on an anticline, and over a smaller surface in the presence of a syncline (Sheriff and Geldart, 1995). The resulting seismic will exhibit stronger reflections associated with synclines (focusing), and weaker reflections (defocusing) in the case of anticlines (Sheriff and Geldart, 1995). This effect is related to a geometry parameter.

b   *Acoustic properties*- Changes to the acoustic properties of a rock occur when the rock undergoes structural deformation (Couples et al., 2007; Skurtveit et al., 2013). Previous studies have modelled fault zones and found that changing acoustic properties associated with fault related deformation results in amplitude variations (Botter et al., 2014, 2016). This is most likely in the high FE facies associated to large deformation (yellow and red, Fig. 10 orange region

Figs. 11 and 12k-m). However, without access to well cores or logs of these rocks, it is not possible to prove if this correlation exists.

c   *Survey Geometry/Illumination mapping* – The seismic data are controlled by the geometry and acquisition direction of the seismic survey (Laurain et al., 2004; Drottning et al., 2006; Gjøystdal et al., 2007). Several studies document that illumination direction also has an effect on the measured seismic amplitudes especially with respect to faults (Drottning et al., 2006; Gjøystdal et al., 2007; Lecomte, 2008; Botter et al., 2014, 2016; Lecomte et al., 2015). The seismic data used in this study are the near-angle stacks (5–20°) of a data cube merged from five 3D streamer surveys. The specifics of the merged survey are not equivalent to the single surveys and therefore it is difficult to quantify the effect shooting direction has on seismic amplitude. It would be an interesting study to explore how illumination direction affects the imaging of structural geometry (i.e. curving the reflectivity surface) and its effect on the seismic amplitude.
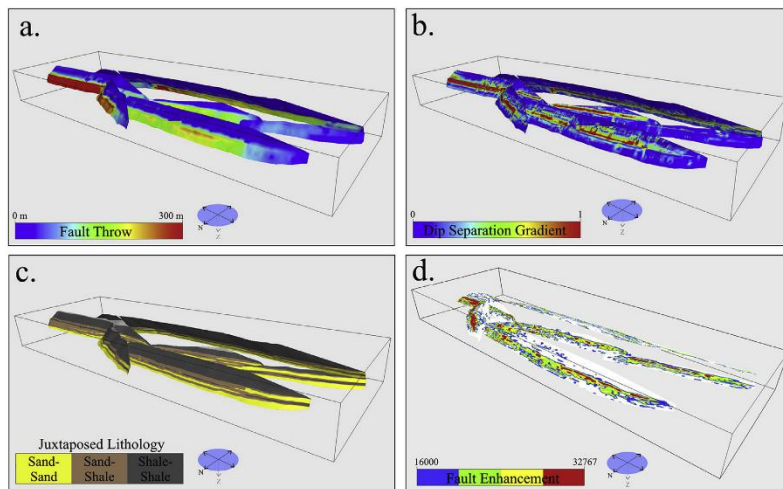
Fig. 14. a. Fault throw, b. Dip separation gradient, c. Juxtaposed lithology, and d. FE (seismic fault facies) along main faults in the area.

5.4. Implications

A common practice for interpreting faults in seismic data is to pick fault sticks on seismic lines (Caine et al., 1996; Faulkner et al., 2010). This is then followed by the construction of faults planes (from the interpolation of fault sticks). When comparing the structure maps (Fig. 6) to the throw (Fig. 7), DD (Fig. 8), and FE (Fig. 10) maps, it is evident that these additional properties help to provide a wealth of information regarding fault extent, displacement patterns and linkage. Having a greater understanding of these three parameters can improve the interpreter's knowledge of fault connectivity, fault seal potential, flow and pressure barriers, top seal integrity, and the mapping of mega sequences (pre-, syn- and post rift). Specifically, DD (Fig. 8) gives a more conclusive understanding of the lateral and vertical extent of faults, fault connectivity and the presence of small (even sub-seismic) scale faults. The application of the FE filter on any structure enhancing attribute volume, or a combination of these attributes, results in a volume where faults are highlighted and easy to interpret. FE (Fig. 10) allows for a more conclusive understanding of the lateral and vertical extent of faults, fault internal structure, and fault facies classification, as it seems that FE correlates with fault deformation. FE, however, is not a great indicator of the subtleties associated with fault-related folding. Seismic attributes (Fig. 9) are also a quick and simple way to understand fault structure in a seismic volume, but a CMY color blend of multiple attributes gives a clearer image of faults for interpretation. In the essence of time, anyone of these properties or their combination can lead to a better understanding of fault formation, linkage, and amplitude anomalies near fault planes. This is not only important for the petroleum industry, but for any industry interested in understanding the geophysical and geological impact of faults.

A brightening and dimming effect towards the fault was witnessed in the seismic amplitudes analysis of this paper. Variations in seismic amplitude near fault planes can be related to seismic signal focusing, changes in acoustic properties, and/or illumination effects from seismic acquisition (Badley, 1985; Sheriff and Geldart, 1995; Laurain et al., 2004; Couples et al., 2007; Skurtveit et al., 2013), all of which are potentially related to the structural geometry of the surface imaged. With limited lithologic control it is difficult to infer the effects lithological variation has on the variations in amplitude witnessed here. In

order to analyze the reason for seismic brightening and dimming more accurately, it is necessary to acquire a dataset where wells are transecting a fault plane.

We analyzed a near-angle stack focusing on PP reflections. Future work will involve analysis of ocean bottom seismic (OBS) data from the Snøhvit Field to compare how PP and PS data signals differ with respect to fault characterization.

References

Aarland, R.K., Skjerven, J., 1998. Fault and fracture characteristics of a major fault zone in the northern North Sea: analysis of 3D seismic and oriented cores in the Brage Field (Block 31/4). Geol. Soc. Lond. Spec. Publ. 127, 209–229.

Alaei, B., 2016. Seismic Attributes and Their Application in Seismic Interpretation.

Ashcroft, W., 2011. A Petroleum Geologists Guide to Seismic Reflection, first ed. Wiley-Blackwell.

Badley, M., 1985. Practical Seismic Interpretation. (Boston, USA).

Bakker, P., 2002. Image Structure Analysis for Seismic Interpretation. Technische Universiteit Delft.

Barnes, A.E., 2000. Attributes for automating seismic facies analysis. In: SEG 70th Annual International Meeting, pp. 553–556.

Barnett, J.A.M., Mortimer, J., Rippon, J.H., Walsh, J.J., Watterson, J., 1987. Displacement geometry in the volume containing a single normal fault. AAPG Bull. 71, 925–937.

Berglund, L.T., Augustson, G., Færseth, R., Ramberg-Moe, H., 1986. The Evolution of the Hammerfest Basin, Habitat of Hydrocarbons on the Norwegian Continental Shelf. Graham & Trotman for the Norwegian Petroleum Society.

Botter, C., Cardozo, N., Hardy, S., Lecomte, I., Escalona, A., 2014. From mechanical modeling to seismic imaging of faults: a synthetic workflow to study the impact of faults on seismic. Mar. Petrol. Geol. 57, 187–207.

Botter, C., Cardozo, N., Hardy, S., Lecomte, I., Paton, G., Escalona, A., 2016. Seismic characterization of fault damage in 3D using mechanical and seismic modelling. Mar. Petrol. Geol. 77, 973–990.

Botter, C., Cardozo, N., Lecomte, I., Rotevatn, A., Paton, G., 2017a. The impact of faults and fluid flow on seismic images of a relay ramp over production time. Petrol. Geosci.

Paper II

23, 17–28.

Botter, C., Cardozo, N., Qu, D., Tveranger, J., Kolyukhin, D., 2017b. Fault damage zones seismic characterization of fault facies models. Interpretation 5, 1–18.

Caine, J.S., Evans, J.P., Forster, C.B., 1996. Fault zone architecture and permeability structure. Geology 24, 1025–1028.

Carcione, J.M., Herman, G.C., ten Kroode, A.P.E., 2002. Seismic modeling. Geophysics 67, 1304–1325.

Childs, C., Manzocchi, T., Walsh, J.J., Bonson, C.G., Nicol, A., Schöpfer, M.P.J., 2009. A geometric model of fault zone and fault rock thickness variations. J. Struct. Geol. 31, 117–127.

Childs, C., Watterson, J., Walsh, J.J., 1995. Fault overlap zones within developing normal fault systems. J. Geol. Soc. 152, 535–549.

Chopra, S., Marfurt, K.J., 2007. Seismic Attributes for Prospect Identification and Reservoir Characterization. Society of Exploration Geophysicists and European Association of Geoscientists and Engineers, Tulsa, OK, United States of America.

Chopra, S., Marfurt, K.J., 2005. Seismic attributes - a historical perspective. Geophysics 70 3SO–28SO. https://doi.org/10.1190/1.2098670.

Corfield, S., Sharp, I.R., 2000. Structural style and stratigraphic architecture of fault propagation folding in extensional settings: a seismic example from the Smorbukk area, Halten Terrace, Mid-Norway. Basin Res. 12, 329–341. https://doi.org/10.1111/j.1365-2117.2000.00133.x.

Couples, G., Ma, J., Lewis, H., Olden, P., Quijano, J., Fasae, T., Maguire, R., 2007. Geomechanics of faults: impacts on seismic imaging. First Break 83–90.

Dalland, A., Worsley, D., Ofstad, K., 1988. A lithostratigraphic scheme for the Mesozoic and Cenozoic succession offshore mid- and northern Norway. Norw. Petrol. Dir. Bull. 4, 1–65.

Doré, A.G., 1995. Barents Sea geology, petroleum resources and commercial potential. Arctic 48, 207–221.

Drottning, Å., Lecomte, I., Gjøystdal, H., Skorstad, A., Kolbjørnsen, O., Huseby, O., 2006. Modelling the seismic response to production: a closer look at the sensitivity to overburden, survey, rock physics model and seismic modelling approach. NPF-Semin. Kristiansand 1–4.

Dumay, J., Fournier, F., 1988. Multivariate statistical analyses applied to seismic facies recognition. Geophysics 53, 1151–1159.

Dutzer, J.-F., Basford, H., Purves, S., 2010. Investigating fault-sealing potential through fault relative seismic volume analysis. In: Petroleum Geology Conference Series, vol. 7. pp. 509–515.

Eichhubl, P., D'Onfro, P.S., Aydin, A., Waters, J., McCarty, D.K., 2005. Structure, petrophysics, and diagenesis of shale entrained along a normal fault at Black Diamond Mines, California - implications for fault seal. AAPG Bull. 89, 1113–1137.

Elliott, G.M., Wilson, P., Jackson, C. a. L., Gawthorpe, R.L., Michelsen, L., Sharp, I.R., 2012. The linkage between fault throw and footwall scarp erosion patterns: an example from the Bremstein Fault Complex, offshore Mid-Norway. Basin Res. 24, 180–197.

Færseth, R.B., Johnsen, E., Sperrevik, S., 2007. Methodology for risking fault seal capacity: implications of fault zone architecture. AAPG Bull. 91, 1231–1246.

Faulkner, D.R., Jackson, C.A.L., Lunn, R.J., Schlische, R.W., Shipton, Z.K., Wibberley, C.A.J., Withjack, M.O., 2010. A review of recent developments concerning the structure, mechanics and fluid flow properties of fault zones. J. Struct. Geol. 32, 1557–1575.

Fournier, F., Derain, J., 1995. A statistical methodology for deriving reservoir properties from seismic data. Geophysics 60, 1437–1450.

Gauthier, B.D.M., Lake, S.D., 1993. Probabilistic modeling of faults below the limit of seismic resolution in Pelican Field, North Sea, offshore United Kingdom. AAPG Bull. 77, 761–777.

Gilani, S.F., Gómez-Martínez, L., 2013. The application of data conditioning, frequency decomposition and DHI from RGB colour blending in the Gohta discovery (Barents Sea, Norway). First Break 33, 39–45.

Gjøystdal, H., Iversen, E., Lecomte, I., Kaschwich, T., Drottning, Å., Mispel, J., 2007. Improved applicability of ray tracing in seismic acquisition, imaging, and interpretation. Geophysics 72, SM261–SM271.

Iacopini, D., Butler, R., Purves, S., McArdle, N., De Freslon, N., 2016. Exploring the seismic expression of fault zones in 3D seismic volumes. J. Struct. Geol. 89, 54–73.

Iacopini, D., Butler, R.W.H., 2011. Imaging deformation in submarine thrust belts using seismic attributes. Earth Planet Sci. Lett. 302, 414–422.

Iacopini, D., Butler, R.W.H., Purves, S., 2012. Seismic imaging of thrust faults and structural damage: a visualization workflow for deepwater thrust belts. First Break 30, 77–84.

Landa, E., 2012. Seismic diffraction: where's the value? SEG Tech. Progr. Expand. Abstr. 1–4.

Landa, E., 2007. Beyond Conventional Seismic Imaging. EAGE.

Landa, E., Keymar, S., 1998. Seismic monitoring of diffraction images for detection of local heterogeneities. Geophysics 63, 1093–1100.

Laurain, R., Vinje, V., Strand, C., 2004. Simulated migration amplitude for improving amplitude estimates in seismic illumination studies. Lead. Edge 23, 240.

Lecomte, I., 2008. Resolution and illumination analyses in PSDM: a ray-based approach. Lead. Edge (Tulsa, OK), vol. 27, 650–663.

Lecomte, I., Lavadera, P.L., Anell, I., Buckley, S.J., Schmid, D.W., Heeremans, M., 2015. Ray-based seismic modelling of geologic models: understanding and analyzing seismic images efficiently. Interpretation 3, SAC71–SAC89.

Lewis, M.M., Jackson, C.A.L., Gawthorpe, R.L., Whipp, P.S., 2015. Early synrift reservoir development on the flanks of extensional forced folds: a seismic-scale outcrop analog from the Hadahid fault system, Suez rift, Egypt. AAPG Bull. 99, 985–1012.

Linjordet, A., Olsen, R.G., 1992. The Jurassic Snøhvit gas field, Hammerfest basin, offshore northern Norway. Giant Oil and Gas Fields of the Decade 1978-1988, Michel T. Halboutypp. 349–370.

Long, J.J., Imber, J., 2012. Strain compatibility and fault linkage in relay zones on normal faults. J. Sediment. Petrol. 36, 16–26.

Long, J.J., Imber, J., 2011. Geological controls on fault relay zone scaling. J. Struct. Geol. 33, 1790–1800.

Long, J.J., Imber, J., 2010. Geometrically coherent continuous deformation in the volume surrounding a seismically imaged normal fault-array. J. Struct. Geol. 32, 222–234.

Marfurt, K.J., 2006. Robust estimates of 3D reflector dip and azimuth. Geophysics 71, P29.

Marfurt, K.J., Kirlin, R.L., Farmer, S.L., Bahorich, M.S., 1998. 3-D seismic attributes using semblance-based coherency algorithm. Geophysics 63, 1150–1165.

Ostanin, I., Anka, Z., di Primio, R., Bernal, A., 2012. Identification of a large Upper Cretaceous polygonal fault network in the Hammerfest basin: implications on the reactivation of regional faulting and gas leakage dynamics, SW Barents Sea. Mar. Geol. 332–334, 109–125.

Paul, D., Mitra, S., 2015. Fault patterns associated with extensional fault-propagation folding. Mar. Petrol. Geol. 67, 120–143.

Peacock, D.C.P., Sanderson, D.J., 1994. Geometry and development of relay ramps in normal fault systems. AAPG Bull. 78, 147–165.

Posamentier, H., Kolla, V., 2003. Seismic geomorphology and stratigraphy of depositional elements in deep-water settings. J. Sediment. Res. 73, 367–388.

Purves, S., Basford, H., 2011. Visualizing geological structure with subtractive color blending. In: In: Marfurt, K.J., Gao, D., Barnes, A., Chopra, S., Corrao, A., Hart, B., James, H., Pacht, J., Rosen, N.C. (Eds.), Attributes: New Views on Seismic Imaging – Their Use in Exploration and Production: 31st Annual SEPM Society for Sedimentary Geology, pp. 120–139.

Rahman, J., 2012. Compactions, Rock Properties Evaluation, Rock Physics Diagnostics, AVO Modelling and Seismic Inversion in the Snohvit Field, SW Barents Sea. University of Oslo.

Rippon, J.H., 1985. Contoured patterns of the throw and hade of normal faults in the Coal Measures (Westphalian) of north-east Derbyshire. Proc. Yorks. Geol. Soc. 45, 147–161.

Schlische, R.W., 1995. Geometry and origin of fault-related folds in extensional settings. AAPG Bull. 79, 1661–1678.

Sheriff, R.E., Geldart, L.P., 1995. Exploration Seismology, second ed. Cambridge University Press, Cambridge.

Shuey, R.T., 1985. A simplification of the Zoeppritz equations. Geophysics 50, 609–614.

Skurtveit, E., Torabi, A., Gabrielsen, R.H., Zoback, M.D., 2013. Experimental investigation of deformation mechanisms during shear-enhanced compaction in poorly lithified sandstone and sand. J. Geophys. Res. Solid Earth 118, 4083–4100.

Sund, T., Skarpnes, O., Nørgård Jensen, L., Larsen, R.M., 1984. Tectonic Development and Hydrocarbon Potential Offshore Troms, Northern Norway. AAPG Special Publication Memoir: Future Petroleum Provinces of the World, pp. 615–627.

Taner, M.T., Koehler, F., Sheriff, R.E., 1979. Complex seismic trace analysis. Geophysics 44, 1041–1063.

Townsend, C., Firth, I.R., Westerman, R., Kirkevollen, L., Harde, M., Andersen, T., 1998. Small seismic-scale fault identification and mapping. Geol. Soc. Lond. Spec. Publ. 147, 1–25.

Widess, M.B., 1973. How thin is a thin bed? Geophysics 38, 1176–1180.

Wilson, P., Elliott, G.M., Gawthorpe, R.L., Jackson, C. a. L., Michelsen, L., Sharp, I.R., 2013. Geometry and segmentation of an evaporite-detached normal fault array: 3D seismic analysis of the southern Bremstein Fault Complex, offshore mid-Norway. J. Struct. Geol. 51, 74–91.

Wilson, P., Hodgetts, D., Rarity, F., Gawthorpe, R.L., Sharp, I.R., 2009. Structural geology and 4D evolution of a half-graben: new digital outcrop modelling techniques applied to the Nukhul half-graben, Suez rift, Egypt. J. Struct. Geol. 31, 328–345.

Withjack, M.O., Olson, J., Peterson, E., 1990. Experimental models of extensional forced folds. AAPG Bull. 74, 1038–1054.

Yielding, G., 2016. The Geometry of Branch Lines Geological Society, London Special Publications 439.

Yielding, G., Freeman, B., 2016. 3-D seismic-structural workflows – examples using the hat creek fault system. In: Krantz, B., Ormand, C., Freeman, B. (Eds.), M111: 3-D Structural Interpretation: Earth, Mind and Machine, pp. 155–171.

PAPER III

THE IMPACT OF SEISMIC INTERPRETATION METHODS ON A FAULT ANALYSIS WORKFLOW: A CASE STUDY FROM THE SNØHVIT FIELD, BARENTS SEA

Jennifer Cunningham, Nestor Cardozo, Chris Townsend, Richard H. T. Callow

The Impact of Seismic Interpretation Methods on the Analysis of Faults: A Case Study from the Snøhvit Field, Barents Sea

Jennifer Cunningham*[1,3], Nestor Cardozo[1], Chris Townsend[1], Richard H. T. Callow[2]

[1] Department of Energy Resources, University of Stavanger, 4036 Stavanger, Norway
[2] Equinor ASA, 4035 Stavanger, Norway
[3] Equinor ASA, Sandslivegen 90 5254 Sandsli, Norway

P3 Abstract

Five seismic interpretation experiments were conducted on an area of interest containing a fault relay in the Snøhvit Field, Barents Sea, Norway, to understand how interpretation method impacts the analysis of fault and horizon morphologies, fault lengths, and vertical displacement (throw). The resulting horizon and fault interpretations from the least and most successful interpretation methods were further analysed to understand the impact of interpretation method on geological modelling and hydrocarbon volume calculation. Generally, the least dense manual interpretation method of horizons (32 inlines (ILs) x 32 crosslines (XLs), 400m) and faults (32 ILs, 400m) resulted in inaccurate fault and horizon interpretations and underdeveloped relay morphologies and throw that can be considered inadequate for any detailed geological analysis. The densest fault interpretations (4 ILs, 50m) and auto-tracked horizons (1 IL x 1 XL, 12.5 m) provided the most detailed interpretations, most developed relay and fault morphologies and geologically realistic throw distributions. Analysis of the geological modelling proved that sparse interpretation grids generate significant issues in the model itself which make it geologically inaccurate and lead to misunderstanding of the structural evolution of the relay. Despite significant differences between the two models the calculated in-place

petroleum reserves are broadly similar in the least and most dense experiments. However, when considered at field-scale the magnitude of the differences in volumes that are generated solely by the contrasting interpretation methodologies clearly demonstrates the importance of applying accurate interpretation strategies.

P3 1 Introduction

An accurate understanding of faults in the subsurface is critical for many elements of the hydrocarbon exploration and production industry. For example faults control sediment and reservoir depositional systems, act either as conduits or baffles to fluid flow, are the defining elements of structural traps and impact the design of exploration and production wells (e.g. Knipe, 1997; Manzocchi et al., 2008b, 2010; Athmer et al., 2010; Athmer and Luthi, 2011; Fachri et al., 2013a; Botter et al., 2017). Subsurface faults are commonly interpreted on either reflection seismic data or attributes of that data by creating fault sticks on vertical cross sections (e.g. inlines ILs or crosslines XLs) which are then used to generate fault surfaces. Fault displacement is analysed by studying the interaction between the displaced horizon reflectors and the fault surface. Although this is a commonly used interpretation method, the impact of changing interpretation density (i.e. inline or crossline spacing), interpretation on vertical vs horizontal sections, and the effects of manual vs auto tracking techniques have not been systematically investigated.

The interpretation of faults in seismic data has been the focus of many studies. Badley et al. (1990) were the first to publish a systematic approach to the seismic interpretation of faults using fault displacement analysis and horizon correlations across multiple intersections. Freeman et al (1990) explained how fault displacement analysis can be used in the quality control process of fault analysis. The interpretation of fault surfaces has been quality controlled by projecting longitudinal and shear strain (vertical and horizontal components of dip separation gradient) onto fault planes and assigning realistic strain limits in order to identify inaccurate interpretations (Freeman et al., 2010). Uncertainty in fault interpretation has also been readily analysed and previous works have focused on how significant uncertainties and interpretation biases exist in 2D and 3D seismic interpretation (Bond et al., 2007, 2011; Bond,

2015; Schaaf and Bond, 2019) and the impact of the image quality of seismic data on uncertainty in seismic interpretation (Alcalde et al., 2017). Uncertainty pertaining to fault properties and the effect fault properties have on fluid flow simulations have also been analysed (Manzocchi et al., 2008a; Miocic et al., 2019).

Many techniques have extended basic fault interpretation techniques in order to better understand the link between faults in seismic and their properties in the subsurface. Dee et al. (2005) studied the application of structural geological analysis to several common industry based techniques and workflows (e.g. fault seal, fluid accumulation, migration, fault property modelling). Seismic attributes have been analysed to study fault architecture and investigate fault sealing potential (Dutzer et al., 2010). Long and Imber (2010, 2012) used interpreted seismic surfaces to measure regional dip changes in order to map fault deformation in both a normal fault array and a relay ramp. Studies such as these, combined with the increasing availability of high-resolution 3D seismic data have driven seismic structural analysis towards more detailed and quantitative studies. Iacopini and Butler (2011) and Iacopini et al. (2012) generated a workflow combining seismic attribute visualization with opacity filtering and frequency decomposition to characterize deep marine thrust faults. In a case study from the Snøhvit Field, a linkage between unsupervised seismic fault facies and fault related deformation was established and seismic amplitude was analysed to understand how folding near faults might influence near fault amplitudes (Cunningham et al., 2019).

Synthetic seismic modelling has shed important light on the impact of seismic frequency on fault imaging, the seismic amplitudes contained in and around faults and their linkage to fault related deformation and fault illumination (Botter et al., 2014, 2016a, 2016b). A comparison of faults in the Snøhvit Field with synthetic seismic showed the importance of survey geometry, azimuthal separation and frequency on fault imaging (Cunningham et al., submitted).

Fluid flow across faults, through deformed bedding and the sealing properties of faults have long been important topics in the petroleum industry (e.g. Knipe, 1997, 1992; Caine et al., 1996; Yielding et al., 1997; Fisher and Knipe, 1998; Cerveny et al., 2004; Davatzes and Aydin, 2005;

Bretan et al., 2011; Fachri et al., 2013b, 2013a, 2016; Edmundson et al., 2019). In addition, reservoir modelling techniques have been used to simulate fluid flow across faults (Fachri et al., 2013a), and synthetic seismic modelling has been used to understand the impact of faulting and fluid flow on seismic images (Botter et al., 2017).

Fault interpretation in seismic data has formed the basis of many studies over the decades but no single study has looked specifically into seismic interpretation methodologies. It would seem logical to assume that increased interpretation density will result in a higher resolution output (i.e. fault and horizon interpretation), but at the expense of the increased time required to perform the interpretation. It has yet to be fully evaluated, whether these more detailed interpretations justify this increased time and effort, or whether the end results are comparable to much more efficient interpretation strategies. Similarly, auto-tracking algorithms would appear to offer a shortcut to high-resolution horizon and fault interpretations, but how do these algorithms compare to the results of detailed manual interpretations? We address the impact of interpretation strategy on the quality of the final products and whether it is possible to identify an optimum balance between interpretation density, time required to do the interpretation, and the accuracy of the end-result.

Our study will test the effect of interpretation method (faults and displaced horizons) on aspects of fault analysis with the aim to provide geoscientists with a better knowledge of seismic interpretation/analysis of faults and an explanation of the implications of improper interpretation and best practice interpretation methods. We have designed five fault and horizon interpretation experiments which were conducted on a seismic volume case study from the Snøhvit Field, Barents Sea. The resulting surfaces from each experiment (faults and horizons) were run through a fault analysis workflow. Key aspects of the workflow include the analysis of: fault length and morphology, displacement of both faults (throw; Badley et al., 1990; Freeman et al., 1990), juxtaposed lithology (Allan, 1989; Knipe, 1992, 1997; Fisher and Knipe, 1998), dip separation gradients (Freeman et al., 2010), and finally geological modelling (i.e. Turner, 2006) and the subsequent petroleum volume calculations.

129

P3 2 Geologic Setting

The Snøhvit gas and condensate field is located in the centre of the Hammerfest Basin on the southwest margin of the Barents Sea (Fig. 1a, b: Linjordet and Olsen, 1992). The ENE-WSW trending Hammerfest basin is ~150 km long by 70 km wide and is bound in the north, southeast and west by the Loppa High, Finnmark Platform and Tromsø Basin respectively. Rifting in the basin initiated in the Late Carboniferous-Early Permian and drove the formation of the NE-SE trending basin bounding faults (Gudlaugsson *et al.* 1998). A second phase of rifting in the Late Jurassic-Early Cretaceous reactivated the basin bounding faults and caused the basin to undergo large amounts of subsidence on both the northern and southern margins (Sund *et al.* 1984; Linjordet & Olsen 1992; Doré 1995; Ostanin *et al.* 2012). Due to differential subsidence during this period, the Hammerfest Basin widened and deepened westward, allowing for the accumulation of thicker sediment packages in the west (Linjordet & Olsen 1992). A dome at the basin's central axis and a subsequent east-west trending fault system formed during basin extension in the Early Jurassic- Barremian (Sund *et al.* 1984). These east-west trending faults define the structure of the Snøhvit Field and divide the field into northern and southern petroleum provinces (Sund et al., 1984). The main petroleum system components of the Snøhvit Field are located within the Upper Triassic-Jurassic strata (Fig. 1c; Linjordet and Olsen, 1992). The focus of this study is in two of the east-west trending faults across the Snøhvit Field (Fig. 1b, blue and red lines). These two faults dip to the north, offset the Jurassic strata, and form a relay ramp structure (Fig. 1d). The area was chosen because relays are structurally complex and require special attention in their interpretation. Relays are also important in petroleum systems as they can create sediment distribution pathways, enable or disable fault seal (as all faults can), act as fluid flow pathways and finally can be a part of trap definitions (Peacock & Sanderson 1994; Knipe 1997; Gupta *et al.* 1999; Rotevatn *et al.* 2007; Athmer *et al.* 2010; Athmer & Luthi 2011; Fachri *et al.* 2013; Fossen & Rotevatn 2016; Botter *et al.* 2017b).
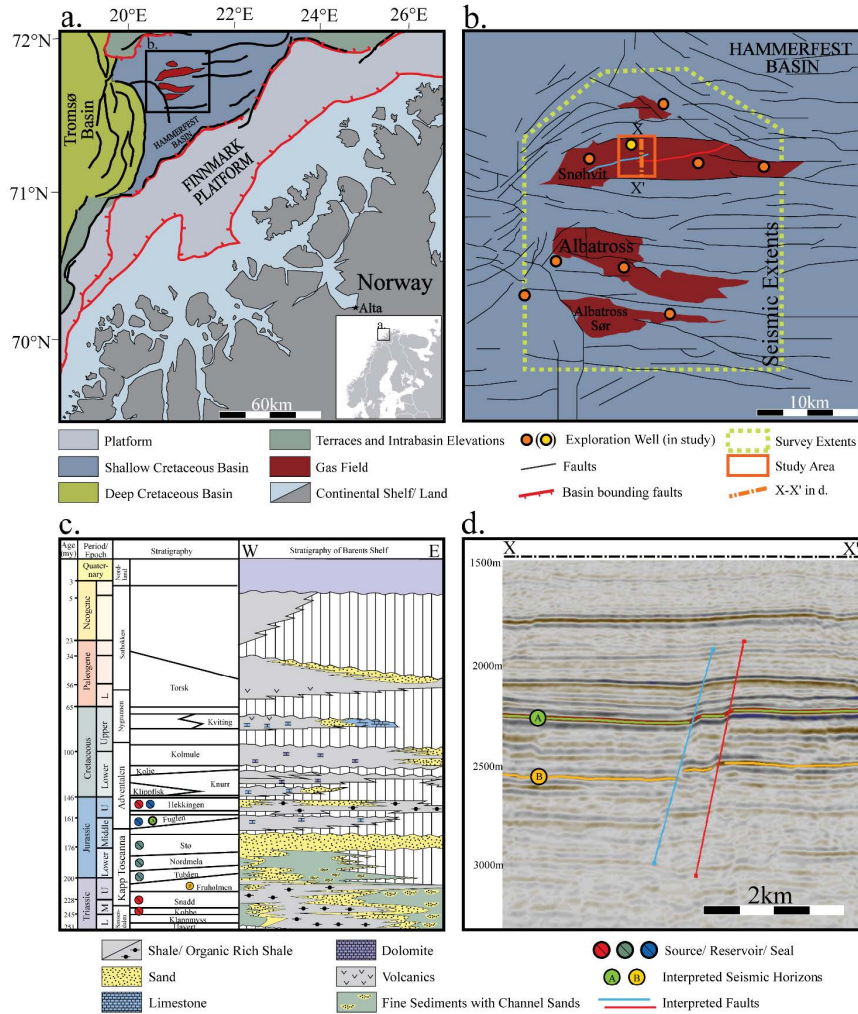
P3 Figure 1: a. Geologic setting of the Hammerfest Basin. The area in b is marked by a black box. Modified from NPD Fact maps. b. Snøhvit Field area. The dashed yellow line shows the extent of seismic data and the orange rectangle highlights the study area. Map modified from Ostanin et al. (2012). The blue background refers to the Jurassic Hammerfest Basin while the red shapes identify the areal extent of Lower-Middle Jurassic gas fields. The western and eastern fault in the study area are coloured blue and red respectively. c. Generalized lithostratigraphic column of the Barents Sea highlighting the horizons of interest. Modified from Ostanin et al. (2012). d. North-south seismic IL (3342) through the middle of the Snøhvit Field (X-X' in b) with interpreted horizons and faults. Interpreted horizons are A: Top Fuglen, and B: Top Fruholmen (c, d).

P3 3 Methodology

Five interpretation experiments (Exps 1-5) were designed to test the impact of different seismic interpretation methods on the analysis of faults (Fig. 2). Each of these experiments (Fig. 2a) was completed on a chosen 5 x 5 km area covering the relay ramp (orange rectangle in Fig. 1b) and a fault analysis workflow was applied to the interpreted seismic horizon and fault surfaces from each experiment (Fig. 2b). The fault analysis workflow (Fig. 2b) integrates a comparison of seismic interpretation results and analyses of fault length, throw, dip separation gradients (longitudinal and shear strain), juxtaposed lithology, geological modelling and a calculation of hydrocarbon volumes. While the individual components of the fault analysis workflow have been applied previously (e.g. Rippon 1985; Townsend *et al.* 1998; Wilson *et al.* 2009, 2013, Long & Imber 2010, 2012a; Elliott *et al.* 2012; Fachri *et al.* 2013), no earlier studies have considered the impact of the seismic interpretation strategy on the outcomes of the fault analysis workflow in its entirety.

The computer programs Petrel™ and T7™ (formerly Trap Tester™) were used in the seismic interpretation and fault analysis workflows respectively. The seismic dataset used in this study is survey ST15M04, a merge of five 3D seismic streamer surveys that was provided by Equinor ASA and their partners (Petoro AS, Total E&P Norge AS, Neptune Energy AS, and Wintershall DEA AS) in the Snøhvit Field, Norwegian Barents Sea. The ST15M04 volume was zero phase pre-stack depth migrated (PSDM, Kirchhoff), and both partial and full offset stacks were available. It is assumed that the velocity model used in the PSDM was correct and that the vertical scale of the processed volume (in depth) represents depth in meters. The inlines (ILs) and crosslines (XL) are spaced at 12.5 m and an increase in acoustic impedance is represented by a red peak (blue-red-blue). The interpretation was performed in depth to give the most representative view of the geological and structural relationships and to avoid re-stretching the data back into time. All five interpretation experiments were conducted on the near stack data (5-20°) as this dataset has been proven to give the most consistent fault imaging and best reflector continuity (i.e. Shuey 1985). As the data is a merge of multiple datasets and vintages, the acquisition orientations geometries
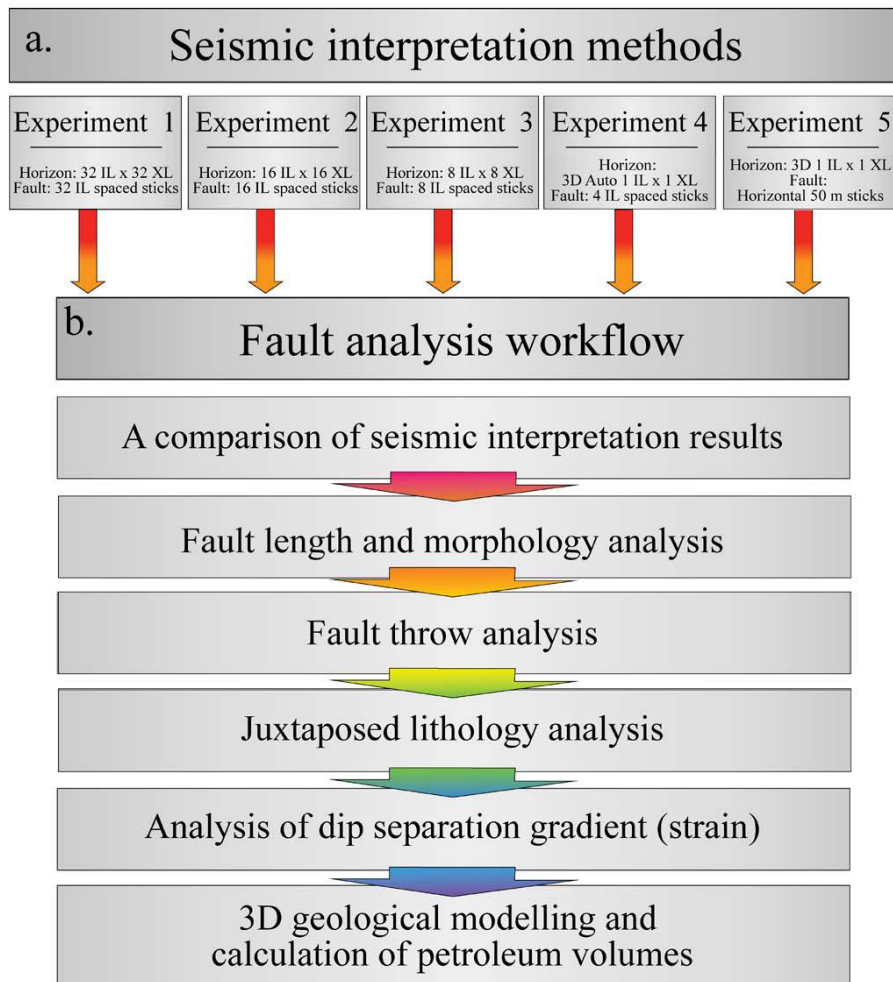
P3 Figure 2: The workflow used in this study. The fault analysis workflow (b) is completed on each of the seismic interpretation experiments (a).

could not be considered although they are known to impact fault imaging (Cunningham *et al.* 2020).
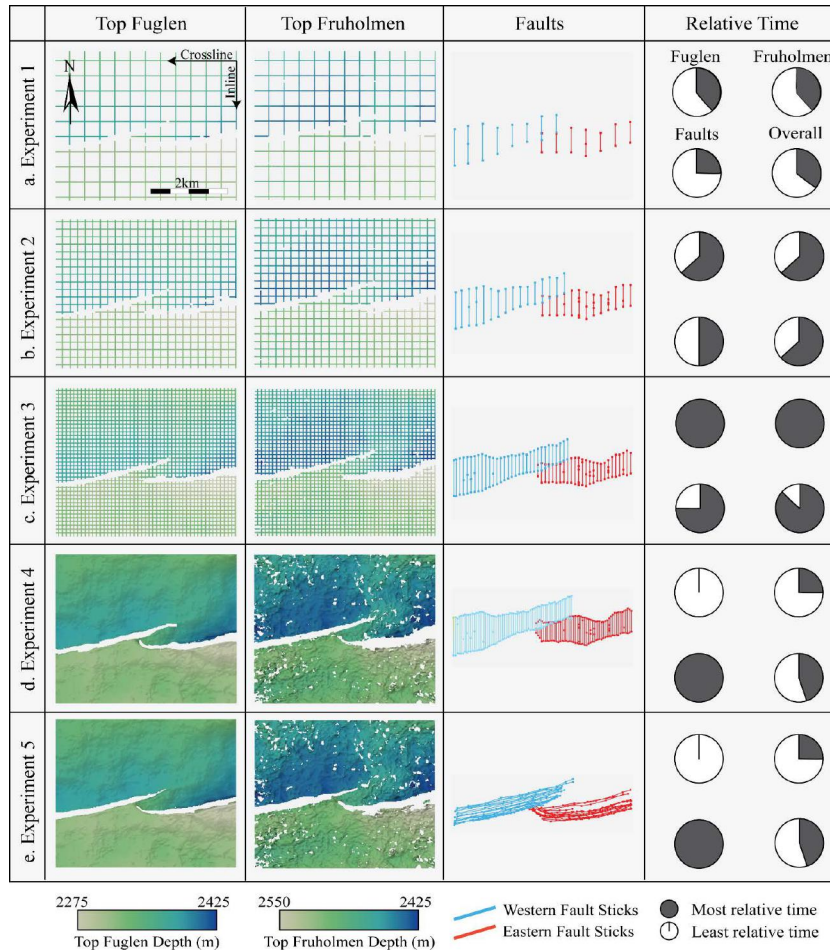
P3 3.1 Seismic Interpretation

The two east-west trending, north dipping faults that form the relay ramp were interpreted (Fig. 1b, d). These two faults are termed the western and eastern faults (Fig. 1b and d, blue and red fault respectively). Two faulted seismic reflectors (top Fuglen and Fruholmen formations; Fig. 1c-d) were also interpreted. These reflectors were chosen because the top Fuglen is a very strong, easily interpreted reflector while the top Fruholmen is poorly imaged and is more challenging to interpret. Both the top Fuglen and top Fruholmen are peaks (increases in acoustic impedance). The Stø Formation, which falls between the tops Fuglen and Fruholmen, is a prolific petroleum reservoir. Five different seismic interpretation methods (Exps 1-5) were used with the aim to systematically study how seismic interpretation techniques (Fig. 2a) influence the fault analysis workflow (Fig. 2b). The first three experiments are manual horizon interpretation techniques with different IL and XL spacing (from every 8 to 32 lines), while the fourth and fifth experiments are a combination of automated (3D auto-tracked horizons) and manual fault interpretations.

P3 3.1.1 Experiment 1 (32 x 32)

The top Fuglen and top Fruholmen reflectors were interpreted on a 32 x 32 IL (north-south) and XL (east-west) grid using 2D auto-tracking (Fig. 3a). Fault sticks were interpreted perpendicular to the average strike of the faults on every 32nd IL and are interpreted as largely planar features (Fig. 3a, faults). The IL/XL spacing in this experiment is equal to 400 m (32 x 12.5 m).

The interpretation of the two horizons and the two faults took the least amount of time when compared to all other experiments because of the large IL/XL spacing (Fig. 3a, relative time). Overall, this experiment was the quickest but sparsest interpretation method. Since the interpretation was manually conducted on an IL and XL basis there was no QC needed for the top Fuglen due to the high quality of this reflector. In particularly

P3 Figure 3: The seismic interpretation methods for experiments 1-5. a. Exp 1: 32 x 32 IL and XL interpretation spacing, fault sticks are interpreted on 32 spaced ILs. b. Exp 2: 16 x 16 IL and XL interpretation spacing, fault sticks are interpreted on 16 spaced ILs. c. Exp 3: 8 x 8 IL and XL interpretation spacing, fault sticks are interpreted on 8 spaced ILs. d. Exp 4: 3D auto-tracking is used to interpret horizons on all ILs and XLs, fault sticks are interpreted on every 4th IL. e. Exp 5: 3D auto-tracking is used to interpret horizons on all ILs and XLs, and faults are interpreted on depth slices of the tensor attribute at a spacing of 50 m. Experiment related time estimations for the top Fuglen, top Fruholmen, the two faults and the average time taken for each experiment are displayed in the last column for each experiment.

135

dim areas, 2D auto-tracking of the top Fruholmen required more manual input and some QC.

P3 3.1.2 Experiment 2 (16 x 16)

The two horizons were interpreted on a 16 x 16 IL and XL grid using 2D auto-tracking of the peaks for each reflector (Fig. 3b). Fault sticks were interpreted on every 16th IL and are largely planar (Fig. 3b, faults). The IL/XL spacing in this experiment is equal to an interpretation spacing of 200 m (16 x 12.5 m).

The interpretations of both the horizons and faults in this experiment took twice the amount of time of Exp 1, since the IL/XL spacing is half. This experiment was ranked the second most time consuming and the second sparsest overall (Fig. 3b, relative time). Since the interpretation in this experiment is manual, a similar level of QC was needed. There is high to lower confidence in the interpretation quality of the top Fuglen and top Fruholmen reflectors, as described in Exp 1.

P3 3.1.3 Experiment 3 (8 x 8)

The two horizons were interpreted on an 8 x 8 IL and XL grid (Fig. 3c). Fault sticks were interpreted on every 8th IL (Fig 3c, faults). The IL/XL spacing in this experiment is equal to an interpretation spacing of 100 m (8 x 12.5 m).

The horizons and faults in this experiment took approximately three times longer to interpret than Exp 1. This experiment was the densest of the manual interpretation methods (experiments 1-3) and was therefore the most time consuming (Fig. 3c, relative time). The quality control and interpretation confidence of the two reflectors is as described for Exps 1 and 2.

P3 3.1.4 Experiment 4 (3D tracked method with dip-parallel fault sticks)

Horizons were tracked using the 3D auto-tracking algorithm in Petrel™, which resulted in complete interpretation coverage for the top Fuglen compared to almost complete coverage for the top Fruholmen (Fig 3d, tops Fuglen and Fruholmen). Initially we planned to apply a 3D

136

automated fault interpretation method (Adaptive Fault Interpretation; Cader 2018) for this experiment but the algorithms currently available do not provide geologically realistic fault sticks that could be used in our workflow. As a result, fault sticks were interpreted on every 4th IL to capture the densest and most geologically realistic morphologies possible (Fig 3d, faults). The IL/XL spacings of horizon and fault interpretations in this experiment are 12.5 and 50 m respectively.

The 3D auto-tracked interpretation of the top Fuglen was the fastest method as the reflector is well imaged. The top Fruholmen was a little slower to run through the auto-track due to its poor seismic imaging (Fig. 3d). As a result, the top Fruholmen required more manual guidance for the auto-track to be successful but was still faster than all three manual interpretation methods (Exps 1-3). The fault interpretation for this experiment was the most time consuming as the spacing of fault sticks was the densest (4 ILs, 50 m). Overall, Exp 4 was tied for the second fastest to interpret (Fig 3d, relative time) but also contains the highest density of interpretation lines for both the horizons and faults. The QC of the top Fuglen was completely unnecessary in this small study area as the reflector was strong and easily auto tracked. The QC of the top Fruholmen was more important since the reflector imaging is quite poor in some areas. The interpretation confidence for this case is high to moderately high for the top Fuglen and top Fruholmen respectively.

P3 3.1.5 Experiment 5 (3D Auto-tracked horizons with horizontal (strike parallel) fault sticks)

This experiment used the same 3D auto-tracked horizons as discussed in Exp 4 (Fig. 3e, tops). However, faults were manually interpreted horizontally on depth slices spaced every 50 m vertically using the tensor attribute to guide the interpretation (Fig. 3b, bottom). The tensor attribute is generated using a symmetric and structurally-oriented tensor which detects the localized reflector orientation and is sensitive to changes in both the amplitude and continuity of the seismic reflectors in question (Bakker 2002). This attribute was chosen as it is a well-known fault enhancing attribute and is widely used in fault interpretation (e.g. Botter *et al.* 2016b; Cunningham *et al.* 2019). The resulting fault sticks have a high degree of horizontal curvature as each stick traces a fault's entire lateral extent. Although the results have the same fault morphology to

Exp 4, the horizontal fault sticks look quite different to the planar dip-parallel fault sticks (Fig. 3e, Faults).

The fault interpretation for this experiment was time consuming as it required the generation of a tensor attribute prior to interpretation. Once the attribute was produced, the time to generate the fault interpretation was in the middle range of the time used for the other experiments. The interpretation confidence of the two reflectors are as described in Exp 4.

P3 3.1.6. A comparison of horizon and fault surface grids

The horizons interpretations and fault sticks were gridded into horizons and fault surfaces using the seismic 12.5 m grid spacing. The horizon surfaces were generated to stay true within 5 m of the interpretations for each of the five experiments and no post-processing smoothing techniques were applied to the horizon gridding. Fault sticks in all five experiments were made into surfaces using a 50 m triangulated surface algorithm. This method was chosen as it generated a surface that was closest to the original fault stick interpretations. The fault and horizon surfaces were used as the input for the fault analysis workflow.

To understand the relative differences between the horizons from each experiment, thickness maps were generated between the most densely interpreted 3D auto-tracked horizons (Exps 4 and 5) and the horizons generated from each of the manual based experiments (Exps 1-3). Anywhere where there is a good correlation between the auto-tracked and manual surfaces, there is very little or no thickness change, while in the case of a poor correlation, a greater range in thickness may result.

P3 3.2 Fault length and morphology

Fault length (Fig. 4a) is defined as the maximum horizontal distance of a fault in three dimensions (Walsh & Watterson 1988; Peacock *et al.* 2016). An analysis of fault length was conducted on the western and eastern faults (Fig. 1b, d) using the gridded fault surfaces. These data were extracted from the edge of the study area to the fault tipline for both faults. The data were graphically compared to understand the impact of interpretation method on fault length.
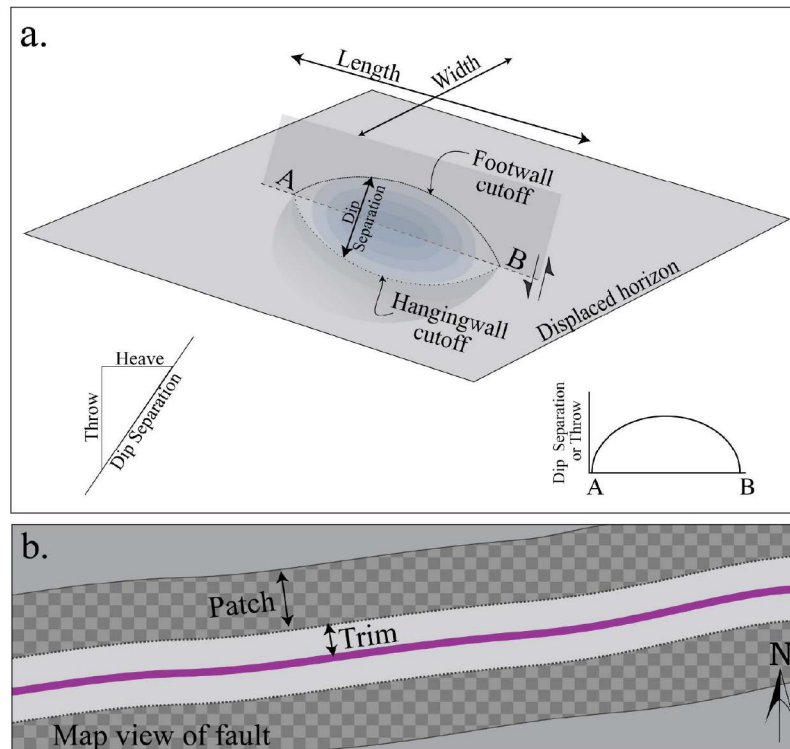
P3 Figure 4: Fault schematic and fault throw methods. a. 3D diagram of an isolated normal fault showing the field of displacement, hangingwall and footwall cut-offs, fault length and width, dip separation, throw and heave. b. Map view of a fault with trim and patch distances used in the determination of hangingwall and footwall cut-offs. The patch and trim distances used in this analysis were 150 and 75 m respectively. Concepts in this figure are based on findings from Rippon, 1985; Watterson, 1986; Barnett et al., 1987; Walsh and Watterson, 1987, 1988; Wilson et al., 2009; Elliott et al., 2012

To analyse fault morphology, the horizon surfaces described in section 3.1.6 were used. In creating the surfaces, all horizon interpretations that fall within the fault polygons were removed, leaving behind a gap in the surface where the faults' extent and morphology through that horizon are clear. These fault polygons were generated using patch and trim distances, this is explained in detail in section *3.3 Fault Throw*. The analysis of morphology considers these voids in the horizon surfaces. The graphical representations of fault throw (next section) can also be used to understand fault length.

P3 3.3 Fault throw

Fault throw is defined as the vertical component of dip separation on a fault (Fig. 4a). Fault throw along the length of an isolated fault typically follows a trend where the highest throw occurs in the centre of the fault and progressively decreases towards the tip lines ((Barnett et al., 1987; Walsh and Watterson, 1990; Fig 4a, inset). In this study, a separate fault throw analysis was created on each of the five experiments. To calculate throw, hanging wall and footwall cut-offs were produced for the top Kolje, top Fuglen and top Fruholmen in each experiment using patch and trim distances on both faults of 150 and 75 m respectively (Fig 4b). These deal with the poor seismic image close to the fault: horizon data within the trim distance are rejected, while those within the patch distance are used to extrapolate the horizon on to the fault (e.g. Wilson et al., 2009, 2013; Elliott et al., 2012). The top Kolje (Fig. 1c) was used only to help in any lithological projections in the sections to follow. This younger horizon is only partially folded at the western margin of the western fault, so it is not discussed further with respect to deformation. The cut-offs and their dip separation were then used to calculate the throw across the fault surface (Fig. 4a, bottom left inset). The results were displayed directly on the fault plane and were also graphically represented to understand how fault throw changes across each of the experiments.

P3 3.4 Dip separation gradient and strain

The dip separation gradient, and the longitudinal and shear strains are useful tools for QC seismic interpretations (Freeman *et al.* 2010). The dip separation gradient was calculated using the top Kolje, top Fuglen and top Fruholmen cut-offs. The longitudinal strain (also known as the

vertical gradient) is the dip separation gradient in the direction of fault dip while shear strain (horizontal gradient) is the dip separation gradient along the strike of the fault (Walsh & Watterson 1989; Freeman *et al.* 2010). In this study, we use the principles introduced in Freeman et al. (2010) to analyse these measurements. This can help us to understand how the different seismic interpretations strategies produce results that differ from what is considered geologically realistic and to compare how the different methods affect the value of these properties.

P3 3.5 Juxtaposed lithology

Juxtaposed lithology (a.k.a. Allan diagram) is a representation of the hanging wall and footwall lithology and their juxtaposition on the fault plane (Allan 1989; Knipe 1997). To calculate juxtaposed lithology (JL), horizons, faults and a well (NO 7120/6-1, Fig. 1b, d) containing lithological information were used. JL was calculated using the resulting horizon and fault surfaces from the five experiments. The key lithological units were defined in the well using a combination of logs, core photographs, information from the NPD Fact pages and post-well reports. Sonic and density logs were used to generate a well synthetic seismogram, which was tied to the seismic. Using the same hanging wall and footwall cut-offs as in the fault throw analysis, and the interpreted horizons as guiding surfaces, the well lithologies were projected onto the faults, and used to generate a JL (Allan) diagram.

P3 3.6 Geological modelling and hydrocarbon volume calculations

The geological modelling and volume calculations were conducted on the least and most densely interpreted experiments (Exps 1 and 4). This analysis was completed using a combination of structural and property modelling workflows in Petrel™ and the 5 x 5 km study area was considered to represent the limits of the hydrocarbon field. Firstly, fault and horizon surfaces from Section 3.1 were used to create a structural model for each experiment (Fig. 5a). A 3D corner-point grid was generated, and the cells were then populated between the top Fuglen and top Fruholmen horizons using a grid cell size of 12.5x12.5x1 m (i, j, k direction) matching the resolution of the original horizon surfaces (Fig. 5b). These two horizons define the main reservoir interval

141
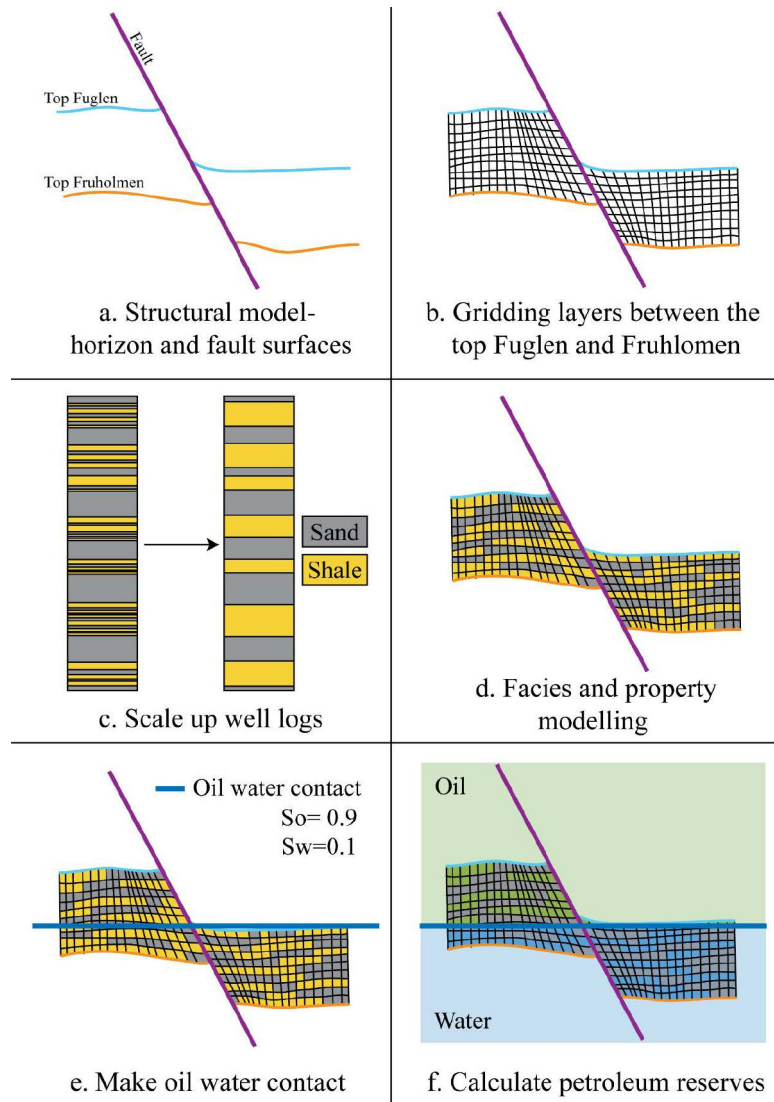
P3 Figure 5: Reservoir modelling and calculation of petroleum volumes method. a. The creation of the structural model. b. Establishing gridded layers between the top Fuglen and top Fruholmen. c. The upscaling of well logs from well 7120/6-1. d. Populating facies and properties such as porosity into the individual grid cells using the upscaled well log data. e. Drawing an oil water contact across the study area. This OWC simulates a spill point at the lowest point of the top Fuglen. f. Running the calculation of petroleum volumes.

(Fig. 5e; Linjordet & Olsen 1992; Ostanin *et al.* 2012). In the depth (k) direction, the cells were divided using the proportional method with an approximate thickness of 1 m (~250 cells in total between the top Fuglen and Fruholmen horizons). The grid follows the shape of the interpreted horizons precisely and the grid pillars align with the fault dip, making an accurate geological representation (Fig. 5b). The faults were included into the grid as zig-zag faults, meaning they were not precisely represented in i and j, but the detailed grid resolution cancelled out most of this effect. Facies and porosity data (Fig. 5c) were upscaled from the logs of a single well (NO 7120/6-1) to the grid cells at the well locations and then populated across the structural models for each experiment. The facies were extrapolated using the sequential indicator simulation method (Fig. 5d). For simplicity, all sands were considered to be net reservoir. A constant oil saturation of 0.9 was used over the whole model for cells located inside the oil-leg. Finally, an area wide oil-water contact (OWC) was placed at a depth of 2420 m, the deepest point of the top Fuglen surface within the model area, to simulate a spill point with a footwall trap. Volumes were calculated, including gross rock volume, pore volume and in-place hydrocarbon volume (STOIIP) for both Exps 1 and 4 (Fig. 5f). This simplified modelling was used to quantify the effects of interpretation methodology on the hydrocarbon related volume calculations.

For the volume calculations, there was a concern that any differences between Exps 1 and 4 might be caused, or at least exaggerated, by the stochastic facies and porosity modelling. Different facies and porosity realizations will result in different volumes. We needed to be certain that any variations in volumetric were caused by the different interpretation methods and not the stochastic property modelling. Several options were examined to negate this possibility. As the grids are identical in their i, j, k dimensions, it was expected that Petrel™ would produce the same realization in the 2 grids when the same seed number was selected; this proved to be an incorrect assumption. The method selected to make sure that the same realizations were being used, and to ensure that an extreme case was not being selected, was to 1) generate 100 realizations on the Exp 1 grid, 2) copy all 100 realizations to Exp 4 grid and 3) then run volumetric analysis on all realizations for both grids. Once the volumes had been calculated for 100 realizations on each grid, they were analysed

to determine the average volumes. This negated the possibility of selecting an extreme case. Using the same set of realizations in the 2 experiments, meant that the differences in volumes could be assigned, with certainty, to the differences in interpretation methods used.

P3 4 Results

P3 4.1 Seismic Interpretation

Five seismic interpretation experiments (Fig. 3) were analysed to understand the effect that the interpretation methodology has on the resulting fault and horizon surfaces.

Firstly, it is important to consider the areal coverage and visible patterns contained in the interpretation before being gridded into surfaces (Fig. 3). When analysing the interpretation of the top Fuglen and top Fruholmen, Exps 1 to 4 have an increase in interpretation density (the horizon interpretation of Exps 4 and 5 is the same; Fig.3 a-d). All the horizon interpretations show the same general trends in topography, but as expected the topography is more detailed and most sharply defined on the most densely interpreted data (Exps 4 and 5; Fig. 3d, e). The top Fuglen is the most clearly imaged reflector which resulted in complete interpretation coverage in all experiments (i.e. no gaps in the interpreted lines; Fig. 3). The clear imaging of this reflector is especially evident in the auto-tracked horizon in Exps 4 and 5 (Fig. 3, top Fuglen). The top Fruholmen is a poorly imaged reflector which consequently resulted in gaps in the interpreted lines (Fig. 3, top Fruholmen). The areas lacking interpretation of this reflector are evident in all experiments but are most clear in the auto-tracked horizon (Fig. 3 d, e; top Fruholmen). The fault polygons for the two horizons do appear to have the same general trends but this will be discussed in detail in the next section.

The horizon and fault interpretations were gridded into surfaces. The horizon surfaces show the same general patterns with respect to topography in all the experiments (Fig. 6). Generally, all top Fruholmen structure maps show a topographic low on the north (hanging wall) side of each fault. The footwall blocks are uplifted relative to the hanging walls and the points of highest elevation are located adjacent to the faults (Fig. 6, top Fruholmen). In the top Fuglen surface, the same overall

144
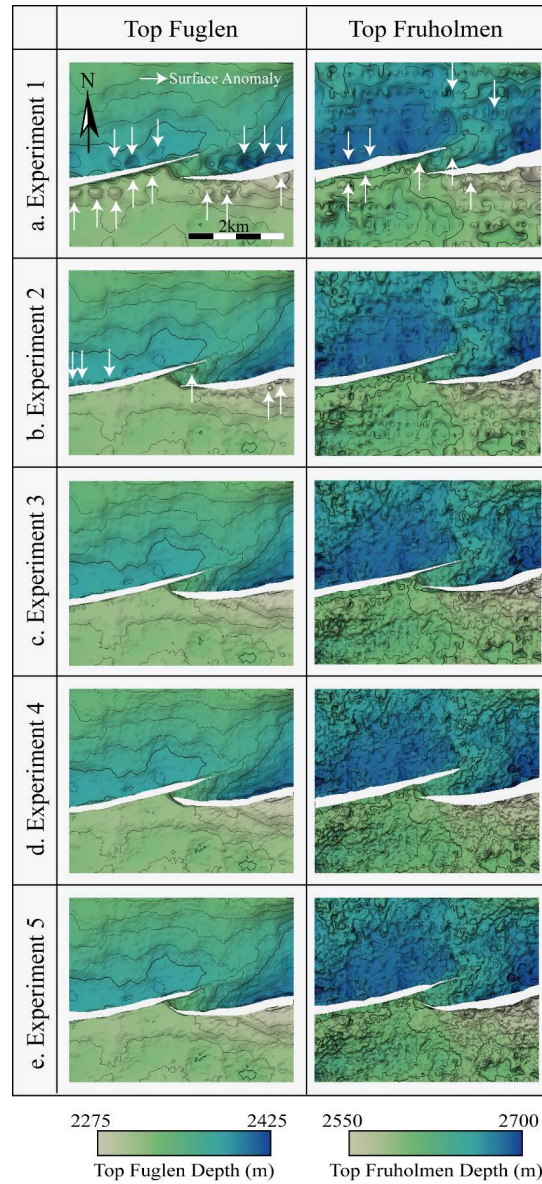
P3 Figure 6: Structure maps of the two interpreted horizons top Fuglen and top Fruholmen (left and right columns respectively). a. Exp 1 (32 IL x 32 XL interpretation, every 32nd IL faults), b. Exp 2 (16 x 16, every 16th IL faults), c. Exp 3 (8 x 8, every 8th IL faults), e. Exp 4 (3D auto-tracked horizons, every 4th IL faults,). d. Exp 5 (3D auto-tracked horizons, every 50 m depth slice).

topographic patterns are evident, but the amount of footwall uplift and depth of topographic lows on the hanging wall are less than on the top Fruholmen surface (Fig. 6a). The greatest differences between the experiments occur in areas where the lateral continuity of the interpretations were disrupted due to the presence of a fault, where horizon interpretations do not continue across the fault plane and when the interpretation density was low (Exps 1-3; Fig. 6a-c). In these cases, it is possible to identify topographic features near the faults which are clearly artefacts (Fig. 6a-b; Exps 1-2).

To better visualize the surface anomalies, thickness difference maps were generated between the surfaces of Exps 1-3 and the most densely surfaces of Exps 4-5. Visual inspection indicates that surfaces 1-3 all contain interpretation anomalies. The difference maps show a decrease in thickness difference with increasing interpretation density (Exps 1 to 3). The maps also show that the top Fuglen surfaces are a closer match to the auto-tracked horizon than the top Fruholmen (Fig. 7).

Exp 1 shows the most significant differences from the 3D auto-tracked horizons due to a sparse interpretation grid and the introduction of gridding anomalies (Fig. 7a). The thickness anomalies in both the top Fuglen and top Fruholmen can measure +/-30 m from the 3D auto-tracked surface and the anomalous areas are up to 400 m wide and long (i.e. comparable to the interpretation spacing; Fig. 7a). The top Fuglen from Exp 1 correlates moderately well in unfaulted areas and all the major anomalies occur close to the faults (Fig. 7a, top Fuglen). On the hanging wall side of the faults the anomalies are predominantly depressions (i.e. sparse interpretation grid generates a surface that is too deep), while on the footwall side the anomalies trend upward (i.e. the surface from the sparse grid is too shallow). The top Fruholmen from Exp 1 is more anomalous across the entire surface; there is no clear correlation between the tendencies of the anomalies on the hanging wall and footwall (Fig. 7a, top Fruholmen). The areas of divergence occur at the gaps between interpreted ILs and XLs.

Exp 2 exhibits much less significant changes in thickness with respect to the auto-tracked horizons on both the top Fuglen and top Fruholmen (Fig. 7b). For the top Fuglen, a pattern like Exp 1 is observed; most thickness anomalies occur near the faults and correspond to gaps in the
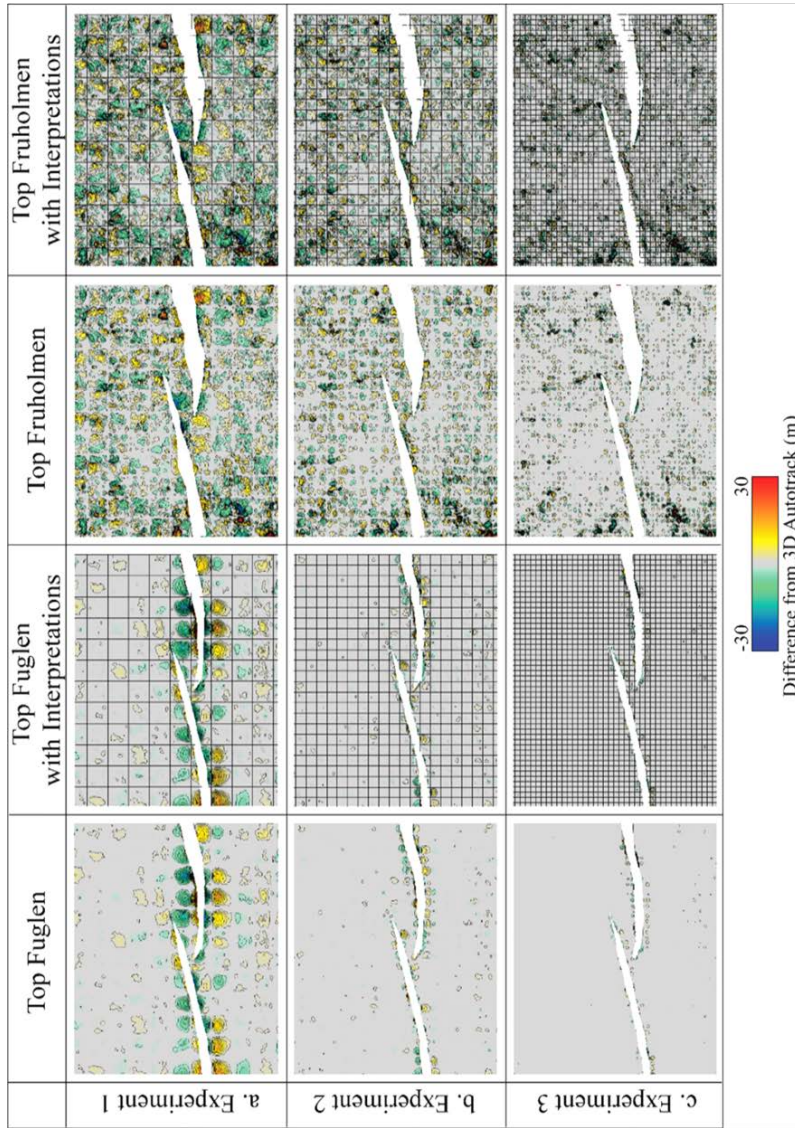
P3 Figure 7: Difference maps of the horizon surfaces for the top Fuglen and top Fruholmen in experiments 1 (a.), 2 (b.) and 3 (c.). The auto-tracked horizon surfaces in Exps 4/5 are the best-case scenario. Difference maps were computed by subtracting the experiments' interpreted horizons from the auto-tracked horizons.

147

interpretation (Fig. 7b, top Fuglen). The top Fruholmen is more chaotic, but in this case the anomalies are smaller (up to 200 x 200 m) and exhibit smaller thickness differences (+/-15 m) than in Exp 1. Like in Exp 1, the thickness differences in both the top Fuglen and Fruholmen correlate with gaps in the interpretation.

Finally, the thickness anomalies for Exp 3 show the same trends as in Exps 1 and 2, but again they are smaller in area (up to 100 x 100 m) and magnitude (+/-5 m; Fig. 7c). The anomalies occur at points of gaps in the interpretation. The thickness anomalies in the top Fuglen are almost always observed near the faults while those on the top Fruholmen are more widespread across the whole surface (Fig. 7c). It is important to keep in mind that the top Fuglen has complete areal coverage in the study area while the top Fruholmen does not. In Exps 1-3, the thickness anomalies in the top Fruholmen structure maps are in some instances linked to inconsistencies in the auto-tracked horizon.

P3 4.2 Fault length and morphology

Fault polygons were displayed on structure maps (Fig. 6) and plotted graphically (Fig. 8, 9) to show how fault length and morphology changes with the interpretation method. Generally, fault length on the interpreted horizons increases with interpretation density from Exp 1 (shortest faults) to Exp 4/5 (longest faults). These observations are clear for both the top Fuglen (Fig. 8a, b) and the top Fruholmen (Fig. 8c, d). In Exp 5 (horizontal fault sticks), the eastern fault is longer than the fault interpreted by vertical fault sticks in Exp 4, while the western fault is shorter than in Exp 4 (Fig. 8).

The morphology of the faults also changes with interpretation. In Exp 1 there is a minimal amount of interaction between the two very straight faults forming the relay (Fig. 6a). In Exp 2 the faults are also straight and do not appear to interact (Fig. 6b). In experiments 3 to 5 the northward curvature and lengthening of the eastern faults towards the western fault increases, which suggests that the relay is close to breaching or may even be breached (Fig. 6c-e). This near breach relay is evident in the top Fuglen for Exps 4 and 5 but is less prominent in the top Fruholmen (Fig. 6d, e).
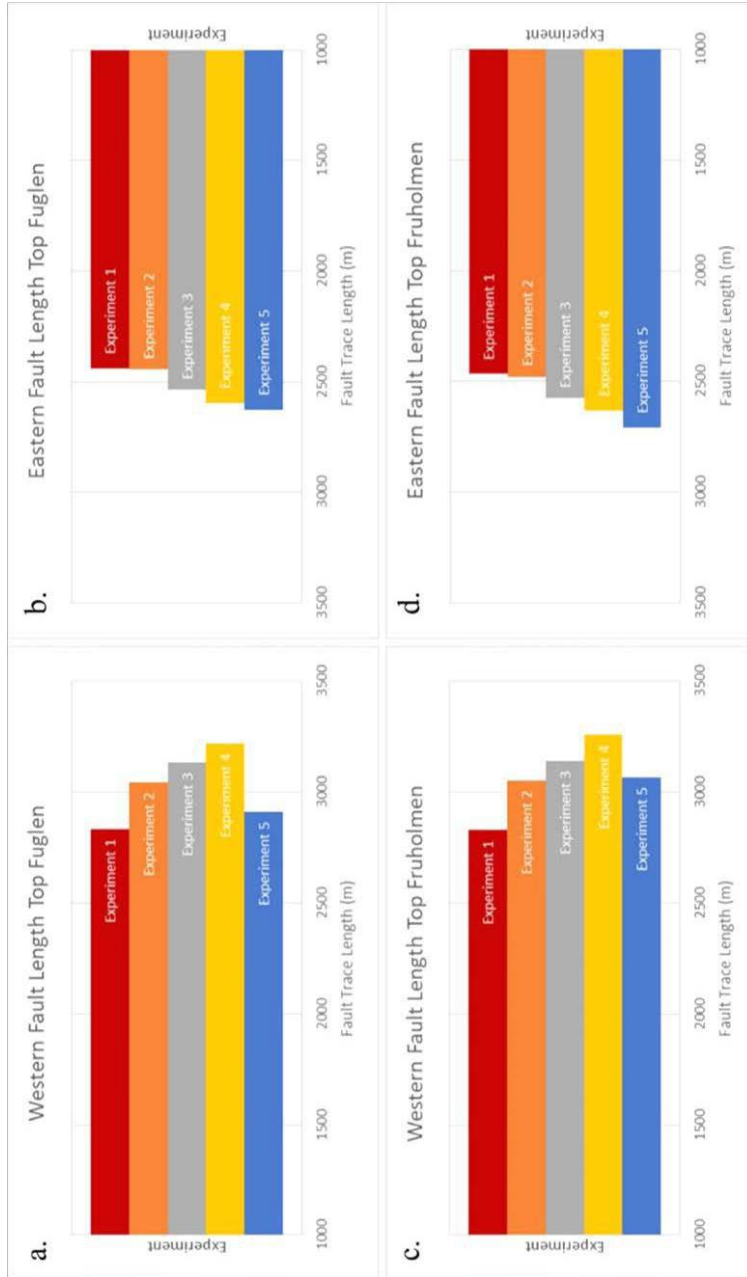
P3 Figure 8: Fault trace lengths of the western and eastern faults for the top Fuglen (a., b. respectively) and the top Fruholmen (c., d. respectively).
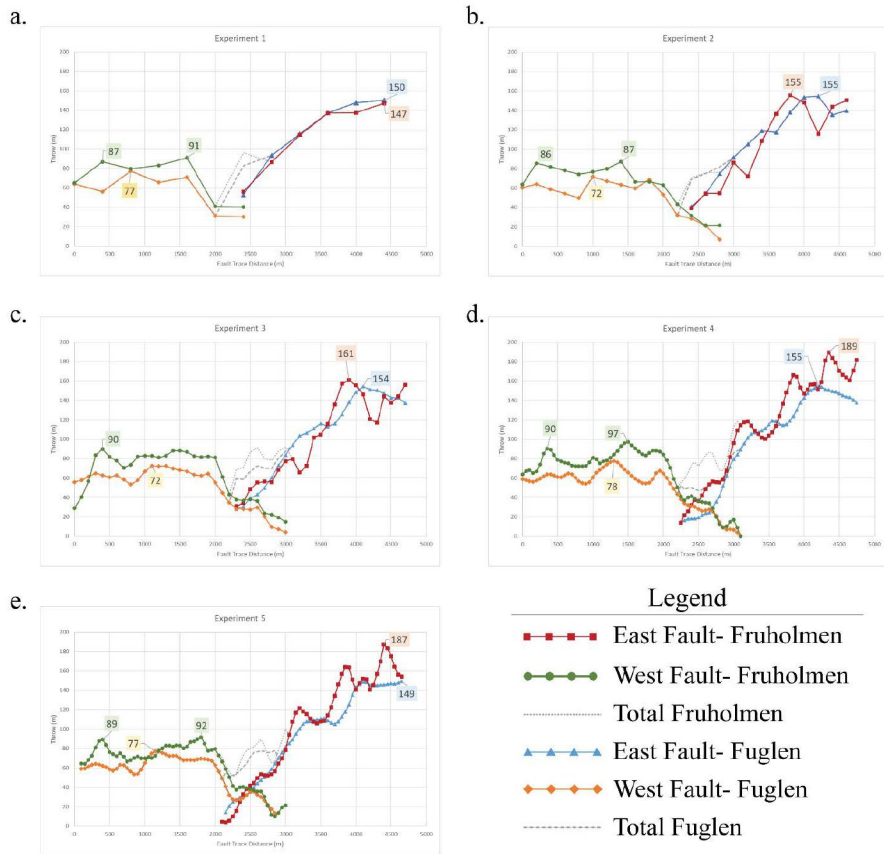
P3 Figure 9: Graphs of fault throw for Exps 1-5 (a-e). Fault throw was extracted for each experiment to match the spacing of the interpreted fault sticks. In Exps 1 (a.), 2 (b.), 3 (c.) and 4 (d.), the fault throw was extracted at 400, 200, 100, and 50 m, respectively. In Exp 5 (e.), the fault sticks are horizontal. Since it is not possible to extract the fault throw horizontally, the same sampling interval used in Exp 4 (50 m) was used.

The effect of interpretation method on fault length is clearly seen in the graphical representation of fault trace distance versus fault throw (Fig. 9). The data in these graphs were sampled on the interpreted fault sticks and show that in Exp 1 there is minimal overlap between the two faults, and the amount of overlap increases towards Exp 4 (Fig. 9a-d). For Exp 5, fault trace distance versus throw shows that the eastern fault is longer while the western fault is shorter than Exp 4 (Fig. 9e), which confirms our observations from Fig. 8.

P3 4.3 Fault throw

Fault throw contours from all five interpretation experiments exhibit in general consistent patterns (Fig. 4a) on the eastern and western faults, but also some bullseye patterns (Fig. 10a). The western fault has similar throw magnitudes across all experiments. The lowest throws occur on the eastern margin and the highest throws (up to 100 m) on the western side. With increasing interpretation density, the throw results for this fault appear smoother and more laterally extensive. For example, in Exp 1 the western fault shows three separate bullseye patterns while in Exps 2 to 4 it shows a progressively smoother throw distribution (Fig. 10a). For the eastern fault, the throw patterns are similar between experiments, but the throw magnitudes increase with increasing interpretation density (Fig. 10a). In Exp 1, fault throw reaches a maximum of ~150 m on the eastern side of the fault. For Exps 2 and 3, the results have slightly higher maximum throw (~175 m) but are segmented into geologically unrealistic bullseye patterns (Fig. 10a). In Exp 4, the maximum throw of the eastern fault is up to 200 m and the results are more concentric, smoother, and geologically realistic than in Exps 1-3. Exp 5 (fault sticks interpreted on depth slices) shows similar patterns to those observed in Exp 4 but with more irregularities.

Fault trace distance versus throw also illustrates how fault displacement is influenced by the interpretation method (Fig. 9). As discussed before, the fault throw of all experiments is greater on the edges of the study area than near the relay (centre of the graphs in Fig. 9). For the western fault, the top Fruholmen is always displaced more than the top Fuglen. For the eastern fault, the top Fruholmen is displaced more than the top Fuglen in Exp 4/5 (Fig. 9d, e) but exhibits similar throws to the top Fuglen in Exps 1-3 (Fig. 9a-c). In all experiments the throw distributions for the top
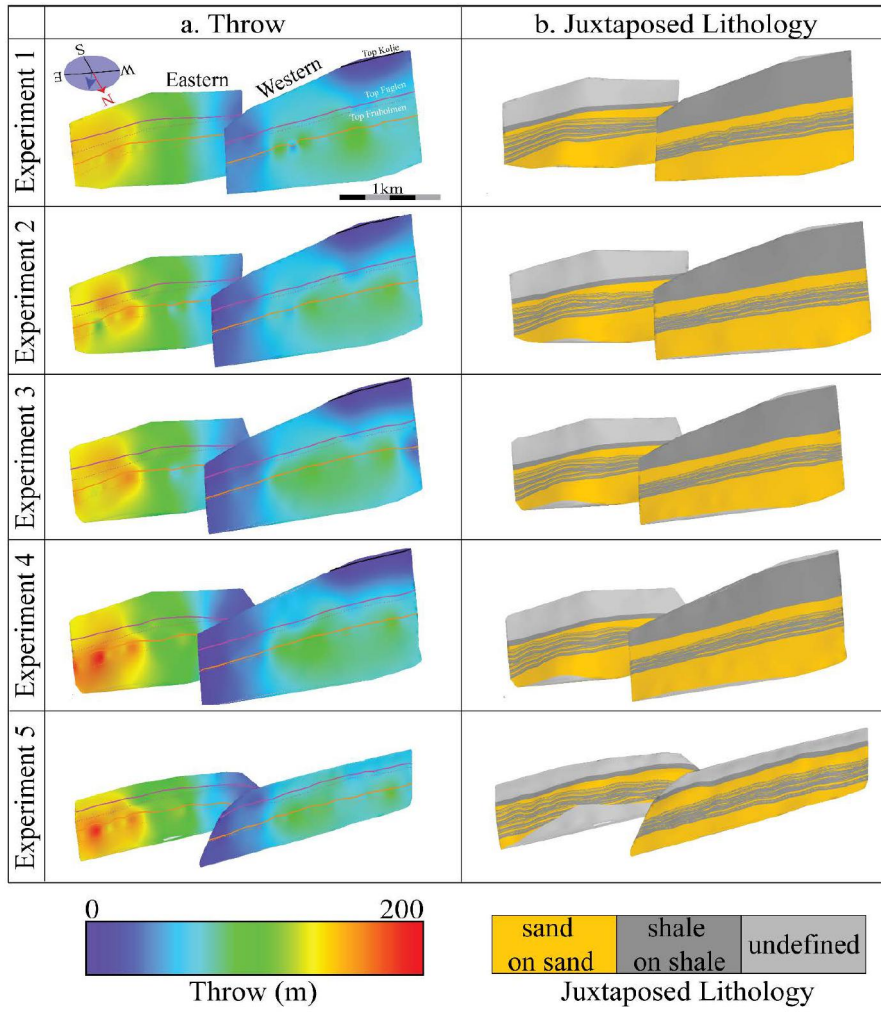
P3 Figure 10: Fault plane projections of. a. fault throw and b. juxtaposed lithology. The projections are imaged on both the eastern and western faults for all the Exps 1-5.

Fuglen are smoother than those for the top Fruholmen. This smoothness is also observable in the throw fault plane projections where the bullseye patterns occur on the top Fruholmen level. The highest throw values for the eastern fault at the top Fruholmen in Exps 1-5 are ~147, 155, 161, 189 and 187 m respectively. These values occur near the eastern margin of the study area (Fig. 9). For the western fault, the top Fruholmen peak throw values in Exps 1-5 are ~91, 87, 90, 97, and 92 m respectively. However, these peaks do not always fall near the western edge of the study area as the western fault is relatively constant in throw outside the relay (Fig. 9). The top Fuglen throw on the eastern and western faults has a similar distribution as observed for the top Fruholmen (Fig. 9). At the top Fuglen level, the eastern fault has maximum throws of ~150, 155, 154, 155, 149 m, and the western fault has maximum throws of ~ 77, 72, 72, 78 and 77 m, for Exps 1-5 respectively. Figure 9 clearly shows that the trends of throw for Exp 1 are overly smooth, while those of Exps 2-4 are similar. Exp 5 shows more or less the same result as Exp 4 with slight changes due to the extent of the faults.

P3 4.4 Juxtaposed lithology

Lithology data projected on to the fault planes can help us to understand how interpretation methods can influence the evaluation of reservoir juxtaposition and the potential for fault sealing. All experiments were populated with the same lithological data from well NO 7120/6-1 (Fig. 1b, yellow dot), the only variation is the interpretation method. On a broad scale, the juxtaposition diagrams for the five experiments look very similar on both the eastern and western faults (Fig 10b). The uppermost section of the faults is characterized by shale-shale juxtaposition (dark grey, western fault) or has not been characterized due to a lack of conformable top Kolje distribution on the eastern side of the study area (light grey, eastern fault). The next unit down is a homogenous sand-sand interval followed by a shale-shale section at the fault centres that is segmented by thin sand-sand units. Finally, the deepest lithology juxtaposition is another homogeneous sand-sand. On closer examination however, comparison of the different experiments reveal that the lateral extent and definition of the intra-shale sand overlaps improve with increasing interpretation density (Fig. 10b). This is especially true when comparing the least dense seismic interpretation (Exp 1) to the densest

(Exp 4). Exp 5 follows the same pattern as Exp 4 in areas where the juxtaposed lithology ran smoothly, but there are some issues with the juxtaposition (light grey triangle at base of eastern fault, Fig. 10b). This anomaly is caused by the horizontal interpretation of the fault on depth slices resulting in some sections of the fault having vertical dips. It is not possible to generate juxtaposition diagrams in these vertical fault areas.

P3 4.5 Dip slip gradients (longitudinal and shear strain)

Dip separation gradient (DSG), longitudinal and shear strain (Freeman et al., 2010) were calculated to understand variations in interpretation confidence between the experiments. The results of dip separation gradient are similar across all five experiments (Fig. 11a). In general, the largest DSG (> 0.2) occur at the top Fruholmen level. The western fault has a larger distribution of high DSG values in the western top part (0.125 gradient), and a main bullseye on the eastern side (Exps 1, 3-5; Fig. 11a). The eastern fault has the same 3-4 bullseyes occurring in all experiments, but Exp 1 has the lowest DSG values.

The longitudinal strain (LS) patterns are similar to those observed in the DSG results (Fig. 11b). The colour bar for longitudinal strain is set so any values outside a geologically realistic threshold (Freeman et al., 2010) occur as red (LS, > 0.1) or purple (LS < -0.1). The results for LS for all experiments are similar and exhibit values that are within the defined threshold. In the western fault for Exp 1, unrealistic LS values at the top Fruholmen level on the eastern side, suggest a problem with the interpretation (Fig. 10b, top row). This problem is not present in the other experiments. High (green) LS values in the western upper half of the western fault in Exps 1-4 are within the acceptable threshold (Fig. 10b). These high values coincide with the area between the top Kolje and top Fuglen. The eastern fault has the same LS bullseyes across its centre as observed in DSG, but they are mostly within the established threshold. In Exps 4 and 5, there are two above thresholds high (red) LS areas at the top Fruholmen level (Fig. 11b, black asterisks). All areas above threshold LS values (red, pink) are less than 250 m across.

For the shear strain (SS), the colour bar is also set to display geologically unrealistic values (+/- 0.05; red and pink, Fig. 10c) (Freeman et al., 2010). Although SS highlights more problematic areas and places more
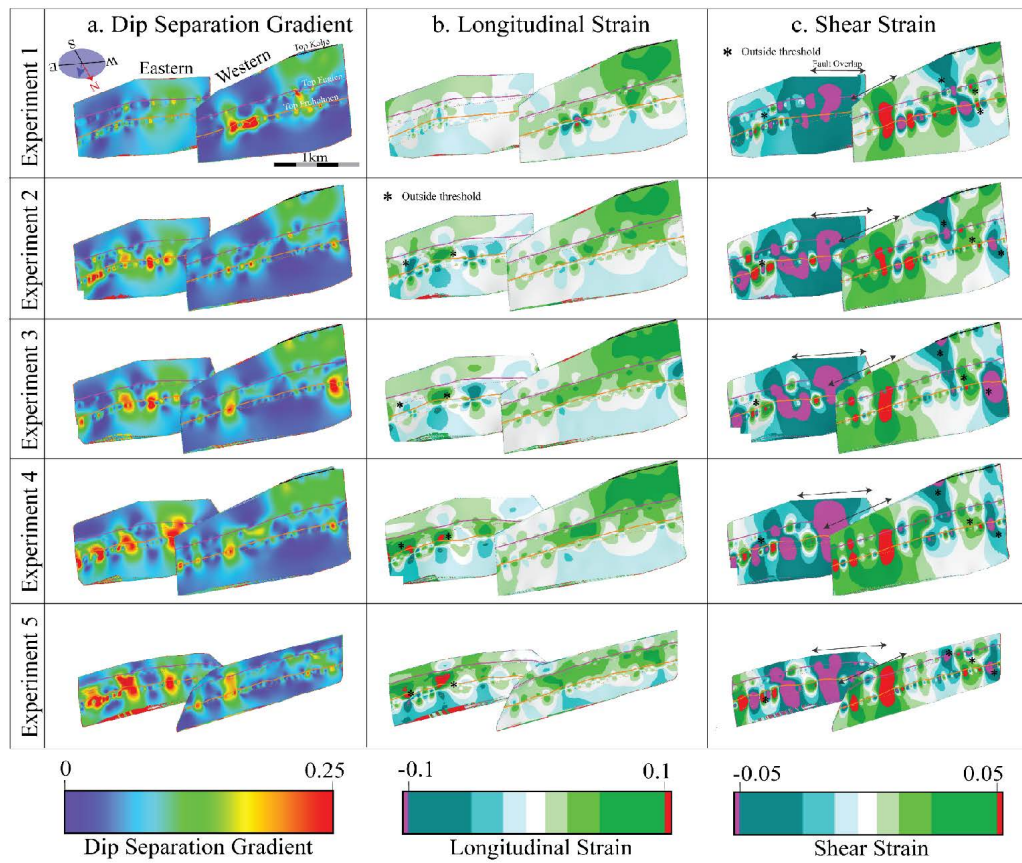
P3 Figure 11: Fault plane projections of a. dip separation gradient, b. longitudinal strain and c. shear strain. The projections are imaged on both the eastern and western faults for all the Exps 1-5.

stringent constraints to the interpretation, it indicates extreme highs and lows of SS at the overlap of the western and eastern faults respectively (Fig. 10c, black arrows). The overlapping sections of the fault are more laterally extensive from Exp 1 through to 5, which is reflected in the lateral extent of extreme SS. Localized (> 250 m) SS bullseyes highlight some slight interpretation problems discussed before in relation to LS (Fig. 11c, black asterisks). Due to the high degree of similarity between the experiments no attempt has been made to analyse SS variations any further.

P3 4.6 Reservoir modelling and hydrocarbon volume calculations

In order to test the implications of interpretation techniques on hydrocarbon volume calculations, the least and most densely populated experiments (Exps 1 and 4) were input through a geological modelling workflow (Fig. 5). A 5 x 5 km geological model was generated for each experiment (Fig. 12a, b) and used to calculate the bulk rock volume, pore volume and STOIIP (Fig. 9c, d).

There are significant differences in fault morphology, horizon resolution and lithology distribution between the two geological models. In Exp 1, the surface anomalies observed in the structural maps (section 4.1, Fig. 6 arrows) are also evident in the 3D grid at the top and base of the gridded interval (Fig. 12a, Inset a, label 1). Since the top Fuglen and Fruholmen are used as the input to define the top and base of the gridded interval and the cells there within, the surface anomalies also greatly impact the facies distribution in Exp 1, which undulate to match surface anomalies. These facies undulations can be observed on the exposed footwall of the eastern fault and on the eastern geological model boundary as the facies pull upwards towards the footwall (Fig. 12a, Inset a label 1). In Exp 1, there are also some problems with respect to the exposed fault planes where some shale cells have bled up and down the fault planes creating unrealistic peaks (Fig. 12 a, Inset label 2). This results in poor modelling of the relay ramp structure, although the exposed footwall and hanging wall blocks appear relatively smooth (Fig. 12a, Inset a label 3).

In Exp 4, the facies distributions do not have the same undulations that are observed in Exp 1. This result is more or less expected since these
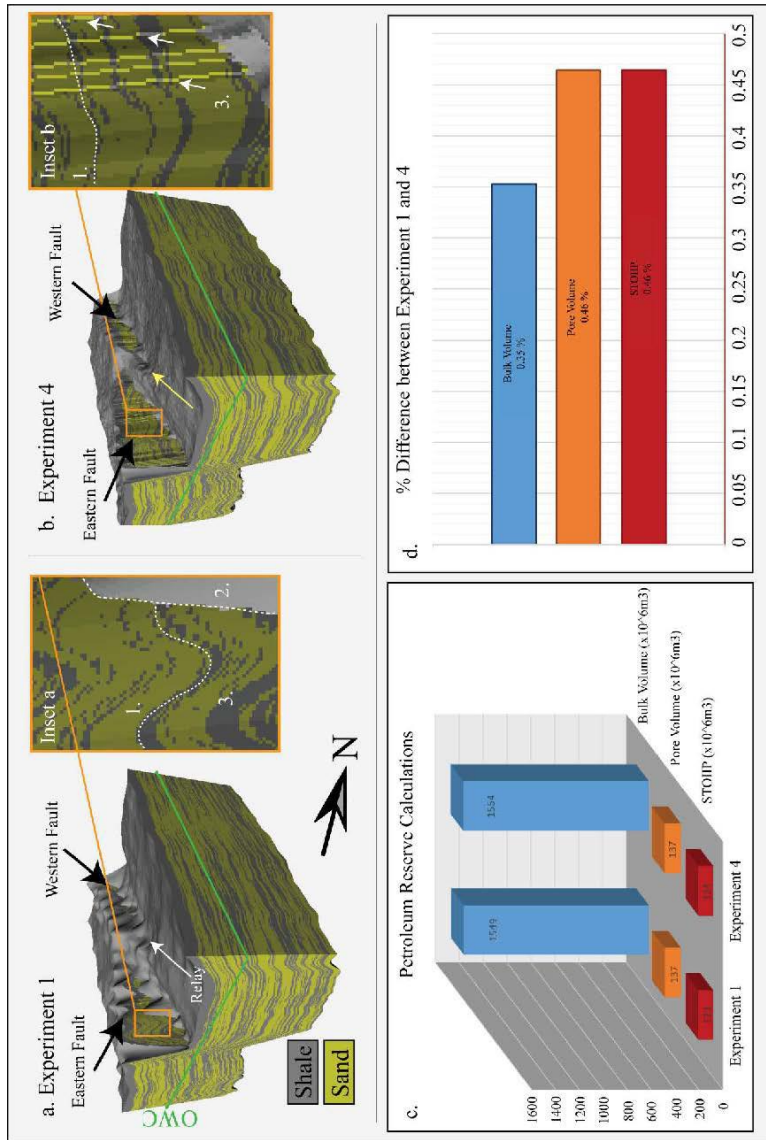
P3 Figure 12: Reservoir modelling and calculation of petroleum volumes. a. The geological model for Exp 1. b. The geological model for Exp 4. c. Graphical representation of the petroleum volume calculations for both experiments. d. Percent difference of the petroleum volume calculation between the experiments.

anomalies were not evident in the top Fuglen and Fruholmen which define the grid. Flat, more geologically representative facies distributions are clear on the uplifted footwall of the eastern and western faults and on the exposed eastern boundary of the model (Fig. 12b, Inset b label 1). A 'bleeding of facies' occurs on the margins of the model and slightly on the edges of the faults (Fig. 12b). The relay ramp is much more clearly defined in this experiment than in Exp 1 (Fig. 12b, yellow arrow). The faults are better defined with respect to length and morphology, but the high density of interpreted fault sticks means that the fault planes have vertical jumps between grid cells in the 3D grid (Fig. 12b, Inset b label 3).

Bulk rock volume, pore volume and oil (STOIIP) were calculated for both geological models, using an oil water contact of 2420 m (Fig 12a, b; OWC). This contact was chosen to mimic a spill point at the lowest point on the top Fuglen surface. The volumetric analysis was run on each of the 100 realizations, the results presented are given as their average. The stochastic facies and porosity realizations used in these calculations were identical for the 2 experiments, which allowed any volume differences to be assigned to the impact of the resolution of the interpretation. The volumetric calculations for Exp 4 were always slightly larger than Exp 1. The bulk volumes for Exps 1 and 4 are 1548.7 and 1554.2 x 10^6 m^3 respectively (a difference of 0.36%). For pore volume 136.8 and 137.4 x10^6 m^3 were calculated from Exps 1 and 4 respectively, which is a difference of 0.46%. Finally, the calculation of oil in place (STOIIP) resulted in 123.1 x10^6 m^3 for Exp 1 and 123.7 x10^6 m^3 for Exp 4 (a % difference of 0.46%).

The volumes in Exp 4 are slightly larger than in Exp 1, with the increase in the bulk rock volume carried through the pore-volume and STOIIP calculations. However, the percentage differences are very small, less than 0.5% for all metrics.

P3 5 Discussion

### P3 5.1 Implications on horizon and fault morphologies

The seismic interpretation method had a significant impact on all aspects of the fault analysis workflow. We found that both Exps 4 and 5 provided

the most geologically accurate representation of the morphologies of horizons, faults, and their intersections. The eastern fault was longest in Exp 5, while the western was longest in Exp 4 which suggests a combination of the methods (i.e. vertical and horizontal interpretation) would be the most rigorous approach to fault interpretation. The horizons in Exps 4 and 5 were quick to interpret because of 3D auto tracking and were the most detailed. When interpreting the Top Fuglen there was no need for a QC process since the imaging of this reflector was clear and the final surface did not contain any artefacts in the interpretation (Fig. 7, Top Fuglen columns). The Top Fruholmen needed some manual guidance/QC and did have some interpretation artefacts but this was unavoidable due to the poor seismic quality (Fig. 7, Top Fruholmen columns). The interpretation of faults was slightly more time consuming for Exp 5 relative to 4 but the attribute volume increased the understanding of fault morphology and length compared to Exp 4 (see Fig. 8, fault lengths). Exp 1 is here considered to be a failure with respect to observed geological morphologies and this methodology cannot be recommended as a method for fault interpretation, even though it was very time efficient. The sparsity of the horizons and fault interpretations led to inaccuracies and gridding anomalies proportional to the spacing of the interpreted inlines (400 m), reduced fault length (Fig. 8, up to 400 m difference between Exps 1 and 4, western fault), and incomplete understanding of the relay morphology. Exps 2 and 3 were an improvement on Exp 1, as expected. They captured some important information but not as much as Exp 4/5. The differences between Exps 2 and 3 were much less significant than those between Exps 1 and 2. As such, if manual interpretation of faults is required then Exp 2 should be considered as the minimum acceptable interpretation density for performing a detailed fault analysis workflow.

The two aspects of the fault analysis workflow that were the most effected by the interpretation method were fault length and throw. Both the length and throw of the faults differed dramatically depending on interpretation density which in turn had a large influence on the apparent morphologies of the faults and of the relay ramp (Figs 8-10). The knock-on effects of these are because the fault lengths and throws impact all other aspects of the workflow. Overall, comparison of the most and least densely interpreted datasets (Exps 4/5, 1 respectively) show that the

159

length, morphology and throws were different at both the Top Fuglen and Fruholmen level (Figs 7-10).

The impact of the interpretation method on the length, morphology, and throw profiles in the relay is critical to understand its formation. Fault displacement/throw relationships in relay ramps are dependent on the stage of relay development in question (Fig. 13). In the first stage of relay development, the faults do not overlap and therefore exhibit isolated fault throw profiles (Barnett *et al.* 1987; Fig. 13 a-b). Stage 2 of relay development is defined by the propagation of faults to form a relay ramp (Fig. 13c). Fractures break up the ramp (that in our case are sub-seismic resolution) and accommodate some of the strain of the relay (Larsen 1988; Peacock & Sanderson 1994). The throw profiles of the faults interact and the total throw of the overlapping fault segments is accommodated by the relay ramp (Peacock & Sanderson 1994; Fig 13d). The fault extents and throw profiles for Exp 1 (Fig. 9a, 10a) fall somewhere between stage 1 and 2, where there is a slight overlap of the faults, but a relay is only just starting to form (Fig. 6a). This is because Exp 1 does not properly capture the full length of the fault. Stage 3 of relay development is defined as when the faults have continued to propagate and fractures have begun to spread through the relay structure as it is near the maximum amount of strain it can accommodate (Peacock & Sanderson 1994; Long & Imber 2012a). The propagation of the fault tips toward the relay and increased fault overlap are evident (Fig. 13e-f). Stage 4 of relay development defines the destruction (breaching) of the relay ramp and the formation of branch lines between the two relay forming faults (Peacock & Sanderson 1994). The original tiplines of the fault are no longer active, and the faults are now joined along branch-lines formed in the weakened and sheared ramp margins (Fig 13g-h). When analysing Exp 4/5, the morphologies are comparable to those observed in stage 3 of the relay formation. The northward propagation and curvature of the eastern faults tipline is clear, and there are likely fractures forming in the relay that are below the resolution of the seismic data. The relay in Exp 4/5 has not breached on either the Top Fuglen or Fruholmen level, although it is very close to breaching in Exp 5 at the Top Fuglen (Fig. 6d/e, 9d/e, 10a). The potential impact of a relay on a working hydrocarbon system and the implications of misinterpreting the relay are discussed in the upcoming section 5.2.

160
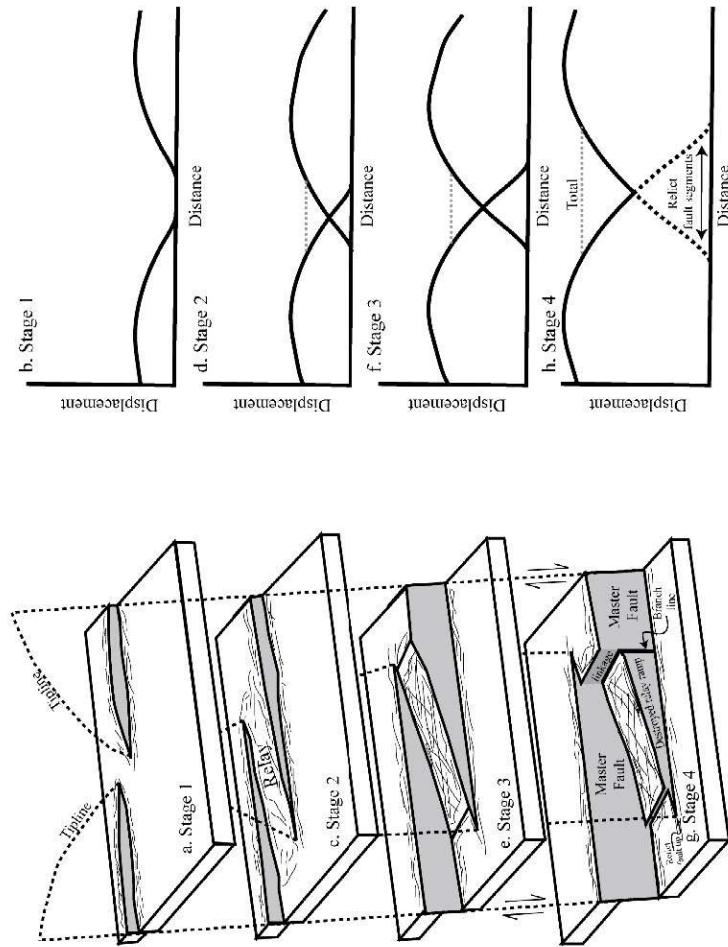
P3 Figure 13: The stages of the relay and the displacement distribution of those stages. Stage 1 (a, b), Stage 2 (c, d), Stage 3 (e, f) Stage 4 (g, h). The displacement of the isolated faults in stage 1 follows Barnett et al. (1987). Figures modified from Peacock and Sanderson (1994), Rotevatn et al. (2007), Long and Imber (2012a) and Fachri et al. (2013).

A study of longitudinal and shear strain was completed to test the accuracy of the interpretation methods (Freeman *et al.* 2010). According to Freeman et al. (2010) longitudinal and shear strain values in isolated faults should remain inside their defined threshold values (+/- 0.1 and +/- 0.05 respectively) in order for the interpretation to be deemed accurate. High and low values of longitudinal and shear strain were observed across all experiments, some of which are outside these defined thresholds (Fig. 11 b, c). There is a high and low shear strain accumulation in all experiments on the western and eastern faults respectively in the parts of the faults exhibiting overlap (Fig. 11 c). Freeman et al. (2010) stated that in the event of overlapping faults, higher shear strains (above their defined limit) are to be expected in the overlapping segments of the fault. The limits in this case are higher than could be expected from an isolated fault (Freeman *et al.* 2010). These highs and lows appear to change with interpretation density and align with the increased overlapping of the faults (Fig. 11 c, double ended black arrows). There were some bullseye patterns (longitudinal and shear strain plots) which were outside of the fault overlap and outside of the defined threshold strains, these are interpreted to be artefacts produced by incorrect fault stick interpretations (Fig. 11 b, c black asterisks). It is important to note that interpretation accuracy with respect to longitudinal strain and shear strain was not the aim when running the initial interpretations, and therefore it is expected that some inconsistencies are present.

P3 5.2 Implications and petroleum studies

### P3 5.2.1 Interpretation and aspects of the petroleum industry

Relay ramps and the faults that define them have significant impact on sediment distribution pathways (deposition of reservoirs), fluid flow/ migration pathways, fault seal/juxtaposition and trap definition (e.g. Knipe 1997; Manzocchi *et al.* 2008, 2010; Athmer *et al.* 2010; Athmer & Luthi 2011; Fachri *et al.* 2013; Botter *et al.* 2017b). By under interpreting the relay with respect to fault length and throw (as discussed in section 5.1, Exp 1) there is a clear misunderstanding of the stage of relay development, and therefore a misunderstanding of fault interactions. Exp 1 exhibits shorter faults with less throw and therefore a

less defined relay (Fig. 14, left column). This under-interpretation of the relay will also have implications on our understanding of sediment distribution pathways (Fig. 14a). Compared with the relay interpreted from Exp 4 (Fig. 14, right column), the results of Exp 1 (left column) also show: less laterally continuous extent of juxtaposed sand-on-sand resulting in different fault sealing (14b), an unsuccessful fluid flow schematic where petroleum does not migrate towards the producer well (14c), and an under estimation of trap size because of the incorrect trap geometry (Fig. 14d). These results are specific for our field area / relay morphology and of course, may differ with changing field parameters. The important thing however is that significant differences can be generated by applying an interpretation method that is unsuitable for the scale of the structures that are being analysed.

P3 5.2.2 The effect of interpretation on geological modelling

A geological modelling workflow was run on the least and most successful interpretation methods (Exps 1 and 4 respectively) in order to understand the impact of the interpretation method on the geological model. In Exp 1 it is possible to identify several clear inaccuracies and problems with the model. The problems include facies undulations which were caused by interpretation sparsity, facies bleeding on the fault planes, and the apparent under interpretation and imaging of the relay ramp due to under interpreted faults. The observed facies undulations can have significant implications if used in dynamic modelling processes such as fluid flow simulations. Since the relay is so under-interpreted in Exp 1 the results can be expected to be false. This poor interpretation can have negative implications for the development of the field, production strategies, drainage strategies and may influence the complete field understanding.

The bleeding of facies on the fault planes is caused by the low interpretation density and is easily avoided with a denser interpretation. Exp. 4 had more realistic horizon morphologies, more geologically realistic facies distributions and much less facies bleed. The only problem with this interpretation was that the inline fault stick spacing resulted in linear cell anomalies and unsmooth fault planes (Fig. 12b).
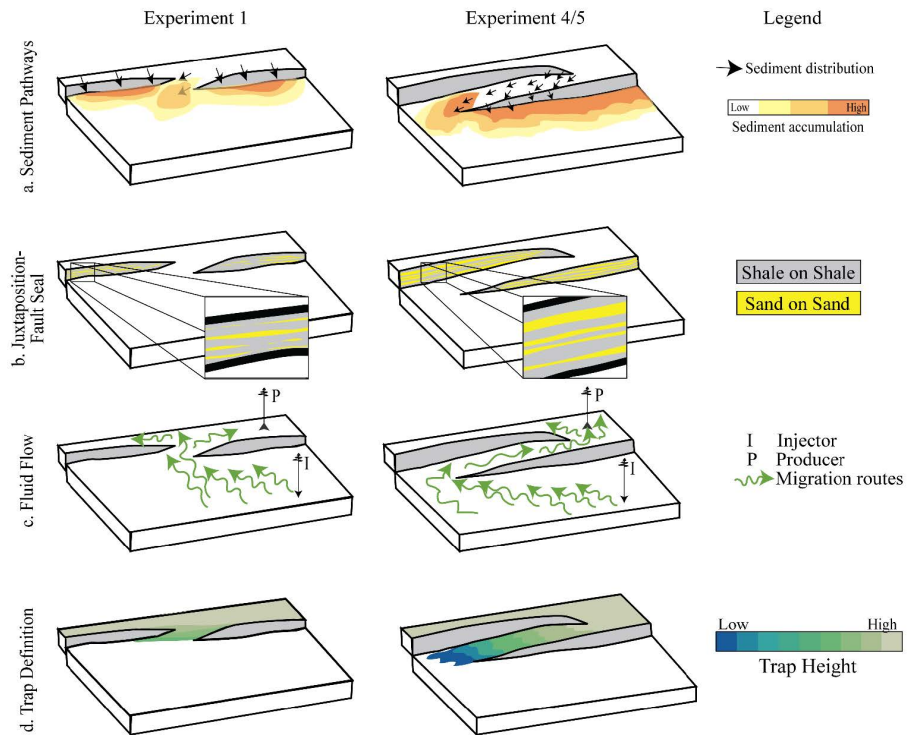
P3 Figure 14: A The comparison of sediment distribution pathways (a), lithological juxtaposition/ fault seal (b), fluid flow (c) and trap definition (d) on an under interpreted version of a relay (Exp 1, column 1) and an accurate interpretation of the relay ramp (Exp 4, column 2). Figures based on Peacock and Sanderson (1994), Knipe (1997), Rotevatn et al. (2007), Athmer et al. (2010), Athmer and Luthi (2011), Fachri et al. (2013) and Botter et al. (2017b).

Therefore, we suggest that when modelling, the removal of fault sticks in the fault's centre may provide clearer results.

Volumetric calculations using the two models revealed that the gross rock volumes were 0.35% larger in Exp 4 when compared to Exp 1 and both the in-place hydrocarbon volume (STOIIP) and pore volume calculations of Exp 4 were 0.46% greater than Exp 1. These differences are small (and certainly much less than the normal uncertainty values considered in the industry) which does suggest for preliminary field analysis/ petroleum calculations, a detailed seismic interpretation is not all that important. However, this result has significant implications when upscaled to the fields dimensions – in this case the Snøhvit Field in its entirety. For simplicity in the calculations we take the values from the Norwegian Petroleum Directorate for field size and the STOIIP in the entire Snøhvit area to be referencing an oil only field. In reality, the field contains gas, condensate and a small oil column (NPD 2020). According to the Norwegian Petroleum Directorate, the Snøhvit Field holds in place volumes of ~400 x10^6 m^3 oil equivalent (NPD 2020). A STOIIP difference of 0.46% between Exps 1 and 4 on this field size is equal to ~1.84 x10^6 m^3 oil in place. This is equal to an underestimation of ~11.6 million barrels (1 m^3 oil = 6.29 bls) of in place oil in Exp 1 versus 4. The NPD lists the recovery factor of the Snøhvit Field to be 64% (NPD 2020) so only 7.4 million barrels can be considered recoverable. Assuming an oil price of 50 USD per barrel, this difference in interpretation method is equivalent to c. 370 million USD. Although this value is relatively small in the industry, it is staggering to consider how the inaccuracy in the calculation of petroleum reserves can be solely based on poor interpretation strategies which are mistakes that are completely avoidable.

P3 5.3 Recommendations for best practice seismic interpretation

P3 5.3.1 Horizon and horizon-fault intersections

The results showed that 3D auto tracking (1 x 1 density) gave the best results in terms of detail in the structure of horizons, horizon-fault intersections (cut-offs, throw, etc.) and was the most time efficient option assuming relatively high-quality data. In the case of high-quality data

and well-defined continuous strong seismic reflectors (e.g. Top Fuglen), little manual quality control of the interpretation is required. If the seismic data is of poorer quality, or the reflector in question is poorly imaged, discontinuous or changes seismic polarity, or there is significant structural complexity and ambiguity, then it is important to reflect on the task at hand. This is because auto tracking algorithms may fail or generate artefacts or erroneous results that require significant manual adjustment to correct. If fault seal or juxtaposed lithologies are critical to the field analysis, then a denser manual/ 2D auto-tracked method might be necessary and worth the significant time commitment (i.e. 8 x 8). If detailed structural analysis is not required then a less dense (i.e. 16 x 16) grid will give sufficient results for geological interpretation, while the results of this study showed that a sparse interpretation spacing (i.e. 32 x 32) gave a geologically unrealistic and inaccurate representation of the subsurface that could lead to critical errors in prospect or field evaluations and, as such cannot be recommended except for broad-scale regional understanding. These results assume a 12.5 m IL and XL spacing and may need to be adjusted in the event of a different spacing.

P3 5.3.2 Faults

The results of Exps 4 and 5 are very similar and give the most accurate results with respect to fault extent, throw and morphology of the relay. In our experiments, it was difficult to capture the entire fault length if using less than a 4 IL spacing, but we also found interpretation on horizontal time/depth slices to be a useful tool to accurately capture fault length in its entirety. Therefore, the recommendations are to interpret faults on a minimum of 8 or 16 IL spacing for the main body of the fault, and on approaching tip lines or complex fault intersections to decrease the line spacing in order to capture the full length, morphologies and relationships. We also recommend the combination of horizontal fault sticks and attributes to understand fault morphology, fault extent and to keep track of fault locations in 3D when interpreting horizons. The results shown here demonstrate that less than 16 IL spacing was insufficient to capture critical details required when performing fault interpretations, and as such should be avoided for critical prospect or field scale mapping. These results are also assuming an IL/XL spacing of 12.5 m and may need adjustment if the data differ.

P3 6 Conclusions

This paper has analysed the effect of the seismic interpretation method on faults, horizons and their intersections and shows some of the implications of these interpretations on the results of a fault analysis workflow. The main findings are summarized as follows:

- Interpretation: The density of fault and horizon interpretations are critical to understand fault relationships and morphologies in structural maps. The 3D auto-tracked horizons and a combination of vertical and horizontal fault sticks give the best results in the relatively high-quality Snøhvit seismic data with moderate to very clear continuous seismic reflectors. However, in other areas or on poorer data, a combination of auto tracking or dense 2D interpretation grids are required to properly capture the geological complexity.
- Fault length is greatly impacted by the interpretation method. Special attention and denser interpretation are needed around fault tiplines and the least dense experiments did not capture these extents.
- The biggest effect on fault throw (and therefore much of the fault analysis workflow) was the interpretation density. If fault seal or dynamic simulation is critical, then denser vertical sticks (8-4 IL) give the most accurate morphology of faults, despite needing more time and manual QC.
- Longitudinal and shear strain are excellent tools for understanding interpretation accuracy and were proven higher in the relay (as observed in Freeman *et al.* 2010). Studies of complex faulted fields and prospects should consider implementing these methods if robust fault interpretation is critical for geological understanding.
- The example showing the effect of interpretation method on geological modelling and the subsequent calculation of petroleum reserves showed that the importance of correct interpretation should not be underestimated. The most geologically realistic results were established when using the densest interpretation (Exp 4). If using Exp 1 interpretations as the model, the results were less geologically accurate

167

(undulating facies, creeping fault cells) and resulted in an under-interpretation of the relay, all of which has implications for dynamic modelling techniques such as fluid flow simulations, production and drainage strategies.

- Calculations of petroleum reserves in the modelling resulted in an under estimation of STOIIP of 0.46% when comparing Exp 1 to 4. The upscaling of this value across the Snøhvit Field results in an under estimation of ~11.6 million barrels or ~370 million USD when comparing Exp 1 to 4. Although this seems small on industry standard, this difference is only caused by inaccuracy of the seismic interpretation method. These inaccuracies in modelling and subsequent economic analyses could be almost completely avoided by applying more robust interpretation methods.

P3 Acknowledgements

P3 References

Alcalde, J., Bond, C.E., Johnson, G., Ellis, J.F., Butler, R.W.H., 2017. Impact of seismic image quality on fault interpretation uncertainty. GSA Today 27, 4–10. https://doi.org/10.1130/GSATG282A.1

Allan, U.S., 1989. Model for hydrocarbon migration and entrapment within faulted structures. American Association of Petroleum Geologists Bulletin 73, 803–811. https://doi.org/10.1306/44b4a271-170a-11d7-8645000102c1865d

Athmer, W., Groenenberg, R.M., Luthi, S.M., Donselaar, M.E., Sokoutis, D., Willingshofer, E., 2010. Relay ramps as pathways for turbidity currents: A study combining analogue sandbox experiments

and numerical flow simulations. Sedimentology 57, 806–823. https://doi.org/10.1111/j.1365-3091.2009.01120.x

Athmer, W., Luthi, S.M., 2011. The effect of relay ramps on sediment routes and deposition: A review. Sedimentary Geology 242, 1–17. https://doi.org/10.1016/j.sedgeo.2011.10.002

Badley, M.E.E., Freeman, B., Roberts, A.M., Thatcher, J.S., Walsh, J.J., Watterson, J., Yielding, G., 1990. Fault interpretation during seismic interpretation and reservoir evaluation. The Integration of Geology, Geophysics, Petrophysics and Petroleum Engineering in Reservoir Delineation, Description and Management 224–241.

Bakker, P., 2002. Image structure analysis for seismic interpretation. Technische Universiteit Delft.

Barnett, J.A.M., Mortimer, J., Rippon, J.H., Walsh, J.J., Watterson, J., 1987. Displacement geometry in the volume containing a single normal fault. AAPG Bulletin 71, 925–937.

Bond, C.E., 2015. Uncertainty in structural interpretation: Lessons to be learnt. Journal of Structural Geology 74, 185–200. https://doi.org/10.1016/j.jsg.2015.03.003

Bond, C.E., Philo, C., Shipton, Z.K., 2011. When there isn't a right answer: Interpretation and reasoning, key skills for twenty-first century geoscience. International Journal of Science Education 33, 629–652. https://doi.org/10.1080/09500691003660364

Bond, E.C., Shipton, Z.K., Jones, S., 2007. What do you think this is? Conceptual Uncertainty in Geoscience Interpretation. GSA Today 17. https://doi.org/https://doi.org/10.1130/GSAT01711A.1, 2007.

Botter, C., Cardozo, N., Hardy, S., Lecomte, I., Escalona, A., 2014. From mechanical modeling to seismic imaging of faults: A synthetic workflow to study the impact of faults on seismic. Marine and Petroleum Geology 57, 187–207. https://doi.org/10.1016/j.marpetgeo.2014.05.013

Botter, C., Cardozo, N., Hardy, S., Lecomte, I., Paton, G., Escalona, A., 2016a. Seismic characterization of fault damage in 3D using mechanical and seismic modelling. Marine and Petroleum Geology 77, 973–990.

Botter, C., Cardozo, N., Hardy, S., Lecomte, I., Paton, G., Escalona, A., 2016b. Seismic characterisation of fault damage in 3D using mechanical and seismic modelling. Marine and Petroleum Geology 77, 973–990. https://doi.org/10.1016/j.marpetgeo.2016.08.002

Botter, C., Cardozo, N., Lecomte, I., Rotevatn, A., Paton, G., 2017. The impact of faults and fluid flow on seismic images of a relay ramp over production time. Petroleum Geoscience 23, 17–28.

Bretan, P., Yielding, G., Mathiassen, O.M., Thorsnes, T., 2011. Fault-seal analysis for CO2 storage: An example from the troll area, Norwegian continental shelf. Petroleum Geoscience 17, 181–192. https://doi.org/10.1144/1354-079310-025

Cader, A., 2018. Rapid Generation of Fault Sticks from an Existing Adaptive Fault Interpretation [WWW Document], Geoteric Blog. URL https://blog.geoteric.com/rapid-generation-of-fault-sticks-from-an-existing-adaptive-fault-interpretation (accessed 4.25.20).

Caine, J.S., Evans, J.P., Forster, C.B., 1996. Fault zone architecture and permeability structure. Geology 24, 1025–1028.

Cerveny, K., Davies, R., Dudley, G., Fox, R., Kaufman, P., Knipe, R.J.J., Krantz, B., 2004. Reducing uncertainty with fault-seal analysis. Oilfield Review 38–51.

Cunningham, J., Cardozo, N., Townsend, C., Iacopini, D., Wærum, G.O., 2019. Fault deformation, seismic amplitude and unsupervised fault facies analysis: Snøhvit Field, Barents Sea. Journal of Structural Geology 118, 165–180. https://doi.org/10.1016/j.jsg.2018.10.010

Cunningham, J., Cardozo, N., Weibull, W.W., Iacopini, D., 2020. Investigating the seismic imaging of faults using PS data from the Snøhvit field, Barents Sea and forward seismic modelling. Petroleum Geoscience submitted.

Davatzes, N.C., Aydin, A., 2005. Distribution and nature of fault architecture in a layered sandstone and shale sequence: An example from the Moab fault, Utah. AAPG Memoir 153–180. https://doi.org/10.1306/1033722m853134

Dee, S., Freeman, B., Yielding, G., Roberts, A., Bretan, P., 2005. Best practice in structural geological analysis. First Break 23, 49–54. https://doi.org/https://doi.org/0.3997/1365-2397.23.4.26500

Doré, A.G., 1995. Barents Sea Geology, Petroleum Resources and Commercial Potential. Arctic 48, 207–221.

Dutzer, J.-F., Basford, H., Purves, S., 2010. Investigating fault-sealing potential through fault relative seismic volume analysis. Petroleum Geology Conference Series 7, 509–515.

Edmundson, I., Rotevatn, A., Davies, R., Yielding, G., Broberg, K., 2019. Key controls on hydrocarbon retention and leakage from structural traps in the Hammerfest Basin, SW Barents Sea: implications for prospect analysis and risk assessment. Petroleum Geoscience petgeo2019-094. https://doi.org/10.1144/petgeo2019-094

Elliott, G.M., Wilson, P., Jackson, C.A.L., Gawthorpe, R.L., Michelsen, L., Sharp, I.R., 2012. The linkage between fault throw and footwall scarp erosion patterns: An example from the Bremstein Fault Complex, offshore Mid-Norway. Basin Research 24, 180–197.

Fachri, M., Rotevatn, A., Tveranger, J., 2013a. Fluid flow in relay zones revisited: Towards an improved representation of small-scale structural heterogeneities in flow models. Marine and Petroleum Geology 46, 144–164. https://doi.org/10.1016/j.marpetgeo.2013.05.016

Fachri, M., Tveranger, J., Braathen, A., Røe, P., 2016. Volumetric faults in field-sized reservoir simulation models: A first case study. AAPG Bulletin 100, 795–817. https://doi.org/10.1306/02011614118

Fachri, M., Tveranger, J., Braathen, A., Schueller, S., 2013b. Sensitivity of fluid flow to deformation-band damage zone heterogeneities: A study using fault facies and truncated gaussian simulation. Journal of Structural Geology 52, 60–79. https://doi.org/10.1016/j.jsg.2013.04.005

Fisher, Q.J., Knipe, R.J., 1998. Fault sealing processes in siliciclastic sediments. Geological Society Special Publication 147, 117–134. https://doi.org/10.1144/GSL.SP.1998.147.01.08

Fossen, H., Rotevatn, A., 2016. Fault linkage and relay structures in extensional settings-A review., Earth-Science Reviews. https://doi.org/10.1016/j.earscirev.2015.11.014

Freeman, B., Boult, P.J., Yielding, G., Menpes, S., 2010. Using empirical geological rules to reduce structural uncertainty in seismic interpretation of faults. Journal of Structural Geology 32, 1668–1676. https://doi.org/10.1016/j.jsg.2009.11.001

Freeman, B., Yielding, G., Badley, M., 1990. Fault correlation during seismic interpretation. First Break 8, 87–95. https://doi.org/10.3997/1365-2397.1990006

Gudlaugsson, S.T., Faleide, J.I., Johansen, S.E., Breivik, A.J., 1998. Late Palaeozoic structural developments of the south-western Barents Sea. Marine and Petroleum Geology 15, 73–102. https://doi.org/10.1016/S0264-8172(97)00048-2

Gupta, S., Underhill, J.R., Sharp, I.R., Gawthorpe, R.L., 1999. Role of fault interactions in controlling synrift sediment dispersal patterns: Miocene, Abu Alaqa Group, Suez Rift, Sinai, Egypt. Basin Research 11, 167–189. https://doi.org/https://doi.org/10.1046/j.1365-2117.1999.00300.x

Iacopini, D., Butler, R.W.H., 2011. Imaging deformation in submarine thrust belts using seismic attributes. Earth and Planetary Science Letters 302, 414–422. https://doi.org/https://doi.org/10.1016/j.epsl.2010.12.041

Iacopini, D., Butler, R.W.H., Purves, S., 2012. Seismic imaging of thrust faults and structural damage: A visualization workflow for deepwater thrust belts. First Break 30, 77–84. https://doi.org/https://doi.org/0.3997/1365-2397.30.5.58681

Knipe, R.J., 1992. Faulting processes and fault seal. Norwegian Petroleum Society Special Publications 1, 325–342. https://doi.org/10.1016/B978-0-444-88607-1.50027-9

172

Knipe, R.J.J., 1997. Juxtaposition and seal diagrams to help analyze fault seals in hydrocarbon reservoirs. AAPG Bulletin 81, 187–195. https://doi.org/10.1306/522B42DF-1727-11D7-8645000102C1865D

Larsen, P.-H., 1988. Relay structures in a Lower Permian basement-involved extension system, East Greenland. Journal of Structural Geology 10, 3–8. https://doi.org/10.1016/0191-8141(88)90122-8

Linjordet, A., Olsen, R.G., 1992. The Jurassic Snøhvit gas field, Hammerfest basin, offshore northern Norway. Giant Oil and Gas Fields of the Decade 1978-1988. American Association of Petroleum Geologists, 349–370.

Long, J.J., Imber, J., 2012. Strain compatibility and fault linkage in relay zones on normal faults. Journal of Sedimentary Petrology 36, 16–26. https://doi.org/http://dx.doi.org/10.1016/j.jsg.2011.12.013

Long, J.J., Imber, J., 2010. Geometrically coherent continuous deformation in the volume surrounding a seismically imaged normal fault-array. Journal of Structural Geology 32, 222–234. https://doi.org/https://doi.org/10.1016/j.jsg.2009.11.009

Manzocchi, T., Carter, J.N., Skorstad, A., Fjellvoll, B., Stephen, K.D., Howell, J.A., Matthews, J.D., Walsh, J.J., Nepveu, M., Bos, C., Cole, J., Egberts, P., Flint, S., Hern, C., Holden, L., Hovland, H., Jackson, H., Kolbjörnsen, O., MacDonald, A., Nell, P.A.R., Onyeagoro, K., Strand, J., Syversveen, A.R., Tchistiakov, A., Yang, C., Yielding, G., Zimmerman, R.W., 2008a. Sensitivity of the impact of geological uncertainty on production from faulted and unfaulted shallow-marine oil reservoirs: Objectives and methods. Petroleum Geoscience 14, 3–15. https://doi.org/10.1144/1354-079307-790

Manzocchi, T., Childs, C., Walsh, J.J., 2010. Faults and fault properties in hydrocarbon flow models. Geofluids 10, 94–113. https://doi.org/10.1111/j.1468-8123.2010.00283.x

Manzocchi, T., Heath, A.E., Palananthakumar, B., Childs, C., Walsh, J.J., 2008b. Faults in conventional flow simulation models: a consideration of representational assumptions and geological

uncertainties. Petroleum Geoscience 14, 91–110. https://doi.org/10.1144/1354-079306-775

Miocic, J.M., Johnson, G., Bond, C.E., 2019. Uncertainty in fault seal parameters: implications for CO2 column height retention and storage capacity in geological CO_2 storage projects. Solid Earth 10, 951–967. https://doi.org/https://doi.org/10.5194/se-10-951-2019

NPD, 2020. Snøhvit Field Overview [WWW Document], Norwegian Petroleum Directorate (NPD). URL https://factpages.npd.no/en/field/pageview/all/2053062 (accessed 4.30.20).

Ostanin, I., Anka, Z., di Primio, R., Bernal, A., 2012. Identification of a large Upper Cretaceous polygonal fault network in the Hammerfest basin: Implications on the reactivation of regional faulting and gas leakage dynamics, SW Barents Sea. Marine Geology 332–334, 109–125. https://doi.org/http://dx.doi.org/10.1016/j.margeo.2012.03.005

Peacock, D.C.P., Nixon, C.W., Rotevatn, A., Sanderson, D.J., Zuluaga, L.F., 2016. Glossary of fault and other fracture networks. Journal of Structural Geology 92, 12–29. https://doi.org/10.1016/j.jsg.2016.09.008

Peacock, D.C.P., Sanderson, D.J., 1994. Geometry and development of relay ramps in normal fault systems. AAPG Bulletin 78, 147–165. https://doi.org/10.1306/BDFF9046-1718-11D7-8645000102C1865D

Rippon, J.H., 1985. Contoured patterns of the throw and hade of normal faults in the Coal Measures (Westphalian) of north-east Derbyshire. Proceedings of the Yorkshire Geological Society 45, 147–161. https://doi.org/https://doi.org/10.1144/pygs.45.3.147

Rotevatn, A., Fossen, H., Hesthammer, J., Aas, T.E., Howell, J.A., 2007. Are relay ramps conduits for fluid flow? Structural analysis of a relay ramp in Arches National Park, Utah. Geological Society, London, Special Publications 270, 55–71. https://doi.org/10.1144/GSL.SP.2007.270.01.04

Schaaf, A., Bond, E.C., 2019. Quantification of uncertainty in 3-D seismic interpretation: Implications for deterministic and stochastic

geomodeling and machine learning. Solid Earth 10, 1049–1061. https://doi.org/10.5194/se-10-1049-2019

Shuey, R.T., 1985. A simplification of the Zoeppritz equations. Geophysics 50, 609–614. https://doi.org/https://doi.org/10.1190/1.1441936

Sund, T., Skarpnes, O., Nørgård Jensen, L., Larsen, R.M., 1984. Tectonic development and hydrocarbon potential offshore Troms, Northern Norway. AAPG Special Publication Memoir: Future Petroleum Provinces of the World. 615–627.

Townsend, C., Firth, I.R., Westerman, R., Kirkevollen, L., Harde, M., Andersen, T., 1998. Small seismic-scale fault identification and mapping. Faulting, Fault Sealing and Fluid Flow in Hydrocarbon Reservoirs, Special Publications 147. Geological Society of London, 1–25. https://doi.org/https://doi.org/10.1144/GSL.SP.1998.147.01.02

Turner, A.K., 2006. Challenges and trends for geological modelling and visualisation. Bulletin of Engineering Geology and the Environment 65, 109–127. https://doi.org/10.1007/s10064-005-0015-0

Walsh, J.J., Watterson, J., 1990. New methods of fault projection for coalmine planning. Proceedings of the Yorkshire Geological Society 42, 209–219. https://doi.org/10.1144/pygs.48.2.209

Walsh, J.J., Watterson, J., 1989. Displacement gradients on fault surfaces. Journal of Structural Geology 11, 307–316. https://doi.org/https://doi.org/10.1016/0191-8141(89)90070-9

Walsh, J.J., Watterson, J., 1988. Analysis of the relationship between displacements and dimensions of faults. Journal of Structural Geology 10, 239–247. https://doi.org/https://doi.org/10.1016/0191-8141(88)90057-0

Walsh, J.J., Watterson, J., 1987. Distributions of cumulative displacement and seismic slip on a single normal fault surface. Journal of Structural Geology 9, 1039–1046. https://doi.org/10.1016/0191-8141(87)90012-5

Watterson, J., 1986. Fault dimensions, displacements and growth. Pure and Applied Geophysics PAGEOPH 124, 365–373. https://doi.org/10.1007/BF00875732

Wilson, P., Elliott, G.M., Gawthorpe, R.L., Jackson, C. a. L., Michelsen, L., Sharp, I.R., 2013. Geometry and segmentation of an evaporite-detached normal fault array: 3D seismic analysis of the southern Bremstein Fault Complex, offshore mid-Norway. Journal of Structural Geology 51, 74–91. https://doi.org/10.1016/j.jsg.2013.03.005

Wilson, P., Hodgetts, D., Rarity, F., Gawthorpe, R.L., Sharp, I.R., 2009. Structural geology and 4D evolution of a half-graben: New digital outcrop modelling techniques applied to the Nukhul half-graben, Suez rift, Egypt. Journal of Structural Geology 31, 328–345.

Yielding, G., Freeman, B., Needham, D.T., 1997. Quantitative fault seal prediction. AAPG Bulletin 81, 897–917. https://doi.org/10.1306/522B498D-1727-11D7-8645000102C1865D

Appendices

Appendices from Paper I

Supplementary material 1: **Seismic modelling parameters of experiments 1 and 2**

The model:

Experiment 1:

The elastic isotropic model used in Experiment 1 is shown in Figure 3 of the paper. It is made of a background model and a perturbation model, the last one representing the faulted reservoir layer. The background model consists of a 300-meter-thick water layer with P-wave velocity of 1500 m/s, S-wave velocity of 0 m/s and density of 1040 kg/m^3. Between 300 m depth and 2300 m depth, the P-wave velocity model increases linearly from 2000 m/s to 3800 m/s, the S-wave velocities are half of the P-wave velocities, and the densities are given by Gardner's rule where $\rho= 310 * V_p^{0.25}$ kg/m^3. Below 2300 m depth, the velocity is constant and equal to 3800 m/s, the S-wave velocities are constant and equal to 1700 m/s, and the densities are constant and equal to 2434 kg/m^3.

The faulted reservoir layer consists of a 300-meter-thick layer centred at a depth of 2725 m. The layer is characterized by a drop of 150 kg/m^3 in density (2284 kg/m^3). A normal fault dipping 55° displaces the reservoir layer 150 m vertically and 105 m horizontally.

Experiment 2:

The model used in Experiment 2 uses the same background elastic isotropic model as Experiment 1, however Experiment 2 has a 65 m wide fault zone that was assigned different types of density transitions as shown in Figure 4b in the paper.

The seismic modelling:

The elastic isotropic model is discretized on a 5 by 5 m grid for the numerical simulation of elastic seismic wave propagation. The simulation is based on a 2D velocity-stress staggered grid finite difference modelling of the elastic isotropic wave equation (Virieux 1986). Absorbing boundary conditions are used to attenuate outgoing waves at all grid boundaries. This simulates an infinite reflection free medium beyond the boundaries of the elastic model. It also means that free surface multiples are not included in the modelling.

The acquisition geometry consists of 41 sources spaced by 350 m, ranging from –7000 to +7000 m on the top of the elastic isotropic model (sea level, Figure 3d-f of paper). The sources are modelled as hydrostatic pressure cylindrical sources (Bessel function of second kind). For each source, the x- and z-components of the particle velocity wavefields are recorded by 1401 receivers spaced by 5 m, placed from –3500 to +3500 m at a depth of 300 m (sea bottom, Figure 3d-f of paper). A total of 6 s of data are modelled and recorded for every source. The wavelet used for the source time function is a zero-phase Tukey window wavelet with an amplitude spectrum consisting of a half-cosine ramp between 4 and 10 Hz, where amplitudes increase from 0 to 1, a flat band with amplitude of 1 extending between 10 and 40 Hz, and a half-cosine ramp between 40 and 70 Hz where amplitudes decrease from 1 to 0 (Virieux 1986).

Seismic processing:

The only processing applied to the recorded x- and z- components of the particle velocity wavefields before migration is the subtraction of the direct and reflected seabed waves. This is done by modelling a dataset containing only these two arrivals (Using the top 300 m of the elastic isotropic model, water column) and subtracting these recordings from the data containing all arrivals. After pre-processing, the particle velocity data are separated in W (negative difference between receiver and source horizontal positions) and E azimuths (positive difference between

receiver and source horizontal positions) and migrated using a shot profile elastic reverse-time migration algorithm. The migration velocities are smooth versions of the true velocity models, and the densities are substituted by a spatially homogeneous model. The migration aperture is the same as the modelling aperture. The imaging principle for the PS images is based on the S-wave velocity gradient expressions used in non-linear elastic full-waveform inversion (Hokstad *et al.* 1998) and adapted to image the contrasts in S-wave impedance (product of density and S-wave velocity). Images of the individual shot migrations can be found in section 3 of the supplementary material.

For the seismic modelling and migration of the multi-layered fault plane models, a similar methodology is used.

The time-frequency analysis was carried out using the S-transform (Stockwell *et al.* 1996). The S-transform used is implemented in the open source seismic software Madagascar (http://www.ahay.org/wiki/Main_Page). The program used is called sfst (http://www.ahay.org/RSF/sfst.html).

To perform the time-frequency analysis, the images in depth were stretched to PS vertical time using the P- and S-wave velocity models. The amplitude spectrum of the S-transformed data was taken at selected points (refer to Figure 10 in the paper for location of extracted spectra).

Angle stacks:

The angle gathers are made from the surface offset migrated image gathers with the aid of an offset to angle table constructed from the P- and S-wave background velocity models. The equation describing the offset to angle table (e.g. Ikelle & Amundsen 2018) is given below:

$$O(\theta, z_n) = p\Delta_z \sum_{i=1}^{n} \frac{V_p(i)}{\sqrt{1 - p^2 V_p(i)^2}} + \sum_{i=s_b}^{n} \frac{V_s(i)}{\sqrt{1 - p^2 V_s(i)^2}}$$

where $O(\theta, z_n)$ is offset, θ is P-wave incidence angle at a depth of z_n and n are the number of layers above, z_n. Δ_z is the depth sampling interval of the velocity models. $V_p(i)$ and $V_s(i)$ are the P- and S- wave velocities of the discrete layer i respectively. $p = \frac{\sin(\theta)}{V_p(n)}$ refers to horizontal slowness. Finally, s_b is the index number of the seabed layer.

Some information on artefacts:

2D seismic lines from this experiment (supplementary material 2) show some minor concaved curved artefacts. In the acquisition of these models, the source emits a P-wave which, on reflection, backscatters as both PP and mode-converted PS-waves. The data are recorded as particle velocities in the horizontal and vertical directions. According to Mittet (1994) in order to distinguish between up- and down-going P- and S- waves, three orthogonal particle velocities and three orthogonal tractions are necessary. In our simple isotropic 2D study, the receivers only collect two orthogonal particle velocities and two tractions while the third particle velocity and traction are assumed zero. Without having this third value and therefore a full set of boundary conditions, it was not possible for P- and S- waves to be separated or to eliminate all artefacts due to crosstalk between P- and S- waves. This also means that, during migration, P-waves present in the receivers were migrated as S-waves, although with incorrect velocities, leading to artefacts. Although these artefacts usually evident, they were not further considered in their effect on imaging since they tend to be stacked out in a similar fashion as multiple reflections are attenuated in conventional stacking of PP data. The complete results of this experiment can be seen in the supplementary material either as a collection of pictures or videos.

Bibliography (Paper I: Supplementary Material 1)

Hokstad, K., Mittet, R. & Landrø, M. 1998. Elastic reverse time migration of marine walkaway vertical seismic profiling data. Geophysics, 63, 1685–1695, https://doi.org/10.1190/1.1444464.

Ikelle, L.T. & Amundsen, L. 2018. Introduction to Petroleum Seismology, https://doi.org/10.1190/1.9781560803447.

Mittet, R. 1994. Implementation of the Kirchhoff integral for elastic waves in staggered-grid modeling schemes. Geophysics, 59, 1894–1901, https://doi.org/10.1190/1.1443576.

Stockwell, R.G., Mansinha, L. & Lowe, R.P. 1996. Localization of the Complex Spectrum: The S-Transform. IEEE Transactions on Signal Processing, 44, 998–1001, https://doi.org/10.1109/78.492555.

Virieux, J. 1986. P-SV wave propagation in heterogeneous media. Geophysics, 51, 889–901, https://doi.org/10.1190/1.1442147.

Supplementary material 2A:

East azimuth processed 2D seismic images
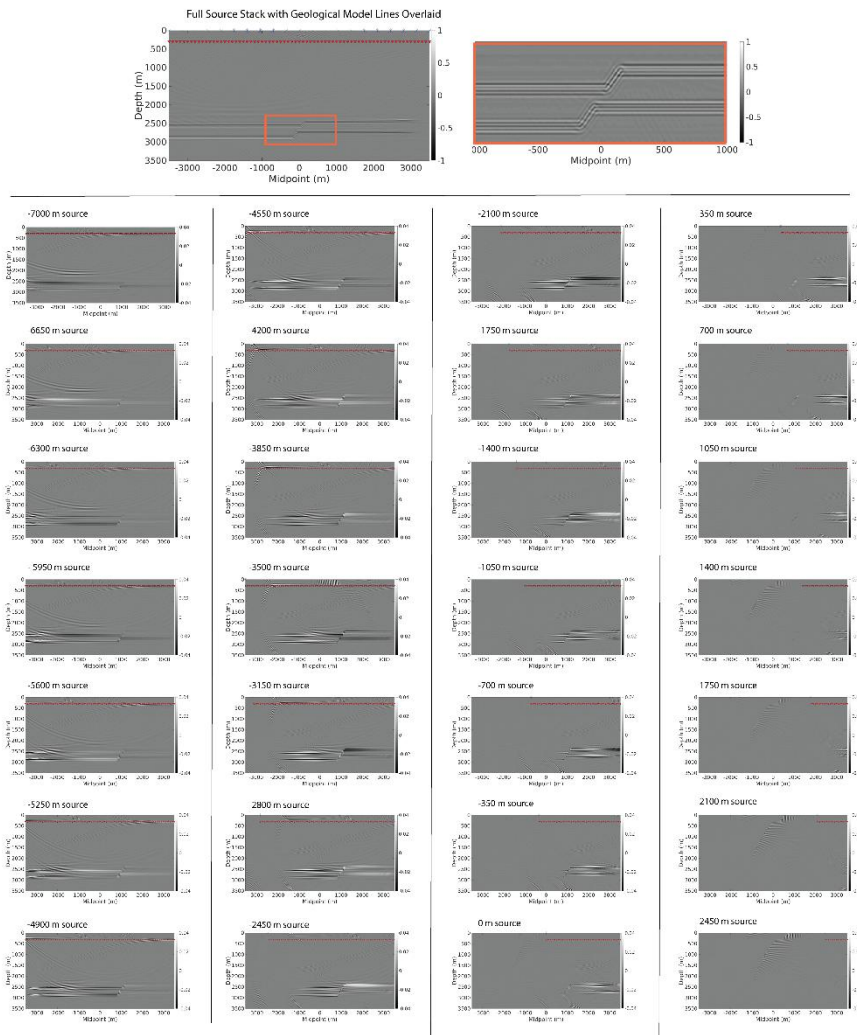
The images are available to download in high resolution at the following link: https://photos.app.goo.gl/8BWrL8DLS2SN6DsR7

Supplementary material 2B:

West azimuth processed 2D seismic images
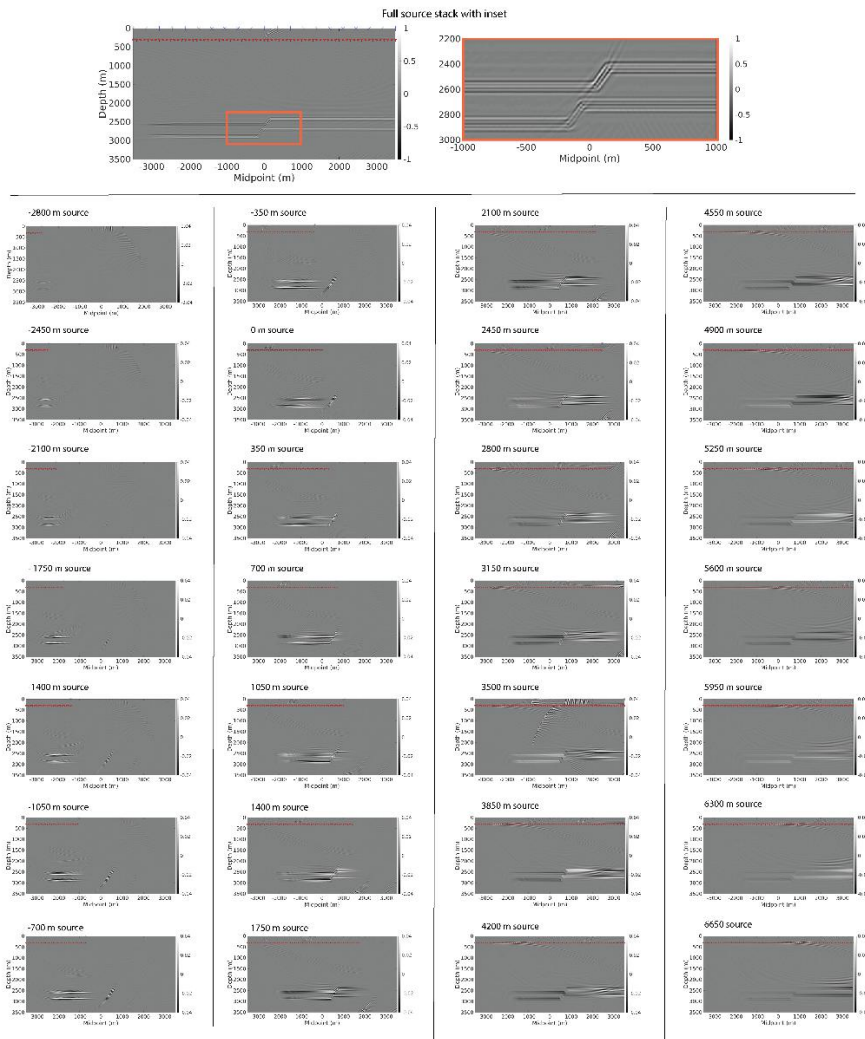
The images are available to download in high resolution at the following link: https://photos.app.goo.gl/yM1RPZYYk31oSbtp9

Supplementary material 3: Seismic modelling videos

Videos of the unprocessed seismic wave simulation for sources placed at -7000 m, -2000, 0, 2000 and 7000 m. The videos are in vertical (Vz) and horizontal (Vx) particle velocities.

Click on the following links to be brought to the video of your choosing:
- [Vx 7000m source location](#)
- [Vx 2000m source location](#)
- [Vx 0m source location](#)
- [Vx -2000m source location](#)
- [Vx -7000m source location](#)
- [Vz 7000m source location](#)
- [Vz 2000m source location](#)
- [Vz 0m source location](#)
- [Vz -2000m source location](#)
- [Vz -7000m source location](#)

The folder of supplementary material 2 and 3 for Paper I can be found here: https://photos.app.goo.gl/spE1wW53nTHCiYJN8

Appendices from Paper II

There were no appendices or supplementary material contained in this publication.

Appendices from Paper III

There were no appendices or supplementary material contained in this publication.